The effect of implantation and heat treatment on the structural evolution and migration behaviour of Selenium in glassy carbon

by

Samuel Adedigba Adeojo

Submitted in partial fulfilment of the requirements for the degree of

DOCTOR OF PHILOSOPHY (PhD) IN PHYSICS

In the Faculty of Natural and Agricultural Sciences at University of Pretoria

April 2023

Supervisor/Promoter: Prof. T.T. Hlatshwayo

Co-supervisor/Co-promoter: Prof. J.B. Malherbe

Co-supervisor/Co-promoter: Prof. E.G. Njoroge

UNIVERSITEIT VAN PRETORIA
UNIVERSITY OF PRETORIA
YUNIBESITHI YA PRETORIA

DECLARATION

I, **Samuel Adedigba Adeojo**, declare that the dissertation, which I, as a result of this, submit for the degree of PhD at the University of Pretoria, is my work and has not been submitted for a degree at this or any other tertiary institution.

Signature: 

Date: 07/07/2023

SUMMARY

The effect of implantation and heat treatment on the structural evolution and migration behaviour of Selenium in glassy carbon

Samuel Adedigba Adeojo

Submitted in partial fulfilment of the requirements for the award of the degree of Doctor of Philosophy (PhD) in Physics in the Faculty of Natural and Agricultural Science, University of Pretoria.

Supervisor/Promoter: Prof. T.T. Hlatshwayo
Co-supervisor/Co-promoter: Prof. J.B. Malherbe
Co-supervisor/Co-promoter: Prof. E.G. Njoroge

The storage and management of nuclear waste is perhaps the most controversial aspect of nuclear power production, as there is no permanent solution to this problem that has existed for centuries. In the last decade, our group at the University of Pretoria, South Africa, has been studying the suitability of glassy carbon (GC) as a nuclear waste storage material. Some of these studies focused on investigating the migration of strontium, caesium, silver, cadmium, indium, europium, and xenon in GC. No research information on the migration of selenium (Se) in GC in the literature, hence this study. A radioisotope of Se, ^{79}Se is a fission product found in spent fuel and reprocessed nuclear fuel. Its release into the environment has associated health hazards.

In this study, Se ions of 150 keV were implanted into GC substrates to a fluence of 1×10^{16} ions/cm^2 at room temperature (RT), 100, 150 and 200 °C. The samples implanted at RT and 200 °C were characterised by transmission electron microscopy (TEM) to compare the radiation damage level with respect to the implantation temperatures. Some as-implanted samples were sequentially annealed at the low-temperature regime (300 – 700 °C) and high-temperature regime (1000 – 1200 °C) for 5 h in steps of 100 °C. A new set of as-implanted samples were isochronally annealed at 1000, 1100 and 1200 °C for 5 h cycles. The migration of Se was monitored by Rutherford backscattering spectrometry (RBS) and secondary ion

mass spectroscopy (SIMS). Raman spectroscopy was used to monitor the microstructural changes in the GC substrates.

Se implantation induces radiation damage at relatively comparable depths in the GC samples implanted at RT and 200 °C. The damaged layer in the RT sample corresponds to about 8.5 dpa, greater than 0.2 critical dpa, which will totally distort the GC microstructure. The microstructures of the as-implanted GC samples were damaged by Se ion implantation, which increases with increasing implantation temperatures. The sample implanted at RT has a more graphitic disorder and the 200 °C sample has the least damaged microstructure and is less graphitic.

Annealing the as-implanted samples at 300 – 700 °C resulted in a limited recovery of the GC substrate and appreciable recovery was observed at the high-temperature regime, 1000 – 1200 °C.

No measurable diffusion of Se atoms occurred in all the as-implanted samples after annealing at the low-temperature regime (300 – 700 °C). At 1000 °C, the RT Se profile broadens, indicating the diffusion of Se atoms. Further annealing at 1100 and 1200 °C resulted in the asymmetrical broadening of Se profiles towards the surface of the RT sample, accompanied by about 5 and 32 % losses of Se atoms, respectively. The Se profiles of the RT sample at 1100 and 1200 °C exhibited tailing towards the bulk, indicating the migration of Se in the bulk of the GC substrate. The diffusion coefficients of Se were calculated to be 4.79×10^{-20} and 5.90×10^{-20} m^2s^{-1} after annealing at 1000 and 1100 °C, respectively. No measurable diffusion of Se occurred in the sample implanted at 100 °C at the high-temperature regime, 1000 – 1200 °C. Segregation of Se at the surfaces of the samples implanted at 150 and 200 °C and sequentially annealed at 1000 – 1200 °C was observed, accompanied by the loss of Se and migration in the bulk of these substrates.

Overall, the SIMS profiles of the new sets of as-implanted samples isochronally annealed at the high-temperature regime were somewhat similar to those obtained by RBS, with minor differences. The differences in the RBS and SIMS profiles were attributed to the resulting different microstructures of these two samples (i.e., the sequentially and isochronally annealed sample types).

Generally, the migration behaviour exhibited by Se atoms in the bulk region of the as-implanted samples (after annealing) can be explained in terms of trapping and de-trapping

of the Se atoms by defects induced during implantation. The high-temperature annealing caused the annealing of defects in the less radiation damage region, creating pathways for Se atoms to migrate deeper into the bulk of the as-implanted and annealed GC samples.

One of the initial concerns in this research was the migration of Se atoms in the bulk of the GC substrates, as this will limit the use of GC as a potential nuclear waste storage container. With a minute concentration of Se atoms estimated in the bulk region of the GC, the integrity of GC (as a nuclear storage container) cannot be limited.

ACKNOWLEDGEMENTS

- Firstly, I am very grateful to God, the giver of life, knowledge and everything I enjoyed, for the successful completion of my PhD study.
- More importantly, my special thanks and appreciation goes to my academic promotor, Prof. T.T. Hlatshwayo, my co-promoters, Prof. E.G. Njoroge and Prof. J.B. Malherbe. Their immense patience, guidance, timely feedbacks, corrections and encouragement, cooperation, support, and tremendous discussions were pivotal to the successful completion of my PhD study. I can boldly say that I have learnt and grown under their collective supervision.
- I want to thank the Head of the Department. Prof. C.C. Theron for the part-time tutor/demmie jobs arranged for me, which helped my finances while studying at the University of Pretoria.
- Mrs. Elfrieda Meyburgh is appreciated for all the assistance she provided at the department during my study.
- I am very grateful to all my friends and colleagues in the nuclear material physics group and the University of Pretoria. I thank you all for your useful advice, discussion, assistance in one way or the other, encouragement and support. Thanks for making my stay in South Africa enjoyable and fun filled.
- A special debt of gratitude is owed to my wonderful wife (Tolulope) and my children (Adebare and Ademola) for releasing me for the PhD program and holding up for all the time I was unavailable. Your immense understanding and support are appreciated.
- I want to thank my parents (Late Pastor Y.A. and Mrs. J.A. Martins-Adeojo) for the training, prayers, support and encouragement. To all my siblings (Emmanuel, Deborah, Ebenezer, Esther and Gideon Adeojo), I want to say thank you for all you do.
- My appreciation goes to Hon. Fola Oyekunle and the Esanju family for their support.
- I wish to express my gratitude to the entire staff members of Obafemi Awolowo University, Ile-Ife, Nigeria, for the opportunity granted to me to commence the PhD program.
- The Federal Government of Nigeria is appreciated for the award of the AST&D TETFund scholarship.
- I appreciate the University of Pretoria for the Postgraduate Bursary award.

LIST OF ABBREVIATIONS

GC – Glassy carbon

FPs - Fission products

VHTR – Very-high-temperature reactor

MSR – Molten salt reactors

PBMR – Pebble bed modular reactors

FWHM – Full width at half maximum

HRTEM – High-resolution transmission electron microscopy

BFTEM – Bright field-transmission electron microscopy

HLW – High-level wastes

ILW – Intermediate-level wastes

LLW – Low-level wastes

MT – Mill tailings

PUREX – Plutonium and uranium recovery by extraction

MCA – Multi-channel analyser

RBS – Rutherford backscattering spectrometry

SIMS – Secondary ion mass spectrometry

TRIM – Transport of ions in matter

CCD – Charged coupled detector

TEM – Transmission electron microscopy

ED – Electron diffraction

EDP – Electron diffraction pattern

SAED – Selected-area electron diffraction

RT – Room temperature

TABLE OF CONTENTS

LIST OF FIGURES

LIST OF TABLES

Chapter 1

Introduction

1.1 Background to the study

The generation and utilization of sustainable and clean energy have become the core pillars of making a healthy economy. The global demand for sustainable energy today, especially in African countries, has led to the development and harnessing of several energy sources. Sources of energy take many forms. Renewable energy sources are wind, solar, hydropower, geothermal, biomass and biofuels, while non-renewable energy sources include nuclear energy and fossil fuels (coal, oil, and natural gas). Renewable energy sources such as hydropower, wind, and solar photovoltaics are mainly described as clean energy sources.

Over the years, these sources have been harnessed for electricity production and industrial activities. Nevertheless, the generation and distribution of these energy sources have been limited by certain factors. These factors include installation/operational factors (high production costs [Cae17] [Saa17], climatic factors (the intensity of sunlight and wind speed varies tremendously) [Cae17] [Cov16], local conditions (e.g., hydroelectric power depends on water availability from rainfall and water storage capability) [Cae17]. Amongst the renewable energy sources, solar and wind energies are more promising yet unstable and unreliable because they sometimes require a backup energy source [Cov16]. The exploitation of biomass and biofuel as renewable energy sources are also dependent on the availability and production of biomass fuels (like wood, crops, algae, manure, municipal wastes, and garbage) and biofuels (ethanol, biodiesel, and renewable gasoline) [Cae17]. Fossil fuels (coal, oil, and natural gas) have been the leading energy source in the last 50 years [Cae17]. They have produced excellent operational control in thermal plants [Sav19]. However, the problem with fossil fuel burning involves releasing of particulates and greenhouse gases (nitrogen monoxide, nitrogen dioxide, carbon monoxide, carbon dioxide, and sulfur dioxide) [Ken03] [Sha12] [Yuy13]. Particulates are the most dangerous type of air pollution [Was19] because of their ability to deeply enter the lungs and bloodstream, causing major problems like heart attacks and respiratory infections [USE16]. The greenhouse gases are responsible for air pollution, global warming [Mar19], acidic rain and eutrophication [And16] [Coo16]. For instance, a report shows that about 23 billion tons of carbon dioxide are released at 730 tons/sec into the atmosphere annually, half of which is

absorbed in the seas and vegetation, while the other half is released into the atmosphere [www1]. Besides releasing greenhouse gases, exploiting fossil fuels can also have a disastrous environmental impact on the ecosystem and humans. For example, gas flaring causes smog, the sudden release of dust during coal mining, the release of radioactive substances from coal mine/mill tailings, and the spillage of oil into seas and coastal bodies due to offshore exploration [Pie09]. All of these can result in serious health issues for humans and animals. It is also inevitable that water sources and edible crops will be contaminated with poisonous and heavy metals, as well as forests will be destroyed [Pie09] [Sha12]. Fossil fuels also deplete over time, raising the fear of their availability and supply in the future [Mar19].

Nuclear energy is a non-renewable energy source with good advantages, unlike other non-renewable energy source features. It is often seen as one of the solutions to the world energy budget because it produces adequate, sustainable, low carbon, and clean energy [Dah14] [Cae17]. Nuclear reactors can produce enormous amounts of energy without carbon emissions from burning fossil fuels. Other advantages of nuclear energy include peak power consumption, high fuel availability, and low radiation exposure per person [Ahe11]. Many developed countries have widely explored and harnessed nuclear energy for electricity generation, hydrogen production, and heat processing. The cons of nuclear energy have then been reviewed for improvement, and modern reactors like the very-high-temperature reactor (VHTR), Molten Salt Reactors (MSR), and Pebble Bed Modular Reactors (PBMR) [Seb01] have been proposed. However, the public has a negative opinion of this energy source, which stems from nuclear accidents that can lead to colossal radioactivity breakouts. Three major nuclear accidents recorded in history are the three-mile island accidents on the 28th of March 1979 in Pennsylvania, United States of America, the Chernobyl nuclear disaster on the 26th of April 1986 at Pripyat in Northern Ukraine in the old Soviet Union [Tom06] and the Fukushima Daiichi nuclear accident of 11th of March 2011 in Japan. Nuclear accidents always negatively impact lives and the environment because a massive amount of radioactivity is released during the event.

For several decades, the use of nuclear energy as a source of clean energy has also been undermined by the lack of proper storage of nuclear waste. Managing nuclear waste is a major problem facing the nuclear industry and has to date, received great attention.

1.2 Nuclear waste characterisation

Nuclear waste is any substance that contains or is polluted by radionuclides at a concentration level higher than the exempted amounts set by the competent authorities and for which no use is foreseen [IAE94]. Since radioactive materials have numerous scientific applications, nuclear waste can be produced from various sources and applications. Nuclear waste can be generated during nuclear engagement activities such as electricity generation through nuclear power plants, nuclear weapons production, and radionuclides production for medical uses [IAE08]. This waste contains a mixture of short-lived and long-lived radioactive and non-radioactive nuclides. The storage of this waste is accompanied by several chemical and nuclear reactions. Nuclear waste is characterised as [www2]:

- Low-level waste
- Intermediate-level waste
- Mill tailings
- High-level waste.

1.2.1 Low-level waste (LLW)

This waste type is identical to municipal waste, such as mops, rags, medical tubes, used surgical equipment and residues, and laboratory animal carcasses [www3]. Low-level waste has a small amount of radioactivity and can be generated from hospitals, industries, pharmaceutical plants, offices, university laboratories, research facilities, oil and gas facilities, mines, and sometimes nuclear fuel cycles [Tan90]. The danger of exposure to LLW radiation varies based on the type and concentration of the radioactivity present. The LLW has a low radiological impact on the environment and human lives, but it could pose a threat when technologically enhanced through human activities [USE06]. For example, radioactive materials used in medical research are not hazardous unless inhaled or consumed. Low-level waste can be disposed of in a landfill and does not require special shielding [www3].

1.2.2 Intermediate-level waste (ILW)

They contain waste with higher amounts of radioactivity than low-level waste. This type of waste includes chemical sludge, resins, heavy metals, nuclear fuel cladding, and contaminated materials from reactor decommissioning. Long-lived radionuclides, such as uranium, thorium, radium, polonium, and radon, can sometimes be found in intermediate-

level waste. Intermediate-level waste can be disposed of by burying them close to the surface in shallow repositories or landfills [www3]. The intermediate-level waste is sometimes referred to as mill tailings.

1.2.3 Mill tailings (MT)

Mill tailings (MT) are referred to as ground solid and liquid waste, residues, or remains from uranium ore processing plants. According to an IAEA report [IAE92], mill tailings solid consists of slimes (clay, silt, and fine particles) and sands (heavier and coarser particles), which may contain chemical residues and precipitates from the mill process and some heavy metal contaminants. The mill tailings retain most of the radioactivity of the ore with large volumes and concentrations of the long-lived radioactive progenies. The volume of mill tailings generated at a particular mill depends largely on factors such as the mill throughput, the concentration of uranium in the ore, and the secondary waste produced during the mining process [IAE92]. Also, the radioactivity concentration in a tailing depends on the ore grade, uranium produced, and the daughter nuclides present. The usual mode of mill tailings disposal is a surface impoundment around the mill [IAE92]. The surface disposal of mill tailings usually exposes a large surface area of the land to radioactive elements, bio-toxic heavy elements, and other toxic compounds because of their consequent interaction with the surface water system [IAE92].

1.2.4 High-level nuclear waste (HLW)

High-level nuclear wastes are high-activity radioactive materials or byproducts of nuclear reactions in a reactor core. High-level nuclear wastes could be in the form of spent nuclear fuel [Lui11] or waste materials remaining after the fuel is reprocessed [Ojo05]. Spent nuclear fuels are used fuel and no longer efficient, but still thermally hot, highly radioactive, and potentially harmful. Every 12 to 18 months, about one-fourth to one-third of the total volume of spent fuel is removed from the reactor and replaced with fresh fuel [Lui11]. Spent fuels are also capable of self-sustained fission and can split uranium and plutonium atoms [Lui11]. Some of the radioactive elements in spent fuel have short half-lives. However, many of the radioactive elements in spent fuel have long half-lives. For example, plutonium-239 and plutonium-240 have half-lives of 24,000 years and 6,800 years, respectively.

1.3 Ways of managing radioactive nuclear waste

Management of radioactive nuclear wastes is vital to ensure minimal exposure to radioactivity. Protecting human health and the environment (now and in the future) is the primary reason for radioactive waste management [IAE95], as improper control of nuclear waste can release radioactivity through many pathways, such as the atmosphere, land, and aquatic ecosystems. Exposures of animals and humans may be through inhaling contaminated air and/or consuming contaminated food crops, vegetables, and animals, or ingesting contaminated waters. However, the pathway that produces the highest radioactivity will be determined by the concentration and waste accumulation in an environment [IAE92]. For example, man can be exposed to ^{222}Rn in aerosols and airborne particulates; ^{226}Ra in surface waters; ^{230}Th, ^{226}Ra, ^{210}Pb, ^{238}U, ^{99}Th, ^{126}Sn, ^{79}Se, ^{135}Cs, ^{222}Rn in soils [IAE92]. Throughout the many years of nuclear applications to benefit humanity, attention has also been given to managing the various types of waste generated. Laws, policies, acts, strategies, and methods, among many others, have been established and tested, which are discussed in the following subsections.

1.3.1 Surface Disposal

This disposal method is useful in managing LLW and short-lived ILW whose half-lives are up to 30 years. The surface disposal method could be at ground level or in caverns. Sometimes, it can be situated below the surface vaults with protective coverings (a few meters thick). Waste containers are placed in the vaults and backfilled until filled up. The vaults are then covered and capped with an impermeable membrane and topsoil. A gas venting system can be used as a form of drainage. Near-surface disposal facilities in caverns are below ground level. Unlike the near-surface disposal at ground level, where the excavations are conducted from the surface, shallow disposal requires underground excavation of caverns. The facility is several tens of metres below the earth's surface and accessed through a drift. The near-surface disposal facilities at ground level are in operation in some countries: South Africa (Vaalputs), United Kingdom (LLW Repository at Drigg in Cumbria), Spain (the LLW and ILW disposal facility in El Cabril); Japan (LLW Disposal Center at Rokkasho-Mura) and the USA (LLW disposal facilities at Texas Compact facility near the New Mexico border, Barnwell, South Carolina, Clive at Utah, Oak Ridge in Tennessee and Richland at Washington). The final repository for short-lived radioactive

waste (SFR) is in Forsmark, Sweden, 50 meters beneath the Baltic Seabed. Underground repositories for LLW and ILW are situated in Olkiluoto and Loviisa in Finland [www3]. Surface disposal storage systems for longer periods have also been suggested as an option for managing high-level nuclear waste (HLW) [www3]. This involves constructing a facility for interim storage that is not backfilled nor sealed to facilitate the monitoring, replacement, and repackaging of the waste every 200 years [www3]. However, permanent storage facilities can also be constructed to house HLW to keep them for thousands of years. These structures are referred to as 'Monolith' stores or 'Mausoleums'[www3].

1.3.2 National policies for managing High-Level waste

Organized plans, policies, strategies, and ways countries manage nuclear waste are imperative to managing LLW and HLW. Some established agencies and organizations are the United States Department of Energy and the United States Environmental Protection Agency, USEPA in the United States of America, ONDRAF in Belgium, NRC, ICRP, POSIVA in Finland, NDA in the United Kingdom, NMWO in Canada, SKB in Sweden, NWRDI in South Africa, etc. Most of these agencies are obligated with responsibilities such as monitoring the radiation dose limit of individuals, making and enforcing laws to regulate illegal dumping of nuclear wastes, enforce nuclear policies, among many others.

1.3.3 Vitrification and ion exchange of nuclear waste

The treatment of high-level nuclear wastes to stabilize and immobilize them for many years can be achieved through two sub-methods: vitrification [Lav13] [Lif03] [Pfi09] and ion exchange [IAE02] [Kim91] [Hal91]. In vitrification, bulk wastes are mixed with sugar and then calcined. The calcination process is followed by heating the solution with fragmented glass, and the new substance is melted and poured into a cylindrical stainless-steel container. The resulting fluid is vitrified and is complemented with other treatments via instrumentations. The resulting wastes after vitrification are expected to be immobilized for thousands of years [Ojo04] and buried in earth trenches [Lif03]. The ion exchange is used to reduce the radioactivity of aqueous nuclear waste into smaller volumes. This method removes radioactive metals from the high-level waste by using a ferric hydroxide floc, and the resulting sludge is mixed with cement and fly ash to form solid waste [Wil05].

1.3.4 Nuclear waste reprocessing

Nuclear waste reprocessing is the chemical treatment of spent fuel to recover plutonium and or uranium from the spent fuel. Reprocessing of nuclear fuel is the process of separating fission products from the actinides remains of spent nuclear fuel. This process has significant consequences regarding waste management policy [Aus79]. Reprocessing of nuclear waste has become the second most popular procedure for managing high-level nuclear waste. This process is useful in reusing uranium fuel that had once been used in a reactor. The plutonium uranium reduction extraction (PUREX) method is a standard reprocessing method". This process involves treating the irradiated or spent fuel with a concentrated nitric acid solution, which dissolves the insoluble solids (see Figure 1.1 for the PUREX method). The next step is to treat the resulting solution with tributyl phosphate and kerosene, which separate other fission products and leave the uranium-plutonium as the remaining mixture. Plutonium and uranium are separated from other fission products using decontamination factors greater than 10^7 [Bai07]. The uranium-plutonium mixture is then separated into uranyl and plutonium nitrates, respectively. Purification of the nitrates is done before converting them into oxides to have liquid products of Uranium oxide (UO_2) and Plutonium (IV) oxide (PuO_2) and can again be used as a reactor fuel [Bol18]. Despite the promising advantages of reprocessing, their operations still produce HLW residue but with reduced radioactivity.

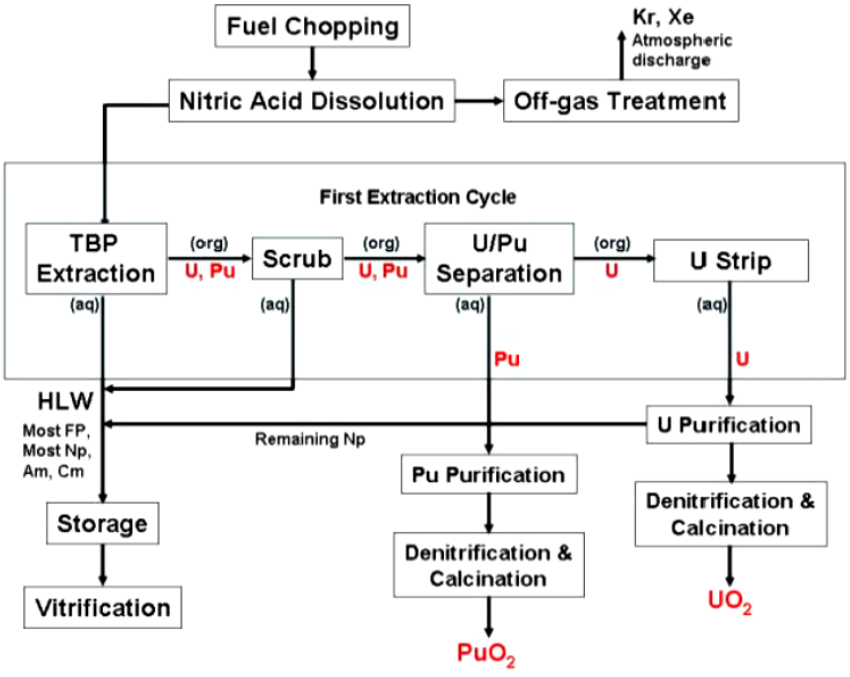

Figure 1.1. *Schematic of PUREX nuclear reprocessing method. Adapted from [Bai07].*

1.3.5 Management of nuclear waste through storage facilities

Nuclear waste management through storage facilities can be achieved through interim and permanent storage systems. These two approaches involve storing spent nuclear fuel for several years.

1.3.5.1 Interim (Wet and Dry) storage systems

Spent fuels characterized as high-level nuclear wastes are stored temporarily via wet and dry storage systems.

Wet storage systems: Spent nuclear fuels (SNF) assemblies are assembled in rods and kept at some depth under a pool of water, where they are allowed to cool down for five years or more [Weg19] [Liu14]. The pools are built with very thick concrete and lined with steel. The water inside the pool serves as a heat conductor to shield against radiation [NRC18], which cools the fuel assemblies [Liu14]. A typical wet storage system is shown in Figure 1.2. This facility is usually situated at reactor sites and some at designated secured places away from reactors. The design of a typical wet storage facility is chosen based on specific indices like fuel designs, operating periods, reactor consumption rate, and capacity to produce spent fuel. An electric pump is placed to prevent the pool's water from heating to the point of vapourization. This pump continuously circulates water through external exchangers, lowering the pool's temperature [Lui11], [Liu14]. The wet storage capacity can be improved with additional pools or by increasing the water volume. Another option is to swap out the pool rack as often as necessary. However, some issues have been discovered with the wet storage systems, which include increasing pool capacity [Weg19] [Sov13], potential degradation mechanisms which might induce uniform corrosion, and galvanic and microbiologically corrosion of the cladding system of the wet storage system [IAE12]. A possible terrorist attack on reactor sites [Weg19] can also endanger the spread of radioactivity. Yet another issue is the limited time of storage [Liu14]. The wet storage usually reaches its maximum capacity in a few years of usage. A natural disaster, like an earthquake, can also affect the wet storage system [Lui11], which is the case of the Fukushima nuclear event on the 11th of March 2011. This event led to the eventual shutdown of the three active nuclear reactors (units 1, 2, and 3) at the site, but the control rods were eventually used to quench the fission chain reaction. Later, a big tsunami wiped out the entire reactor site after the earthquake. It was recorded that about 18,000 TBq of the radioactive isotope of ^{137}Cs was released into the Pacific Ocean during the accident. In 2013, another report showed that 30 Gigabecquerel (GBq) of contaminated Cs-137 still flowed

into the ocean daily [Sov13]. Ever since this terrible nuclear accident, efforts have been made to decontaminate the affected areas [McC14]. For example, new walls were erected along the coast, and a 1.5 km-long “ice wall” of frozen earth was constructed to stop the flow of contaminated water [Mar16].

Figure 1.2. *Storage pond for used fuel at the Thermal Oxide Reprocessing Plant (Thorp) at the UK’s Sellafield site (Sellafield Ltd). Adapted from [www3].*

Dry storage systems are large tanks (containers or casks) where the fuel rods are stored. Figure 1.3 shows a typical cask with all its assemblages. The fuel rods inside are surrounded by inert Helium or Nitrogen gas [NRC02]. The steel cylinder provides leak-tight containment of the spent fuel. Each cylinder is sometimes covered by additional components, such as steel and concrete, which are meant to provide radiation shielding. There are various dry storage cask designs and types. For some, the cylinder is placed horizontally, while others can be oriented vertically on a concrete vault at a storage facility. Metals or concrete are used for radiation shielding in any cask configuration [Lui11]. Metals are usually made from steel, cast iron, lead, copper, and titanium alloys. The concrete cask

has the same inner configurations as the metallic cask, but its cylinder is surrounded by thick concrete. Some casks are designed for storage and transportation [NRC02].

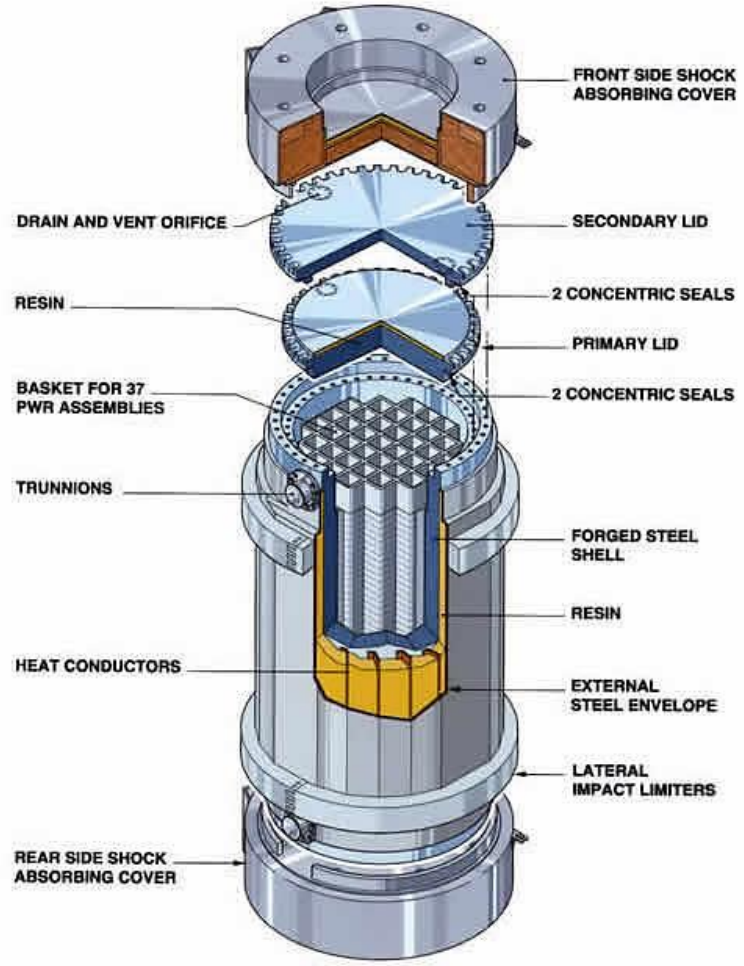

***Figure 1.3**. A typical-used fuel canister. Adapted from [www1].*

1.3.5.2 Deep geological repository system

This method entails burying the HLW in deep underground structures in an impermeable geological environment. Typically, geological repositories are located at least 300 meters (1000 feet) below ground to prevent human interference and erosion [IRS11]. Good geology, hydrogeology, and geochemistry most favour a geological repository. Geological repositories are preferred for the long-term management of long-lived and high-level waste [IAE89] [NEA95] [ICR98]. A geological repository's natural and engineered components include host rocks (e.g., granite), backfill, buffer, seal materials (e.g., cement), waste container materials (e.g., copper), and waste matrix (e.g., bitumen, glass) [IAE01]. Each of these components has its specific functions. For example, the rock formation within

the dug repositories protects the HLW from human access and against natural processes like earthquakes and climate change [NEA08]. The deep repository system relies on the multi-barrier concept for safety [IAE01].

The deep-level repository has not been widely accepted by many [Van07]. Until now, several underground research laboratories (URLs) are still working on overcoming potential challenges (like the suitability of rock salts as repository host formation and engineered barrier systems) facing deep geological repository projects.

1.4 Research Justification

Improving the quality and performance of the dry casks is pivotal to the effective storage of HLW. In other words, the casks must fulfil certain requirements to ensure the safety of people and the environment. The container should shield the nuclear waste from physical and chemical stress while being transported, stored, and thrown away. It must also be able to resist chemical attacks and must not be costly [Yim00]. One of the recently identified problems with dry casks is the materials used in their fabrication. These materials (copper, titanium alloys, nickel-based alloys, stainless steel, graphite) are briefly described alongside their shortcomings, which discredit their recommendation and suitability:

i. Copper has excellent environmental stability [Mil94] but performs poorly in brine and radiation environments [Wer92].
ii. Titanium alloys have excellent corrosion resistance and are mechanically robust but are expensive and susceptible to brittle failure [Yim00].
iii. Nickel-based alloys are also resistant to corrosion but costly [Yim00].
iv. Stainless steels are highly resistant to corrosion and have outstanding mechanical features, yet they are vulnerable to catastrophic failures from intergranular corrosion [Yim00].
v. Graphite is a common ceramic material with exceptional corrosion resistance properties but is presented with poor mechanical strength [Yim98].

Owing to the identified problems with the materials mentioned above, a replacement with a material, glassy carbon (GC), that is thermally stable, corrosion and radiation resistant, environmentally stable, and durable is proposed in this study. Glassy carbon performance is critical to ensure the safety of our ecosystem against the leakage of radioactive elements from HLW. The properties of GC are discussed in detail in Chapter 2 of this thesis.

1.5 Scope of Research

This study investigates the candidature of GC for constructing casks used in nuclear waste storage. Glassy carbon's suitability as a nuclear waste containment material would necessitate it being highly resistant to radiation damage caused by high-level radioactive nuclear waste. Additionally, it should function as a reliable diffusion barrier against fission product elements and actinides present in HLW.

Selenium has seven major natural isotopes, five of which are stable (^{74}Se, ^{76}Se, ^{77}Se, ^{78}Se, and ^{80}Se), and the other two (^{79}Se and ^{82}Se) are long-lived radioactive isotopes. Table 1.1 shows the isotopes of selenium with descriptions of their abundance, nature, origin/mode of formation, decay mode, decay product, and half-lives. The half-lives of ^{79}Se and ^{82}Se are approximately 377,000 [Bie07] and 10^{19} years [Aud17] (see Table 1.1). ^{79}Se is the only radioisotope of selenium that falls among the seven most long-lived radioactive fission products. It is found in trace amounts (about 0.0487% yield) [Nic07] in uranium ores, spent, and reprocessed nuclear fuel. As shown in Table 1.1, ^{79}Se can also be produced by the neutron activation of isotopic ^{78}Se [Sha10]. The decay of ^{79}Se is via beta particles, with an average energy/decay of ~0.0053 MeV [Eck08]. Because of its long half-life, the presence of ^{79}Se could be used to estimate the long-term radiological impact of a geological repository on the environment. Therefore, the leakage of any amount of ^{79}Se from geological repositories could lead to them being accumulated via a different environmental medium such as soil, sediments, and water and transported to humans and animals. The migration of radioactive selenium (^{79}Se) in the biosphere is expected to be similar to other non-radioactive selenium isotopes [Jac89]. Food crops have a low selenium tolerance but can pick up enough to be toxic to humans and animals [Jac89]. Selenium has been considered one of the macro elements needed for a healthy human body. However, ingestion or absorption in the body at concentrations higher than 400 μg/day is toxic and harmful [WHO96] and should be discouraged.

Table 1.1. *Main isotopes of selenium. Reproduced from references [Bow79] [Wil66] [Bie07] [Wik20] [www2].*

Isotope	Abundance (%)	Origin/mode of formation	Decay mode	Decay product	Half-life, $t_{1/2}$ (years)
^{74}Se	0.87	naturally occurring	stable		∞
^{76}Se	9.0	naturally occurring	stable		∞
^{77}Se	7.6	fission product	stable		∞
^{78}Se	23.5	naturally occurring, fission product	stable		∞
^{79}Se	Trace	fission product, ^{78}Se (n, γ) ^{79}Se	β^-	^{79}Br	377000
^{80}Se	49.8	naturally occurring, fission product	stable		∞
^{82}Se	9.2	fission product	$\beta^-\beta^-$	^{82}Kr	~10^{20}

This study reports on the migration behaviour of Se in glassy carbon. Glassy carbon was implanted with selenium (Se) at different implantation temperatures. The implanted samples were subsequently annealed at temperatures higher than the maximum implantation temperature. The structural analysis of the as-implanted and annealed samples was performed by Raman spectroscopy and transmission electron microscopy (TEM), while the migration behaviour of implanted Se was monitored by Rutherford backscattering spectrometry (RBS) and secondary ion mass spectrometry (SIMS).

1.6 Thesis Outline

There are eight (8) chapters in total in this thesis. Chapter 1 introduces energy forms and emphasizes nuclear power and its main challenges (i.e., nuclear accidents and waste management). Characterisation of radioactive nuclear waste, procedures and difficulties associated with its management are also discussed in this chapter. Chapter 1 also discusses the scope and justification of this research work. Chapter 2 discusses carbon, its various forms (allotropes), and their hybridizations and structures. Chapter 3 illustrates diffusion theory, while the ion implantation theory is provided in Chapter 4. Chapter 5 gives an overview of the analytical techniques. The experimental procedures are described in Chapter 6. The results are presented and discussed in Chapter 7 and finally, Chapter 8 gives the conclusions and recommendations.

References

[Ahe11] J.F. Ahearne. Prospect for nuclear energy. *Energy Economics*, **33 (4),** (2011), 572 – 580.

[And16] T.R. Anderson, E. Hawkins & P.D. Jones. CO_2, the greenhouse effect and global warming: from the pioneering work of Arrhenius and calendar to today's Earth system models. *Endeavour* **40 (3),** (2016), 178 – 187.

[Aud17] G. Audi, F.G. Kondev, M. Wang, W.J. Huang & S. Naimi. The NUBASE 2016 evaluation of nuclear properties. *Chinese Physics C*. **41 (3),** (2017).

[Aus79] R. Ausness, High-Level Radioactive Waste Management: The Nuclear Dilemma. *Wis. L. Rev.* (1979), 707 – 766.

[Bai07] P.A. Baisden & G.R. Choppin. Nuclear waste management and the Nuclear Fuel Cycle, in Radiochemistry and Nuclear Chemistry. S. Nagy (Ed.). In Encyclopedia of Life Support Systems (EOLSS), Developed under the Auspices of the UNESCO, EOLSS Publishers, Oxford, UK, (2007). Available at http://www.eolss.net. Accessed 15 July 2021.

[Bie07] Ph. Bienvenu, Ph. Cassette, G. Andreoletti, M. Bé, J. Comte & M. Lépy. A new determination of ^{79}Se half-life. *Appl. Radiat. Isot.* **65,** (2007), 355 – 364.

[Bol18] D. Bolgren & J. Menes. Nuclear Fuel Reprocessing. Nuclear Engineering course material, (2018), 1 – 25.

[Bow79] H.J.M. Bowen. Environmental Chemistry of the Elements. Academic Press, New York. (1979). 1 – 320.

[Cae17] N.S. Caetano, T.M. Mata, A.A. Martins & M.C. Felgueiras, New trends in energy production and utilization, *Energy Procedia*, **107,** (2017), 7 – 14.

[Coo16] J. Cook, N. Oreskes, P.T. Doran, W.R.L. Anderegg, B. Verheggen, E.W. Maibach, J.S. Carlton, S. Lewandowsky, A.G Skuce & S.A. Green. Consensus on consensus: A synthesis of consensus estimates on human-caused global warming. *Env. Res. Lett.* **11(4),** (2016), 1 – 7.

[Cov16] T. Covert, M. Greenstone & C.R. Knittel. Will we ever stop using fossil fuels? *J. Econ. Pers*. **30,** (2016), 117 – 138.

[Dah14] N.Y. Dahlan, A. Ibrahim, M.F Rajemi, M.N.M Nawi & F. Baharum, Analysis of the impact of nuclear power plant on Malaysia's power systems: Costs, CO_2 emission and system reliability. IEEE International Conference on Power and Energy (PECon), (2014). Accessed at http://ieeexplore.ieee.org/document/7062442/.

[Hal91] S. Halaszovich & M. Gomoll. Incineration of ion exchange resins from NPP, Waste Management. *Proc. Int. Conf. Tucson, AZ*. **91 (2),** (1991), 397 – 399.

[IAE89] International Atomic Energy Agency (IAEA). Safety Principles and Technical Criteria for the Underground Disposal of High Level Wastes, IAEA Safety Series No. 99, IAEA, Vienna, (1989), 1 – 67.

[IAE92] International Atomic Energy Agency (IAEA). Current Practices for the Management and Confinement of Uranium Mill Tailings, IAEA, Vienna, Austria, *Technical Report Series No. 355*, (1992), 1 – 139.

[IAE94] International Atomic Energy Agency (IAEA). Nuclear power, nuclear fuel cycle and waste management: Status and trends. Part C of the IAEA Yearbook, Vienna, Austria, (1994), 13 – 20.

[IAE95] International Atomic Energy Agency (IAEA). The principles of radioactive waste management, IAEA Safety Series No. 111-F, (1995), 1 – 21.

[IAE01] International Atomic Energy Agency (IAEA). The use of scientific and technical results from underground research laboratory investigations for the geological disposal of radioactive waste. IAEA-TECDOC-1243, IAEA, Vienna, Austria. (2001), 22 – 26.

[IAE02] International Atomic Energy Agency (IAEA), "Application of ion exchange processes for the treatment of radioactive waste and management of spent ion exchangers", IAEA, Vienna, Austria. *Technical Report Series TR – 804*, (2002), 67 – 85.

[IAE08] International Atomic Energy Agency (IAEA). Estimation of Global Inventories of Radioactive Waste and Other Radioactive Materials, *IAEA-TECDOC-1591,* (2008), 25 – 32.

[IAE12] International Atomic Energy Agency, Spent Fuel Performance Assessment and Research, Final Report of a Co-ordinated Research Project on Spent Fuel Performance Assessment and Research (SPAR-II). IAEA-TECDOC-1680, IAEA Vienna, Austria, (2012), 26.

[ICR98] International Commission on Radiological Protection (ICRP). Radiation Protection Recommendations as Applied to the Disposal of Long-lived Solid Radioactive Waste: ICRP Publication 81. *Ann. of the ICRP* **28 (4),** (1998), 1 – 2.

[Eck08] K. Eckerman & A. Endo. ICRP Publication 107. International Commission on Radiological Protection (ICRP), Nuclear decay data for dosimetric calculations, *Ann. ICRP*. **38 (3),** (2008), 7 – 96.

[IRS11] The French Institute for Radiological Protection and Nuclear Safety (IRSN). Radioactive Waste Management, Collecting, sorting, treating, conditioning, storing and disposing safely radioactive waste. (2011), 1 – 28.

[Jac89] L.W. Jacobs, Selenium in agriculture and the environment. *Am. Soc. Agron. Soil Sci. Soc. Am*., (1989), 37 – 65.

[Ken03] C. Kenneth & M. Greenstone. The Impact of Air Pollution on Infant Mortality: Evidence from Geographic Variation in Pollution Shocks Induced by a Recession. *Quarterly J. Econ*. **118 (3),** (2003), 1121 – 1167.

[Kim91] K.H. Kim. Solidification of spent ion exchange resins in polymers. *Proc. Int. Conf. on Waste Management*, Seoul, (1991), 12 – 86.

[Lav13] N.P. Laverov, B.I. Omel'yanenko, S.V. Yudintsev, S.V. Stefanovsky & B.S. Nikonov. Glasses for immobilization of low- and intermediate-level radioactive waste. *Geo. Ore Deps.* **55 (2),** (2013), 71 – 95.

[Lif03] F.A. Lifanov, I.A. Sobolev, S.A. Dmitriev, S.V. Stefanovsky, M.I. Ojovan, W.E. Lee & R. Burcl. Vitrification of Low and Intermediate Level Waste: Technology and Glass Performance. *Proc. WM '04 Conference*, Tucson, AZ. (2004), 3 – 8.

[Liu14] Y.Y. Liu, M.C. Billone, D.R. Diercks & O.K. Chopra. Ageing management for extended storage and transportation of used fuel. *In: Proc. 1st Intern. Conference on Ageing of Materials & Structures*, Delft, The Netherlands. (2014), 119 – 137.

[Lui11] S.R. Luiz. Advantages of dry hardened cask storage over wet storage for spent nuclear fuel. International Nuclear Atlantic Conference – INAC, Belo Horizonte, MG, Brazil, (2011), 3 – 8.

[Mar16] F. Martin. Japan's $320 Million Gamble at Fukushima: An Underground Ice Wall. *The New York Times*, (2016). Accessed 18 September 2022.

[Mar19] F. Martins, C. Felgueiras, M. Smitkova & N. Caetano. Analysis of Fossil Fuel Energy Consumption and Environmental Impacts in European Countries. *Energies.* **12,** (2019), 964.

[McC14] J. McCurry. Fukushima operator may have to dump contaminated water into Pacific. *The Guardian*. (2014). Accessed online at https://www.theguardian.com/environment/2014/mar/10/fukushima-operator-dump-contaminated-water-pacific on 19 October, 2022.

[Mil94] W. Miller, N. Chapman, R. Alexander, I. McKinley & J. Smellie. Natural analogue studies in the geological disposal of radioactive wastes (DOE-HMIP-RR-94031). United Kingdom, (1994), 47 – 95.

[NEA95] Nuclear Energy Agency (NEA). The Environmental and Ethical Basis of Geological Disposal. A Collective Opinion of the NEA Radioactive Waste Management Committee, OECD, Paris (1995), 2 – 15.

[NEA08] Nuclear Energy Agency, Moving forward with geological disposal of radioactive waste – A Collective Statement by the NEA Radioactive Waste Management Committee (RWMC), OECD, Paris. NEA (2008). Available at www.nea.fr/html/rwm/reports/2008/nea6433-statement.pdf.

[Nic07] A.L. Nichols, D.L. Aldama & M. Valleti, Handbook of Nuclear Data for Safeguards, IAEA Nuclear Data Section, INDC (NDS)-0502, Vienna, Austria, (2007), 1 – 94.

[NRC02] United States Nuclear Regulatory Commission (NRC). Radioactive waste: Production, storage and disposal, NRC, Washington, DC, United States of America, (2002). Available at https://www.nrc.gov. Accessed 15 August 2019.

[NRC18] United States Nuclear Regulatory Commission (NRC) (2018). Available online at https://www.nrc.gov. Accessed 15 August 2019.

[Ojo04] M.I. Ojovan, W.E Lee, J.H. Russell & N.V. Ojovan. Corrosion of nuclear waste glasses in non-saturated conditions: Time-Temperature behaviour. Proc. XX Congress on Glass, Kyoto, Japan, (2004).

[Ojo05] M.I. Ojovan & W.E. Lee. An Introduction to Nuclear Waste Immobilization, Elsevier Science Publishers, Amsterdam. (2005), 315.

[Pfi09] R. Pflieger, L. Lefebvre, M. Malki & M. Allix, A. Grandjean. Behaviour of Ruthenium Dioxide Particles in Borosilicate Glasses and Melts. *J. Nucl. Mat.* **389 (3)**, (2009), 450 – 457.

[Pie09] B. Pieprzyk, N. Kortlüke & P.R. Hilje. The impact of fossil fuels Greenhouse gas emissions, environmental consequences and socio socio-economic effects. Final Report of era – energy research architecture, prepared on behalf of Bundesverband Erneuerbare Energie e.V. November, (2009), 1 – 98.

[Saa17] M.A. Saad, F.A. Ismail, F.M. Fauzi & M.K. Rahmat. Consideration for Nuclear Energy in Malaysia. Proc. of the International Conference on Engineering Technologies & Technopreneurship, Kuala Lumpur, Malaysia, (2017), 1 – 7.

[Sav19] G. Savvidis, K. Siala, C. Weissbart, L. Schmidt, F. Borggrefe, S. Kumar, K. Pittel, R. Madlener & K. Hufendiek. The gap between energy policy challenges and model capabilities. *Energy* Policy, **125,** (2019), 503 – 520.

[Seb01] V. Sebian, V. Necas & P. Darilek, Transmutation of Spent Fuel in Reactors VVER-440, *Journal of Electrical Engineering*, **52 (9-10)**, (2001), 299 – 302.

[Sha10] G. Shaw & D. Ashworth. Selenium: radionuclides, Encycl. Inorg. Chem. Wiley, New York, (2010). Available at https://doi.org/10.1002/0470862106.ia718.

[Sha12] U. Shahzad. The Need for Renewable Energy Sources. *Int. J. Inf. Technology and Electrical Engineering*, **15,** (2012), 16 – 18.

[Sov13] B.K. Sovacool & A. Funk. Wrestling with the Hydra of Nuclear Waste Storage in the United States. *Electr. J.* **26,** (2013), 67 – 78.

[Tan90] Y.S. Tang & J.H. Saling. Radioactive waste management, Hemisphere Pub. Corp, New York. (1990), 212 – 260.

[Tom06] P. Tom. Opinion remains divided over Chernobyl's true toll. *The Lancet*. (2006), 1305 – 1306.

[USE06] USEPA, Technologically Enhanced Naturally Occurring Radioactive (TENORM) Materials from Uranium mining, Vol 1: Mining and Reclamation Background. USEPA, Washington, DC. *Technical Report*, EPA 402-R-05-007, (2006), 2-1 – 4-19.

[USE16] USEPA, OAR. Health and Environmental Effects of Particulate Matter (PM)". USEPA, (2016). Accessed 25 June 2021.

[Van07] R. Vandenbosch & S.E. Vandenbosch. Nuclear waste stalemate. Political and Scientific Controversies. The University of Utah Press, (2007), 140 – 250.

[Was19] A. Wasley, A. Heal, F. Harvey & M. Lainio. Revealed: UK government failing to tackle rise of serious air pollutant. *The Guardian 13th June 2019*. Accessed 15 May 2020.

[Weg19] S. Wegel, V. Czempinski, P. Oei & B. Wealer. Transporting and Storing High-Level Nuclear Waste in the U.S. – Insights from a Mathematical Model. *Appl. Sci.* **9,** (2019), 2 – 23.

[Wer92] L. Werme, P. Sellin, & N. Kjellbert. Copper Canisters for Nuclear High Level Waste Disposal. Corrosion Aspects, SKB Technical Report, TR-92-26 Stockholm, Norway: SKB, (1992), 2 – 18.

[WHO96] World Health Organization (WHO). Trace Elements in Human Nutrition and Health, World Health Organization, Geneva, (1996), 285.

[Wil05] W.R. Wilmarth, J.T. Mills & V.H. Dukes. Removal of Silicon from High-Level Waste Streams via Ferric Flocculation. *Sep. Sci. Tech.* **40,** (2005), 255 – 265.

[www1] http://www.epubs.surrey.ac.uk. Accessed 26 July 2019.

[www2] http://www.ecolo.org/documents/ Accessed 20 August 2019.

[www3] http://www.world-nuclear.org Accessed 12 August 2019.

[Yuy13] C. Yuyu, A. Ebenstein, M. Greenstone & H. Li. Evidence on the impact of sustained exposure to air pollution on life expectancy from China's Huai River policy. *Proc. Nat. Acad. Sci.* **110 (32),** (2013), 12936 – 12941.

[Yim98] M.S. Yim. Evaluation of Waste Forms for Immobilization of C-14 and I-129, EPRI Report TR-110096 (Rockville, MD: EPRI) (1998).

[Yim00] M. Yim & K.L. Murty, Materials issues in nuclear-waste management, *J. Min, Met. & Mat Soc*. **52 (9),** (2000), 26 – 29.

Chapter 2

Carbon and its allotropes

2.1 Carbon

Carbon is one of the essential elements in life. Carbon is the earth's fourth most abundant element (by mass). Carbon is known for combining itself and other elements to produce other compounds. Each carbon atom is identical in that they all have four valence electrons, which makes them easily bond with themselves to form long chains or rings [Fal07], resulting in various allotropes of carbon. Its common allotropes are graphene, graphite, diamond, amorphous carbon, GC, and fullerenes. The hybridization model can be used to explain the tetravalent structure of the carbon atom. The properties of carbon are listed in Table 2.1.

Table 2.1. *Properties of carbon*

Symbol	C
Atomic Number	6
Atomic Mass	12.0107 amu
Boiling point	4287 °C (for graphite)
Melting point	3500 °C
Classification	Metalloid
Natural isotopes	^{12}C and ^{13}C (stable), ^{14}C (radioactive)
Crystal structure	Hexagonal (graphite), cubic (diamond)
Density	GC (1.42 gcm^{-3}), graphite (2.26 gcm^{-3}) and diamond (3.35 gcm^{-3})
Ground state electronic configuration	$1s^2\ 2s^2\ 2p^2$
Oxidation states	+2, +3, and +4

2.1.1 Hybridization

Hybridization refers to the blending of two or more atomic orbitals to produce the same number of hybrid orbitals with the same shape and energy. The hybridizations peculiar to carbon and its allotropes are sp, sp^2 and sp^3, which can be obtained by mixing 2s and 2p orbitals of the carbon atom. For instance, diamond is sp hybridised, graphite has sp^2 hybridization, and GC has sp^2 and a small fraction of sp^3 hybridizations [Miy98]. The hybridization in the carbon atom is the basis that determines the structure and reactivity to form many carbon compounds.

2.1.1.1 *sp* Hybridization

When carbon (the central atom) is linked to two other atoms via two double bonds or one single and one triple bond, it is said to have undergone a *sp* hybridization [www1]. The 2s-orbital and one of the 2p-orbitals are mixed to form two sp orbitals, each containing 50% s-character and 50% p-character [Har21]. The s and p orbitals are pointed in opposite directions, resulting in a linear geometry of the hybridised atoms, and an angle of 180° is between the formed sigma (σ) bonds. A typical sp hybrid configuration is shown in Figure 2.1. The sp hybridised orbital increases electron density in the bonding region for a σ-bond to the atom's left and another σ-bond to the atom's right [Har21]. The two free outer electrons will enter the π-orbitals, where they can form π-bonds similar to the sp^2 configuration. The sp bonds are found in the structure of carbyne [Liu13], a substance known for its strength.

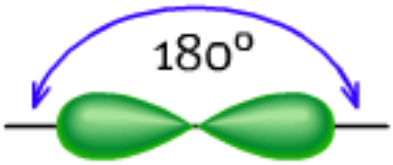

Figure 2.1. *sp hybrid configuration [Pes11]*

2.1.1.2 sp^2 Hybridization

The sp^2 hybridization is obtained by mixing one 2s-orbital with two 2p-orbitals (i.e., P_x and P_y) to form three *sp* orbitals, each containing 33% s-character and 67% p-character [Har21]. Two single bonds and one double bond are formed between the participating hybrid atoms, as shown in Figure 2.2 [www1]. The structure of the hybrids formed is trigonal planar with σ-bonds oriented at 120° to one another. The free unhybridised P_z orbital is perpendicular to the plane of the already formed sp^2 hybrid orbitals, resulting in weak π-bonds [Ans06]. Graphite has a sp^2 hybridization.

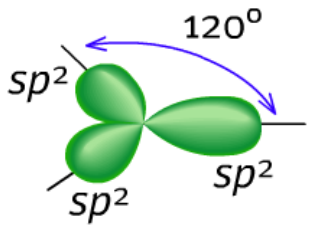

Figure 2.2. *sp^2 hybrid configuration [Pes11]*

2.1.1.3 sp^3 Hybridization

Figure 2.3 shows the sp^3 configuration, formed by mixing one 2s-orbital with three 2p-orbitals (i.e., P_x, P_y, and P_z). Each of the four sp^3 hybrids comprises 25% s-character and 75% p-character [www1]. Each sp^3 hybrid orbital is oriented at a bond angle of 109.5° from the other. A very strong σ-bond can be formed when the sp^3 hybrids overlap with the orbitals of different atoms. Diamond has sp^3 hybridization.

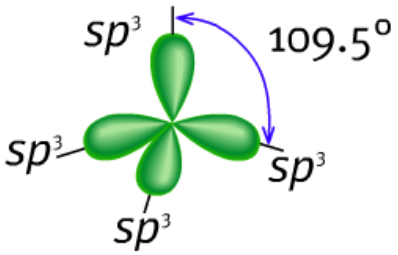

Figure 2.3. *sp3 hybrid configuration [Pes11]*

2.2 Carbon forms

The existence of a chemical element in two or more distinct forms (allotropes) is known as allotropy. Allotropes can have different atomic arrangements in crystalline solids or varying numbers of atoms in their molecules. Carbon is one of the elements that exhibits allotropy, whose allotropes are depicted in Figure 2.4.

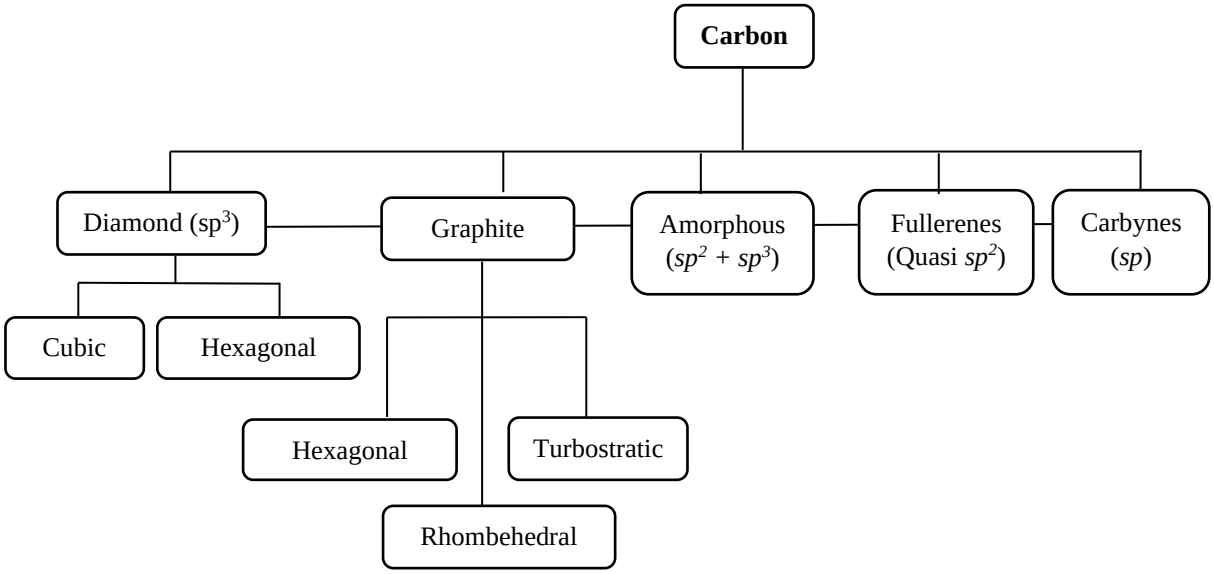

Figure 2.4*. Different forms of carbon*

2.2.1 Graphite

Graphite is a black, opaque allotrope of carbon made up of stacked graphene layers. Graphite was named by Abraham Gottlob Werner in 1789 from the Greek word meaning “to draw/write.” It is the most stable form of carbon. The primary source of graphite is graphite ore, which is created by the activity of organic matter in the layer of the earth’s crust. Graphite is made up of parallel rows of infinitely layered graphene planes. The graphene sheets are weakly linked by Van der Waals forces and are 3.354 Å apart from each other, with three covalent bonds holding each carbon atom to its layer [Pie93]. Each atom has an extra electron, which combines to produce a delocalized “sea” of electrons that loosely holds the layers together. The movement of these delocalized electrons (together) is responsible for the excellent electrical conductivity of graphite. Graphite can occur in hexagonal, rhombohedral, and turbostratic forms, as shown in Figure 2.5 and Figure 2.6.

The hexagonal form is the natural graphite, where the carbon layers are stacked in an ABAB… sequence, as shown in Figure 2.5 (left). Hexagonal graphite is also referred to as α-graphite. The C-C atoms in this graphite structure are separated by an inter-atomic distance of 1.41 Å and an inter-planar separation of 3.354 Å. The hexagonal graphite has an in-plane lattice parameter (a_o) of 2.456 Å, and the *c*-axis parameter is 6.708 Å [Pie93]. Hexagonal graphite has a high degree of stability and is abundant in nature. The rhombohedral or β-graphite has similar physical properties as the hexagonal graphite. It can be produced by the deformation (grinding) of hexagonal graphite, resulting in a different stacking sequence of the carbon layers (i.e., ABCABC... sequence). The fraction of rhombohedral graphite can be reduced by heat treatment at high temperatures, showing its instability compared to the stable hexagonal graphite. Figure 2.5 (right) shows the rhombohedral structure which has a lattice parameter of 0.3635 Å and cell angle $\alpha = 39.49°$. In comparison, the hexagonal structure within rhombohedral graphite has an in-plane lattice parameter of 2.456 Å and a *c*-axis parameter of 10.006 Å.

Both hexagonal and rhombohedral can be converted to yield a turbostratic or disordered graphite structure. In turbostratic graphite structure (shown in Figure 2.6), adjacent graphene layers are rotated relative to one another with no ideal orientation or stacking order. As a result, the interlayer spacing between the graphene layers is inconsistent, and turbostratic graphite is formed. Also, turbostratic graphite structure can be achieved by introducing rotational stacking faults in natural graphite.

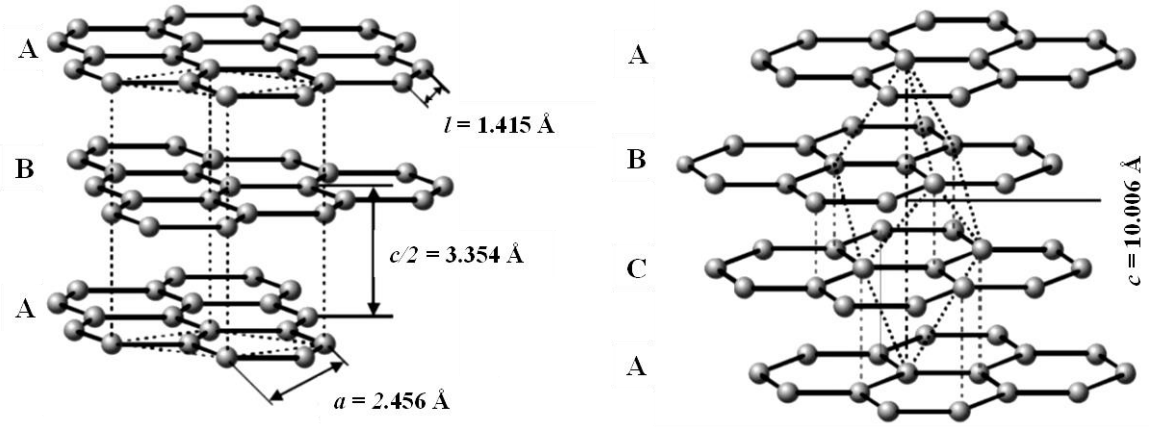

Figure 2.5. *The crystal structures of hexagonal graphite (left) and rhombohedral graphite (right). Modified from [Fra09].*

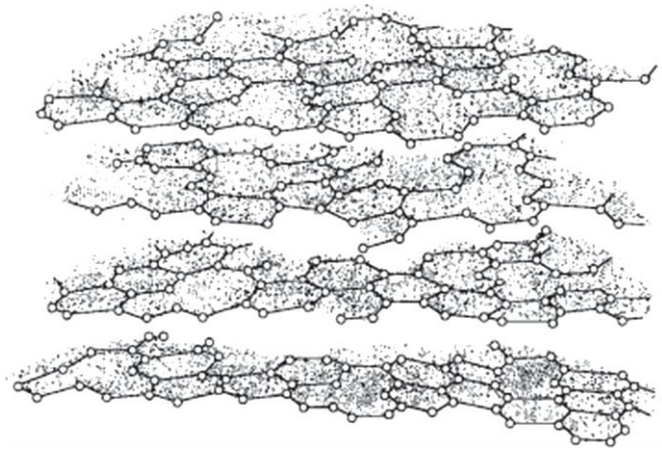

Figure 2.6. *Turbostratic graphite structure [Taken from Kin11]*

2.2.1.1 Properties of Graphite

Table 2.2. *Properties of crystalline (hexagonal and rhombohedral) graphite [Pie93*

1. Crystalline form	(a) Hexagonal (b) Rhombohedral
2. Lattice parameters	a_o = 2.456 Å c_o = 6.706 Å
3. Colour	Greyish black
4. Phase at STP	Solid
5. Young's modulus of elasticity	11.5 GPa
6. Density at 1.0 atm and room temperature	2260 kgm^{-3}
7. Brinell hardness	5 BHN
8. Atomic volume	5.315 cm^3/mol
9. Melting point	4450 K
10. Boiling point	4560 K
11. Carbon-carbon bond distance	1.41 Å
12. Atomic number density	1.14×10^{23} atoms/cm^3
13. Heat of vapourisation	355.8 – 598.2 kJ/mol
14. Specific heat capacity	0.690 - 0.719 kJ/kg-K
15. Binding energy	7.4 eV/C atom
16. Thermal conductivity at room temperature	*ab* direction – 398 W/m.K *c* direction – 2.2 W/m.K
17. Band gap	– 0.04 eV
18. Magnetic susceptibility	0.141×10^{-6} cm^3/g

Other properties of graphite include low friction and self-lubrication, good machinability, low coefficient of thermal expansion, high thermal resistance, high chemical and corrosion resistance, outstanding oxidation resistance, high radiation emissivity, high resistance to neutron radiation, ability to absorb radio waves, and ability to absorb gases [Pie93].

2.2.1.2 Applications of different forms of graphite

The many properties of graphite imply that there are numerous applications, as highlighted below:

- Graphite is primarily utilized as a refractory material, foundry facings, and steel production, as shown in Figure 2.7 [Yvo20]. Due to its exceptional high-temperature stability and chemical inertness, graphite is an excellent choice for refractory applications. Graphite is the source of the electrodes used in many electrical metallurgical furnaces. It is also used to make refractories that are useful for casting steel and refractories like Mag-Carbon bricks. Crucibles, ladles, and moulds for

holding molten metals are also made of graphite [Yvo20] [Pie93]. A portion of the blast furnace lining in the production of iron is made using graphite blocks.

- Crystalline graphite can be used to make pencils by combining them with clay [Pie93].
- Graphite is used in the chemical industry to produce phosphorus and calcium carbide in arc furnaces [Pie93]. It can also be used as an anode in aqueous electrolytic processes such as chlorine and fluorine production.
- Moderator rods and reflector parts in nuclear reactors are produced using significant volumes of highly pure electrographite [Pie93], [Yvo93]. Electrographite's applicability is due to its low neutron absorption, strong thermal conductivity, and high strength at higher temperatures [Man68].
- Carbon brushes for electric motors are mostly made from graphite [Pie93].
- Graphite is frequently utilized as a material in a wide range of engineering applications, including piston rings, brake pads, thrust bearings, journal bearings, and vanes [Pie93]. The fuel pumps and shafts of some aircraft jet engines employ seals made of carbon [Pie93], [Yvo20].
- Graphite makes an excellent battery component. Graphite also makes up the carbon rods in conventional batteries [Pie93], [Yvo20].

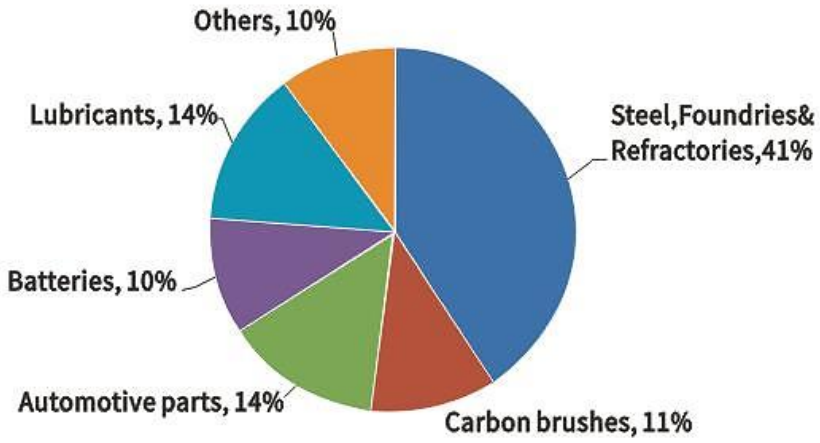

Figure 2.7. *Applications of graphite. Adapted from [Yvo20]*

2.2.2 Diamond

Diamond is the purest crystalline form of carbon allotropes and is the hardest solid known. It is one of the earth's scarcest, most sought-after solids. Many crystalline forms of diamond exist, but cubic and hexagonal diamond crystal structures are popular. The hexagonal diamond is generally found as lonsdaleite, which is less hard compared to cubic diamond [Pie93]. The carbon atoms in the hexagonal diamond are arranged in ABCABC… stacking, while the ABAB… stacking is the arrangement in the cubic diamond (see Figure 2.8).

From this point onward, the cubic diamond will be discussed and referred to (as diamond) because it is common and its structure is isotropic and similar to graphite. Each carbon atom in diamond (with sp^3 hybridisation) is covalently bonded to four carbon atoms, forming a tetrahedral lattice network [Pie93]. A dense three-dimensional structure of the diamond is created when a lattice unit is connected to two different carbon atoms, which are further bonded to four carbon atoms to yield similar tetrahedral configurations, as shown in Figure 2.9. The features of the densely conjugated arrangement of carbon atoms, the short bond length of 1.55 Å between nearest neighbouring carbon atoms and the high bond energy of 170 kCal/mol are responsible for most of its physical properties and applications. The structure of crystals in a cubic diamond can be described as a pile of puckered infinite layers (111 planes) or two face-centred (interpenetrating) cubic lattices (including one at 0,0,0 and the other at 1/4,1/4,1/4 with parallel axes) [Pie93].

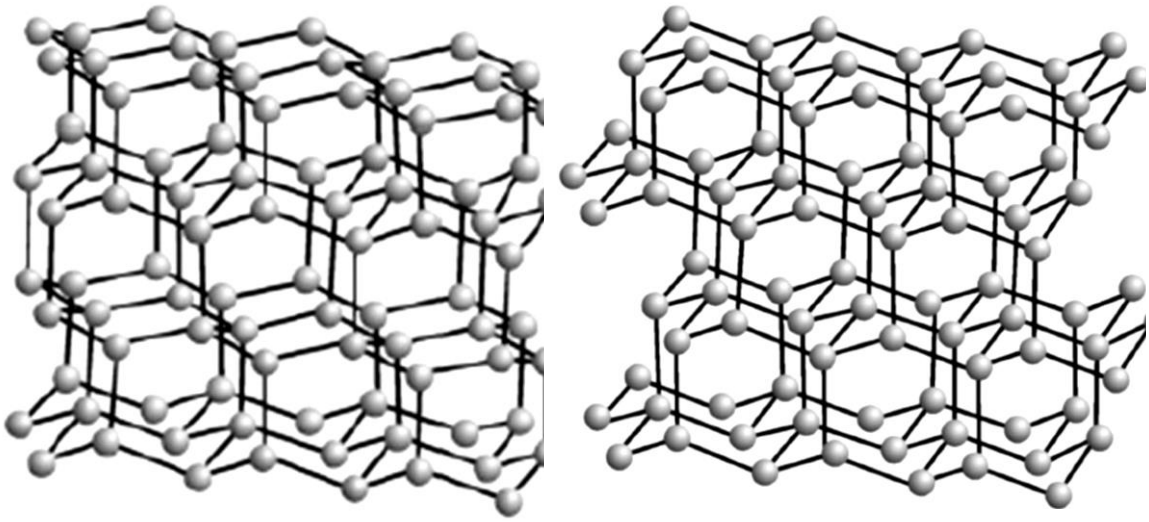

Figure 2.8. *Hexagonal diamond (left) and Cubic diamond (right) (Taken from [Kru10])*

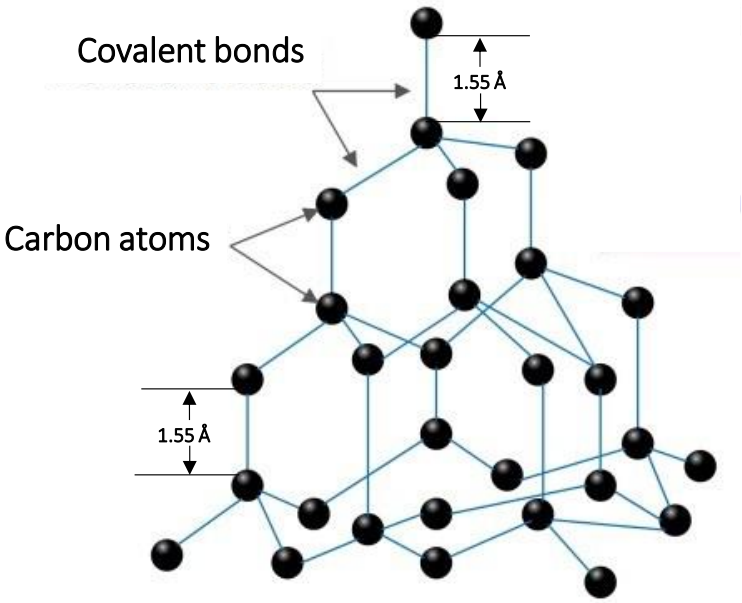

Figure 2.9. *Structure of diamond lattice (Modified from [Mal99])*

2.2.2.1 Properties of Diamond

Diamond has high hardness. It has a high thermal conductivity due to its four neighbours and the sp^3 hybridization. By doping with other elements like nitrogen, boron, etc., diamond can act as an excellent electrical insulator and as a wide bandgap in a semiconductor. Diamond has a good radiation barrier to neutrons. Its high refraction index is the basis for its primary industrial application. See Table 2.3 below for more properties of cubic and hexagonal diamonds.

Table 2.3. *Properties of cubic and hexagonal diamond [Pie93] [Dre96] [Hay17].*

1. Crystalline form	(a) Cubic (b) Hexagonal
2. Lattice parameter	a_o = 2.52 Å c_o = 4.12 Å
3. Density	3.52 g/cm^3
4. Band gap	– 5.5 eV
5. C-C Bond length	1.54 Å
6. Interplanar distance in hexagonal diamond structure	2.05 Å
7. Thermal expansion coefficient (at room temperature)	1.06 × 10^{-6} °C^{-1}
8. Thermal conductivity (at room temperature)	20 W/cm-K
9. Hardness	10000 kg/mm^2
10. Tensile strength	> 1.2 GPa
11. Compressive strength	> 110 GPa
12. Young's modulus	1.22 Gpa
13. Resistivity	10^{18} Ω-m
14. Dielectric strength	1 × 10^7 V/cm
15. Coefficient of friction	
(a) in Air	0.05 – 0.1
(b) in Vacuum	~1

2.2.2.2 Applications of Diamond

The application of diamonds in many aspects of science and industry is based on their excellent properties.

- Because it is the hardest substance known, it is suitable for abrasive devices and tribological applications [Fal07].
- Its high dielectric breakdown, high dielectric constant, low loss tangent, and low mass density make it a perfect material for energy storage [Che08].
- It is practically the only capacitor material suited for significant temperature variations because of its low coefficient of thermal expansion and high-temperature endurance [Che08].
- Diamond is a good candidate for heat exchangers because of its outstanding thermal properties, hardness, and chemical inertness [Che08].
- It is a valuable heat sink material for electronic equipment due to its high thermal conductivity and electrical resistivity [Che08].

- The diamond protective coating can be utilised as windows in a variety of applications since it also exhibits outstanding optical transparency across a broad wavelength range; as a semiconductor [Che08]
- Due to its remarkable hardness and abrasion resistance, diamond is useful in manufacturing drilling, cutting, and grinding tools [Pie93].
- Due to its high-temperature stability, diamond is significantly superior to typical wide energy-gap semiconductors, making it particularly applicable for the next generation of computer chips [Che08].

2.2.3 Amorphous Carbon

Amorphous carbon is a class of carbon material that lacks crystalline structural order. Before the fullerenes and nanotubes were discovered, amorphous carbon was thought to be the third allotrope of carbon. It is made up of a combination of tetrahedral (sp^3), trigonal (sp^2), and linear (sp) bonds. Amorphous carbon usually contains impurities such as some nitrogen and hydrogen atoms. Amorphous carbons are produced when an organic polymer or hydrocarbon precursors are pyrolysed at temperatures below 1500 °C. After additional heat treatment, the initial material's composition and preparation history significantly impact how it develops structurally and its final quality [Fal07]. The ratio of sp^2 to sp^3 hybridised bonds in amorphous carbon determines its characteristics. Amorphous carbon is renowned for its toughness, abrasion-resistant, and low thermal and electrical conductivities.

2.2.4 Fullerenes

Fullerene is a synthetic carbon allotrope. It can be described as a fused ring system made up of pentagons and hexagons of carbon atoms clusters in the molecular range of C_{30} – C_{100}. Eiji Osawa of Japan originally predicted the existence of buckyballs in 1970 when he noticed that corannulene was a component of the football framework and proposed the full ball structure would be possible [Hal06]. The first fullerene, Buckminsterfullerene (C_{60}), was later discovered in 1985 by a group of scientists working together at Rice University. The scientists are Smalley, Curl, Heath, O'Brien and Kroto. The various methods of producing fullerenes include arc heating, electric, laser ablation, and hydrocarbon pyrolysis (for the large production of fullerenes). There are 60 carbon atoms in the C_{60} molecule, which are organised into 12 pentagons and 20 hexagons [Tay93]. The double bonds are highly conjugated, and all rings are joined. The 120 symmetrical actions in the molecule, including rotation (about an axis) and reflection (in a plane), map the

molecule onto itself, accounting for the fullerene's remarkable degree of symmetry. The ability of the C_{60} molecule to accept one to six electrons, despite being highly electron-rich, and generate corresponding anions is one of the most remarkable findings made from all the research that has already been done on fullerenes [Por19]. Other types of fullerenes are C_{20}, C_{28}, C_{32}, C_{44}, C_{50}, C_{58}, C_{70}, C_{76}, C_{84}, C_{240}, C_{540}, and C_{960}. Different types of fullerenes can be built using hexagons and pentagons configurations. Notably, regardless of the number of hexagons, each form of the structure must always have 12 pentagons. Pentagons are required in a closed fullerene structure. In every type of fullerene, the number of vertices must also be even. The C_{60} and C_{70} members are the most common, while other fullerenes are rare. Fullerenes can appear in other definitions such as nanotubes, mega tubes, polymers, nano "onions," and linked "ball-and-chain" dimers. The 2D and 3D molecular structures of buckminsterfullerene are shown in Figure 2.10.

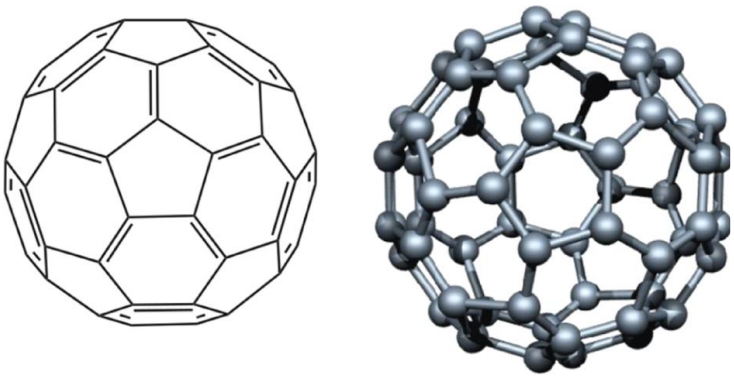

Figure 2.10. *2D and 3D molecular structure representations of buckminsterfullerene (C60) [Adapted from Por19]*

2.2.4.1 Properties of Fullerenes (Buckminsterfullerene)

Table 2.4 shows some physical properties of buckminsterfullerene, C_{60} [Dre96].

Table 2.4. *Properties of Buckminsterfullerenes*

Crystal structure	*Face-centred cubic (fcc)*
Lattice constant	1.417 nm
Density (1 atom)	1.72 gcm^{-3}
Molecular number density	$1.44 \times 10^{21} cm^{-3}$
C_{60}-C_{60} bond distance	1.002 nm
C_{60}-C_{60} cohesive energy	1.6 eV
Thermal conductivity (300 K)	0.40 $Wm^{-1}K^{-1}$
Electrical conductivity (300 K)	1.7×10^{-9} Sm^{-1}
Melting Point	1180°C
Sublimation temperature	434°C
Bulk Modulus (300 K)	6.8 GPa
Compressibility	6.9×10^{-11} m^2/N

2.2.4.2 Applications of fullerenes

- Fullerenes have neuroprotective and antioxidant properties. They can interact with oxygen species like O_2 (Superoxide) and -OH (Hydroxyl) radicals, which can destroy lipids, proteins, DNA, and other macromolecules without consuming themselves [Kru91]. As research has established the characteristics of fullerenes, they are regarded as the most effective and potent natural antioxidants globally [Tok93].
- Fullerenes have been discovered to have potential antimicrobial properties. Positive results were obtained on a variety of bacterial and fungal species, including Candida albicans, Bacillus subtilis, Escherichia coli, and Mycobacterium avium [Mas99].
- Carbon nanotubes and nanohorns control genes and atoms in creating bioimaging genomes, proteomics, and tissue engineering [Pai06]. The capacity of nanotubes and nanohorns to adhere different antigens to their surfaces makes them potential antigen sources for vaccines. As a result, using dead bacteria, which can sometimes be harmful, can be avoided by using nanotubes as an antigen source [Pai06].
- Fullerenes can be used to maintain solid material compositions vulnerable to oxidation because of their antioxidant properties. In formulations to stop oxidation, they are included as a preservative in anti-ageing cosmetics and zinc oxide [Hir09].
- Fullerenes have been proven to have antioxidant activity and antibacterial and antiproliferative properties, respectively [Ray12], [Bak07], [Mar05], [Mas05]. Specifically, the fullerene derivatives of the cationic and anionic types prevent the reproduction of the HIV-RT and Hepatitis C viruses.

2.2.5 Carbyne

A carbyne is any molecule that is characterized by three unbonded electrons and an electrically neutral carbon atom joined by a single covalent bond [McN97]. It has an infinite chain of *sp*-hybridised carbon atoms likened to an infinite polyene molecule [Pan15]. Evidence of naturally formed carbyne has been reported in meteorites, interstellar dust, and shock-compressed graphite [Gor68] [Web80]. According to theoretical predictions, carbyne may be stable at high temperatures (3000 K) [Whi78].

2.2.5.1 Properties of Carbyne

Carbynes are difficult to synthesize in a well-defined form in the lab; hence their properties have not yet been established [Hal10]. The properties highlighted in Table 2.5 below are for carbyne crystal (a condensed form of carbyne) [Pan15]. Carbyne crystals were produced by repeatedly dropping a carbyne solution onto silicon substrates [Pan15].

Table 2.5. *Properties of Carbyne crystal [Pan15].*

Crystal structure	Hexagonal
Hybridization	*sp*
Lattice parameters	a = b = 5.78 Å, c = 9.92 Å, = α = 90°, β = 90°, γ = 120
Length of C-C single bonds (Å)	1.30
Length of C-C triple bonds (Å)	1.27
Binding energy (eV/atom)	-6.347

2.2.5.2 Applications of Carbyne nanocrystals (CNCs)

Theoretically, carbynes have been proposed for use in a variety of physical applications, including:

- Optoelectronic applications: A new field of study called carbyne optoelectronics has been made possible by the discovery that CNCs are naturally purple-blue luminous, with the wavelength being modulated by the length of the carbon chain [Pan15].
- Non-linear optical material: Carbynes nanocrystals with two degenerate π-electron bands have shown a higher nonlinear optical response when compared with graphene. Typically, nonlinear optical (NLO) materials are applied for frequency conversion [Fra61], information storage [Wei11], optical switching [Cas13], and biomedical imaging [Gle05].
- High-temperature Deep Ultraviolet photodetectors (DUVs): Deep Ultraviolet photodetectors made from CNCs can operate at a temperature of 300 °C, have good thermal stability, and perform excellently [Yan21]. This is the highest working temperature realized so far for DUVs photodetectors [Yan21]. The thermal stability feature of the CNCs can be traced to the connections between its carbon chains and the van der Waals forces [Yan21].
- Biomedical applications: CNCs exhibit unusual luminescence characteristics. Due to their small sizes and low toxicity, they can be used as fluorescent probes to

identify biomacromolecules and cancerous cells. Specifically, the carbon chain length is used to control the molecular luminescence [Pan15].

- CNCs have shown dual-functional nanosensors for fluorescent and colourimetric detection of metallic ions, which are trace elements with significant applications in the environment and biological systems [Che20].

2.2.6 Glassy carbon

Glassy carbon is an artificial allotrope of carbon, commonly referred to as vitreous carbon. It belongs to the family of non-graphitizing carbon materials. Typically, GC is produced by heating organic polymers relatively slowly in an inert atmosphere to high temperatures ranging from 1000 to 3000 °C. The slow heating prevents the carbon network from disruption and breakage [Har97]. The organic precursor breaks down into a carbon residue at a high temperature while the volatile chemicals are diffused into the atmosphere. The type of precursor and the temperature employed during pyrolysis affect how much carbon is in the residue. By weight, the carbon content approaches 90% yield at 900 °C, and a higher yield, about 99%, can be achieved at 1300 °C [Pie93]. The precursor type must also possess these three features to ensure a higher yield of GC: (i) The organic molecule's structure must be three-dimensional and cross-linked [Pie93]; (ii) the carbonization process must also produce a char and occur in the solid state without any mesophase formation [Pie93]; (iii) the benzene rings in the precursors as well as their molecular weight, must be high enough to give a reasonably high carbon yield [Pie93]. The GC produced is characterized by tiny graphitic crystallites, which have a significant number of pores and cross-linked polymeric chains that are randomly orientated. The carbonized substance lacks long-range crystallographic order and is sometimes characterized as amorphous.

Numerous grades of GC have been produced using polyfurfuryl alcohol and phenolic resin precursors [Agg88]. Polyfurfuryl alcohol is produced by polymerizing the furfuryl alcohol monomer with the influence of maleic acid as a catalyst. The class of organic polymers known as phenolic resins is produced through formaldehyde and phenol condensation reactions [Fit84]. This monomer unit, which joins with other units to create the polymer, has the chemical structure shown in Figure 2.11 (b). A hard, inflexible, and insoluble polymer is produced when materials are heated to a temperature of 250 °C due to substantial cross-linking.

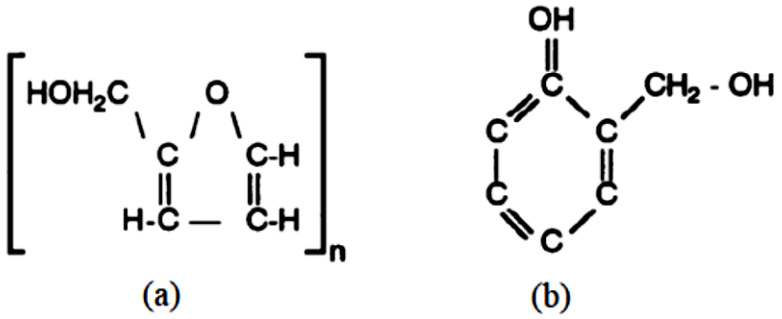

Figure 2.11. *The unit structure of (a) polyfurfuryl alcohol and (b) phenolic resin monomer*

2.2.6.1 Properties of GC

In addition to ensuring a high carbon yield of the GC, the carbonization temperature also determines the structural and mechanical properties of the GC fabricated. The Sigradur®G and Sigradur®K are the two most common kinds of GC. They are produced by pyrolyzing organic precursors (phenolic resins) in an inert atmosphere at temperatures ranging from 1000 to 3000 °C, respectively. The properties of these two GC variants differ due to the different carbonization temperatures. Table 2.6 shows some of the properties of the Sigradur®G and Sigradur®K GC, as compared [www2].

It is clear from Table 2.6 below that Sigradur®G GC type is harder and denser than Sigradur®G GC. However, the Sigradur®G type is the preferable option for this study due to its better thermal conductivity, high corrosion resistance, and particularly high-temperature resistance (approximately 3000 °C) compared to Sigradur®K.

Table 2.6. *Properties of Sigradur®K and Sigradur®G GC [www2].*

Property	**Sigradur® K**	**Sigradur® G**
1) Maximum service temperature (in vacuum or inert gas) (°C)	1000	3000
2) Density (g/cm^3)	1.54	1.42
3) Open porosity (%)	0	0
4) Permeability coefficient (cm^2/s)	10^{-11}	10^{-9}
5) Vickers hardness (HV)	340	230
6) Flexural strength (MPa)	210	260
7) Young's modulus (GPa)	35	35
8) Compressive strength (MPa)	580	480
9) Specific electrical resistance (30 °C) (Ωμm)	50	45
10) Thermal conductivity (30 °C) W/(km)	4.6	6.3
11) Median linear coefficient of expansion (20 – 200 °C) (K^{-1})	3.5×10^{-6}	2.6×10^{-6}

Due to structural differences, the properties of GC differ from those of graphite and other carbon allotropes. The general properties of GC would include the following:

a) Glassy carbon has high-temperature stability; it does not transform into graphite at temperatures above 3000 °C [Pie93].
b) Glassy carbon show excellent resistance to chemical attacks [Har04].
c) It does not react with concentrated hydrofluoric, sulphuric, chromic, and nitric acids at room temperature, even after prolonged exposure. This property is attributed to GC's low permeability and low porosity.
d) Unlike other graphitic materials, GC is not readily affected by halogens such as bromine, even at extremely high temperatures [Pie93].
e) Glassy carbon shows an outstanding performance against corrosion. It does not form intercalation compounds due to its closed structure. This feature makes it difficult to erode with acids and alkali agents [Pie93].
f) Glassy carbon is impermeable to liquids and gases [Nod68].
g) Glassy carbon is strong and hard. Its strength increases with increasing formation temperature up to 2430 °C [Pie93].
h) It is highly biocompatible, making it applicable as dental implants [Huc73] and prosthetic implants [Tar95].
i) Glassy carbon has good electrical conductivity and is chemically inert [Pie93].

2.2.6.2 Structure of GC

The structure of GC has been a subject of interest to many researchers since it was initially discovered in the 1960s. Researchers have put forth several models to describe the GC structure. According to one of the earliest models, Noda and Inagaki [Nod64] report that GC comprises a network of triangular carbon atoms arranged in three dimensions. According to the model, GC consists of graphitic (G) and tetrahedral (T) components, as illustrated in Figure 2.12 (a) [Nod64] [Nod68]. According to Noda and Inagaki's X-ray diffraction studies of GC, the T section of the structure corresponds to a single covalent bond located around a tetrahedral carbon like diamonds. The neighbouring distance in T is 1.55Å [Nod64] [Nod68]. The authors also noted that the first neighbour distance in the G component is 1.42Å, typical of graphite [Nod64] [Nod68]. The study by Furukawa confirms the one by Noda and Inagaki [Fur64].

In another study, Yamada hypothesized the presence of oxygen in GC and estimated it to be about 5 – 6 wt% [Yam64]. Kakinoki [Kak65] proposed an updated model of Noda

and Inagaki by considering the information provided by Yamada's study. The author sandwiched some oxygen atoms between the carbon tetrahedral and the graphite, as shown in Figure 2.12 (b). He proposed that the presence of oxygen in the matrix explains the non-graphitization of GC at temperatures lower than 1100 – 1200 °C. He concluded that heat treatments between 2500 and 3000 °C could remove oxygen yield from the GC.

Many other previous studies have shown that the above models are unacceptable [Pie93], [Har04], [Har05]. A recent study by Odutemowo et al. using ultra-violet Raman spectroscopy shows that no 'T' peak is found in the GC structure, which confirms that GC contains predominantly sp^2 bonds [Odu18]. The existence of a T peak would indicate tetrahedral sp^3 bonds.

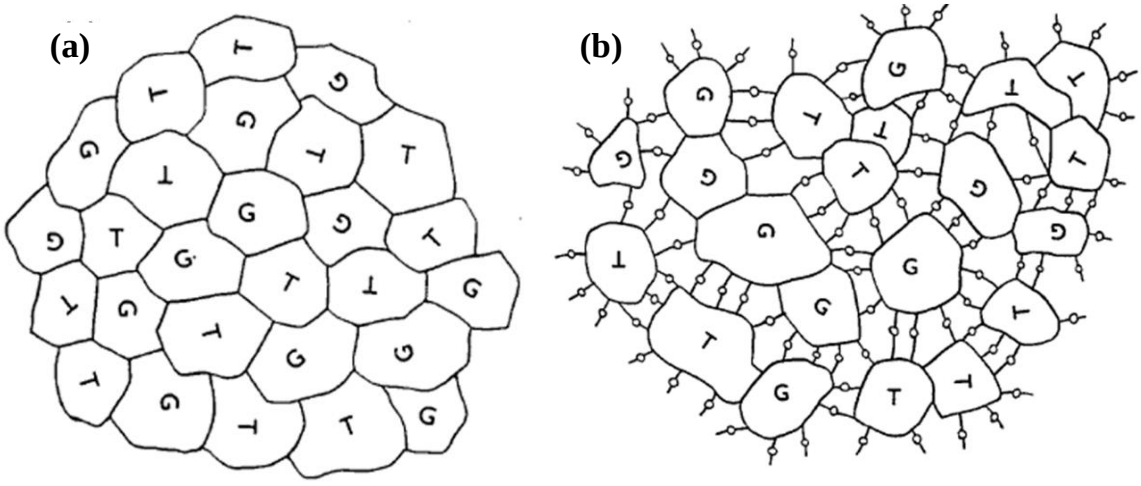

Figure 2.12*. The GC structural models (a) by Noda and Inagaki [Nod64] and (b) by Yamada [Yam64]. The T represents the tetrahedral part in which the first neighbour distance is 1.55 Å, and 'G' is the graphitic part in which the first neighbour distance is 1.55 Å, and 'G' is the graphitic part in which the first neighbour distance is 1.42 Å. -o- represents the oxygen bridge.*

Jenkins and Kawamura gave another popular model on the structure of GC. Their model was based on the assumption that the molecular structure of GC is highly comparable to that of a polymer whose graphite ribbons "fibrils" constitute the polymer (as shown in Figure 2.13). Two flaws are noted in the Jenkins and Kawamura model. The model proposed (in Figure 2.13) contains many pores. A structure like this should be easily permeable to gases, which is against the impermeability property of GC [Har05]. Secondly, this model also has a large proportion of edge atoms, which are thought to have a higher reactivity against the low reactivity property of GC. Despite these shortcomings, the Jenkins and Kawamura model gained widespread acceptance.

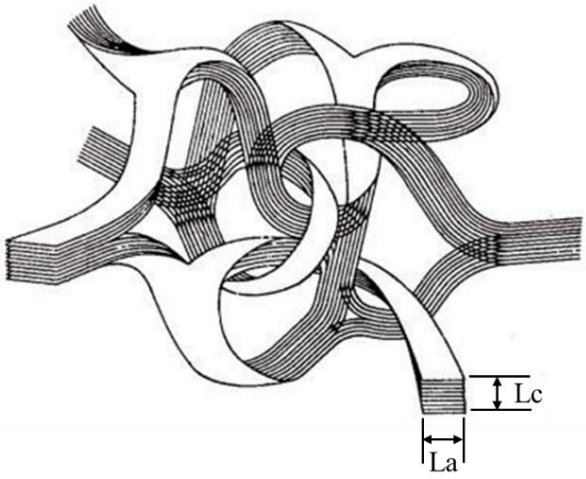

Figure 2.13. *Jenkins and Kawamura model of GC structure, La and Lc represent the lengths of the graphitic domains perpendicular and parallel to the graphite c-axis [Pie93].*

Figure 2.14 shows a more recent GC structure model, as Harris [Har04], [Har05] presented. Harris studied the structure of four commercially produced GC samples using a high-resolution transmission electron microscope (HRTEM). Some closed carbon nanostructure that resembles imperfect multilayered fullerene were reportedly present in the GC structure [Har05]. The fullerene-like feature is typical of most non-graphitizing carbon. Some curved graphitic layer planes were also observed in the structure of the GC, as shown in Figure 2.14. The low reactivity and impermeability characteristics of GC were suggested to be caused by the fullerene-like feature [Har04], [Har05].

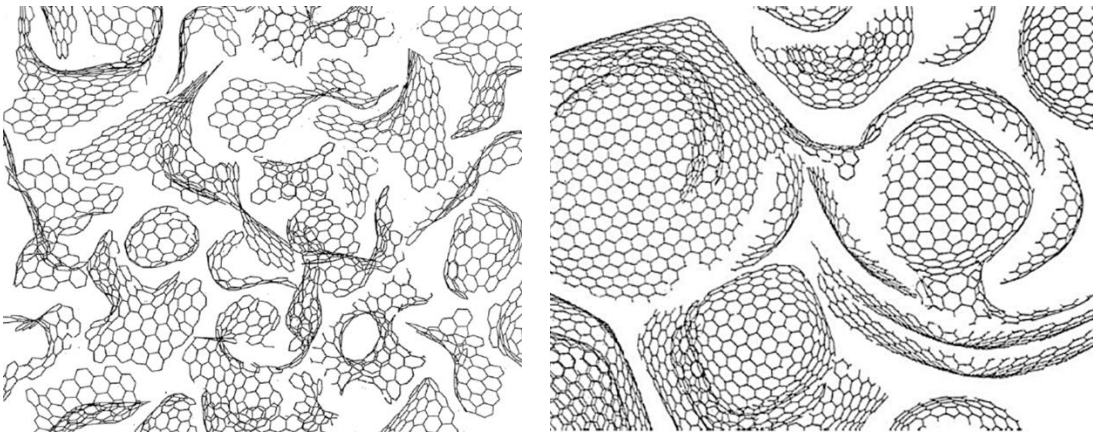

Figure 2.14. *Models for the structure of low-temperature and high-temperature non-graphitizing GC by Harris [Har05].*

2.2.6.3 Applications of GC

The applications of GC are based on its exceptional properties, some of which are highlighted below:

- Due to its high-temperature stability, GC has been suggested as an alternative material to contain nuclear waste for long-term material stability and radiation isolation of high-level nuclear waste [Hro80], [Ber09].
- Because acids cannot attack GC, it is utilised as crucibles, beakers, dishes, reaction tubes, and pressure vessel liners. It is also used as electrode material in electrochemistry [Pie93].
- Glassy carbon is used as crucibles for melting noble metals and specialised alloys, particularly in the dental industry. This is because of its chemical inertness [Pie93].
- It is an excellent candidate for an acid-battery electrode because of its chemical inertness and good electrical conductivity.
- Many glass items and optical lenses are moulded using GC.
- Glassy carbon has been proposed as a protective layer on molten salt breeder reactors' graphite reactor core surface.

References

[Agg88] R. Aggarwal, G. Bhatia, O. Bah & M. Malik. Development of glasslike carbon from phenol formaldehyde resins employing monohydric and dihydric phenols. *J. Mat. Sci.* **23 (5),** (1988), 1677 – 1684.

[Ans06] E.V. Anslyn & D.A. Dougherty. Modern physical organic chemistry, University Science Books. (2006), 8.

[Bak07] R. Bakry, R.M Vallant, M. Najam-ul-Haq, M. Rainer, Z. Szabo, C.W. Huck & G.K. Bonn. Medicinal applications of fullerenes. *Int. J. Nanomed*. **2 (4),** (2007), 639 – 649.

[Ber09] V. Bernardet, S. Gomes, S. Delpeux, M. Dubois, K. Guérin, D. Avignant, G. Renaudin, & L. Duclaux. Protection of nuclear graphite toward fluoride molten salt by glassy carbon deposit. *J. Nucl. Mat.* **384,** (2009), 292 – 302.

[Cas13] F. Castet, V. Rodriguez, J.L. Pozzo, L. Ducasse, A. Plaquet & B. Champagne. Design and Characterization of Molecular Nonlinear Optical Switches. *Acc. Chem. Res*. **46,** (2013), 2656 – 2665.

[Che08] C. Chen & Q. Chen. Recent Development in Diamond Synthesis. *Int. J. Mod Phy. B.*, **22 (4),** (2008), 309.

[Dre96] M.S. Dresselhaus, G. Dresselhaus & P.C. Eklund. Science of Fullerenes and Carbon Nanotubes. *J. Am. Chem. Soc.* **118,** (1996), 8987.

[Fal07] E. Falcao & F. Wudl. Carbon allotropes: beyond graphite and diamond. *J. Chem. Tech. & Biot. Int. Res in Proc, Env. Clean Tech*. **82,** (2007), 524 – 31.

[Fit84] E. Fitzer, Polymer carbon the start into a new age of polymer application. In: E.J. Vandenberg (Eds). Contemporary Topics in Polymer Science. Springer, Boston, MA. (1984), 101 – 138.

[Fra61] P.A. Franken, A.E. Hill, C.W. Peters & G. Weinreich. Generation of Harmonics. *Phys. Rev. Lett*. **7,** (1961), 118 – 119.

[Fra09] F. Béguin & E. Frackowiak. Carbons for electrochemical energy storage and conversion systems. (1st ed.). CRC Press. (2009), 201.

[Fur64] K. Furukawa. Structure of Glassy Carbon. *Nihon Kessho Gakkaishi*. **6,** (1964), 101.

[Hal06] B. Halford. The World According to Rick. *Chem. & Eng. News.* **84 (41),** (2006) 13 – 19.

[Gor68] A.E. Goresy & G.A. Donnay. New Allotropic Form of Carbon from the Ries Crater. *Science.* **161,** (1968), 363 – 364.

[Gle05] B. Gleich & J. Weizenecker. Tomographic imaging using the nonlinear response of magnetic particles. *Nature.* **435,** (2005), 1214 – 1217.

[Har97] P.J.F. Harris & S.C. Tsang. High-resolution electron microscopy studies of non-graphitizing carbons. *Philos. Mag. A Phys. Condens. Matter, Struct. Defects Mech. Prop*. **76,** (1997), 667 – 677.

[Har04] P.J.F. Harris. Fullerene-related structure of commercial glassy carbons, *Phil. Mag*. **84,** (2004), 3159 – 3167.

[Har05] P.J.F. Harris. New perspectives on the structure of graphitic carbons. *Crit. Rev. Sol. St. Mat. Sci*. **30**, (2005), 235 – 253.

[Har21] C. Harpreet & Y. Farah, Hybrid orbitals. Accessed online at https://chem.libretexts.org/@go/page/837. Accessed 21 July 2021.

[Hal10] M.M. Haley. Carbon allotropes: On the road to carbyne. *Nat. Chem*. **2,** (2010), 912 – 913.

[Hir09] R. Hirlekar, M. Yamagar, H. Garse, M. Vij & V. Kadam. Carbon Nanotubes and its Applications: A Review. *Asian J. Pharm. Clin. Res.* **2 (4),** (2009), 17 – 27.

[Hir10] A. Hirsch. The era of carbon allotropes. *Nat. Mat*. **9,** (2010), 868 – 871.

[Hro80] M. Hrovat, H. Huschka & L. Rachor. Process for conditioning radioactive and toxic wastes. US Patent 4407742 (1980). 1 – 14.

[Hoo14] R. Hoover, Need to Track Organic Nano-Particles Across the Universe? NASA's Got an App for That. NASA (2014). Accessed 2 February 2022.

[Huc73] E.E. Hucke, R.A. Fuys & R.G. Craig, Glassy carbon: a potential dental implant Material. *J. Biomed. Mater. Res. Symposium*. **274,** (1973), 263 – 274.

[Jen71] G.M. Jenkins & K. Kawamura. Structure of glassy carbon. *Nature.* **231,** (1971), 175 – 176.

[Kak65] J. Kakinoki. A model for the structure of 'glassy carbon', Acta *Crystallographica*. **18**, (1965), 578.

[Kin11] K. Kingsley, A.C. Ho, H. Qia & A. Bismarck. Carbon Fiber: Surface Properties, Wiley Encyclopedia of Composites, (2011), 1 – 11.

[Kru91] P.J. Krusic, E. Wasserman, P.N. Keizer, J.R. Morton & K.F. Preston. Radical reactions of C60. *Science*, **254,** (1991), 1183 – 1185.

[Kru10] A. Krueger, Carbon materials and nanotechnology, Wiley, Wurzburg, Germany, (2010), 120 – 132.

[Liu13] M. Liu, V.I. Artyukhov, H. Lee, F. Xu & B.I. Yakobson. "Carbyne from first principles: Chain of C atoms, a nanorod or a nanorope.," *ACS nano*, **7, (11**) (2013), 10075 – 10082.

[Mal99] K. Mallika, R.C. DeVries & R. Komanduri. On the low pressure transformation of graphite to diamond in the presence of a 'catalyst-solvent.', *Thin Solid Films*, **339 (1–2),** (1999), 19 – 33.

[Man68] C.L. Mantell, Carbon and Graphite Handbook. Interscience Publishers, New York. (1968), 391 – 424.

[Mar05] S. Marchesan, T. Da Ros, G. Spalluto, J. Balzarinib & M. Pratoa, Anti-HIV properties of cationic fullerene derivatives. *Bioorg. Med. Chem. Lett.* **15,** (2005), 3615 – 3618.

[Mas99] T. Mashino, K. Okuda, T. Hirota, M. Hirobe, T. Nagano & M. Mochizuki. Inhibition of E-coli growth by fullerene derivatives and inhibition mechanism. *Bioorg. Med. Chem. Lett*. **9,** (1999), 2959 – 2962.

[Mas05] T. Mashino, K. Shimotohno, N. Ikegami, D. Nishikawa, K. Okuda, K. Takahashi, S. Nakamura & M. Mochizuki. Human immunodeficiency virus-reverse transcriptase inhibition and hepatitis C virus RNA-dependent RNA polymerase inhibition activities of fullerene derivatives. *Bioorg. Med. Chem. Lett*., **15,** (2005), 1107 – 1109.

[McN97] A.D. McNaught & A. Wilkinson, IUPAC Compendium of Chemical Terminology. The "Gold Book" Blackwell Scientific Publications, Oxford. (2nd ed.). (1997).

[Miy98] K. Miyoshi. Structures and Mechanical Properties of Natural and Synthetic Diamonds. In: NASA/TM-1998-107249, Chapter 8. Lewis Research Center, Ohio. (1998), 1 – 9.

[Nod64] T. Noda & M. Inagaki. The structure of glassy carbon. *Bull. Chem. Soc. Jpn*, **37 (10),** (1964), 1534 – 1538.

[Nod68] T. Noda, M. Inagaki & S. Yamada. A comment on the structure of glassy carbon. *Bull. Chem. Soc. Jpn.* **41,** (1968), 3023 – 3024.

[Odu18] O.S. Odutemowo, J.B. Malherbe, L.C. Prinsloo, E.G. Njoroge, R. Erasmus, E. Wendler, A. Undisz & M. Rettenmayr. Structural and surface changes in glassy carbon due to strontium implantation and heat treatment. *J. Nucl. Mat*. **498,** (2018), 103 – 116.

[Pai06] P. Pai, K. Nair, S. Jamade, R. Shah, V. Ekshinge & N. Jadhav. Pharmaceutical applications of carbon tubes and nanohorns. *Curr. Pharm. Res*., **1,** (2006), 11 – 15.

[Pan15] B. Pan, J. Xiao, J. Li, P. Liu, C. Wang & C. Yang. Carbyne with finite length: The one-dimensional *sp* carbon. *Sci. Adv.* **1 (9),** (2015).

[Pie93] H.O. Pierson. Handbook of Carbon, Graphite, Diamond and Fullerenes: Properties, Processing and Applications, Noyes Publications, New Jersey, (1993), 244 – 371.

[Por19] L.S. Porto, D.N. Silva, A.E. De Oliveira, A.C. Pereira & K.B. Borges, Carbon nanomaterials: synthesis and applications to development of electrochemical sensors in determination of drugs and Abstract. *Rev. Anal. Chem*, (2019), 1 – 16.

[Ray12] A. Ray. Fullerene (C60) Molecule – A Review. *Asian J. Pharm. Res*. **2,** (2012), 47 – 50.

[Tay93] R. Taylor & R.M. Walton. The chemistry of fullerenes. *Nature*. **363,** (1993), 685.

[Tar95] T. Tarvainen, H. Pätiälä, T. Tunturi, I. Paronen, K. Lauslahti & P. Rokkanen, Bone growth into glassy carbon implants: a rabbit experiment. *Acta Orthop. Scand.* **56,** (1995), 63 – 66.

[Tok93] H. Tokuyama, S. Yamago, E. Nakamura, T. Shiraki & Y. Sugiura. Photoinduced biochemical activity of fullerene carboxylic acid. *J. Am. Chem. Soc.* **115,** (1993), 7918 – 7919.

[Web80] A. Webster. Carbyne as a Possible Constituent of the Interstellar. Dust. *Mon. Not. R. Astron. Soc.* **192,** (1980), 7 – 9.

[Wei11] J. Wei, S. Liu, Y. Geng, Y. Wang, X. Li, Y. Wu & A. Dun. Nano-optical information storage induced by the nonlinear saturable absorption effect. *Nanoscale*. **3,** (2011), 3233 – 3237.

[Whi78] A.G. Whittaker. Carbon: A New View of Its High-Temperature Behavior. *Science*. **200,** (1978), 763 – 764.

[www1] https://byjus.com/jee/hybridization-of-carbon/. Hybridization of Carbon. Accessed online 19 July 2021.

[www2] http://www.htw-germany.com/technology.php5?lang=en&nav0=2. Hochtemperatur-werkstoffe GmbH, Germany, properties of glassy carbon. Accessed 19 February 2020.

[Yam64] S. Yamada. A review of glasslike carbons. Battele memorial inst. Columbus OH, Defense ceramic information center, *Tech. Rep*. (1968).

[Yan21] F. Yang, Z. Zheng, Y. He, P. Liu & G Yang. A New Wide Bandgap Semiconductor: Carbyne Nanocrystals Yang, *Adv. Funct. Mater*. **31,** (2021), 1 – 7.

[Yvo20] Yvonne, What are the main uses of graphite? Graphite applications. Obtained online from https://www.dancarbon.com/q/carbon/116.html. Accessed 5 August 2022.

Chapter 3

Ion implantation

Ion implantation is a process of introducing impurities into solid materials by controlling the fluence and energy of the implanted ions [www1]. Ion implantation can otherwise be described as mechanically accelerating an ionized atom of an element to a particular depth into a target/substrate to achieve different material modification purposes [Goo12]. The target properties altered during this process include the physical, chemical, and electrical properties [www1], [Goo12]. The accelerated energetic ion distributes its energy within the atoms of the target/substrate before it eventually comes to rest. Ion implantation is advantageous over diffusion as an alternative to doping a semiconductor material because the impurity concentration, junction depth and temperature can easily be controlled [Bli03]. During ion implantation, the crystal structure of the target material changes or gets damaged due to the collision cascade formed by the incoming energetic ions and the atoms of the substrate. Sometimes, nuclear transmutation can be induced if the ions are implanted at higher energy (order of MeV). Besides its general application in the semiconductor industry, ion implantation has been widely applied to study the properties of different materials, typically carbon. Some of these investigations focused on the tribological properties of ion-implanted diamond-like carbon thin films [Iwa02] and GC [Iwa89]; the electrical conductivity properties of ion-implanted GC [Vir02]; the chemical [Lav08], and electrochemical properties of ion-implanted GC [Tak85].

Radiation damage is induced when light or heavy ions are implanted into GC. The effect of ion implantation is sometimes noticed in the defects introduced along the collision cascades through the rapid energy dissipation in the near-surface regions of any material (e.g., GC). Previous but fewer studies have shown that the effects of ion implantation are useful in studying the migration behaviour and structural modification of ion-implanted GC for its applicability in nuclear applications [Kos08], [Lan12], [Odu16a], [Odu16b], [Hla17], [Njo17], [Odu18], [Ism18], [Odu20] [Ade20], [Ism21], [Njo21]. This chapter explores the physics and processes involved during selenium (Se) ions implantation.

3.1 Theory of ion implantation

In principle, the ion of the desired element to be implanted is produced from an ion source and then directed into an accelerator where the ions are electrostatically accelerated to specific energy (typically keV) of interest. The energetic ions then hit the target in the target chamber, losing energy (via electronic and nuclear collisions) as they finally come to rest and are embedded into the substrate. A typical ion implanter is shown in Figure 3.1. During implantation, the collision of the ion with the nuclei of the lattice atoms and the target's electrons may cause the atom's crystal structure to be damaged or may not cause any significant damage to the crystal structure. Several processes are involved as the implanted ions traverse the material of interest (GC in this case). These processes must be understood to predict the distribution and final position of the ions in the target matrix. The following sections elucidate the processes and topics in ion implantation.

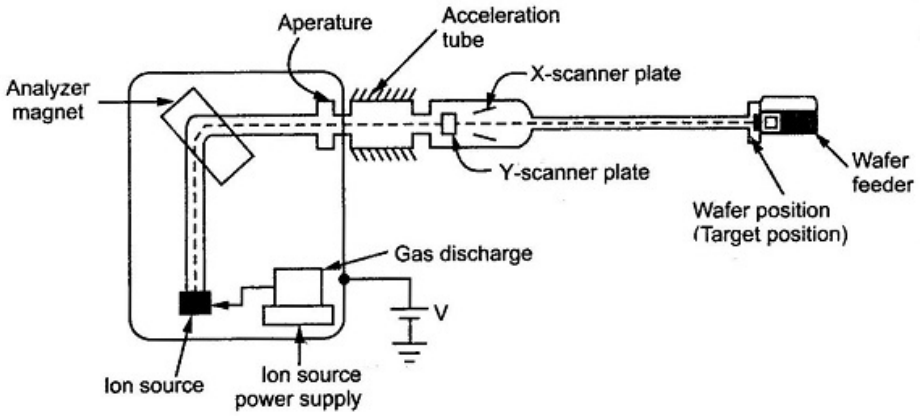

Figure 3.1. *An ion implanter. Taken from [www2]*

3.2 Ion stopping power

During ion implantation, the target material exerts a stopping power on the incoming particle/projectile, thereby resulting in the loss of energy by the ions [Boh48]. In other words, the stopping power determines the distribution of the incoming particle and the defects created in the substrate. The ion stopping power (sometimes termed as stopping force) can be defined as the average energy loss (E) per unit path length (x) due to the interaction of the incoming particle with the substrate atoms [Tay70]. Ion stopping power is described by equation (3.1):

$$S(E) = -\left(\frac{dE}{dx}\right) \text{ eV/µm} \tag{3.1}$$

where *E* is the kinetic energy of the projectile and *x* is the distance along the particle path in the substrate, measured from the surface of the target material. The negative sign indicates a decrease in the projectile's energy after the collisions along the ion tracks in the target matrix.

As the projectile penetrates the target, it loses energy via two mechanisms: the first occurs when the projectile interacts with the electrons of target atoms (electronic energy loss), and the second occurs when the ion interacts with the nuclei of the target atoms (nuclear energy loss). Based on the energy losses above, the "stopping power" can also be regarded as electronic and nuclear stopping. The total stopping power is the sum of electronic stopping, nuclear stopping, and radiative stopping [ICR11]. The radiative stopping power is only noticeable at high projectile energies [Räi03], its effect can thence be neglected at energies below the speed of light, reducing the total stopping power to electronic and nuclear stopping powers, as given by equation (3.2):

$$S(E) = \left(\frac{dE}{dx}\right) = \left[\left(\frac{dE}{dx}\right)_e + \left(\frac{dE}{dx}\right)_n\right] \tag{3.2}$$

the subscripts *n* and *e,* denote the electronic and nuclear stopping powers, respectively.

The stopping cross-section or stopping power 'ε' is an important parameter needed to understand the average energy losses. The stopping cross-section 'ε' can be obtained by dividing the total stopping by the atomic density of the target, *N* (atoms/cm^3), as in equation (3.3) [Chu78]:

$$\varepsilon = -\frac{1}{N}\left(\frac{dE}{dx}\right) \text{eV cm}^2/(10^{15}\ atoms) \tag{3.3}$$

The unit eV.cm^2 is used in Rutherford backscattering spectrometry analysis. The stopping cross section can also take another form, 'ε^*,' obtained by dividing the total stopping power by the target mass density as in equation (3.4):

$$\varepsilon^* = -\frac{1}{\rho}\left(\frac{dE}{dx}\right) \text{ keV cm}^2/\text{mg} \tag{3.4}$$

Equations (3.3) and (3.4) can be merged to give equation (3.5):

$$\rho = N\left(\frac{M}{N_0}\right) \quad \rightarrow \quad \varepsilon^* = \varepsilon\left(\frac{N_0}{M}\right) \tag{3.5}$$

where ρ is the mass density in g/cm^3, N carries its usual meaning as stated above, M is the atomic mass of the target, and N_0 is Avogadro's constant, 6.02×10^{23} in atoms/mole.

Nuclear stopping and electronic stopping are processes in close collisions; the electronic stopping can sufficiently dominate and slow down the projectile at high energies before the nuclear stopping takes over at the low energies until the ion finally comes to rest. As correlated as these two processes are, they can also be separated and treated independently [Fin05]. The nuclear and electronic stopping powers are discussed in the following subsections, 3.2.1 and 3.2.2.

3.2.1 Nuclear stopping

Nuclear stopping power relates to all the elastic collision processes between the nuclei of a projectile ion and the target atoms. The collision involved results in the transfer of energy and momentum from the projectile ion to the target atoms, consequently leading to a change in the direction of the projectile ion and the target atoms displaced.

Nuclear power is the energy a moving particle loses per length travelled in a material at a specific depth (owing to elastic collisions), as given by the relation below [ICR11], [Nas06]:

$$S_n = \frac{\mathrm{dE}}{\mathrm{dx}}\Big|_n \tag{3.6}$$

An interatomic potential is used to determine the nuclear stopping ion penetration in the target material. In other words, an interatomic potential may control how an ion interacts with the target. This interatomic potential applies to each electron as well as the projectile and target's nuclei. A relation to calculate the interatomic potential between two positive charges (of the ion and the target atom) is given by equation (3.7):

$$V = \frac{Z_1 Z_2 e^2}{4\pi\varepsilon_o r} \tag{3.7}$$

where Z_1 and Z_2 are the atomic numbers of the projectile ion and the target atom, respectively; e is the electronic charge, ε_o is the permittivity of free space, and r is the interatomic distance. Equation (3.7) is a Coulomb potential that works for small interatomic distances 'r,' i.e., $0 < r << a_o$, where $a_o = 0.053$ nm is the Bohr's atomic radius in a hydrogen atom. The Coulomb potential 'V' is not valid to describe an atomic nucleus that is separated

by a longer interatomic distance, 'r'. The reason is that at longer atomic separation, the potential between the colliding nuclei is limited by the electronic screening effect.

Several methods have been proposed to calculate interatomic potentials by taking into consideration, the screening effects. Some notable models include the Sommerfeld approximation of the Thomas-Fermi potential, the Moliere approximation, the Lenz-Jensen, the Bohr potential, and the Ziegler-Biersack-Littmark (ZBL) potential. Each of these models (potentials) can be expressed as the product of the Coulombic potential (V) and a 'screening function' (Φ(r/a)), which is referred to as the universal atomic potential, $V(r)$ as expressed in equation 3.8 [Tes95].

$$V(r) = \frac{Z_1 Z_2 e^2}{4\pi\varepsilon_o r}\Phi\left(\frac{r}{a}\right) \tag{3.8}$$

where a is the screening length, $\Phi\left(\frac{r}{a}\right)$ is the screening function, which depends on the charges, other terms in equation (3.8) carry their usual meaning, as stated above.

The Ziegler-Biersack-Littmark (ZBL) screening function, $\Phi\left(\frac{r}{a}\right)$ [Zie85], is the most widely applied because of its accuracy and large experimental validation. The ZBL screening function was derived using the Hartree-Fock charge distribution method to calculate the interatomic potentials of many randomly selected atomic pairs that fall in the range 1 – 82 for the projectile ion (Z_1) and the target atom (Z_2), respectively [Zie85]. Based on this calculation, the ZBL universal screening function is given by equation (3.9):

$$\Phi(r/a) = 0.1818e^{-3.2\frac{r}{a}} + 0.5099e^{-0.9432\frac{r}{a}} + 0.2802e^{-0.4028\frac{r}{a}} + 0.02817e^{-0.2016\frac{r}{a}} \tag{3.9}$$

where r is the radius and the screening length, $a = 0.8854a_o / (Z_1^{0.23} + Z_2^{0.23})^{½}$ [Zie85].

To calculate the energy transfer from the projectile ion to target atoms in terms of the interatomic potential, the binary collision approximation (BCA) was proposed. The BCA method considers isolating the projectile ion and a target atom and ignoring the interactions with other target atoms or ions. The BCA method breaks down at low energy when many-body effects become important [Rim95].

The elastic collision between the projectile and the target is treated as binary, and interactions from other target nuclei are ignored.

Figure 3.2 illustrates a two-body scattering process of a projectile and the target atom in the laboratory frame. After the collision, the projectile was deflected at an angle β relative to the impact parameter '*b*'. The projectile's energy loss (T) to the target atom can be calculated by applying the conservation of energy and momentum principle. In the centre of mass frame, this energy 'T' is given by equation (3.10) below:

$$T = \left(\frac{4E_0M_1M_2}{(M_1+M_2)^2}\right) sin^2\left(\frac{\beta}{2}\right) \tag{3.10}$$

where E_0 is the initial energy of the projectile, M_1 is the mass of the projectile, M_2 is the target mass and θ is the scattering angle.

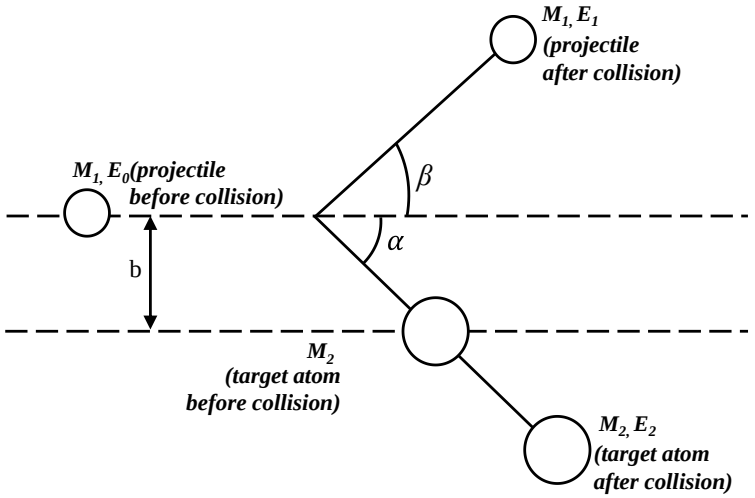

Figure 3.2. *Illustration of a two-body scattering process (in the laboratory frame).*

According to Ziegler et al. [Zie85], the scattering angle, β, can be calculated as a function of the impact parameter '*b*' for a given universal atomic potential, *V(r)* (refer to equation (3.8)).

$$\beta = \pi - 2b \int_{r_{min}}^{\infty} \frac{dr}{r^2\left[1 - \frac{V(r)}{E_c} - \frac{b^2}{r^2}\right]} \tag{3.11}$$

where *b* is the impact parameter, E_c is the centre of mass energy, and *r* is the polar coordinate connecting the projectile to the target atom. With the expressions in equations (3.7) and (3.8), it is evident that the energy (*T*) transferred from the projectile to the target atom is a function of the projectile's energy and the impact parameter '*b*', i.e., T*(E,b)*. The average

energy transferred to all the target atoms (i.e., the nuclear stopping power) is determined when integrated over all the impact parameters, *b* as given by equation (3.12) below:

$$\left(\frac{dE}{dx}\right)_n = 2\pi \int_0^{b_{max}} b\, T(E,b) db = 2\pi \frac{4M_1M_2}{(M_1+M_2)^2} E_0 \int_0^{b_{max}} sin^2\left(\frac{\beta}{2}\right) b db \qquad (3.12)$$

3.2.2 Electronic stopping

Electronic stopping occurs when an energetic ion (projectile) transfers its energy to target electrons via inelastic collisions. Some processes involved during electronic stopping include electron-electron collision, excitation, ionization of target atoms, and electron capture of the projectile [Zie85]. Unlike nuclear stopping, electronic stopping involves an infinite energy loss cross-section [Zie85], making describing it with a single model complicated. The theory to apply depends on the energies of the different ions as they interact with the target electrons. These energies can be divided into three regimes (low, intermediate, and high energy regions). According to the Thomas-Fermi quantum mechanical model, as an ion interacts with the target electrons, the ion's velocity can be compared with Bohr's velocity in these three energy regions. The Bohr's velocity, $v_0 = {e^2}/{4\pi\varepsilon_0\hbar}$, where *e*, ε_0, and $\hbar=(h/2\pi)$ represent the electronic charge, permittivity of free space, and Planck's constant, respectively. The Thomas-Fermi model considers that in the low-energy regime, the velocity of the projectile ions must be less than $v_0 Z^{2/3}$, i.e., $v_1 < v_0 Z^{2/3}$, where *Z* is the atomic number of the projectile. For selenium, the term $v_0 Z^{2/3}$ is 2.3×10^6 m/s. In this study, the velocity of Se ions, v_1 was calculated to be about 6.1×10^5 m/s, which is less than $v_0 Z^{2/3}$ (2.3×10^6 m/s). This implies that the Se ions in the low energy region (characterized by 150 keV and 6.1×10^5 m/s) cannot transfer adequate energy to the electrons with energy less than the Fermi energy level. As a result, electrons do not contribute to the energy loss mechanism for Se ions implantation in this study. However, the electrons having energy close to or equal to the Fermi level would contribute to the electronic energy loss. To calculate the electronic stopping of electrons in the low energy region, a free electron gas of density ρ was assumed [Lin53]. The electronic stopping cross-section, ε_e, of an ion with atomic number Z_1 is given by equation (3.13) [Zie85]:

$$\varepsilon_e = \int I(v,\rho)(Z_1(v))^2 \rho\, dV \qquad (3.13)$$

where *I,* is the stopping interaction function of an ion of unit charge with velocity *v*, with a free electron density gas 'ρ' of the target, Z_1 is the charge of the ion. The integral is over each volume element, *dV* of the target.

The second energy regime is a region where the velocity of the ion is almost equal to $v_0 z^{2/3}$, (i.e., $v_1 \approx v_0 z^{2/3}$). The ion in this region is partly ionized and the electronic stopping would reach a maximum value.

The third energy regime also called the Bethe-Bloch region, where the velocity of the ion is much greater than $v_0 Z^{2/3}$ (i.e., $v_1 \gg v_0 Z^{2/3}$). The ion is stripped of its electron(s) in this region. According to Bethe and Bloch, electronic energy loss is proportional to Z_1^2 [Bet30], [Blo33]. The Bethe-Bloch stopping power formula (given by equation (3.14)) can be used to calculate the electronic energy loss in the intermediate energy regime [Boh48], [Bet30], [Blo33].

$$\varepsilon_e = \frac{4\pi Z_1^2 Z_2 e^4}{m_e v_1^2}\left[\ln\left(\frac{2m_e v_i^2}{\mathrm{I}}\right) + \ln\left(\frac{1}{1-\beta^2}\right) - \beta^2 - \frac{C}{Z_2} - \frac{\delta}{2}\right] \tag{3.14}$$

where m_e represents the electron mass, v_1 is the velocity of the projectile ion, $\beta = v/c$, c is the speed of light, C/Z_2 is the shell correction factor (which accounts for the interaction of electrons on various electronic shells), δ is the density correction factor. The density correction factor may sometimes be excluded from Equation (3.13) except at high ion energies; I is the mean excitation potential of the target (not dependent on the projectile). A relation for finding I is given in equation (3.15) [Kam84]:

$$\ln \mathrm{I} = \sum\nolimits_{\mathrm{n}} f_n \ln\left(\mathrm{E_n} - \mathrm{E_0}\right) \tag{3.15}$$

where E_0 and E_n represent the ground state energy and higher energy transitions with their corresponding dipole oscillator strengths, f_n, the values of I have been estimated using different models. A standard approximation called Block's rule is given in (equation 3.16) [Blo33]. The values of 'I' for many elements and different materials/compounds can be found in the ICRU database (www.icru.org).

$$\mathrm{I} = 10\mathrm{Z_2}\ (\mathrm{eV}) \tag{3.16}$$

Three energies, 10 keV, 150 keV and 1.6 MeV, were used in this study. These energies fall in the low and intermediate energy regimes. Selenium implantation in GC was done at 150 keV and the implanted/annealed samples were characterized with Rutherford backscattering

spectrometry using $^{4}He^{+}$ at 1.6 MeV. Secondary ion mass spectrometry (SIMS) was also used to characterize the implanted and annealed isochronally. SIMS measurements were carried out using 10 keV O^{2+} beam.

Figure 3.3 shows how energy influences the nuclear and electronic stopping power for Se ions implanted in GC. It is clear from this figure that nuclear stopping dominates the energy loss mechanism at low energies (i.e., < $E_{critical}$). The 1 keV/nm at 50 keV corresponds to the maximum nuclear stopping, which drops progressively as the ion energy increases. Electronic stopping dominates the stopping mechanism at high energies (i.e., > $E_{critical}$). Since 150 keV energy of implantation is lower than the 620 keV critical energy, the nuclear stopping power is dominant during the ion implantation process. This further indicates that the nuclear stopping force is responsible for the sample damage.

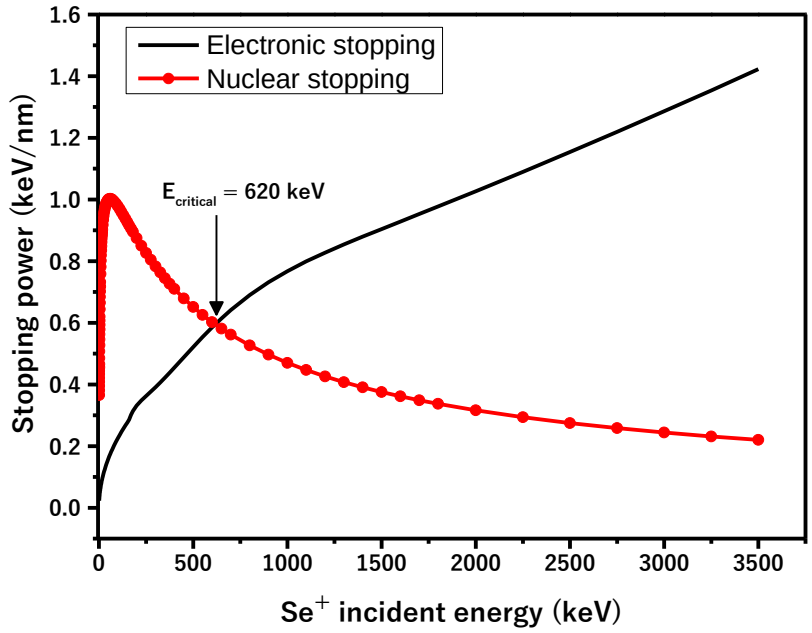

Figure 3.3. *Plots of nuclear and electronic stopping power for Se^{+} implanted in GC at room temperature obtained from SRIM [Zie13].*

3.3 Energy straggling

An energetic ion that traverses a target loses energy due to many interactions with the target nuclei. These different interactions lead to statistical fluctuation, evident in the energy loss, ΔE. These statistical fluctuations are responsible for all the incident ions initially having the same initial energy when entering the target material to possess different energies after penetrating the same thickness, Δt of the same material. This is because the collision of the ions with the target atoms would result in different scattering of the ions [Chu78]. The energy loss (ΔE) by the ions is also affected by the statistical fluctuations so much that uncertainty in the energy loss δΔE must be considered during ion implantation and/or Rutherford backscattering spectrometry [Chu78]. The process described above is called energy straggling [Chu78]. Figure 3.4 shows how a mono-energetic beam of initial energy, E_0 penetrated a thin target material of thickness (Δt). On the left side of Figure 3.4, the energy peak broadens after penetrating the material, leading to an energy loss (ΔE) and a spread in the energy distribution (δΔE) attributed to statistical fluctuations, as mentioned above.

The energy distribution and the straggling of a projectile depend on the projectile's depth in the target [Räi03]. In other words, the projectile could traverse short and long pathlengths in the target. Typically, when the projectile penetrates with a short pathlength in a target (typical of ion penetration in thin films target), the energy distribution of the projectile is not symmetric and the energy straggling (i.e., energy distribution losses) is estimated by the Landau-Vavilov approximation [Räi03]. The Vavilov distribution has a long tail extending towards the high energy losses side. The stopping power of such a projectile can be considered a constant during the projectile path [Räi03]; hence the energy straggling is negligibly small. The projectile can also penetrate deep into the target (i.e., travel a long pathlength). An example of this type of case is when a projectile traversed a thick target leading to an approximately Gaussian energy distribution. When the energy loss is significant enough that the stopping cross-section may vary over the entire projectile path, then the statistical fluctuation in the electronic energy loss is termed Bohr's straggling (Ω_B) (see Equation 3.17). Bohr's straggling was derived from the Bethe-Bloch equation [Boh15] based on the following assumptions:

(i) Atoms in the target are randomly distributed.

(ii) The energy loss for a single interaction is much less than the total energy loss over the path.

(iii) The projectile's velocity is much greater than the orbital electron velocity of the target atoms [Zie85].

$$\Omega_B^2 = 4\pi Z_1^2 Z_2 e^4 N\Delta t \tag{3.17}$$

Ω^2_B is the variance of the average energy loss of the projectile as it penetrates the target; taking the square root of Ω^2_B will give the straggling. Z_1 and Z_2 represent the atomic numbers of the projectile and target atoms, N is the atomic density, e is the electronic charge and Δt is the thickness of the target. Since the energy distribution for the several independent collisions is approximately Gaussian, the full width at half maximum (FWHM) of the energy loss distribution can be represented as $2\Omega_B\sqrt{2\ln 2}$. Bohr's straggling breaks down when the projectile ions lose an appreciable amount of energy [Zie85]. Several improvements have been made to the theory of straggling where previous assumptions did not apply. These improvements include the works by Lindhard and Scharff [Lin53], Bonderup and Hvelplund [Bon71], Chu [Chu76], Sigmund [Sig76], Besenbacher et al. [Bes80] and Yang et al. [Yan91]. The contributions from these works have yielded several correction terms that can be added quadratically to account for the total electronic energy straggling (Ω^2) involved in an experiment [Tes95].

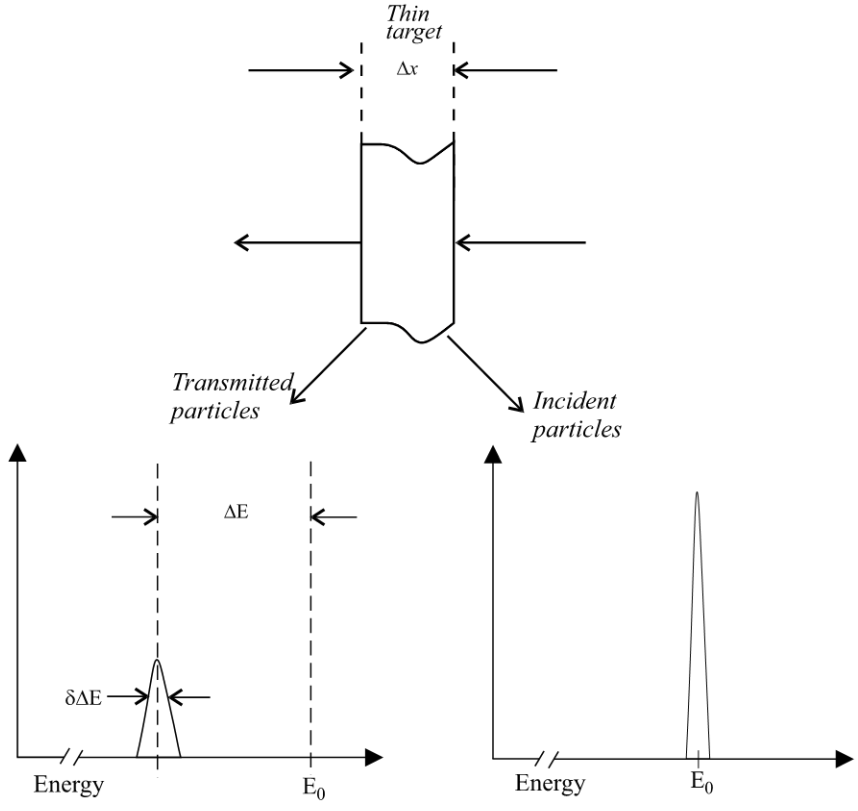

***Figure 3.4**. A mono-energetic beam of energy (E_0) loses energy (ΔE) after passing through a thin target of thickness Δx. Redrawn from [Chu78].*

3.4 The range of an ion implant

The range or total range is the depth at which a mono-energetic projectile (of initial energy, E_o) penetrates the target until it comes to rest. It can be estimated with the target atomic density N, energy loss (dE) and the stopping cross cross-section given by equation (3.18):

$$R = \frac{1}{N}\int_0^{E_0} \frac{dE}{dE/dx} \tag{3.18}$$

The total range depends on the material it traversed, the type of projectile and the initial energy involved. As the ions travel through the target, they experience varying energy losses before finally coming to rest. This implies that "not all the ions are stopped at the same depth". The mean penetration depth from where the projectile enters the target to where it eventually comes to rest is called the projected Range (R_p). The projected Range is measured parallel to the initial ion direction, while the perpendicular Range ($R_\perp$) is measured perpendicular to the ion direction. The distribution around the R_p (i.e., the standard deviation) is known as the projected Range straggling, ΔR_p. For most ion implantation studies, the projected Range is considered a quantity of practical importance more than the total Range. Since the projected Range involved many ion deflections caused by the multiple scattering processes, the projected Range is less than the total Range. An illustration in Figure 3.5 shows how two different energetic projectiles penetrate the same target. The first projectile (a) is the one with lower incident energy, and the other (b) is with high incident energy; both penetrating the same target display different projectile Ranges. The projectile with the lower incident energy has a shorter projected Range because of the multiple scattering processes. For the high incident energetic projectile, the projected Range is more extended because the ions first traversed the target in almost a straight line and later encountered a few multiple scatterings before coming to rest. The multiple collision of the implanted ions within the target matrix will result in an ion distribution like a Gaussian profile [Mal17].

The following parameters can describe an ion implantation profile, viz. the projected Range (R_p), projected Range straggling (ΔR_p), skewness (γ) and kurtosis (β). These parameters are also called moments of an implant profile. The projected Range with straggling is already defined above.

The ion implantation concentration C(x) at a penetration depth (x) is related to the straggling (ΔR_p) as given in equation (3.19) [Hic07]:

$$C(x) = \left(\frac{\varphi}{\sqrt{2\pi N \Delta R_p}}\right) \exp^{\left(\frac{-(x-R_p)}{2\pi \Delta R_p^2}\right)} \tag{3.19}$$

The first term in the bracket in this Equation represents the maximum concentration or the peak value of the distribution [Agu88]. The parameter φ means the ion dose in ion/cm^2 while N is the atomic density of the projectile.

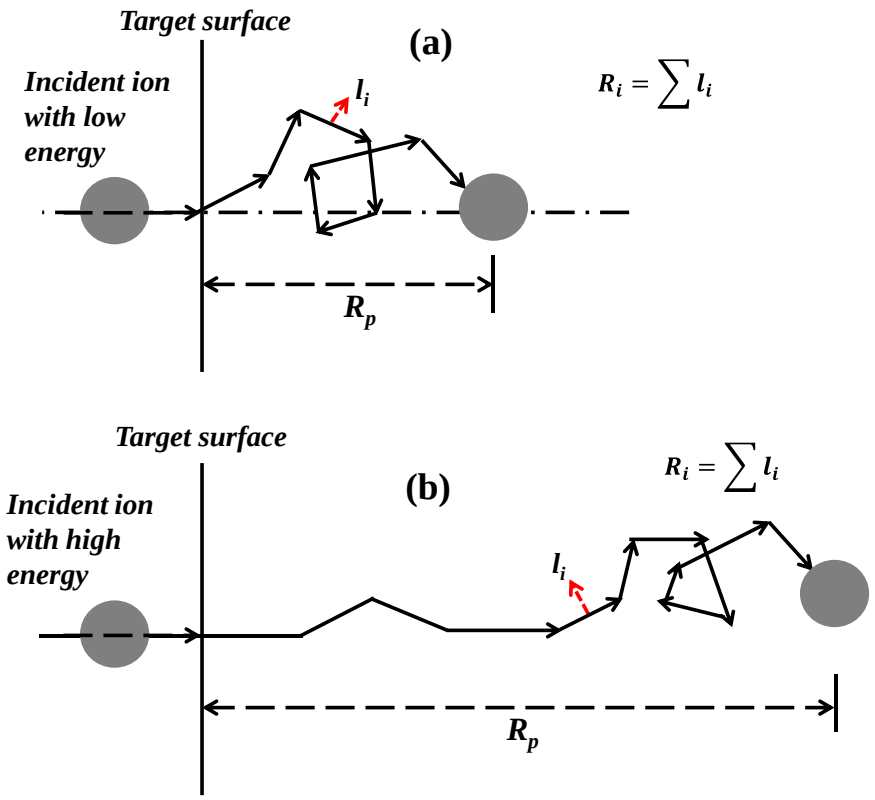

Figure 3.5. *The projected range and the total range for a projectile penetrating a target material with incident ion with (a) low energy and (b) high energy.*

The projected Range straggling, ΔR_p, is given by equation (3.20) below:

$$\Delta R_p = {}^{1}/_{\varphi} \int_{-\infty}^{\infty} (x - R_p)^2 \, C(x) dx \tag{3.20}$$

The skewness, γ of an implant profile, can be seen as the asymmetry of the distribution about its mean value. A distribution's skewness can have negative, zero, or positive values. For a Gaussian profile in the case of an ion implantation distribution, the skewness is equal to

zero (i.e., the tail on both sides is expected to balance out around the projected Range). The skewness γ is given by equation (3.21):

$$\gamma = \frac{\int_{-\infty}^{\infty}(x - R_p)^3 C(x)dx}{\varphi \Delta R_p^3} \tag{3.21}$$

The kurtosis (β), as expressed in equation (3.22), refers to the heavy-tailed or light-tailed relative to a normal distribution. The kurtosis of a normal distribution (Gaussian) equals 3, the value to which the kurtosis of other distributions is compared.

$$\beta = \frac{\int_{-\infty}^{\infty}(x - R_p)^4 C(x)dx}{\varphi \Delta R_p^4} \tag{3.22}$$

The values of the four experimental moments, viz. R_p, ΔR_p, γ, and kurtosis β were obtained by fitting the depth profile of Se implanted GC to an Edgeworth distribution function. An Edgeworth distribution is given by the expression below:

$$N(x) = Af(x)\exp^{\left[\frac{(x-R_p)^2}{2\Delta R_p^2}\right]} \tag{3.23}$$

where,

$$f(x) = 1 + \frac{\gamma}{6}\left[\left(\frac{(x - R_p}{\Delta R_p}\right)^3 - 3\left(\frac{x - R_p}{\Delta R_p}\right)\right] + \frac{\beta - 3}{24}\left[\left(\frac{(x - R_p}{\Delta R_p}\right)^4 - 6\left(\frac{(x - R_p}{\Delta R_p}\right)^2 + 3\right] \tag{3.24}$$

3.5 Implantation induced defects

An energetic projectile produces radiation damage when implanted into a target. After receiving adequate energy from the energetic projectile ion, the target atoms become agitated and displaced from their lattice sites. The displaced atoms can, in turn, displace several other target atoms, and this process can continue, eventually leading to an atomic collision cascade within the target matrix. This collision process leads to several structural changes known as "defects" within the lattice sites of the target material. These defects are mainly vacancies and interstitials in the material of interest. Defects can be created in a material (during a collision process) if the energy of the projectile ion (E_0) is larger than the displacement energy (E_d) of the target atoms. To put it simply, there is no displacement of the host/target atom when $E_0 < E_d$; hence no defects are introduced, but the defects are created when $E_0 > E_d$ (a single displacement of the target atom) or when $E_0 > 2E_d$ (a cascade

of displacement of the target atom occurs). The displacement energy, E_d (of the target atoms), can be defined as the minimum kinetic energy required by the target atoms to be permanently displaced from a lattice site to a defect location. The defects can also be referred to as radiation damage. The degree of radiation damage created during ion implantation depends on the ion fluence, ion energy, the implantation temperature and the type and nature of the target [Tak90], [Hla10]. For instance, studies have shown that the level of radiation damage in GC is dependent on the ion type(s), the implantation dose(s) [Mc94], [Lan12], [Odu15], [Hla17], [Njo17], and the implantation temperature(s) [Mc95] [Ade22]. As alluded to above, defects are manifested in different ways, and the various types of defects found in ion-irradiated materials will be discussed in the next few subsections. These defects include point defects, linear defects, planar defects, and volume defects. Defects can also play an important role in the diffusion of atomic species in crystalline materials. The role of defects in the diffusion of Se implanted in GC is emphasized in the results and discussions chapter of this study.

3.5.1 Point defect

Point defects occur when an atom is missing or in an odd position within a lattice structure. Point defects include:

(i) Vacancies and self-interstitials (intrinsic defects): These defects are also common in ion-irradiated materials [Nas06], [Gib72]. Vacancies can be described as empty, unoccupied atomic sites where an atom is missing from its lattice position. An interstitial (self-interstitial) atom does not occupy any regular lattice position but is found in a void (interstitial sites) within the crystal lattice structure. Sometimes, the self-interstitial formation could result in some deformation of the lattice atoms within the vicinity of the interstitial site. This occurs when lattice atoms' size is larger than the interstitial site. Self-interstitials are common in metals at low concentrations [www3]. An illustration of vacancies and self-interstitials is shown in Figure 3.6.

(ii) Interstitial and substitutional impurity atoms (extrinsic/foreign defects): are foreign atoms introduced into a crystal lattice arrangement [www3]. The interstitial atoms can be smaller than the atoms within the bulk matrix of the crystal. However, if the size of the interstitial impurity atom is larger than the interstitial site, the atoms near the interstitial site will experience some distortions. A substitutional impurity is an atomic species different from the

target atoms. Its size could be similar to that of an atom with which it replaced in the lattice position [www3]. Substitutional atoms often have lower strain energy since they are smaller than the atoms in the lattice. An illustration of interstitial and substitutional impurity is shown in Figure 3.6

(iii) Frenkel defect/pair is formed when an atom (mostly a smaller cation) is knocked out from a lattice position, creating a vacancy and occupying an interstitial in a nearby position (as shown in Figure 3.6). The vacancy-interstitial pair is called the Frenkel defect or pair, although this defect is not common to ion-bombarded materials [www3].

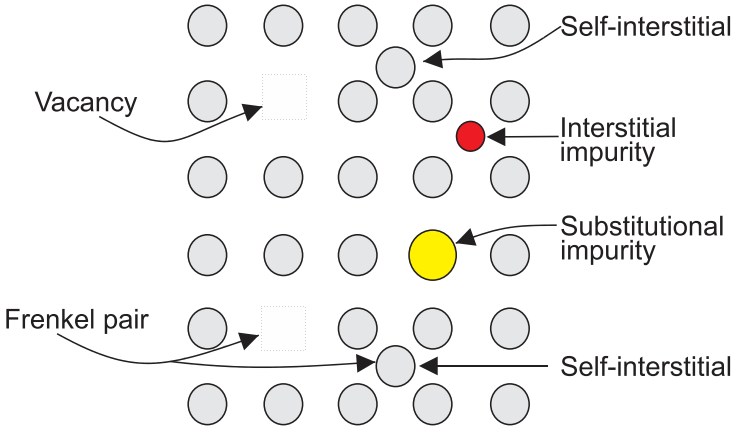

***Figure 3.6**. Schematic illustration of point defects*

3.5.2 Linear Defects – Dislocations

The lines along which the rows of atoms in a lattice are arranged irregularly are called line defects or dislocations [www3]. Dislocations mainly occur when stress is induced in a crystal structure. Such stress could be when an additional plane of atoms was introduced somewhere at the edge of a lattice (edge dislocations) or when the defect line moves perpendicularly to the direction of the stress and atom displacements (screw dislocations). Dislocations are at the edge of a crystal lattice or in other locations but not from within the crystal [Cal13]. Examples of edge and screw dislocations are illustrated in Figure 3.7

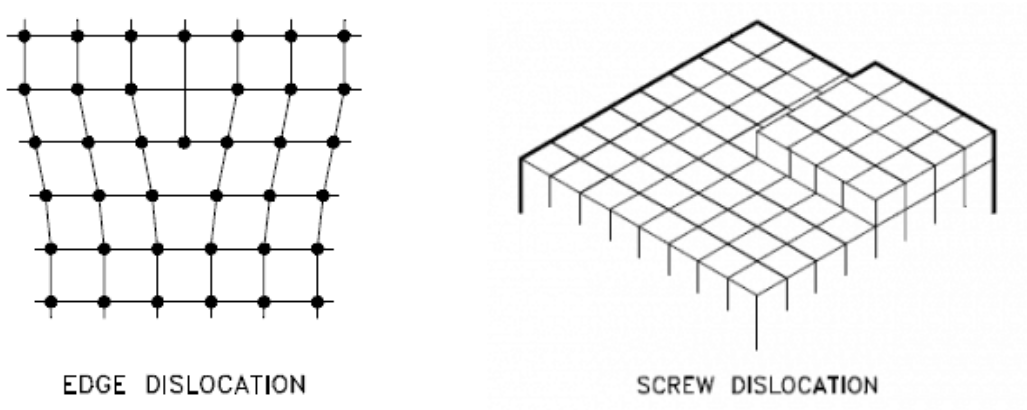

Figure 3.7. *Schematic illustration of edge (left) and screw dislocations (right). [DOE93]*

3.5.3 Planar defects

A planar defect is a distortion in the atomic stacking sequence of crystals [www3]. The planar defects include stacking faults, twin and grain boundaries. A discontinuity of the stacking sequence of the atom planes of a crystal structure is known as a stacking fault. The twin boundary defect type has lattice structures that are mirror reflections of one another in the boundary plane. Grain boundaries are boundaries at the interfaces between grains or crystallites of various orientations in a polycrystalline material. The length and motion of dislocations are terminated at the grain boundaries [www3].

3.5.4 Bulk defects

Bulk or volume defects occur on a macroscopic scale compared to other microscopic defect types. They include voids and precipitates in small regions within a lattice without many atoms. Voids can also be regarded as groups of vacancies within a crystal structure.

The point, line, planar, and bulk defects are common in crystalline materials. However, bulk (voids) defects can occur in amorphous materials. Defects in amorphous materials are based on empty or densely packed atoms, and the properties of defects in amorphous materials can be likened to vacancies and interstitials in crystals [Nor05].

3.6 Amorphisation

As alluded to above, ion implantation can induce damage in solid materials. The magnitude of the damage in the material determines whether an amorphous layer is formed or not. A disorder usually occurs when an energetic incident ion impinges on the target atoms during an ion implantation process. The increasing disorderliness as a function of increasing ion dose is critical to the ion displacements and consequently to the amorphous layer formation [Nas06].

The degree of amorphisation of any material would depend on factors such as the mass of the projectile ion, the mass of the target atoms, the target structure, and the ion implantation parameters (temperature, fluence, and energy) [Hic07] [Wil10]. Low temperature is the best temperature to induce amorphisation during an ion implantation process [McH93], although it is not the case for every material. For example, studies have reported that ion implantation induced amorphisation at room temperature in Si [Moo70], SiC [Wen98] and in GC [McC93], [McC94], [Hla17], [Njo17], [Ade20]. Amorphisation may not occur at a higher implantation temperature, although the recrystallization of an already amorphised layer is possible [Wil10]. At higher implantation temperatures, defects become mobile, interact, and eventually annihilate, preventing amorphisation [Wil10]. Aside from the implantation temperature, the ion dose also plays a role in the amorphisation of a material. Studies have revealed that ion implantation in GC at doses in the order of magnitude $10^{12} – 10^{16}$ ions/cm^2 produces amorphisation in the GC substrates [Iwa89], [McC93], [McC94], [Iwa20], [Hla17], [Njo18], [Ade20]. An important yardstick to determine a material's susceptibility to amorphisation is the nature of the bonding in such material [Nag75]. Amorphisation by ion implantation in crystalline solids containing predominantly covalent bonds was reported to be easy to achieve [Odu18]. However, amorphisation by ion bombardment is complex in intermetallic compounds because it depends on the implantation parameters and the pre-existing microstructure of the material [Mot97]. Amorphisation in GC by ion implantation is a complex phenomenon because of the complexity of the microstructure of the material [Odu15]. In the previous chapter, the structure of GC was described as containing some pockets of graphite, each pocket having an aggregate of smaller crystallites that are randomly oriented [Mal15]. The different orientations of the graphite crystallites in the GC indicate that it is without long-range crystalline order. However, the smaller degree of crystallinity in the GC makes it possible for its structure to be damaged by ion implantation and the introduction of a highly defective layer.

Studies have shown that defective layer introduction in GC due to ion implantation is usually accompanied by compaction of the GC substrate [Iwa89], [McC93], [McC94]. The increase in wear resistance is typical of the surface layer of ion-implanted GC [Pra88], [Iwa89], [McC94], [Toi01]. The increase in the wear resistance of ion-implanted GC has been attributed to the highly defective layer and the compaction of the implanted layer in the substrate [McC93], [McC94]. The amorphised and compacted layer formation in the GC also depends on the ion type and the implantation energy [Iwa89], [McC93]. To this end, it is reasonable to note that the properties of GC (needed as a storage material for high-level nuclear waste) will also be sensitive to introducing defects and compaction of the damaged layer due to ion implantation.

3.7 Simulation of selenium implanted into GC

In this study, the stopping range of ions in matter (SRIM) software was used to simulate the Se ion range and distribution and the damage events. SRIM is a popular Monte Carlo code applied for over three decades in simulation studies related to ion implantation, reflection and transmission of ions and sputtering [Bie80]. The software can also determine backscattered and transmitted ions' energy and angular distributions in many materials. The transport of Ions in Matter (TRIM) is the heart of the SRIM program. TRIM was run to predict implanted Se depth distribution in GC. The Se ion trajectory and the ion distribution in GC are shown in Figure 3.8. The four moments of Se ion distribution in GC were extracted from the ion range file. They include the projected Range, projected Range straggling, skewness, and kurtosis. These calculated projected Range values were compared with the experimental ones (i.e., SIMS and RBS results) and found comparable within the 5% estimated uncertainty of the SRIM program. The details of comparing other moments of Se distributions are discussed in Chapter 7. The differences between the calculations and the experimental projected Range are expected because the TRIM program is efficient with about 5–10% error [Zie13]. The SRIM program has some limitations: it does not consider the dynamic compositional changes of the target material upon projectile ion penetrating it. As a result, this program works on the following assumptions:

- The interaction of atoms is treated as a binary collision and the interaction of neighbouring atoms is neglected.
- Recombination of vacancies and knocked-off atoms is neglected.

- The stopping power is an averaged fit onto many experimental stopping power data points.
- The target material is treated as amorphous.
- The target atom that reaches the surface can be sputtered if sufficient momentum and energy to overcome the surface barrier.

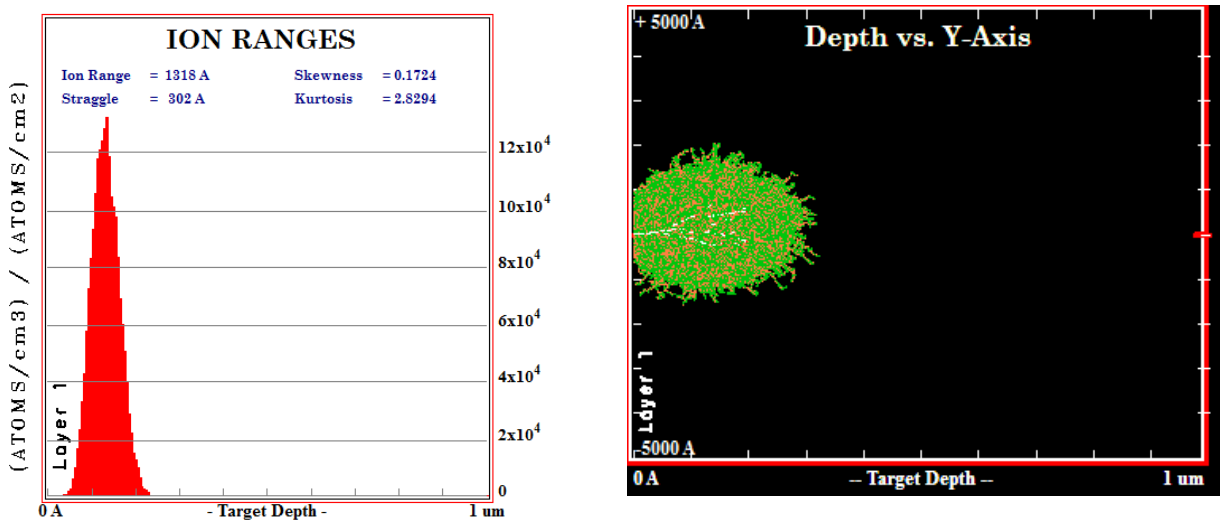

***Figure 3.8**. SRIM simulation of 150 keV Se ion distribution in GC (left) and the corresponding Se ion trajectory (right) Se ions implanted in GC.*

References

[Ade20] S.A. Adeojo, J.B. Malherbe, E.G. Njoroge, M. Mlambo, O.S. Odutemowo, T.T. Thabethe, Z.A.Y. Abdalla & T.T. Hlatshwayo. Effect of sequential isochronal annealing on the structure and migration behaviour of selenium-ion implanted in glassy carbon. *Vacuum*. **182,** (2020), 1 – 12.

[Ade22] S.A. Adeojo, A. Azarov, O.S. Odutemowo, E. Njoroge, H.A.A. Abdelbagi, J.B. Malherbe & T.T. Hlatshwayo. The influence of implantation temperature and annealing on ion-implanted selenium in glassy carbon: structural changes and migration behaviour investigation. *Solid State Sciences.* **129,** (2022), 1 – 10.

[Agu88] F. Agullo-Lopez, C.R.A. Catlow & P.D. Townsend. Point defects in materials. Academic press, London (1988), 1.

[Bes80] F. Besenbacher, J.U. Andersen & E. Bonderup. Straggling in Energy loss of energetic Hydrogen and Helium ions. *Nucl. Inst. & Methods in Phys. Res. B.* **168,** (1980), 1.

[Bet30] H. Bethe, Zur Theorie des Durchgangs schneller Korpuskularstrahlen durch Materie. *Ann. Phys. Leipzig*, **5,** (1930), 324.

[Bie80] J.P. Biersack & L.G. Haggmark. A Monte Carlo computer program for the transport of energetic ions in amorphous targets. *Nucl. Inst. & Methods in Phys. Res., B.* **174**, (1980), 257.

[Bli03] A. Blicher, I.H. Kalish & K.F. Brennan. Field-Effect Transistors, Robert A. Meyers In Encyclopedia of Physical Science and Technology (3rd ed.). Academic Press, (2003), 831 – 849.

[Blo33] F. Bloch. Zur Bremsung rasch bewegter Teilchen beim Durchgang durch Materie. *Ann. Phys. Leipzig*. **16,** (1933), 285.

[Boh48] N. Bohr. The penetration of atomic particles through matter. *Mat. Fys. Medd. Dan. Vid. Selsk.* **18 (8)**, (1948).

[Bon71] E. Bonderup & P. Hvelplund. Stopping power and energy straggling for swift Protons. *Phys. Rev. A.* **4,** (1971), 562.

[Cal13] W.D. Callister Jr & D.G. Rethwisch. Materials Science and Engineering: An Introduction. Wiley, New York. (9th ed.). (2013), 120 – 128.

[Chu78] W. Chu, J. W. Mayer & M. Nicolet. Backscattering spectrometry. Academic Press, (1978).

[Chu76] W.K Chu. Calculation of energy straggling for protons and helium ions, *Phys. Rev. A* **13,** (1976), 2057.

[DOE93] DOE Fundamentals Handbook, Science. Vol. 1 & 2. FSC-6910, U.S. Department of Energy, Washington D.C. (1993), 20585.

[Fin05] D. Fink, L.T. Chadderton. Ion-solid interaction: status and perspectives, *Brazilian J. Phys*. **35,** (2005), 735 – 740.

[Gib75] J. Gibbons, W. Johnson & S. Mylroie, Projected range statistics, semiconductors and related materials. (2nd ed). Dowden, Hutchingson & Ros, Pennsylvania.

(1975).

[Goo12] Goorsky, M. (Ed.). Ion Implantation. *InTech*. (2012), 3 – 235.

[Har73] J.M. Harris, W.K. Chu & M. A. Nicolet, energy straggling of 4 He below 2 MeV in Pt, *Thin Solid Films*, **19 (2),** (1973), 259 – 265.

[Hic07] D.P. Hickey. Ion implantation induced defect formation and amorphization in the Group IV semiconductors: Diamond, silicon and germanium, (2007). Available at: http://etd.fcla.edu,

[Hla10] T.T. Hlatshwayo, Diffusion of silver in 6H-SiC, University of Pretoria, Pretoria, South Africa, PhD Thesis (2010). http://upetd.up.ac.za/thesis/available/etd-06182011-165556/.

[Hla17] T.T. Hlatshwayo, L.D. Sebitla, E.G. Njoroge, M. Mlambo & J.B. Malherbe. Annealing effects on the migration of ion-implanted cadmium in glassy carbon. *Nucl. Inst. & Methods in Phys. Res., B.* **395**, (2017), 34–38.

[ICR11] International Commission on Radiation Units and Measurements (ICRU). Seltzer, Stephen M. (Ed.). "Fundamental Quantities and Units for Ionizing Radiation" (PDF). *J. ICRU* (Rev. ed.). Oxford Univ. Press. 11 (1), (2011) ICRU Report 85a. Accessed 12 June 2023.

[Ism18] M.Y.A. Ismail, J.B. Malherbe, O.S. Odutemowo, E.G. Njoroge, T.T. Hlatshwayo, M. Mlambo & E. Wendler. Investigating the effect of heat treatment on the diffusion behaviour of xenon implanted in glassy carbon. *Vacuum*, **149,** (2018), 74 – 78.

[Ism21] M.Y.A. Ismail, Z.A.Y. Abdalla, E.G. Njoroge, O.S. Odutemowo & T.T. Hlatshwayo. Effect of high temperature annealing and SHI irradiation on the migration behaviour of Xe implanted into glassy carbon. *Nucl. Inst. & Methods in Phys. Res. B.* **489,** (2021), 11 – 19.

[Iwa02] M. Iwaki. Estimation of the atomic density of amorphous carbon using ion implantation, SIMS and RBS. *Surf. Coats. Tech.* **158 – 159,** (2002), 377 – 381.

[Iwa89] M. Iwaki, K. Takahashi, K. Yoshida & Y. Okabe. Improvement of wear properties of glassy carbon surface layer modified by ion implantations. *Nucl. Inst. & Methods in Phys. Res. B.* **39,** (1989), 700 – 703.

[Kam84] E. Kamaratos. The mean excitation energy for stopping power I, the Bragg rule, and chemical and phase effects. Application of a statistical treatment to the determination of I for chemically bound particles. *Chem. Rev.* **84,** (1984), 561 – 576.

[Kos08] O. Koskelo, U. Köster, I. Riihimäki & J. Räisänen. Migration kinetics of ion-implanted beryllium in glassy carbon, *Diam. Relat. Mater.* **17,** (2008), 1991 – 1993.

[Lan12] D.F. Langa, N.G. Van Der Berg, E. Friedland, J.B. Malherbe, A.J. Botha, P. Chakraborty, E. Wendler & W. Wesch. Heat treatment of glassy carbon implanted with cesium at room and high temperatures. *Nucl. Inst. & Methods in Phys. Res., B.* **273,** (2012), 68 – 71.

[Lav08] V. Lavrentiev, J. Vacik & H. Naramoto. Structural phenomena in glassy carbon

induced by cobalt ion implantation. *Appl. Phys. A Mater. Sci. Process.* **92**, (2008), 673 – 680.

[Lin53] J. Lindhard, M. Scharff & K. Dan. Energy loss in matter by fast particles of low charge. *Kgl. Vidensk. Selsk. Mat. Fys. Medd.* **27,** (1953), 1 – 32.

[Mal17] J. B. Malherbe, P.A. Selyshchev, O.S. Odutemowo, C.C. Theron, E.G. Njoroge, D.F. Langa & T.T. Hlatshwayo. Diffusion of a mono-energetic implanted species with a Gaussian profile. *Nucl. Inst. & Methods in Phys. Res. B.* **406,** (2017), 708 – 713.

[McC93] D. McCulloch, A. Hoffman, P.J. Evans & S. Prawer. Structural and chemical bonding investigation of tungsten implanted glassy carbon. *Nucl. Inst. & Methods in Phys. Res., B.* **80,** (1993), 1460 – 1463.

[McC94] D.G. McCulloch, S. Prawer & A. Hoffman. Structural investigation of xenon-ion-beam-irradiated glassy carbon, *Phys. Rev. B.* **50,** (1994), 5905 – 5917.

[McC95] D.G. McCulloch & S. Prawer, The effect of annealing and implantation temperature on the structure of C ion-beam-irradiated glassy carbon. *J. Appl. Phys.* **78**, (1995), 3040 – 3047.

[Moo70] F. F. Moorehead, Jr. & B.L. Crowder. A model for the formation of amorphous Si by ion bombardment. *Radiat. Eff.* **6,** (1970), 27 – 32.

[Mot97] Motta, A.T. Amorphization of intermetallic compounds under irradiation – a review. *J. Nucl. Mat*. **244,** (1997), 227 – 250.

[Nag75] H. Nagiub & R. Kelly. Criteria for bombardment-induced structural changes in non-metallic solids. *Rad. Effects.* **25,** (1975), 1 – 12.

[Njo17] E.G. Njoroge, L.D. Sebitla, C.C. Theron, M. Mlambo, T.T. Hlatshwayo, O.S. Odutemowo, V.A. Skuratov, E. Wendler & J.B. Malherbe. Structural modification of indium implanted glassy carbon by thermal annealing and SHI irradiation, *Vacuum*, **144,** (2017), 63 – 71.

[Njo21] E.G. Njoroge, T.T. Hlatshwayo, M. Mlambo, O. Odutemowo, K.A. Annan, A. Skuratov, M. Ismail & J.B. Malherbe. Effect of thermal annealing on SHI irradiated indium implanted glassy carbon. *Nucl. Inst. & Methods in Phys. Res. B.* **502** (2021), 66 – 72.

[Nor05] K. Nordlund, Y. Ashkenazy, R.S. Averback & A.V. Granato. Strings and interstitials in liquids, glasses and crystals. *Europhysics Letters*. **71 (4),** (2005), 625 – 631.

[Odu16a] O.S. Odutemowo, J.B. Malherbe, C.C. Theron, E.G. Njoroge & E. Wendler. In-situ RBS studies of strontium implanted glassy carbon. *Vacuum*, **126,** (2016), 101 – 105.

[Odu16b] O.S. Odutemowo, J.B. Malherbe, L. Prinsloo, D.F. Langa & E. Wendler. High temperature annealing studies of strontium ion implanted glassy carbon. *Nucl. Inst. & Methods in Phys. Res., B.* **371**, (2016), 332 – 335.

[Odu18] O.S. Odutemowo, J.B. Malherbe, L.C. Prinsloo, E.G. Njoroge, R. Erasmus, E. Wendler, A. Undisz & M. Rettenmayr. Structural and surface changes in glassy carbon due to strontium implantation and heat treatment. *J. Nucl. Mat*. **498,**

(2018), 103 – 116.

[Odu20] O.S. Odutemowo, M.S. Dhlamini, E. Wendler, D.F. Langa, M.Y.A. Ismail & J.B. Malherbe. Effect of heat treatment on the migration behaviour of Sr and Ag CO-implanted in glassy carbon. *Vacuum*, **171,** (2020), 109027.

[Pra88] S. Prawer & C.J. Rossouw. Structural investigation of helium ion-beam-irradiated glassy carbon, *J. Appl. Phys*. **63,** (1988), 4435 – 4439.

[Räi03] J. Räisänen. Ion-solid interactions. *Surf. Interface Anal*. **35,** (2003), 743 – 752.

[Rim95] E. Rimin. Ion Implantation: Basics to Device Fabrication, Kluwer Academic Publisher, (1995).

[Sig76] P. Sigmund. Energy loss of charged particles to molecular gas targets. *Phys. Rev. A.* **14**, (1976), 996.

[Tak85] K. Takahashi, K. Yoshida & M. Iwaki. Effect of ion implantation on electrochemical and surface properties of glassy carbon. *Nucl. Inst. & Methods in Phys. Res., B.* **7 – 8,** (1985), 526 – 529.

[Tak90] K. Takahashi, M. Iwaki & A. Sekiguchi, Wear Property and Structure of Nitrogen Implanted Glassy Carbon. *J. Mat. Res.* **5,** (1990), 2562 – 2566.

[Tay70] L.S. Taylor, M. Tubiana, H.O. Wyckoff, A. Allisy, J.W. Boag, R. Chamberlain, E.P. Cowan, F. Ellis, J.F. Fowler, H. Franz, F. Gauwerky, J.R. Greening, H.E. Johns, K. Lide´n, R.H. Morgan, V.A Petrov, H.H. Rossi A. & Tsuya. ‘‘Linear Energy Transfer.’’ ICRU Report 16. International Commission on Radiation Units and Measurements, Washington, D.C. (1970).

[Tes95] J.R. Tesmen & M. Nastasi. Handbook of modern ion beam materials analysis. MRS. Pittsburgh, USA, (1995), 4 – 79.

[Toi01] H. Toida, K. Terashima, T. Koboyashi, M. Osada, K. Watanabe & I. Masaya, Densification of glassy carbon by fluorine ion implantation. *Nucl. Inst. & Methods in Phys. Res., B.* **175 – 177,** (2001), 532 – 536.

[Vir02] Y.S. Virgil & I.G. Lebedev. Effect of neutron irradiation on properties of glassy carbon. *Inorg. Mat.* **38 (7),** (2002), 668 – 673.

[Vol91] C.A. Volkert. Stress and plastic flow in silicon during amorphization by ion bombardment. *J. Appl. Phys.* **70 (7)** (1991), 3521 – 3527.

[Wen98] E. Wendler, A. Heft & W. Wesch. Ion-beam induced damage and annealing behaviour in SiC. *Nucl. Inst. & Methods in Phys. Res., B.* **141,** (1998), 105 – 117.

[Wer06] M. Werner. Damage formation and annealing studies of low energy ion implants in silicon using medium energy ion scattering. PhD Thesis submitted to the University of Salford, UK, (2006).

[Wil10] J.S. Williams, H. Bernas, Ion-beam-induced amorphization and epitaxial crystallization of silicon. Topics in applied physics: Materials science with ion beams, **116,** (2010), 73 – 111.

[www1] https://en.wikipedia.org/wiki/Ion_implantation#cite_note-2. Accessed 12 July 2023.

[www2] https://www.eeeguide.com/ion-implantation-process-in-ic-fabrication/.

[www3] https://www.nde-ed.org/Physics/Materials/Structure/metallic_structures.xhtml. Accessed 10 July 2020.

[Yan91] Q. Yang, D.J. O'Connor & Z. Wang. Empirical formulae for energy loss straggling of ions in matter. *Nucl. Inst. & Methods in Phys. Res., B.* **61,** (1991), 149.

[Zie85] J. F. Ziegler, J. P. Biersack & Y. Littmark. The Stopping and Range of Ions in Solids, Pergamon Press, (1985).

[Zie13] J. F. Ziegler, www.SRIM.org, USA, (2013). Accessed 25 February 2021

Chapter 4

Diffusion in solids

Diffusion involves a sequence of atomic movements of matter from a higher concentration region to a lower concentration region within a crystal lattice. Diffusion is a transport phenomenon that causes chemical reactions and microstructural changes in materials. The diffusion process can be primarily influenced by the constituent molecules' thermal energy, mechanical energy, and concentration gradient variations. The minimization of Gibb's free energy is also a driving force for the diffusion process.

4.1 Diffusion mechanism

Understanding the diffusion mechanism in solids is important to know how different materials behave and the physical changes that occur in them. Diffusion in a crystalline material is strongly related to the presence of defects [Meh07]. Volume diffusion and short circuit diffusion are the primary mechanisms of diffusion. The temperature and crystal structure both play a significant role in determining whether volume or short circuit diffusion processes predominate in a solid. Volume and short circuit diffusion mechanisms are discussed in the following subsections.

4.1.1 Volume Diffusion

The volume diffusion in a lattice occurs by the movement of point defects, which can be vacancies, interstitial atoms, and self-interstitial atoms. However, the magnitude of volume diffusion depends on which type of defect is present in the lattice structure.

4.1.1.1 Vacancy Diffusion

A lattice site that is ordinarily occupied but is empty is called a vacancy [Cal13], as indicated by the long arrow in Figure 4.1. An atom (either a host atom or a substitutional atom) can move from one lattice site to another when vacancies or vacant ones exist. The movement of atoms is in the opposite direction of the vacancy, which results in vacancy diffusion [She16], as indicated by the short arrow in Figure 4.1. The time it takes for an atom to move to a nearby vacancy equals the reciprocal of Debye's frequency ($\approx 10^{-13}$s). In vacancy diffusion, the vacancies can move relatively quickly, but self-atoms or the atom of the substitutional solute are affected by nearby vacancies with which they can exchange positions. The energy needed by an atom to break its bonds to neighbouring atoms and

diffuse to a vacant lattice site is primarily small since the displacement of one lattice atom results in fewer atoms being bonded to the atoms near the vacant site.

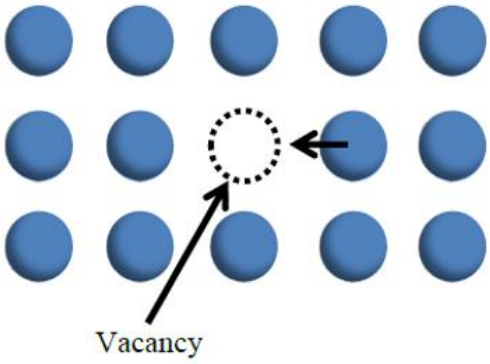

Figure 4.1. *Vacancy diffusion (Adapted from [Jac06])*

4.1.1.2 Interstitial Diffusion

An atom is considered to diffuse by an interstitial process when it moves from an interstitial site to its closest neighbouring interstitial site [She16]. There is no permanent displacement of any solvent atom in this diffusion mechanism. The impurity atoms require less energy (compared with vacancy diffusion) to move from one interstitial lattice site to another. This energy is derived from the thermal energy of atomic vibrations. The host atoms are not designed to occupy the interstitial sites, and the interstitial solute atoms that do so are often smaller than the host atoms. Atoms diffusing through the interstitial diffusion mechanism frequently have very high diffusion coefficients.

Figure 4.2 shows interstitial diffusion, mainly between two materials with significantly different atomic radii. The lattice structure of the host atoms is slightly distorted as the interstitial atoms diffuse from one site to another. In general, the presence of several interstitial solutes causes a significant increase in the degree of lattice distortion, which can significantly alter the host material's properties.

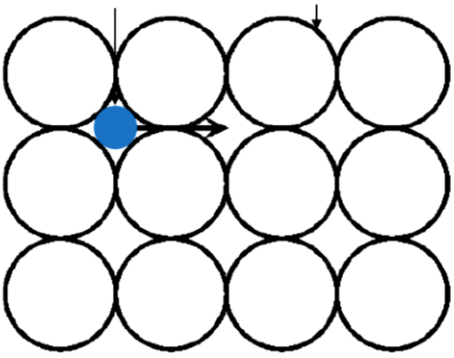

Figure 4.2. *Interstitial diffusion mechanisms (Taken from [Jac06])*

4.1.1.3 Interstitialcy diffusion

As illustrated in Figure 4.3, interstitialcy diffusion mechanism involves self-interstitials or additional atoms found between the lattice sites that push a neighbouring atom into an interstitial position. Contrary to interstitial diffusion mechanisms, self-interstitials have atoms that are the same size as those found in the lattice locations [Hei05].

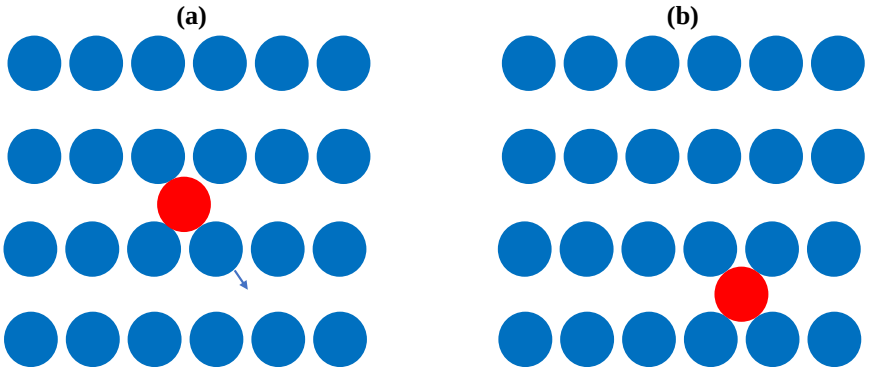

Figure 4.3*. Interstitialcy diffusion mechanism, indicating the position of the self-interstitial atom (a) before and (b) after its diffusion.*

4.1.2 Short circuit diffusion

The short circuit involves the movement of atoms and molecules along linear and surface defects. It is mainly manifested as dislocations or grain boundary diffusion mechanisms. The interface between two crystallites is known as the grain boundary and is present in polycrystalline solids. They can serve as point defect sinks and transport pathways. A dislocation is a plane of atoms out of place in a crystal lattice. Low temperatures favour grain boundary and dislocation diffusion mechanisms over lattice diffusion because they have a lower activation energy and a higher degree of disorder along

the borders. However, lattice diffusion takes over at high temperatures. Unlike volume diffusion, grain boundaries and dislocations are frequently referred to as high diffusivity paths because of high diffusion rates within their regions.

4.2 Theory of diffusion

The presence of a concentration gradient significantly influences diffusion in solids. It is critical to understand how quickly atoms or molecules move from a location of high concentration to one of lower concentration to comprehend the diffusion process. The flux is a variable that indicates how quickly diffusion progresses. It measures how many atoms, *m* (or how much material) diffuse through a given region of area (*A*) in a given amount of time (*t*), as illustrated in Figure 4.4. The flux is given by equation (4.1) [Njo14]:

$$J_i = \frac{1}{A}\frac{dm}{dt} \tag{4.1}$$

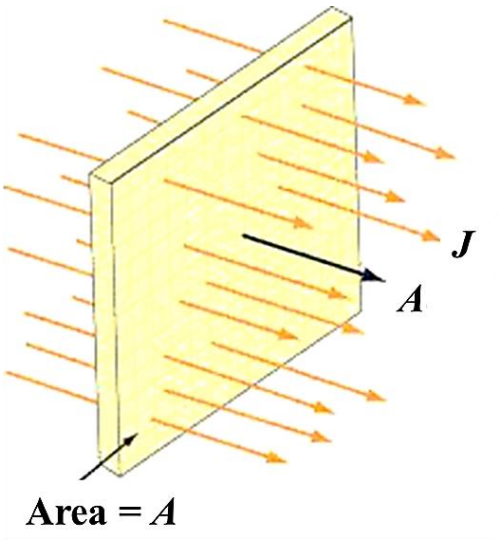

Figure 4.4. *Flux through a unit area A*

4.2.1 Fick's first law

Fick's first law is comparable to the heat flow law, which illustrates a diffusion process and states that the flow occurs from the high-concentration region to the low-concentration region [Gup05]. The relationship between the concentration and the diffusivity (in one dimension) for steady-state diffusion is described by Fick's first law given by equation (4.2):

$$J_i = -D_i \frac{\partial N_i}{\partial x} \tag{4.2}$$

where D is the diffusivity (or diffusion coefficient), which relates to the diffusion flux and the concentration gradients, $\frac{\partial N_i}{\partial x}$. The number of particles moving perpendicular to an area in a given amount of time is the unit of diffusivity flux, and the number of particles in a given volume is the unit of concentration. Hence, the unit of concentration gradient is (atoms/cm^4). The unit of D will then be cm^{2}s^{-1}. The negative sign implies that diffusion occurs along the concentration gradient. According to equation (4.2), the diffusion flow goes to zero when the sample becomes homogeneous. Fick's first law (in three dimensions) is generally expressed as follows: [Hei05]:

$$J_i = -D\ \vec{\nabla} N_i \tag{4.3}$$

where J_i is the diffusivity flux, D is the diffusion coefficient, and $\vec{\nabla}$ is a gradient operator of the three-dimensional space.

Fick's first law does not apply to solid-state diffusion measurement due to the time dependency of its concentration. The concentration must be constant over time, and the sample must be in a steady state to estimate the flux by Fick's first law [She89].

4.2.2 Fick's second law

Diffusion involves a concentration gradient that varies with distance (x) and time (t). This implies that the concentration depends on time (t) and distance (Δx) and this type of diffusion process is known as non-steady state diffusion. This diffusion process can best be explained by Fick's second law, as illustrated by equation (4.4), which was derived from equation (4.2).

Considering a volume element of a block characterized by cross-sectional area A and a small distance Δx, as shown in Figure 4.5. Assuming there is a concentration gradient (diffusivity

flux) inside the block, a plot of the concentration, $C(x)$, versus distance, x, along the block can be made, as illustrated in Figure 4.5. Applying Fick's first law to the volume element (ΔV), a concentration gradient will build up with flux (J_x) entering the block at x. The concentration gradient at $x+\Delta x$ will result in another flux $J_{x+\Delta x}$ leaving the block.

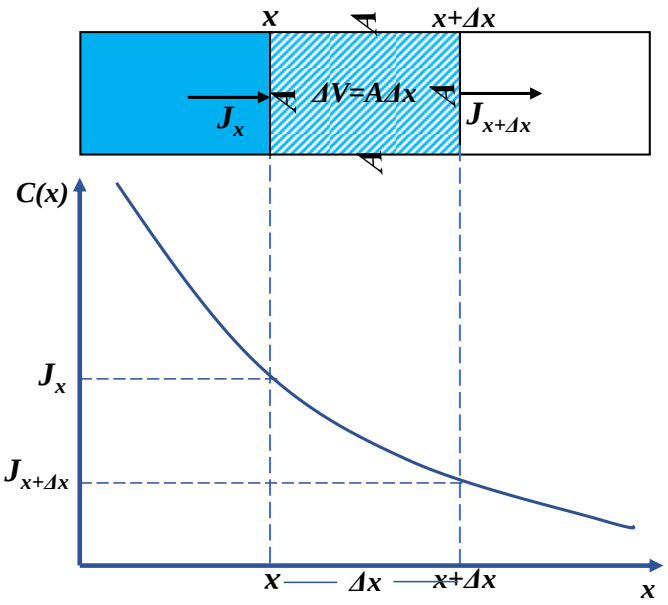

Figure 4.5. *A differential volume element (ΔV) of a block with a cross-sectional area (A) and flux Jx and Jx+Δx entering and leaving the block.*

To estimate how much the concentration gradient of the volume changes in time Δt, equation (4.1) can be inferred and applied to points x and $x+\Delta x$.

The mass entering ΔV within Δx region in the time interval, Δt, is given by equation (4.4):

$$m_x = J_x A \Delta t \tag{4.4}$$

Similarly, mass leaving the volume ΔV at $x+\Delta x$ in the same time interval Δt is given by equation (4.5):

$$m_{x+\Delta x} = J_{x+\Delta x} A \Delta t \tag{4.5}$$

Taking the difference between equations (4.4) and (4.5) will produce equation (4.6):

$$\Delta m = m_x - m_{x+\Delta x}$$

$$= -(J_{x+\Delta x} - J_x)\, A\Delta t$$

$$\Delta m = -\Delta J A \Delta t \tag{4.6}$$

The concentration change in ΔV in time Δt is given by equation (4.7).

$$\Delta N_i = \frac{\Delta m}{\Delta V} \tag{4.7}$$

The substitution of Δm and $\Delta V = A\Delta x$ into this equation (4.7) yield equation (4.8):

$$\Delta N_i = \frac{-\Delta J}{\Delta x}\Delta t$$

$$\frac{\Delta N_i}{\Delta t} = \frac{-\Delta J}{\Delta x} \tag{4.8}$$

Taking the limit of the above equation gives the differential form of Fick's second law of diffusion as given in Equation (4.9)

$$\lim_{\Delta t \to 0} \frac{\Delta N_i}{\Delta t} = \lim_{\Delta x \to 0} \frac{\Delta J}{\Delta x}$$

$$\frac{\partial N_i}{\partial t} = -\frac{\partial J}{\partial x} \tag{4.9}$$

Another form of Fick's second law can be obtained by replacing *J* in equation (4.9) with Fick's first law (in equation 4.2).

$$\frac{\partial N_i}{\partial t} = -\frac{\partial}{\partial x}\left(-D\frac{\partial N_i)}{\partial x}\right) \tag{4.10}$$

Assuming that the diffusion coefficient (*D*) is treated as a constant (which is independent of position *x*), Equation (4.10) can be rewritten as:

$$\frac{\partial N_i}{\partial t} = -D\frac{\partial^2 N_i)}{\partial x^2} \tag{4.11}$$

The diffusion coefficient, *D*, roughly complies with the Arrhenius relation (within a limited temperature range), which is given by equation (4.12) below:

$$D = D_0 \exp\left(-\frac{E_a}{k_B T}\right) \tag{4.12}$$

In this Equation, D_0 is the temperature-independent pre-exponential factor; E_a is the activation energy, k_B is Boltzmann's constant, and T is the temperature in Kelvin. Fick's second law can be applied to all solid-state diffusion measurements.

4.2.3 Estimating the diffusion coefficients

Several analytical techniques are used in estimating the diffusion coefficients of impurities in solid materials, as given in the literature [Hei05], [Poa78]. The method employed in this research is Rutherford backscattering spectrometry (RBS), which requires fitting the RBS experimental data onto appropriate solutions to time-dependent Fick's diffusion equations [Mal17]. The RBS technique is discussed in detail in chapter 5 of this thesis. The derived diffusion coefficients in this work were governed by equations (4.13), (4.14), and (4.15), given below. Equation (4.13) works for an initially perfectly Gaussian profile of a mono-energetic ion (Selenium as in this study) implanted in an isotropic material, as shown below:

$$N(\xi,0) = A_0 \exp\left(-\frac{(\xi - R_p)^2}{2\Delta R_p^2}\right) \tag{4.13}$$

where $N(\xi,0)$ represents the original distribution of Se impurity in the GC substrate. R_p and ΔR_p are the projected range and projected range straggling, respectively. equation (4.14) is the solution to Fick's diffusion equations, which was used to calculate the diffusion coefficient of implanted ions after annealing [Mal17]:

$$N(x,t) = \frac{1}{2\sqrt{\pi Dt}} \int \left[N(\xi,0) exp\left(-\frac{(\xi-x)^2}{4Dt}\right) d\xi + N_1(-\xi,0) exp\left(-\frac{(\xi+x)^2}{4Dt}\right)\right] d\xi \tag{4.14}$$

ξ is the depth below the substrate surface. The solution to this equation is then given by equation (4.15):

$$N(x,t) = \frac{A_0 \cdot \Delta R_p}{2\sqrt{2Dt+\Delta R_p^2}} e^{\left(-\frac{(x-R_p)^2}{4Dt+2\Delta R_p^2}\right)} \times \left[\begin{array}{c} 1 + \mathrm{erf}\left(\frac{2DtR_p + x\Delta R_p^2}{\Delta R_p \sqrt{2(2Dt)^2 + 4Dt\Delta R_p^2}}\right) - k\, exp^{\left(-\frac{xR_p}{Dt+\frac{\Delta R_p^2}{2}}\right)} \\ \times \left\{ 1 + erf\left(\frac{2DtR_p + x\Delta R_p^2}{\Delta R_p \sqrt{2(2Dt)^2 + 4Dt\Delta R_p^2}}\right)\right\} \end{array} \right] \tag{4.15}$$

$$\text{where } k = 1 - \left[\frac{2C_o}{A_o} \frac{\sqrt{2Dt+\Delta R_p^2}}{\Delta R_p} \exp\left(\frac{R_p^2}{4Dt+2\Delta R_p^2}\right) \Bigg/ \left\{ 1 + erf\left(\frac{R_p\sqrt{Dt}}{\Delta R_p \sqrt{2Dt+\Delta R_p^2}} \right) \right\} \right] \tag{4.16}$$

$N(x,t)$ represents the distribution of the implanted impurities with either a perfect sink at the surface or a reflecting surface and depends on the concentration *x* and annealing time *t* for the fitted spectra. The pre-bracket term in equation (4.15) is the dominating term that represents the Gaussian equation. The parameter (*k*) is a fitting variable that can be set to 1 or -1. A perfect reflecting surface is represented by k = -1, while a perfect sink at the substrate's surface is defined by k = 1. The solutions above were incorporated into a MATLAB code by Malherbe et al. [Mal17]. This code fits RBS experimental data and the diffusion coefficient estimated. The code works provided that the diffusion profile is Fickian at the various annealing temperatures and time durations. The code accepts data with a non-zero on the sample surface. A detailed explanation of the code and the parameters in Equations (4.13 – 4.16) is provided in [Mal17].

References

[Cal13] W.D. Callister Jr & D.G. Rethwisch, Materials Science and Engineering: An Introduction. Wiley, USA. (9th ed.). (2013), 120 – 128.

[DOE93] DOE Fundamentals Handbook, Science. Vol. 1 & 2. FSC-6910, U.S. Department of Energy, Washington D.C. (1993), 20585.

[Gup05] D. Gupta. Diffusion processes in advanced technological materials, William Andrew, New York, (2005).

[Hei05] A.P. Heitjans & J. Kärger. Diffusion in condensed matter, Springer, Berlin, (2005).

[Jac06] K.A. Jackson. Kinetic processes: Crystal growth, diffusion, and phase transformations in materials. Wiley, New York, (2006).

[Mal17] J.B. Malherbe, P.A. Selyshchev, O.S. Odutemowo, C.C. Theron, E.G. Njoroge, D.F. Langa & T.T. Hlatshwayo. Diffusion of a mono-energetic implanted species with a Gaussian profile. *Nucl. Inst. & Methods in Phys. Res., B.* **406,** (2017), 708 – 713.

[Mat01] S. Matsumoto. Silicon: Diffusion, K.H. Jürgen Buschow, R,W. Cahn, M.C. Flemings, B. Ilschner, E.J. Kramer, S. Mahajan & P. Veyssière (Eds.). Encyclopedia of Materials: Science & Technology. *Elsevier*. (2001), Accessed online at https://www.sciencedirect.com/science/article/pii/B0080431526015242.

[Meh07] H. Mehrer. Diffusion in solids: Fundamentals, methods, materials, diffusion controlled processes. Springer Science & Business Media, Dresden, Germany, (2007).

[Njo14] E.G. Njoroge. PhD thesis, University of Pretoria, Pretoria. (2014).

[Poa78] J.M. Poate, K.N. Tu & J.W. Mayer. Thin films-interdiffusion and reactions. Wiley, New York. (1978), 578.

[She16] P. Shewmon. Diffusion in solids. Springer, Switzerland. (2016).

[Was16] G.S. Was. Fundamentals of radiation materials science: Metals and alloys. Springer, New York, (2016).

Chapter 5

Analytical techniques

The migration behaviour and the structural evolution of Selenium in GC after implantation and heat treatment were investigated in this study. The analysis techniques used are Rutherford backscattering spectrometry (RBS), secondary ion mass spectrometry (SIMS), Raman spectroscopy and transmission electron microscopy (TEM).

5.1 Rutherford backscattering spectrometry

Following the success of the gold foil experiment by Ernest Rutherford and his students (Geiger and Marsden) in 1911, Rutherford backscattering spectrometry (RBS) was established and recommended by physicists as an excellent tool to characterize the surfaces of solid materials. The first time the RBS technique was described was in 1957 by Rubin *et al*. [Rub57]. The authors gave a detailed description of the principles, instrumentation and results obtained from various nuclear reaction analytical techniques, of which RBS was included. Several applications of RBS emerged to date. Among many other applications, RBS can be applied to accurately determine the distribution of impurity in a target as a function of the depth [Per87], elemental density determination, and stoichiometry (composition and concentration) distribution in thin films. One of the advantages of RBS over other ion beam techniques is that it is non-destructive and can give accurate information about a sample within 10 – 15 minutes of analysis time. The RBS has excellent sensitivity for heavy elements of the order of parts per million (ppm). A typical RBS setup is costly in that it requires an expensive accelerator, hence a disadvantage of the technique. The RBS technique has a low sensitivity to light elements such as hydrogen, oxygen, and carbon [Alo93]. Another setback of the RBS is its inability to give the chemical bonding information of a sample, as X-ray photoelectron spectroscopy (XPS) will do. Also, an ambiguity exists for elements with very close masses in some compounds [Per87]. Other disadvantages of the RBS technique include decreasing depth and mass resolution, especially for the target elements with high atomic masses. To characterize any solid material with the RBS technique, a beam of projectile ions with an energy of 0.5 – 4.0 MeV (mostly ^{4}He or ^{1}H) is incident on the material of interest. The projectile then interacts with the nuclei of the material. After the interaction, the projectile gets backscattered (at a specific angle) within the target matrix. The solid-state detector detects the backscattered projectile particles, digitalized and displayed as an energy spectrum and counted in the computer

[Chi17]. Since the backscattering cross-section for the individual element is known, elemental information about the sample matrix is quantitatively determined [Chi17]. The components of RBS and the theory of the technique will be discussed in the following subsections.

5.1.1 The Rutherford backscattering spectrometry (RBS) setup

A typical RBS setup at the University of Pretoria, South Africa, shown in Figure 5.1, has three main components: Van de Graaf accelerator, scattering chamber, and detector.

The Van de Graaf accelerator consists of a high-frequency RF ion source, a high-voltage generator and a continuous carrier belt. The ion source produces a positively charged He ion beam repelled by the positive potential around the accelerator tube for further acceleration. The Van de Graaf principle governs the acceleration of the $^{4}He^{+}$ ions. A Van de Graaff (VDG) accelerator can produce ion beams with energies from a few hundred kilo electron volts (keV) up to a few Mega electron volts (MeV). The accelerator facility at the University of Pretoria can be used to generate ions of maximum energy of 2.7 MeV, but energies ranging between 1.4 and 1.6 MeV were used in this study to achieve a good depth resolution of the RBS technique.

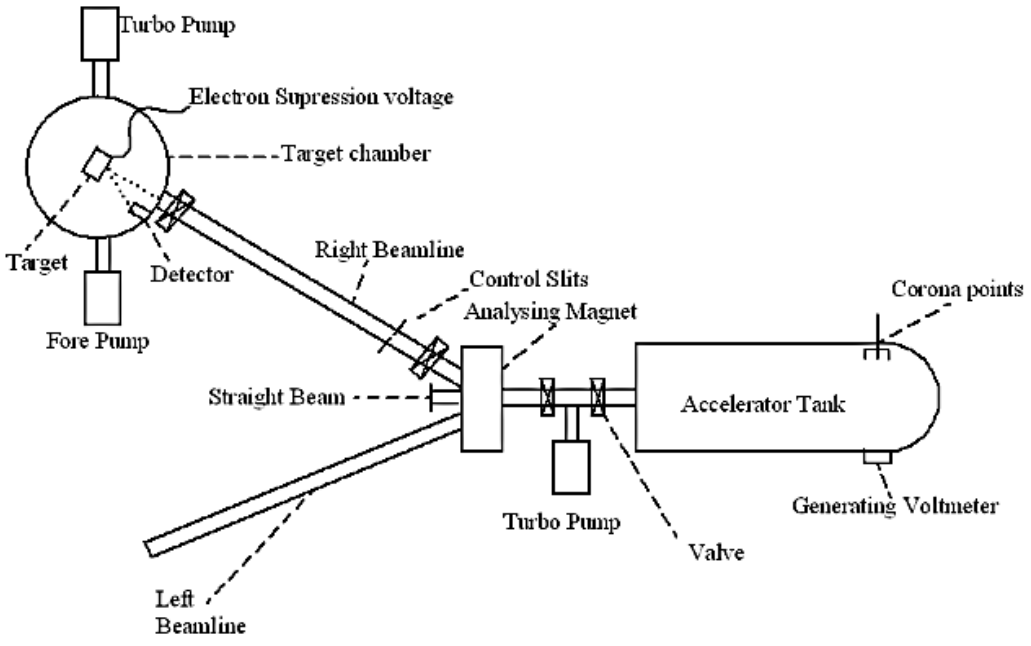

Figure 5.1. *Van der Graaff accelerator. Taken from [Kuh15]*

The energetic, positive He ions first pass through an analysing magnet, which separates the beam based on the mass and charge and then deflects the beam to the left or right beamline (see Figure 5.1). The ion beam passes through the focusing magnets, whose function is to focus the beam. The right beamline was employed in this study, which has a series of horizontal and vertical slits that focus and direct the beam into the scattering chamber. The helium ion beam was used in this research.

The scattering chamber is another vital segment of the RBS setup, shown in Figure 5.2 and has a platform (and holder) where the sample is mounted. A tri-axial goniometer is also a component of the scattering chamber that controls the tilt and rotation of the target sample. The uncertainty of the goniometer is 0.02° for any angle setting. A collimator of a diameter of 1 mm (which connects the beamline) is another essential component in the scattering chamber, as illustrated in Figure 5.2. Its function is to shape the beam into a specific size. Secondary electrons are produced during the interactions between the He ions and the target atoms. These electrons are suppressed by applying a -200 V attached to a ring-shaped electrode in front of the target sample.

A solid-state detector (illustrated in Figure 5.2) and a vacuum pump system (not shown) are also connected to the scattering chamber. A solid-state detector is inside the scattering chamber at 15° with respect to the incoming beam, which is shown in Figure 5.2. The vacuum pump system consists of a fore pump system and a turbopump. The fore pump system is used to pump from atmospheric pressure down to 10^{-3} mbar and then the turbo pump further pumps up to 10^{-6} mbar.

During the RBS measurement, the beam current is regulated to prevent sample heating. It was kept below 15 nA in this study. Other critical factors that could alter the measurement, like the dead time and pile-up, were also controlled. Dead time is the interval after each event when the counting system cannot record another new event [Leo94]. Pile-up occurs when more than one ion arrives within the detector response time. The measurement is thence affected because of the possibility of two occurrences being recorded as one.

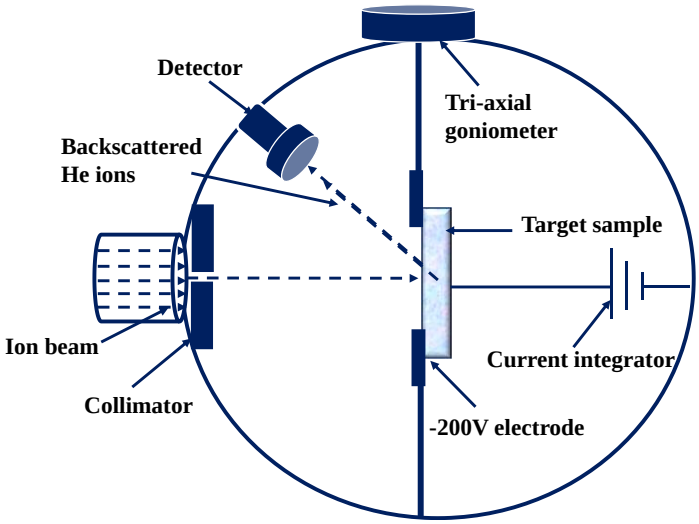

Figure 5.2. *Schematic diagram of the scattering chamber.*

The counting system comprises the Si surface barrier detector, the pre-amplifier, the amplifier, the multichannel analyser and the computer (see Figure 5.3). The detector, which operates at a reverse bias voltage of 40 V electric field, detects the backscattered alpha particles at an angle of 165 °. The pre-amplifier integrates the output charge signal into a voltage signal which is equivalent to the energy of the backscattered He ions. The amplifier amplifies the voltage and feeds it to the digital oscilloscope (to show the shape of the amplified voltage signal). The digital converter (ADC) component of the multichannel analyzer (MCA) digitizes the signal and the data is finally displayed on the computer screen (as count versus channel number). The displayed data can be printed or saved. The count or yield represents the total number of the backscattered alpha particles, and the channel number is proportional to the backscattered energy.

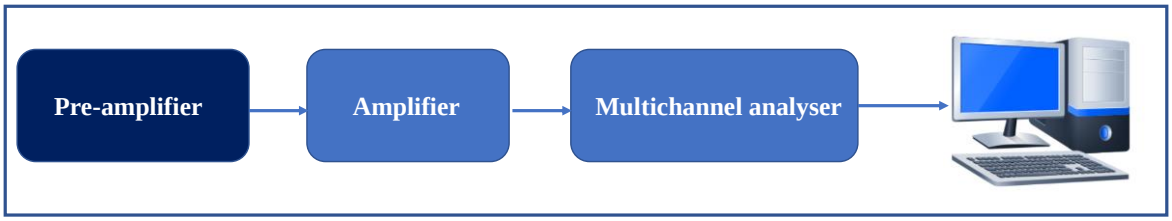

Figure 5.3. *RBS counting system*

5.1.2 The Rutherford backscattering spectrometry theory

The material (target sample) to be characterized is mounted on a sample holder in a vacuum chamber. A projectile ion (mostly charged alpha particle in the energy range of 1.4 – 1.6 MeV) is made to interact with the target sample. After interaction with the target's nuclei, some alpha particles are backscattered at an angle (between 160 and 170 degrees) and then detected at the detector. If only the backscattered alpha particles are detected, the backscattered yield versus the channel number is produced. Therefore, if the ions' stopping power, kinematic factor, and scattering cross-section are well known, information regarding masses and the depth distribution of the target elements can be determined. The analysis of the energy of the backscattered particles from the target material is the basis of the RBS technique.

5.1.3 Kinematic factor

The kinematic factor is an important parameter in the RBS technique. Typically, the RBS spectrum is calibrated using the kinematic factor. Assuming there is an elastic collision between an energetically moving projectile (of mass M_1 and energy E_1) and a target atom (of Mass M_2) at rest (as illustrated in Figure 5.4). The energy of the backscattered particle can be calculated from the kinematic factor and the energy of the standard beam. The projectile will transfer some of its energy to the target atom. While the target atom moves away with an energy E_2 at an angle, α, the projectile is scattered at an angle, φ, as shown in Figure 5.4. The interaction between the two colliding bodies rests on two assumptions:

(i) The projectile energy, E_0, is significantly greater than the binding energy.

(ii) Likewise, nuclear reaction and nuclear resonance are absent.

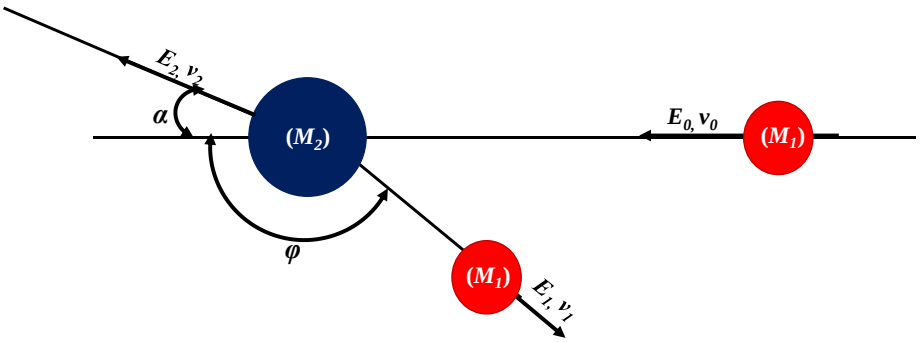

Figure 5.4. *Schematic illustration of the scattering event between a projectile and a target atom (Binary collision phenomenon)*

Applying the conservation of energy and momentum to the interacting two bodies, the energy of the backscattered projectile is given by the relation:

$$E_1 = KE_0 \tag{5.1}$$

K is the kinematic factor – the ratio of the backscattered particle's energy to the projectile energy before scattering. It can be calculated from equation (5.2):

$$K = {}^{E_1}/_{E_0} = \left[\frac{M_1 cos\varphi \pm \sqrt{M_1^2 - M_1^2 sin^2\varphi}}{M_1 + M_2}\right] \tag{5.2}$$

where E_0 and E_1 are the energy of the projectile and backscattered particles, respectively, M_1 and M_2 are the masses of the projectile (α-particle) and the target atom, and θ is the backscattering angle.

The kinematic factor, *K*, can then be used to identify the mass of an unknown target atom from a measured backscattered (RBS) energy spectrum. The kinematic factor increases with the target mass and approaches unity for heavy masses. Consequently, as mass increases, there will be a decrease in the mass resolution on the RBS energy spectrum.

5.1.4 Rutherford Scattering Cross-section

The exact number of the projectile ions that are backscattered from the target atoms into the differential solid angle (dΩ) is expressed in terms of the differential scattering cross section, dσ/dΩ. The cross-section is the number to determine how frequently elastic collisions between a projectile and a target atom occur. Typically, only a small portion of the incoming particles from the incident ion beam is backscattered by the target atoms and counted by the detector. Suppose a projectile beam (Q) strikes a thin, uniform target wider than the beam (see Figure 5.5).

Only a few ions (dQ) that enter the system are backscattered in the small differential solid angle, dΩ. The differential cross section is given by equation (5.3):

$$\frac{d\sigma}{d\Omega} = \frac{1}{N_v t}\left({}^{dQ}/_{d\Omega}\right)\frac{1}{Q} \tag{5.3}$$

where N_v represents the volume density of target atoms and t is the thickness. The number of target atoms per unit area is then $N_v t$, which assumes a relatively small solid angle, $\leq 10^{-2}$ sr.

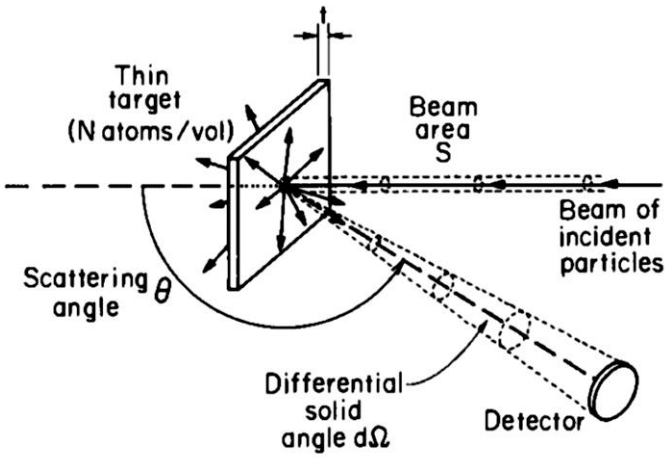

Figure 5.5. *A laboratory setup to demonstrate differential scattering cross-section. The detector only counts the few ions scattered within the small solid angle. Adapted from [Chu78].*

In the laboratory frame of reference, the differential scattering cross section is given by [Gro84]:

$$\frac{d\sigma}{d\Omega} = \left(\frac{Z_1 Z_2 e^2}{4E_i}\right)^2 \frac{4(\sqrt{M_2^2 - M_1^2 \sin^2\theta} + M_2 cos\theta)^2}{M_2 \sin^4\theta \sqrt{M_2^2 - M_1^2 \sin^2\theta}} \tag{5.4}$$

where Z_1 and M_1 are the atomic number and mass of the projectile, Z_2 and M_2 represent the atomic number and mass of the target, e is the electronic charge and E_i is the energy of the projectile before scattering.

The scattering cross-section is used in RBS to determine the average value of differential cross-section (dσ/dΩ) over a solid angle (dΩ) which is given by:

$$\sigma = {}^{1}/_{\Omega} \int \left(\frac{d\sigma}{d\Omega}\right) d\Omega \tag{5.5}$$

The substitution of equation (5.3) into equation (5.5) results in:

$$\sigma = {}^{A}/_{(\Omega . Q . N_v t)} \tag{5.6}$$

where A gives the total number of projectile particles that are backscattered and detected by the detector; the solid angle of the detector is denoted by Ω, which is equal to 3.41 mSr in

this study. The probability that the scattering events will result in some backscattered ions arriving at the detector is known as scattering cross section, σ, which has a unit of barns (1 barn = 1×10^{-24} cm^2) [Chu78]. When σ and Ω are known, the incident ions, Q and detected ions, A, can be calculated, thereby leading to the quantification of the experimental results. equation (5.6) can then be applied to determine the number of target atoms per unit area N_vt, which shows the ability of the RBS to give precise information about the number of atoms (per unit area) present in a sample.

RBS is more sensitive to the detection of higher Z elements because of the direct relationship of the differential cross section with the atomic number of the target, Z_2^2. One could also predict more backscattered count/yield when working with lower energies compared to higher energies because of the inverse relationship between the differential cross section and E_0^2.

5.1.5 Depth Profiling

Depth profiling gives the relationship between the backscattered particle energy (E_1) at a depth x inside the target and the projectile energy (E_0) that backscatters at the sample surface. An energetic particle loses kinetic energy when it is transversing a sample. The projectile type, the target's composition, and the projectile's initial velocity significantly affect the amount of energy loss (ΔE) per length travelled (Δx). An illustration in Figure 5.6 can be used to establish the relationship between the inwards and outwards energy losses as well as the depth of the projectile in the target. As seen in Figure 5.6, θ_1 would represent the angle between the target normal and the projectile beam direction. At the same time, θ_2 is the angle between the target normal and backscattered ion direction, respectively.

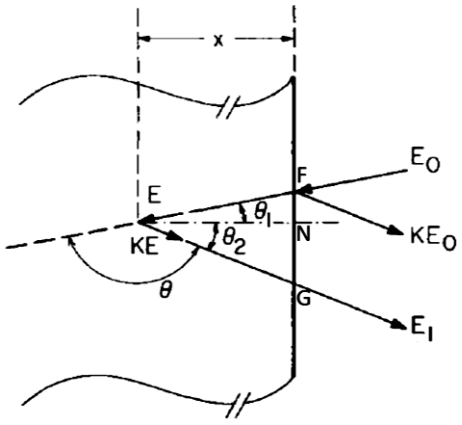

Figure 5.6. *Schematic description of the backscattering event of a projectile at the surface and at a depth x in a target sample. Taken from [Chu78]*

The triangle *EFN* (in the inward path) indicates that:

$$\cos\theta_1 = \frac{EN}{EF} = \frac{x}{E_0 - E} \tag{5.7}$$

With an assumption that the energy loss (dE/dx) along the inward (*in*) and outward (*out*) pathways are set to a constant value, we have:

$$E = E_0 - \frac{x}{cos\theta_1}\left(\frac{dE}{dx}\right)_{in} \tag{5.8}$$

For the outward path, the triangle *EGN* gives:

$$E_1 = KE - \frac{x}{cos\theta_2}\left(\frac{dE}{dx}\right)_{out} \tag{5.9}$$

Combining equations (5.8) and (5.9) and eliminating *E*, we have:

$$KE_0 - E_1 = \left[\frac{K}{cos\theta_1}\left(\frac{dE}{dx}\right)_{in} + \frac{1}{cos\theta_2}\left(\frac{dE}{dx}\right)_{out}\right]x \tag{5.10}$$

KE_0 is the energy of the backscattered ions from the surface of the target. equation (5.10) can be rewritten as a product of the backscattering energy loss factor (S) and the depth *x*, as in equation (5.11):

$$\Delta E = [S]x \tag{5.11}$$

where [*S*] is equal to:

$$\left[\frac{K}{cos\theta_1}\left(\frac{dE}{dx}\right)_{in} + \frac{1}{cos\theta_2}\left(\frac{dE}{dx}\right)_{out}\right] \tag{5.12}$$

ΔE is the difference between the two energies, KE_0 and E_1, counted by the detector. The ability of RBS depth determination is based on equation (5.11). This equation demonstrates that the energy lost by an energetic projectile on encountering a target is inversely proportional to the depth of penetration into the target. RBS measurement unit is given in atoms per unit area (i.e., at/cm^2). As a result, equation (5.11) can be expressed as follows:

$$\Delta E \propto N_v x \tag{5.13}$$

By introducing a constant of proportionality, ε, equation (5.13) can be rewritten as:

$$\Delta E = \varepsilon N_v x$$

$$\varepsilon = \frac{1}{N_v}\frac{dE}{dx} \tag{5.14}$$

where N_v is the atomic density of the target material and the constant ε is known as the stopping cross-section factor. By considering, the expressions in Equation (5.12) and (5.14), Equation (5.11) can be expressed as a product of stopping power cross section [ε], atomic density, N_v, and the depth x (see equation (5.15) below).

$$\Delta E = [\varepsilon] N_v x \tag{5.15}$$

where [ε] is equal to:

$$[\varepsilon] = \left[\frac{K}{cos\theta_1}(\varepsilon)_{in} + \frac{1}{cos\theta_2}(\varepsilon)_{out}\right] \tag{5.16}$$

The values of [S] and [ε] for different elements can be found in the literature.

5.1.6 RBS calibration

Each time an RBS measurement is performed, systematic, statistical, and human errors are unavoidable. These errors can hamper the accurate estimation of RBS measurement, and because of this, energy calibration is important for precise RBS measurement and analysis of RBS results. The conversion of experimental RBS data, usually obtained in channel numbers, to corresponding backscattered ion energy can be performed through energy calibration, as given in equation (5.17).

$$E = ax + c \tag{5.17}$$

where *a* is the energy per channel (keV/channel), referred to as a conversion factor, *x* is the channel number and *b* is the offset value (keV) or the intercept. The plot of the detected backscattered ions energy against the channel numbers produces a linear graph (see a typical RBS energy calibration plot in Figure 5.7.

Before carrying out the RBS measurements on the GC substrate samples each day, energy calibration was first carried out by measuring SiC samples or any other compounds containing carbon (C) elements. For uniformity of the energy calibration data, SiC was used throughout the study. The first step in the calibration method was to extract the surface channel numbers of these elements (SiC) from their individual RBS spectra. It is thus possible to determine the surface energy values by multiplying the projectile beam energy (1.4 and 1.6 MeV) by the kinematic factor (K) of these elements using equation (5.2).

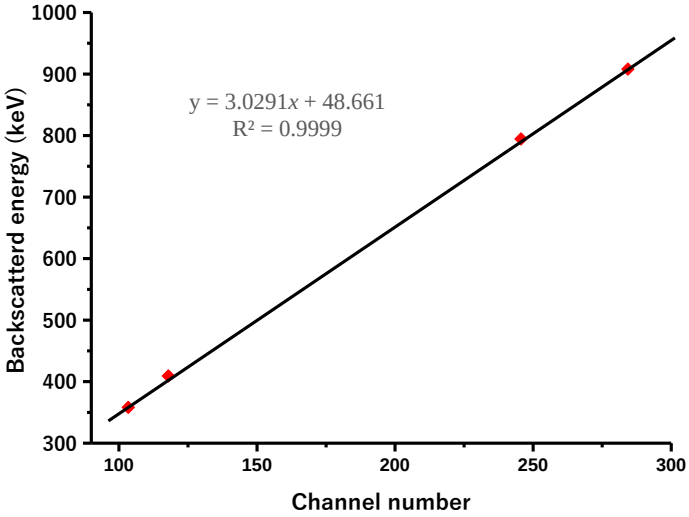

***Figure 5.7**. A typical RBS energy calibration plot*

5.2 Secondary ion mass spectrometry (SIMS)

Secondary ion mass spectrometry (SIMS) is a popular analytical technique to directly determine the concentration of trace elements in a solid material. SIMS is an excellent tool for obtaining precise information about the concentrations as well as depth distributions of all elements and their isotopes in a solid matrix. The molecular composition of a solid material can also be determined with SIMS. While the SIMS technique has helped advance the understanding of the fundamental properties of different materials, its popularity stems from the following [Por07]:

(i) It can identify all elements in the periodic table, from Hydrogen to Uranium.
(ii) Quick element mapping is achievable with SIMS.
(iii) SIMS can achieve lateral resolutions dependent on the ion beam diameter, typically below 0.2 μm.
(iv) SIMS has excellent sensitivity to detect trace concentrations as low as parts per billion (ppb) level.
(v) SIMS can detect small concentration differences as well as precise isotopic measurements.
(vi) Excellent depth resolution (in the nm range) [Por07].
(vii) The minimal sample preparation steps are necessary before analysis (in most cases, no sample preparation is required.

The SIMS measurements were performed at the Universities of Oslo, Norway.

5.2.1 Principle of Secondary ion mass spectrometry (SIMS)

The last few decades have seen the advancement of mass spectrometry since the inception of the first evidence of secondary ions by J.J. Thomson in 1910 [Tho10]. Over these years, three main SIMS instrumentations have been developed: magnetic sector [Cas62], [Lie67], [Her49], quadrupole [Ben71], [Wit75], [Mag78] and time-of-flight [Cha81]. Magnetic sector SIMS (Cameca IMS-7f) was employed for measurement in this study. This instrument can be operated in two main modes: the mass spectrum and the dynamic modes [Van14].

For the mass spectrum mode, the sample (target) is investigated for a variety of elements. This involves raster scanning an area of a material surface with a primary ion beam, and the ejected ions (secondary ions) are scanned by a magnetic field analyzer so that each element's mass per charge ratio can be counted at a specific time at the detector [Van14]. The detector

displays a spectrum of signal intensity as a function of the mass per charge ratio. Additionally, absolute concentrations can be measured accurately with ±10% error using reference standards.

The dynamic mode was used for the depth profile measurement in this study. A primary ion beam was raster scanned on an area of the sample surface, which resulted in the ejection of some ions (secondary ions) [Van14]. Continued rastering in the same area of the sample results in the formation of a crater on its surface. A magnetic field analyzer separates the ejected ion(s) by mass-to-charge ratio. The relevant ion's profile is then received and counted at the detector as a function of time. The time scale is then converted into depth by measuring the crater depth using a Dektak 8 stylus profilometer (in this study). The accuracy of the crater depth depends on the proper calibration of SIMS. The depth calibration was achieved by ensuring a constant erosion rate along the whole profile, which is acceptable given that the material is homogenous.

5.2.2 Sputtering and ionization

Sputtering is the process of removing atoms from the surface of a sample by bombarding it with ions from a primary beam source. See Figure 5.8 for the illustration of sputtering. The available ion sources in the Cameca IMS-7f SIMS are caesium (Cs) or oxygen (O_2) ions, chosen based on the electron affinity and ionization potential of the secondary atoms to be measured. It is well known, for instance, that caesium bombardment enhances the yield of negative secondary ions, whereas oxygen bombardment increases the yield of positive secondary ions [Vic89]. A collision cascade model by Sigmund [Sig69] can be used to explain the interaction of the primary ions with the target atoms that results in sputtering. The model considers that each primary ion transfers energy to target atoms in a sequence of binary collisions. The energetic target atoms, known as recoils, subsequently collide with several other target atoms. The process continues until many atomic species (secondary ions) are ejected (sputtered) from the sample surface. The energy range (1 – 30 keV) for most SIMS measurements is sufficient to energize most atoms in the near-surface region to overcome the surface barrier and eventually get ejected from the target surface [Zal94].

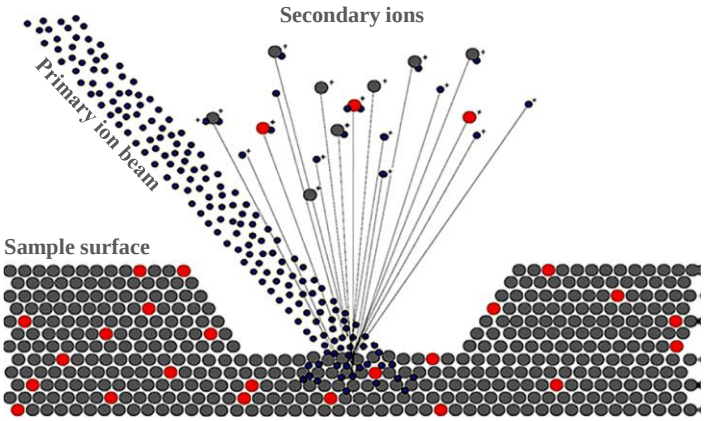

***Figure 5.8**. An illustration of the sputtering and ionization process in SIMS. Adapted from [EKB19].*

The sputter yield is the average number of atoms sputtered (from the target) per primary ion beam. This parameter depends on the primary ion mass and energy, the target atomic mass and height of the surface barrier to escape the target atoms, and the angle of incidence of the primary ion beam. The usual sputtering yield, *Y*, falls between 1 and 10 atoms/ion [Stev15].

Sputtered atoms must be ionized to be analyzed. The number of sputtered atoms that became ionized is referred to as the "Secondary ion yield." The yield is low (about 1%) but can increase when reactive species like Cs or O_2 are employed as the primary ion beam. The sputtered atom has a high electron affinity and ionization potential when Cs and O_2 ion sources are used, respectively. As a result, the secondary ion yield can vary with the substrate effect (also known as the matrix effect), which is the primary reason SIMS is not -self-quantitative and depends on standardized reference samples. The most common matrix effects are caused by changes in the sample's oxygen atom density [www2]. Ion-implanted reference samples provide the most accurate form of measurement. The ion implantation technique provides information about the dose of the implanted ions, enabling precise measurement of absolute concentrations with less than 10% error [Hei14]. The reference standard used for all the SIMS measurements in this study is the selenium as-implanted GC sample.

The primary beam energy and angle of incidence are other factors that can affect the ion yield. SIMS analysis is done at incidence angles between 0 and 60° because the secondary ion yield and the sputtering have opposite dependence on the angle of incidence [Stev15].

The secondary ion yield can also be affected by structural changes in the sample brought about by sputtering.

The secondary ion yield *Y'* of a given element in a target sample is expressed by Equation (5.18) [Fel86]:

$$Y' = \int_0^{E_m} \alpha(E) Y(E) dE \tag{5.18}$$

where the ionization probability is denoted by α and depends on the sample compositions; Y is the total sputtering yield per primary ion impact, which also depends on the target material. E_m is the peak energy of the sputtered atoms.

As given in Equation (5.19), the intensity of the secondary ions (I_i) of element *i* in the target sample that (reaches the electron multiplier) depends on many parameters: primary ion beam intensity (I_p); the species concentration, the SIMS setup transmission function, T (such as the apertures type used and the thickness of the slits); the ionization probability, α_i and the sputtering yield, Y [Fel86]

$$I_i = I_p T \alpha_i Y C_i \tag{5.19}$$

The atomic concentration cannot be directly evaluated from Equation (5.19) because C_i (the concentration of the secondary ion of interest) and αi are unknown, so SIMS rely on a standard reference sample. The first four proportionality parameters on the right-hand side of Equation (5.19) are directly measured from a standard reference sample under the same conditions as for the sample being studied. Typically, these parameters are combined to what is referred to as a sensitivity factor $\mathrm{SF} = (I_p T \alpha Y)^{-1}$, which converts the intensity of the signal (counts per second) to concentration (cm^{-3}).

The relationship between the concentration and sensitivity factor is given by:

$$C = \mathrm{SF}\left(\frac{I_i}{I_m}\right) \tag{5.20}$$

where I_i and I_m are the intensities of the secondary ions and the matrix impurity intensity, respectively.

A slight variation in the height of the sample holder may affect the extraction of the ionized species because of the complex design of the magnetic sector instrumentation (only 4.5 mm separates the sample holder and extraction electrode). In order to address this fluctuation,

the impurity intensity is normalized to the intensity of a matrix specie, and the sensitivity factor (SF) is renamed relative sensitivity factor (RSF) [www2]:

$$RSF = \frac{\phi C I_m}{d\sum I_i - dI_b C}\left(\frac{EM}{FC}\right) \tag{5.21}$$

where ϕ is the implanted ion fluence (atoms/cm^3), C is the number of SIMS measurements or the data cycles, EM/FC is the ratio of the electron multiplier (EM) to Faraday cup (FC) counting efficiency ratio, d is the crater depth (cm), I_i is the sum of the secondary ion counts of the impurity isotopes over the depth profile, I_b.

5.2.3 Analysis in SIMS

The secondary ions generated close to the sample surface are accelerated toward the mass spectrometer by an extraction electrode close to the sample surface (see Figure 5.9. Only secondary ions from the crater's centre are detected after this secondary beam first travels through a set of apertures. The secondary ions will then go into an electrostatic energy analyzer (ESA), which comprises two curved metallic plates at various potentials (see illustration in Figure 5.9 [Hei14].

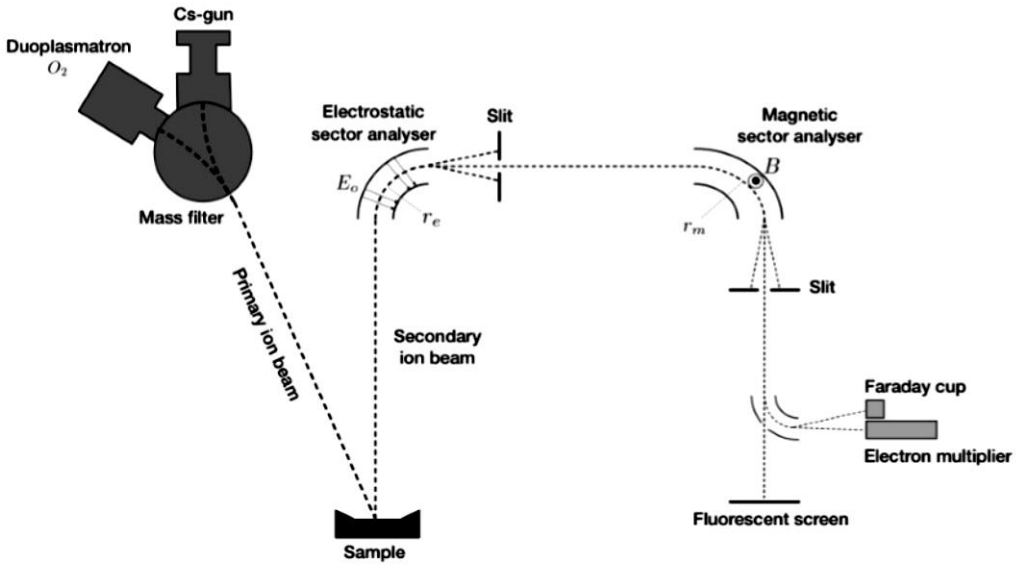

***Figure 5.9**. Cameca IMS-7F secondary ion mass spectrometry (SIMS) instrumentation. Taken from [Sky14]*

The ESA then separates the larger ions and lower energy-charged molecules from the high-energy ions. A centripetal force acts on the separated ions:

$$F = qE_0 \tag{5.22}$$

where E_0 represents the electric field and q *is* the charge.

The centripetal force experienced by an ion of mass m travelling at a tangential speed of v_e through the ESA along a direction with curvature radius r_e is illustrated as follows:

$$F = \frac{mv_e^2}{r_e} \tag{5.23}$$

Combining these two Equations, (5.22) and (5.23) gives:

$$qE_0 = \frac{mv_e^2}{r_e} \tag{5.24}$$

Equation (5.24) is the electric field part of the Lorentz force. It follows from equation (5.24) that only ions with kinetic energies that match r_e will be bent to pass through the ESA end slit and continue moving toward the magnetic sector analyser (MSA) for further separation and analysis.

As the ions enter the MSA, they experience the Lorentz force given by Equation (5.25) from a magnetic field, B, perpendicular to their direction. The MSA separates the ion by their mass per charge ratio and only allows masses with path radius, r_m, to pass through to the detector.

$$F = qv_mB \tag{5.25}$$

The centripetal force acting on the ion of mass m travelling at a tangential speed v_m through the MSA along a path of curvature radius, r_m, is expressed as:

$$F = \frac{mv_m^2}{r_m} \tag{5.26}$$

Combining Equations (5.25) and (5.26) yields:

$$F = qB = \frac{mv_m}{r_m} \tag{5.27}$$

By setting $v_e = v_m$ and assuming that the velocity of the ions does not change as they move from the ESA to the MSA, the two Equations, (5.23) and (5.27), can be combined to give Equation (5.28):

$$\frac{m}{q} = \frac{(r_m B)^2}{r_e E_0} \tag{5.28}$$

Only the ions that satisfy Equation (5.28) will be counted at the detector.

The primary reason for using the ESA is to reduce the range of ion energies that will enter the MSA thereby enabling high mass resolution, which may be further improved by narrowing the MSA exit slit [Hei14]. Additionally, compared to heavier or larger molecules, the energy distribution of the sputtered particles is often higher for single ions. The unwanted ionized ions or molecules that would be easily mistaken for a faster-moving single ion can be suppressed by orienting the ESA exit slit so that only the higher energy ions are allowed.

5.3 Raman spectroscopy

An Austrian physicist, Adolf Smekal, in the early 20th century predicted the scattering of monochromatic light with change in frequency [Sme23]. This prediction led to the development of Raman spectroscopy by Dr C.V. Raman. In 1928, Raman and Krishna performed an experiment that confirmed that light could be scattered inelastically by different materials [Ram28]. Sunlight was the monochromatic light source; a telescope was used as the collector and the eyes served as the detector. The experiment was the basis of Raman spectroscopy.

Raman spectroscopy is a non-destructive technique for determining the chemical and structural properties of a sample through the Raman effect. Raman spectroscopy can provide extensive information on the chemical structure, crystallinity, and polymorphism of the sample [Ros16]. The basis of Raman spectroscopy is the interaction of monochromatic light with the sample, which results in photon emission at different frequencies. After interaction with the material, the up or down vibrations of the photon frequencies represent the Raman shift (wavenumbers), which are then used as fingerprints to identify the properties of interest in the studied material. The rotational and several other low-frequency modes of a sample can also be observed using Raman spectroscopy. This technique can be used to determine the crystallinity of a material by providing information on the chemical and intermolecular bonds [Gar89].

5.3.1 Principle of Raman spectroscopy

When a sample is exposed to a light source, such as a laser, the photons of frequency ($h\nu_0$) interact with the atoms and molecules of the sample, thereby distorting the electronic structure and creating a virtual state (as illustrated in Figure 5.10). While the photons are emitted as quickly as they are formed, the electrons return to a more stable state either by elastic or inelastic scattering. Elastic scattering of the photons (also known as Rayleigh scattering) occurs when an electron in the ground state is excited to a higher energy state and de-excited to the initial state without losing or gaining energy. This causes most photons to scatter elastically with the same frequency ($h\nu_0$) as the incident photons, as illustrated in Figure 5.10).

The sample can also gain or lose energy when it is excited to a higher energy state and falls back to a vibrational energy level, which is lower or above the initial energy state. The

frequency of the scattered photons changes (shifted upward or downward) relative to the incident light due to the energy difference between the incident and scattered photons. This phenomenon is known as the Raman shift. The Raman shift provides the needed information (like the vibrational, rotational and electronic energy modes) about the sample.

Anti-Stokes and Stokes Raman lines are used to describe the upward or downward Raman shift, respectively. Stokes Raman scattering occurs when an excited electron absorbs some energy from the incident photons and de-excites to a vibrational energy state, not the ground state. In the process, the scattered photon has less energy (given by $h\nu - h\nu_0$) and a longer wavelength than the incident photon. On the other hand, anti-stokes Raman scattering describes when an electron in the vibrational excitation state absorbs energy from the incident photon and returns to the original ground state via the emission of a scattered photon that is more energetic ($h\nu + h\nu_0$) than the incident photon. Also, the scattered photon has a shorter wavelength.

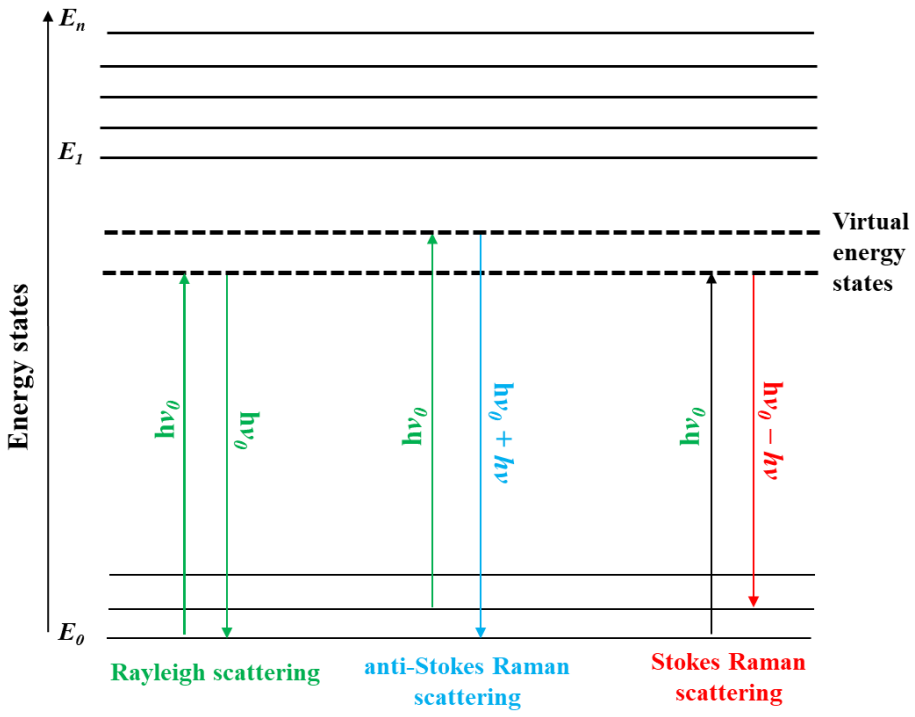

Figure 5.10. *Illustration of Rayleigh scattering, anti-Stokes Raman scattering and Stokes Raman scattering*

5.3.2 Raman instrumentation

As shown in Figure 5.11 below, a typical Raman system has four major components, which include: (a) an excitation light source or laser beam; (b) a spectrometer system (c) a charged coupled detector (CCD) to detect the Raman signal and (d) a computer system where the Raman spectrum is displayed.

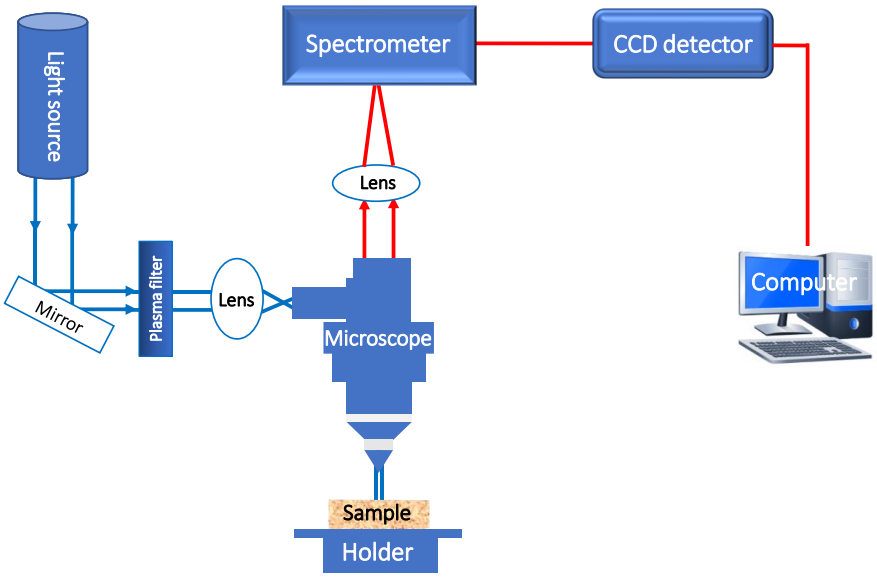

Figure 5.11. *Raman instrumentation*

The material (to study) is illuminated by a laser beam in the visible (Vis) or near-infrared (NIR) range or Ultraviolet (UV) range. The interaction of the light with the sample results in scattered photons, which contain information about the vibrational energy modes of the sample's atoms and or molecules. The interaction of the incident light with the sample results in scattered photons that include information about the molecular vibrational energy modes. The Raman spectrum of the analytes is obtained by collecting the scattered light with a lens and sending them via a spectrometer or interference filter system. The detector receives the scattered photon that exits the spectrometer (as an optical signal) and processes it into an electrical signal, which is the Raman data required. Finally, the data is stored in a computer system in a viewable and manipulatable format. By using notch filters, it is possible to increase the sensitivity of the Raman scattering.

It is most challenging to distinguish the weak Raman scattering from the dominant Rayleigh scattering. The Raman instrument's sensitivity to Raman scattering can be increased by using notch filters. Likewise, the Raman scattering can become more sensitive by increasing

the sensitivity of the detection system using multichannel detectors, such as charge-coupled devices (CCD) [Smi05].

5.3.3 Raman theory

When light interacts with a substance (as in Raman spectroscopy), the electric field component of the incident photon distorts the molecule electron cloud and induces an electronic dipole moment. The dipole moment is directly related to the time-dependent electric field intensity, *E*, as given in equation (5.29) [Col12]:

$$\mu = \alpha E \tag{5.29}$$

where α is the polarizability, which measures how the electric field distorts the molecule's electron cloud. A change in polarizability often accompanies all molecular vibrations that are Raman active.

The electric field *E* of the incident is given by [Opi13]:

$$E = E_0 \cos 2\pi\, \nu t \tag{5.30}$$

where E_0 is a constant representing the electric field's peak value, ν is the radiation frequency, and *t* is the time.

Combining equations (5.29) and (5.30) gives:

$$\mu = \alpha E_0 \cos 2\pi\, \nu t \tag{5.31}$$

The polarizability (α) parameter is not a constant as it changes with each vibrational or rotational motion of the molecule(s) involved [Gra91]. For example, a diatomic molecule alternately experiences compression and tension during its vibration, just like a spiral spring does [Col12].

The polarizability (α) can be expanded in the Taylor series for small displacement (*Q*) of the molecule from its equilibrium position:

$$\alpha = \alpha_0 + \frac{\partial \alpha}{\partial Q} Q + \cdots \tag{5.32}$$

where α_0 is the equilibrium polarizability and $\frac{\partial \alpha}{\partial Q}$ is the rate at which the polarizability changes in relation to the displacement, *Q*, as measured from the equilibrium position.

The displacement, *Q*, of the molecule about its equilibrium position in vibration mode is given by:

$$Q = Q_0 \cos 2\pi v_v t \tag{5.33}$$

where v_v is the frequency of vibration of Q and Q_0, this parameter v_v is a constant (the maximum value for Q). The substitution of Q into equation (5.32) gives:

$$\alpha = \alpha_0 + \frac{\partial \alpha}{\partial Q} Q_0 \cos 2\pi v_v t + \cdots \tag{5.34}$$

By using harmonic approximations, the higher order terms in Equation (5.34) can be ignored, then the equation changes to:

$$\alpha = \alpha_0 + \frac{\partial \alpha}{\partial Q} Q_0 \cos 2\pi v t \tag{5.35}$$

The substitution of α into equation (5.31) yields:

$$\mu = \alpha_0 E_0 \cos 2\pi\, vt + \frac{\partial \alpha}{\partial Q} Q_0 E_0 \cos 2\pi\, vt \cos 2\pi v t \tag{5.36}$$

Using the trigonometric identity for the product of two cosines, equation (5.36) can be rewritten as:

$$\mu = \alpha_0 E_0 \cos 2\pi\, vt + \frac{Q_0 E_0}{2} \frac{\partial \alpha}{\partial Q} [\cos 2\pi (v - v_v) t + \cos 2\pi (v + v_v)\, t] \tag{5.37}$$

Equation (5.37) above demonstrates that the induced dipole moment would change with the three frequencies, v, $v - v_v$ and $v + v_v$. These frequencies are the major scattering phenomena in Raman spectroscopy: Rayleigh scattering, Stokes Raman scattering, and anti-Stokes Raman scattering, respectively (as illustrated in Figure 5.10 above).

5.3.4 Raman spectra of some forms of carbon materials

Raman spectroscopy is a non-destructive excellent technique for characterizing all forms of carbon materials. Properties such as internal stress, microstructural changes, and bonds in any form of carbon materials can be observed with high precision using Raman spectroscopy [Fer00].

Figure 5.12 depicts the Raman spectrum of a natural diamond, measured with a 514.5 nm laser excitation wavelength source. There is only one distinct peak in the spectrum, T_{2g} symmetry zone centre mode at about a wavenumber of 1332 cm^{-1} [Sol70]. The FWHM of the pure diamond is approximately 2 cm^{-1} when fitted with a Lorentzian function [www1].

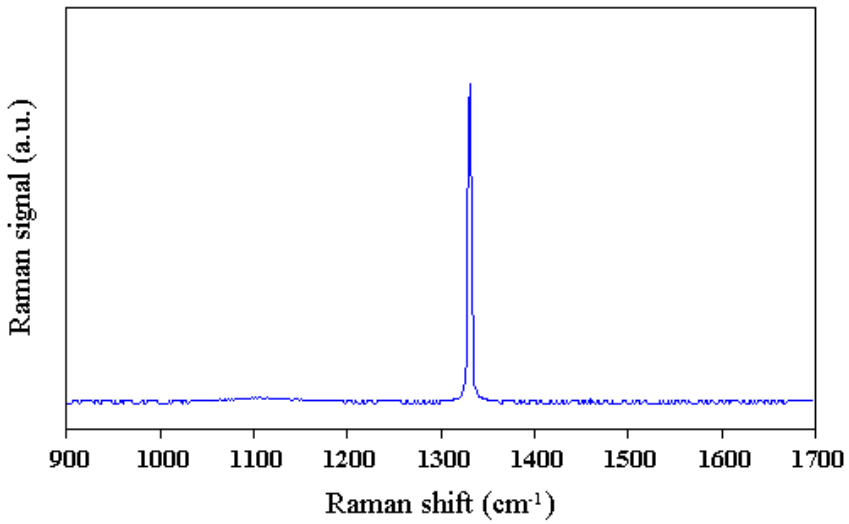

Figure 5.12. *Raman spectrum of a natural diamond taken with a 514.5 nm laser excitation wavelength. Obtained from [www1].*

Figure 5.13 is the Raman spectrum of single-crystal graphite measured by Tuinstra and Koening [Tui70]. The authors reported a peak (G peak) at 1575 cm^{-1}. This peak is attributed to the zone centre phonons of the E_{2g} symmetry [Fer00]. The G peak is the identity of all graphitic materials.

Figure 5.14 shows the Raman spectra of some other forms of non-crystalline graphitic carbons that exhibit some degree of disorder (charcoal, coke, diamond-like carbon and GC). Apart from the G peak around 1580 – 1600 cm^{-1}, another peak can be seen at 1343 – 1360 cm^{-1} (see Figure 5.14). This peak (D peak) is attributed to the Raman breathing mode of A_{1g} symmetry. The D peak intensity increases (compared to the G peak) as the degree of disorder in the graphitic carbon increases.

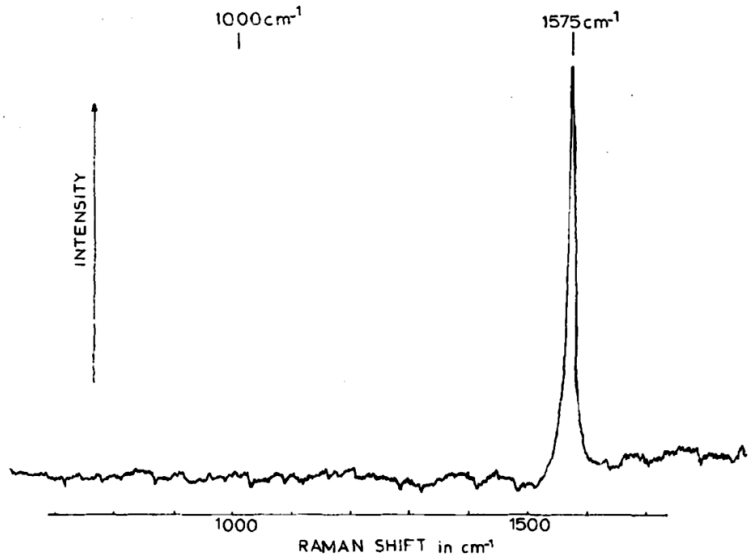

Figure 5.13. *Raman spectrum of single crystal graphite. Adapted from [Tui70].*

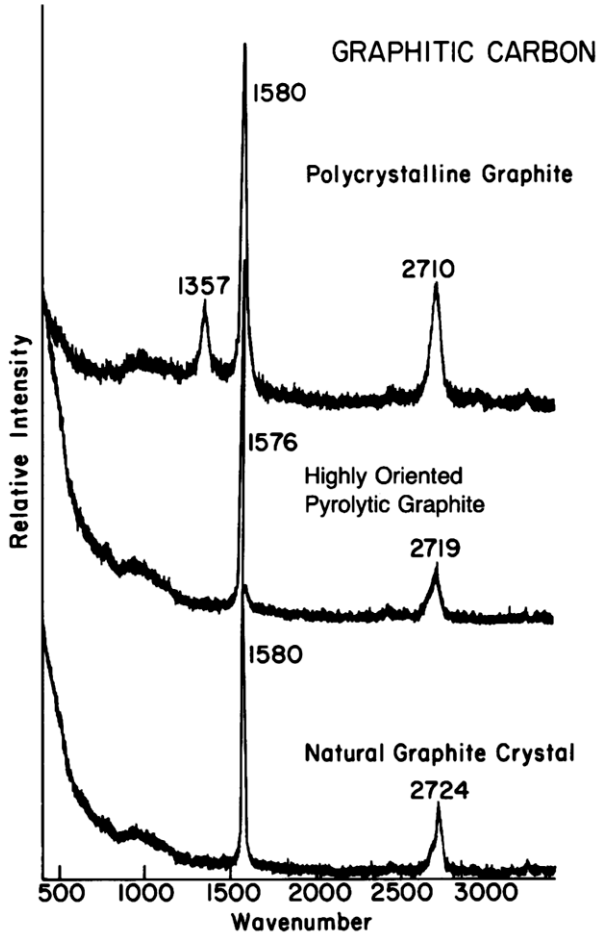

Figure 5.14*. Raman spectrum of some non-crystalline graphitic carbons. Adapted from [Kni89].*

5.4 Transmission electron microscopy (TEM)

The human eye's limitation in viewing objects (at the microscopic level) lies in its poor resolution. Human eyes can only see within the nearest 0.1 and 0.2 mm [Wil09]. The light microscope (LM) is an early technique used for studying objects with optical lenses, which rely on the visible light source. Following the development of LM, it was found that electrons could be utilized as the light source to increase imaging resolution, as demonstrated by Ernst Ruska and Max Knoll in their paper in 1932 [Rus32]. By 1933, the resolution of this microscope had improved, and as a result, numerous electron microscope (EM) techniques were created to explore different sample types [Wil09]. For example, bulk samples can be studied by several EM techniques, such as the scanning electron microscope (SEM), the electron microprobe analyzer (EMPA), the electron probe microanalyzer (EPMA), the scanning Auger microscope (SAM), the scanning Auger microprobe (SAM) and the transmission electron microscopy (TEM). All these methods rely on electron-sample interactions to generate a variety of signals. Transmission electron microscopy (TEM) involves using electromagnetic lenses to create images, allowing electrons to pass through a very thin sample. TEM is a very effective instrument for studying the microstructure of different materials [Boz99], [Edi91], [Tho79]. This technique can deliver excellent image resolution within the angstrom (Å) range, reveal structural information from electron diffraction, and provide chemical composition data from high-energy electron interactions with the core electrons of the sample (studied). TEM can also be used to examine the internal and sub-micrometre fine structure of solid materials [Goo11].

Today, TEM has been extensively used in various fields and purposes ranging from physical sciences, forensic investigations, product inspection, technical development, biological sciences, and engineering. According to Goodhew [Goo75], four key parameters determine the scope and amount of information that can be recovered from the TEM technique. These include the resolving power of the microscope (often lower than 0.3 nm), the energy distribution of the electron beam (typically hundreds of eV), the thickness of the specimen (nearly always much less than 1μm), and the composition of the sample.

TEM works the same way as a projector, except it shines a beam of electrons and not a beam of light (like in a projector). Transmission electron microscopes use a high-voltage electron beam to produce images. An electron gun (located at the very top of the instrument) generates a stream of electrons that passes through a set of lenses. Two condenser lenses, C1 and C2 (as in Figure 5.15), are used to focus this electron stream into a narrow, coherent

beam and hit the sample. Several signals are produced when the electron beam hits the specimen, as depicted in Figure 5.16. Each of these signals is useful in one or two surface analysis measurements. For example, auger electrons, backscattered electrons, secondary electrons, characteristic X-rays and continuum X-rays are useful in Auger spectroscopy, scanning electron microscopy (SEM), and X-ray energy dispersive spectroscopy (XEDS or EDS), respectively. The unscattered transmitted electrons and the unscattered elastically and inelastically electrons are useful for TEM measurement. The unscattered transmitted electrons as well as elastically scattered and inelastically scattered electrons are important signals in TEM measurement. Specifically, these electrons are used in the following TEM applications [Luo16]:

(i) Electron diffraction, including selected-area electron diffraction (SAED), convergent-beam electron diffraction (CBED), Kikuchi diffraction, and nano-beam electron diffraction (NBED)
(ii) TEM Imaging, including diffraction contrast imaging, high-resolution TEM (HRTEM), mass-thickness contrast imaging, Z-contrast imaging, and high-resolution electron microscopy (HREM).

The objective lens concentrates the transmitted electrons component into an image. Optional metal apertures called objective and diffraction apertures can be used to limit the beam's path. The objective aperture improves contrast by excluding high-angle electrons that have been diffracted, while the diffraction aperture enables users to look at the periodic diffraction of electrons caused by organized arrangements of atoms in the sample. The image is expanded as it travels down the column through the intermediate and projector lenses. Light is produced when an image hits a phosphor viewing screen (nowadays, a CCD camera is used), enabling the observer to view the image with each component coloured differently depending on density.

5.4.1 TEM instrumentation

As illustrated in Figure 5.15, transmission electron microscopy (TEM) instrumentation can be categorized into three main components: an illumination system (electron source), a set of lenses and apertures, and a sensitive detector system.

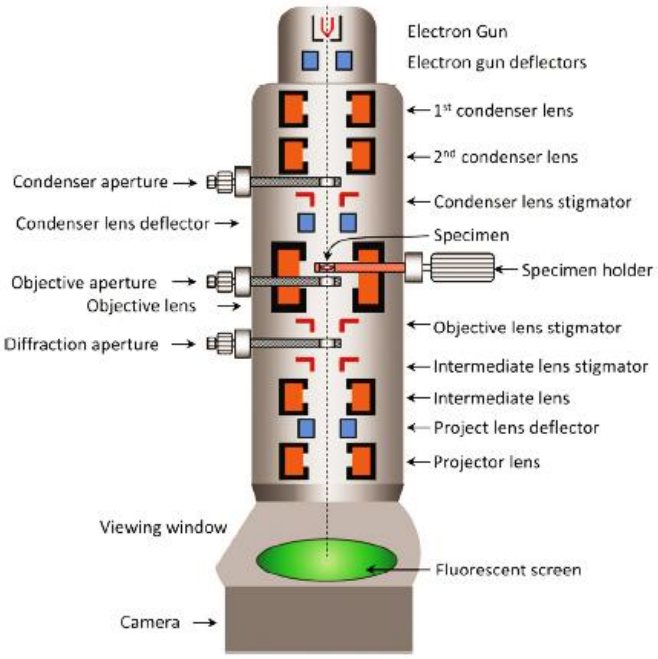

Figure 5.15. *TEM instrumentation. Adapted from [Luo16].*

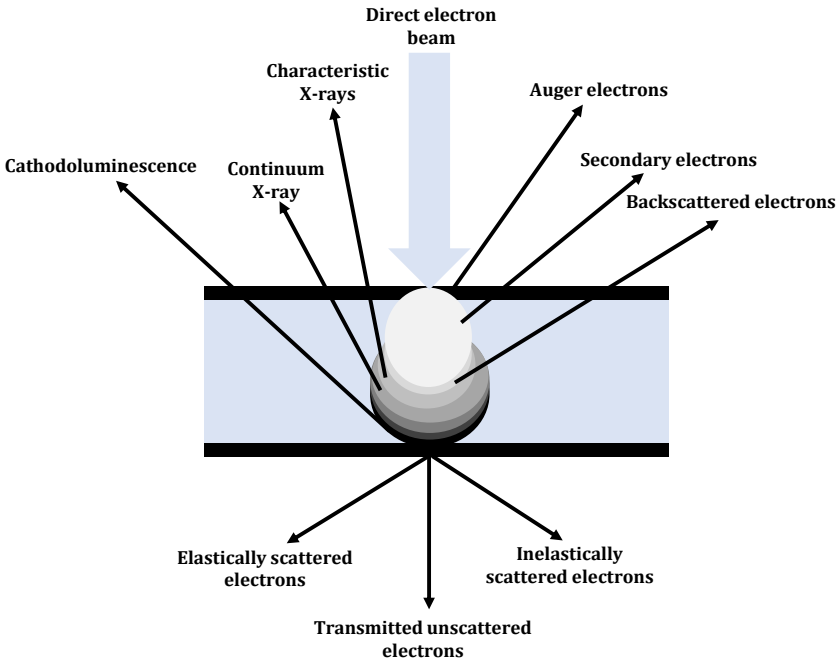

Figure 5.16. *Electron interaction with a sample to generate different signals.*

5.4.1.1 Illumination system

The illumination system, also known as an electron lighting source, provides rays that travel straight down the microscope before impacting the sample [Ful08]. This source is usually an electron gun characterized by high voltage [Luo16]. The most common types of guns are thermionic and field-emission electron guns (FEG) [Luo16]. The function of the electron gun is to direct and focus the beam of accelerated electrons (through a condenser aperture) onto the sample (to be measured) [Ful08].

5.4.1.2 Electromagnetic lenses and apertures

The electromagnetic lenses function as a control for the trajectories (path deflection) of the electrons when focusing them on the sample. These electromagnetic lenses can demagnify or magnify the image by adjusting the focal lengths, f through the lens current, i. As illustrated in Figure 5.17, the lens current can be controlled to modify the focal length to achieve an under-focused image (below the image plane), an in-focus image (in the image plane) and overfocused image (above the image plane). There exists a relationship between the focal length and the lens current, as given in equation (5.38) [Luo16]:

$$f = K\left(\frac{V}{i^2}\right) \tag{5.38}$$

V is the accelerating voltage, i is the lens current, and K is a constant.

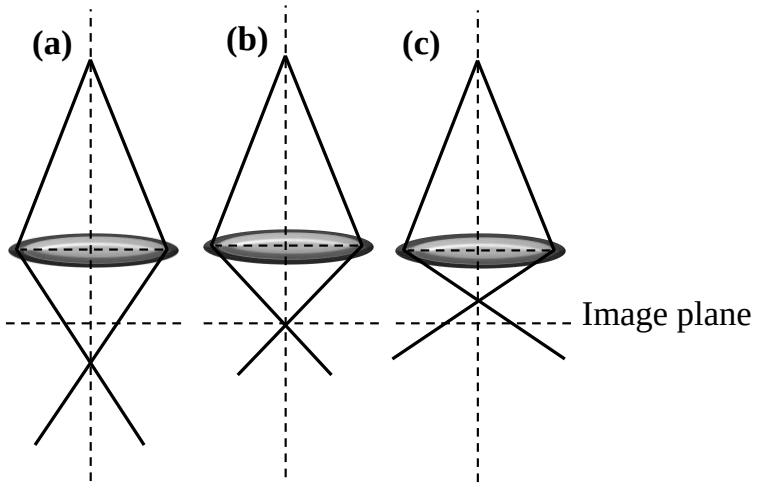

Figure 5.17. *Focus of the lens to achieve (a) under-focused image (b) in-focus image (c) overfocused image. Redrawn from [Luo16].*

The lens and apertures in TEM include the condenser lenses, optical lenses and their corresponding apertures.

❖ **Condenser lenses and condenser apertures:** As seen in Figure 5.18, the condenser lenses are positioned above the sample to control how the electron beam illuminates the sample. There are two condenser lenses: condenser lens 1 (C1): regulates the beam size, while condenser lens 2 (C2) regulates the beam brightness. For imaging, the C2 is kept overfocused so the rays can be parallel before reaching the sample. A weaker beam suggests an overfocused beam, whereas a stronger one suggests an under-focused beam [Luo16]. The "spot size"— the general size range of the last spot that strikes the sample is primarily determined by the first condenser lens (often regulated by controlled by the "spot size knob"). By altering the size of the spot on the sample, the second lens (specifically controlled by the "intensity or brightness knob") changes it from a broadly dispersed spot to a pinpoint beam. Below the C1 lens are located the condenser apertures. The condenser apertures remove high-angle electrons from the beam, which is user-selectable. The C1 aperture size is fixed, while the C2 aperture size can be adjusted. The condenser apertures regulate the electron beam intensity and the semi angle, α. As seen in Figure 5.18, a smaller condenser aperture decreases the semi angle and reduces the intensity; a larger condenser aperture increases the semi angle and yields a stronger intensity. Larger apertures can be selected for general TEM observations, while a smaller aperture is a good option for high-resolution images [Luo16].

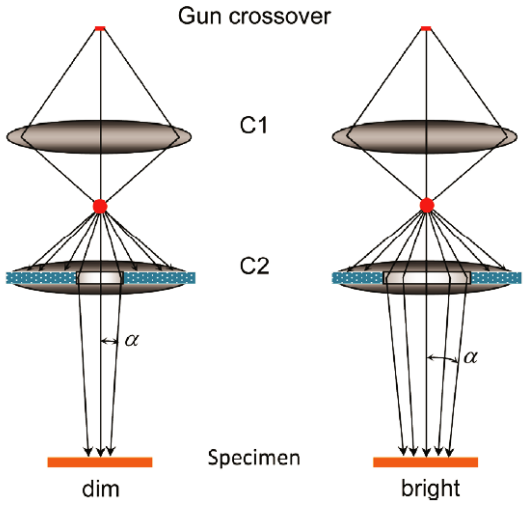

***Figure 5.18**. Condenser apertures: a smaller aperture (left) and a larger aperture (right). Adapted from [Luo16].*

❖ **Optical lenses and objective aperture:** The objective lens is employed to focus and magnify the sample. The first image and diffraction pattern of the object is formed by this lens, making it the most significant lens because the subsequent intermediate

and project lenses will further enlarge the image and diffraction pattern [Luo16]. After high magnifications, any distortions in the first image or diffraction pattern will worsen. The objective aperture is used for regular TEM imaging [Luo16] and the stabilization of nonconductive samples, as in a thin polymer section [Bri98]. As illustrated in Figure 5.19, the TEM sample is placed in the space (gap) between the lower and upper objective lens polepiece. The configuration of the polepiece varies depending on the TEM application. A high-resolution TEM (HRTEM) application has a narrower gap for higher imaging resolution. In contrast, an analytical TEM type has a larger gap for large angle tilting and EDS detector setups [Luo16].

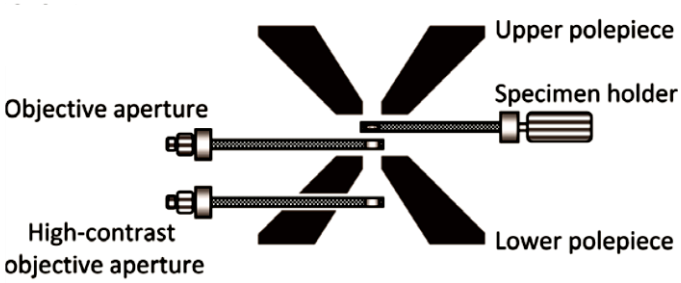

Figure 5.19. *TEM objective lens and objective apertures. Taken from [Luo16].*

- **The intermediate lens and diffraction (or SAED) aperture**: The intermediate lens control the image's magnification and is used for switching between the imaging and diffraction modes [Luo16]. After the passage of the electrons through the sample, a diffraction pattern is created, followed by the first image formation. No matter the mode in which the TEM is operated, the diffraction pattern is formed in the rear back focal plane [Luo16]. With the intermediate lens in focus on the first image formed (as shown in Figure 5.20 (a)), the image is further magnified by the subsequent lenses, and an enlarged image is displayed on the screen. As illustrated in Figure 5.20 (b), when the intermediate lens is in focus on the first diffraction pattern, the pattern is further enlarged (by the following lenses) and displayed on the screen.

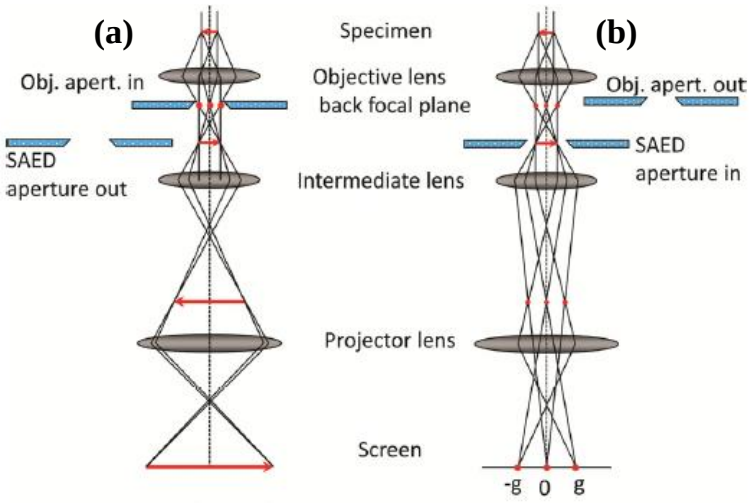

Figure 5.20. *(a) Imaging and (b) diffraction modes as determined by the intermediate lens. Taken from [Luo16].*

The diffraction or selected-area selected diffraction (SAED) aperture is used when a small sample area is to be diffracted. The result is a SAED pattern. The position of the diffraction apertures is below the sample in the first image plane. The SAED aperture is positioned below the sample in the first image plane along the optical axis to limit the diffraction information to a small central area of a sample. See an illustration in Figure 5.21 (a). However, when the SAED aperture position is off the optical axis, it can still be used to select an area. The diffraction pattern comes from this specific region on the sample (see Figure 5.21(b)). A quality SAED pattern can be obtained with the diffraction aperture aligned in the optical centre [Luo16].

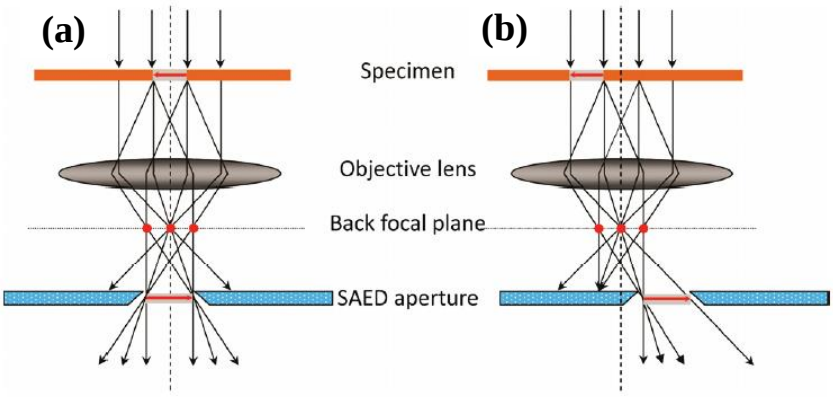

Figure 5.21*. Selecting an area to be diffracted with the SAED apertures (a) centred and (b) off the central axis*

- **Projector Lens**: A projection lens is employed to enlarge further the images created by the intermediate lens and projected on the screen. The projector lens has a large

depth of focus, allowing the images to remain in focus over a wide area along the central axis. The magnification, *M*, of the final image is given by [Luo16]:

$$M = M_O \times M_I \times M_P \tag{5.39}$$

Where M_O, M_1 and M_p represent the magnifications of the objective, intermediate and projector lenses, respectively.

5.4.1.3 Screen and Camera

The viewing screen is a phosphor screen (i.e., coated with phosphorescent powder), so it can produce visible light when struck by highly energetic electrons. Strong intensities from diffraction spots (in the diffraction mode) or focused beam crossovers (in the image mode) at low magnification could damage the viewing screen. The beam's intensity can be regulated using a beam stopper or viewing the beam on a small screen to protect the larger one. A film camera or a charged coupled detector (CCD) records the TEM data.

5.4.2 Diffraction

Diffraction is an essential tool for assessing the level of structural disorder in a sample. It is the primary tool in most electron microscopes techniques such as X-ray diffractometry, Scanning electron microscope (SEM), and transmission electron microscopy. In TEM, the diffraction technique is electron diffraction, which can be used for constituent phase identification, in situ or ex-situ phase transition observations, crystallographic orientation determination and sample thickness observations [Goo11].

An illustration of electron diffraction is given in Figure 5.22 [Luo16]. The diagram describes how an electron beam penetrates a crystal lattice (of a material) at an incident angle, θ. This results in scattering along the two parallel planes in the material. The scattered waves are accompanied by either constructive or destructive interference along the directions of the atoms. The electron diffraction phenomenon produces a periodic array of bright spots called an electron diffraction pattern (EDP). This electron diffraction pattern contains more information about a material. Also, there is a close geometric relationship between the constructively interfering wave directions (which comprise the "diffraction pattern") and the crystal structure of the material [Ful08]. In TEM equipment, EDP studies are often carried out using highly energetic electrons.

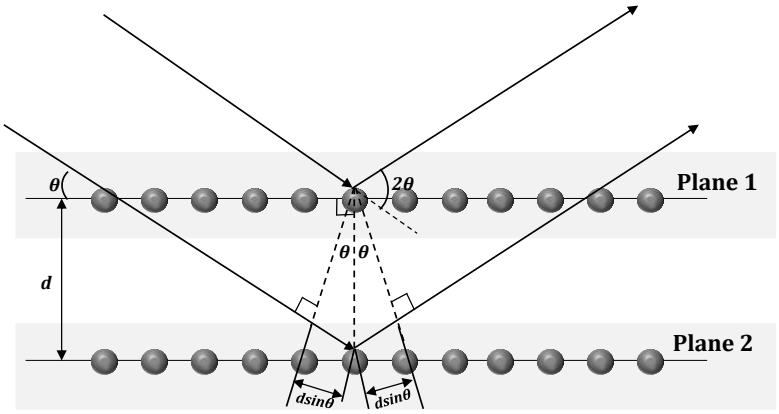

Figure 5.22. *Illustration of electron diffraction according to Bragg's law [Redrawn from Luo16].*

As predicted by Bragg's law, the scattering event of the electron beams (illustrated in Figure 5.22), similar to X-ray diffraction, can be described by equation (5.40). This Equation expresses the difference in pathlength between the constructive waves scattered from two consecutive planes.

$$n\lambda = 2dsin\theta \tag{5.40}$$

where n represents the order of scattering (takes integer value), λ is the radiation wavelength, and d is the distance between the two successive planes where two adjacent waves are scattered. Typically, the diffraction pattern of a material will have numerous distinct peaks, each corresponding to a unique interplanar distance, d [Ful08]. As stated in Equation (5.40), constructive interference (strong diffraction) would occur along specific directions when the path length difference equals one wavelength (i.e., $n\lambda = 1$). In contrast, some electrons also contribute to the background of the diffraction pattern along other directions [Luo16].

Compared to other diffraction techniques like X-ray diffraction, electron diffraction (ED) has some advantages, which include the following:

a) When using electrons instead of X-rays, the sampling area is substantially greater. The electron diffraction patterns (EDP) offer more reflections for crystallographic analysis because it has more spots than other techniques.
b) The imaging capabilities of the (TEM) microscope can be employed while the EDP is being recorded. This is crucial when only extremely small sample features are required, which is the case of low-dimensional materials science.
c) In TEM, electron optics can change the camera length and focus on altering the geometry of the EDP. This makes it possible to collect ED from very small crystals

of a sample. To do this, a TEM parallel beam is incident on the sample, and an aperture is placed in the objective lens's image plane to direct the beam's pattern to a particular area of the specimen. This method is called selected-area electron diffraction (SAED). Because of how the spherical aberration controls the objective lens, SAED cannot be used on an area not much smaller than 0.5 μm in diameter.

The separation of diffraction spots (seen on the viewing screen) can be used to determine the interplanar spacings in the crystal (of the samples) under investigation. The "camera equation" is required to do this. Figure 5.23 shows the geometry of a SAED pattern. The camera length, *L*, is unique to the optics of the microscope. It follows from this Figure that:

$$tan2\theta = \frac{r}{L} \tag{5.41}$$

where *L* is the length of the Camera, *r* is the separation of the diffraction spots, and θ is the diffraction angle.

Rearranging Bragg's law from equation (5.40) gives:

$$\sin\theta = \frac{r}{2d}\lambda \tag{5.42}$$

For low-order electron diffractions from many materials, it is required that θ is very small (~1) so that [Ful08]:

$$\sin\theta \approx tan\,\theta \approx \tfrac{1}{2}\tan(2\theta). \tag{5.43}$$

Substituting the above into equation (5.42) yields:

$$\frac{1}{2}\tan(2\theta) = \frac{r}{2d}\lambda \tag{5.44}$$

Similarly, $\tan(2\theta) = \frac{r}{L}$ can be substituted to give:

$$\frac{1}{2}\frac{r}{L} = \frac{r}{2d}\lambda$$

$$rd = \lambda L \tag{5.45}$$

The product, λL (Å.cm), is referred to as the camera constant and once it is known, the distance of the diffraction spot, *r*, from the origin, can be measured and the interplanar spacing *d* can be determined [Ful08].

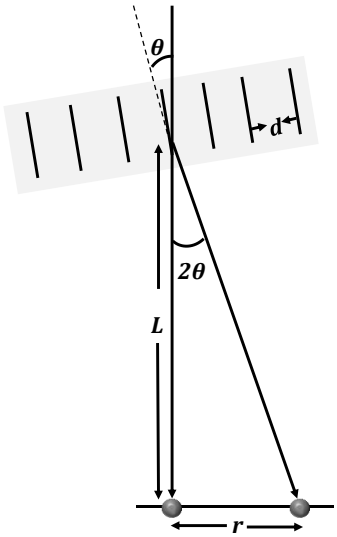

Figure 5.23. *Geometry of electron diffraction and concept of Camera length, L. Redrawn from [Luo16]*

References

[Alo93] P. Aloupogiannis & A. Travlos. Rare-earth silicide thin film study, Comparison of heavy ion and conventional RBS. *Vacuum*, **44 (1)**, (1993), 37 – 39.

[Ben71] A. Benninghoven & E. Loebach. Tandem Mass Spectrometer for Secondary Ion Studies, *Rev Sci Instr*. **42 (1),** (1971), 49 – 52.

[Bri98] J. Brink, M.B. Sherman, J. Berriman & W. Chiu. Evaluation of charging on macromolecules in electron cryomicroscopy. *Ultramicroscopy*. **72**, (1998), 41 – 52.

[Boz99] J.J. Bozzola & L.D. Russell. Electron Microscopy: Principles and Techniques for Biologists. Jones and Bartlett Learning, Massachusetts. (1999).

[Cas62] R. Castaing, & G.J. Slodzian. Optique corpusculaire – premiers essais de microanalyse par emission ionique secondaire. *Microscopie*. **1**, (1962), 395 – 399.

[Cha81] B.T. Chait & K.G. Standing. A time-of-flight mass spectrometer for measurement of secondary ion mass spectra, *Int. J. Mass Spectrom. Ion Phys.* **40 (2)**, (1981), 185.

[Chi17] C.J. Chirayil, J. Abraham, R.K. Mishra, S.C. George & S. Thomas. Instrumental Techniques for the Characterization of Nanoparticles, (Eds): S. Thomas, S. Thomas, A.K. Zachariah, R.K. Mishra: In Micro and Nano Technologies, Thermal and Rheological Measurement Techniques for Nanomaterials Characterization. *Elsevier*, (2017), 22.

[Chu78] W.K. Chu, J.W. Mayer & M.A. Nicolet. Backscattering spectroscopy, Jounral of Vacuum Science and Technology, (1978).

[Col12] N. Colthup & D. Lawrence. Introduction to infrared and Raman spectroscopy. Academic Press, New York. (2012).

[Edi91] J.W. Edington. Practical Electron Microscopy in Materials Science. Techbooks, Herndon, Virginia, (1991).

[Fel86] L. Feldman & J. Meyer. Fundamentals of Surface and Thin Film Analysis. Elsevier Science Publishing Co, New York, (1986).

[Fer00] A.C. Ferrari & J. Robertson. Interpretation of Raman spectra of disordered and amorphous carbon. *Phys. Rev. B.* **61**, (2000), 14095 – 14107,

[Ful08] B. Fultz & J.M. Howe. Transmission Electron Microscopy and Diffractometry of Materials. (3rd ed.). Springer Berlin Heidelberg, New York, (2008), 21 – 25.

[Gar89] D.J. Gardiner, P.R. Graves & H.J. Bowley. Practical Raman Spectroscopy, Springer Verlag, (1989).

[Gra91] J.G. Grasselli & B.J. Bulkin. Analytical Raman Spectroscopy, Wiley, New York, (1991).

[Goo75] P.J. Goodhew & F.J. Humphreys. Electron Microscopy and Analysis. Taylor and Francis Ltd., London. (2nd d.). (1975).

[Goo11] P.J. Goodhew. Aberration-Corrected Analytical Transmission Electron Microscopy, Edited by Rik Brydson. Wiley, New York. (1st ed.). (2011).

[Gro84] J.B. Grob & P. Siffert. "Rutherford Backscattering Spectroscopy (RBS)" Progress in crystal growth and characterization, **(1-2),** (1984), 59 – 106.

[Hei14] P. Van der Heide. Secondary ion mass spectrometry: an introduction to principles and practices. Wiley, New York. (2014).

[Her49] R.F.K. Herzog & F. Viehboeck. Ion source for mass spectrography. *Phys. Rev.* **76 (6),** (1949), 855 – 856.

[Kni89] D.S. Knight & W.B. White. Characterization of diamond films by Raman spectroscopy, *J. Mats. Res.*, **4 (2)**, (1989), 385 – 393.

[Kuh15] R.J. Kuhudzai. Diffusion and surface effects for SiC implanted with fission product elements, PhD Thesis, University of Pretoria, (2015).

[Lie67] H.J. Liebl. Ion microprobe mass analyzer. *J. Appl. Phys.* **38 (13)** (1967), 5277 – 5280.

[Leo94] W.R. Leo. Techniques for Nuclear and Particle Physics Experiments. Springer, (1994), 122 – 127.

[Luo16] Z. Luo. A practical guide to Transmission electron microscopy Fundamentals, Momentum Press, (2016), 1 – 375.

[Mag78] C.W. Magee & H.E. Richard. Secondary ion quadrupole mass spectrometer for depth profiling design and performance evaluation. *Rev. of Sci. Inst.* **49 (4)**, (1978), 477 – 485.

[EKB19] Essential Knowledge Briefing (EKB). Microscopy and analysis, Dynamic Secondary Ion mass Spectrometry, Wiley, United Kingdom, (1st ed.). (2019). 4 – 19.

[Opi13] L. Opilik, T. Schmid, & R. Zenobi. Modern Raman imaging: Vibrational spectroscopy on the micrometer and nanometer scales. *Ann. Rev. Anal Chem*, **6,** (2013), 379 – 398.

[Per87] J. Perriere. Rutherford backscattering spectrometry. *Vacuum*. **37(5/6),** (1987) 429 – 432.

[Por07] S. Portier, S. Bremier & C. Walker. Secondary Ion Mass Spectrometry of Irradiated Nuclear Fuel and Cladding - an overview. *Int. J. Mass Spec*. **263** (2007), 113.

[Ram28] C.V. Raman & K.S. Krishnan. The optical analogue of the Compton effect. *Nature*. **121** (1928), 711.

[Ros16] P. Rostron, S. Gaber & D. Gaber. Raman spectroscopy, review. *Int. J. Eng. & Tech*. Res. **6,** (2016), 50 – 64.

[Rub57] S. Rubin, T.O. Passel & L.E. Bailey. Chemical analysis of surface by Nuclear methods, *Analy. Chem.* **29(5)**, (1957).

[Rus32] E. Ruska & M. Knoll. Das Elektronenmikroskop. *Z. Phys.* **78,** (1932), 318 – 339.

[Sig69] P. Sigmund. Theory of Sputtering. I. Sputtering Yield of Amorphous and Polycrystalline Targets. *Phys. Rev.* **184 (2),** (1969), 383 – 416

[Sme23] A. Smekal, The quantum theory of dispersion. Naturwissenschaften, **11 (43),** (1923), 873 – 875.

[Smi05] E. Smith & G. Dent. Modern Raman spectroscopy: a practical approach, Wiley, New Jersey, (2005).

[Sol70] S.A. Solin & K. Ramdas. Raman spectrum of Diamond. Phys. Rev. B, **1,** (1970), 1687.

[Stev15] F. Stevie. Secondary Ion Mass Spectrometry: Applications for Depth Profiling and Surface Characterization. Momentum Press, (2015). Google-Books-ID: UXe0CgAAQBAJ.

[Sky14] T.N. Sky, Nickel Diffusion and configuration in crystalline Zinc Oxide. Masters thesis, University of Oslo, (2014).

[Tho79] G. Thomas & M.J. Goringe. Transmission Electron Microscopy of Materials. John Wiley & Sons, New York, (1979).

[Van14] P. van der Heide. Secondary ion mass spectrometry: an Introduction to principles and practices. Wiley, New Jersey, (2014).

[Vic89] J. Vickerman, A. Brown & N. Reed. Secondary Ion Mass Spectrometry, Principles and Applications. Clarendon Press, Oxford University Press, New York, (1989).

[Wil09] D.B. Williams & C.B. Carter. Transmission Electron Microscopy: A Textbook for Materials Science. Springer, New York, (2009).

[Wit75] K. Wittmaack. Pre-equilibrium variation of secondary ion yield. *Int. J. Mass Spectrom. Ion Phys.* **17 (1),** (1975), 39 – 50.

[www1] http://www.chm.bris.ac.uk/pt/diamond/stuthesis/chapter2.htm#_edn1. Accessed 5 October 2022.

[www2] https://www.semitracks.com/reference-material/failure-and-yield-analysis/failure-analysis-materials-characterization/secondary-ion-mass-spectrometry.php. Accessed 15 September 2022.

[Zal94] P.C. Zalm. Secondary ion mass spectrometry. *Vacuum*. **45 (6/7),** (1994), 753 – 772.

Chapter 6

Experimental Procedures

This chapter discusses the experimental procedure used in this study. This includes sample preparation of the starting material (GC samples), selenium ion implantation, annealing of samples, and characterisation techniques.

6.1 Sample Preparation

The starting materials are commercially SIGRADUR®G GC strips purchased from Hochtemperatur-Werkstoffe GmbH, Germany. Each GC strip has dimensions of 50 mm × 10 mm, with a thickness of 2 mm. According to the manufacturer, the SIGRADUR®G GC grade has a density of 1.42 g/cm^3, a thermal conductivity of 6.3 Wm^{-1}K^{-1}, a flexural strength of 260 MPa, compressive strength of 480 MPa, and a maximum service temperature of 3273 °C [www1]. The as-received GC strips were polished on both sides. Each GC strip was marked into uniform ten (10) rectangular (4 × 4 mm^2) sections to enable easy sample separation after implantation. The samples were cleaned using the following steps: at first, a soap solution was used to clean the samples in an ultrasonic bath, followed by deionized water (to remove the soap solution). The next step was cleaning the samples with methanol to remove the deionized water. Finally, nitrogen gas was blown on the samples to dry them.

6.2 Implantations

The cleaned GC samples were implanted with 150 keV Se ions at room temperature (RT), 100, 150 and 200 °C. The Se ions were raster scanned across the entire area (50 × 10 mm) of the GC strip to ensure uniform implantation, and an implantation fluence of 1×10^{16} ions/cm^2 was attained in all the implanted samples. The implantation flux was maintained at 10^{12} cm^{-2}s^{-1} to avoid a temperature spike in the substrate. An increase in temperature can induce annealing of radiation damage in the substrate, which is not wanted because one of the objectives of this study was to investigate how radiation damage from ion bombardment affects the microstructure of the GC samples. It is important to mention that the substrate temperature reached about 55 °C (during the implantation of Se ions at room temperature). This temperature is not expected to anneal the sample. The Se ions implantation was done with a 400 kV implanter (ROMEO) at the Institut für Festkörperphysik, Friedrich-Schiller-Universität, Jena Germany. Following implantation, the samples were divided into smaller sizes through the initial incision on the GC strips.

6.3 Annealing

Annealing has been an effective tool (used by material scientists) for achieving different material modification purposes. It can be used to improve the physical and chemical (rarely) properties of a material. The annealing procedure used in this study involves heating the Se-implanted GC substrate at a specific temperature for a specified duration under high vacuum pressure, 1×10^{-6} mbar. Annealing was carried out in two vacuum annealing systems: tube furnace system for sequential annealing at the low-temperature regime (300 – 700 °C) and Webb *77*® graphite furnace system for the isochronal annealing at the high-temperature regime (1000 – 1200 °C).

The vacuum tube annealing system (schematically shown in Figure 6.1) can anneal up to 1000 °C. The sample holder (a smaller quartz tube) is connected to a thermocouple that reads the furnace's temperature. The other end of the thermocouple is connected to a data acquisition system, which collects and saves the annealing data. A big quartz tube encloses the smaller tube in the turbo pump chamber. The turbo pump chamber has two rubber seals to ensure no air leaks when the big tube is pulled in. The furnace has two white circular aluminium oxide ceramics, which can be inserted at both ends of the large tube to prevent heat loss to the surrounding. The process of annealing in the vacuum tube system starts with carefully removing the big tube (from the turbo pump chamber) and loading the sample towards the tip of the smaller tube. The sample loading process was followed by pumping down to 10^{-3} mbar with a fore pump and by turbo pump 10^{-6} mbar. The two pumps were left to run concurrently for some minutes until the vacuum pressure was stable at 10^{-6} mbar or lower. The annealing temperature was first set, and then the furnace was switched on. The temperature ramps to the set temperature and stabilizes before the furnace was pulled over the quartz tube to start the annealing. The furnace's centre portion reaches its highest temperature first and radiates to the other sides of the furnace. The data acquisition program (which serves as a monitor) displays the temperature of the furnace during annealing. After annealing, the big quartz tube was removed from the furnace so that the sample could cool to room temperature (RT) before removing it. The cooling down to RT is important to prevent oxidation of the samples. The four sets of as-implanted samples (RT, 100, 150 and 200 °C Se-GC substrates) were annealed sequentially at low-temperature (300 – 700 °C) and high-temperature (1000 – 1200 °C) regimes. The duration for each annealing step was 5 hours. After each annealing step, the samples were characterized by RBS and Raman spectroscopy to investigate diffusion (of Se) and the structural changes in the GC substrates.

A new set of as-implanted samples were annealed isochronally at the high-temperature regime (1000 – 1200 °C) and characterized by SIMS to investigate the effect of radiation damage on the migration behaviour of Se atoms in the GC substrates.

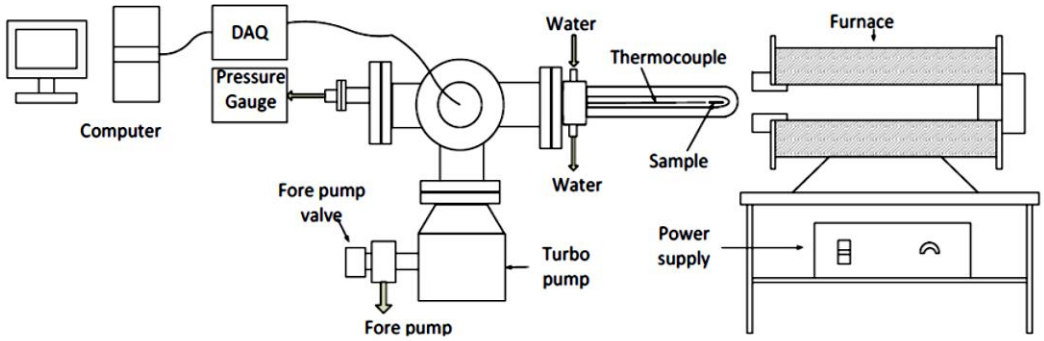

Figure 6.1. *Vacuum tube furnace annealing system at the University of Pretoria, South Africa. Taken from [Njo14].*

The samples were annealed at the high-temperature regime in separate GC crucibles (with lids) in the Webb 77® graphite furnace system. The maximum attainable temperature with the Webb system is 2300 °C. A Eurotherm 2704 controller coupled to a thermocouple and a pyrometer is used to monitor the Webb 77® temperature. The pyrometer monitors temperatures above 1525 °C, while the thermocouple can only measure temperatures as high as 1475 °C. Before using the Webb system, the furnace was first evacuated to a pressure of about 10^{-7} mbar with a fore pump and a turbo pump. After the pumping, the furnace was heated to 200 °C for one hour to begin the degassing phase (as indicated in Figure 6.2). The degassing would remove the water vapour and any other gas pollutants that may have been adsorbed onto the fibrous insulating carbon material inside the furnace. Degassing also aids in shortening the pumping time required to reach the 10^{-6} mbar prior to annealing and ensures that the pressure during annealing was about 10^{-5} mbar.

During the degassing phase, the temperature first overshoots by about 100 °C (so that the initial temperature is 300 °C), as shown in Figure 6.2. A spike in the initial current accompanied this observation, as the current reached a maximum of 28 A. After some time, it decreases to 0 A and the fluctuated temperature is regulated at 200 °C. The fluctuation in the temperature and initial current are linked to the inherent set-up of the annealing equipment by the manufacturer.

After the degassing stage, the furnace heats to the required (set) temperature for about 1 h before the annealing begins and runs for the required annealing time (5 h for this study).

The samples were annealed slowly by programming the heating rate of the furnace at 20 °C/min. The current increases from 0 to 18 A, causing the temperature inside the furnace to regulate to the set temperature. The current drops and stabilizes at 8 A during the annealing time. Figure 6.2 shows the graph of the annealing process of a sample annealed at 1100 °C for 5 hours. The red line is the set point representing the annealing program, while the black line is the output point to monitor the progress of annealing.

The current is automatically turned off after the annealing (for the required duration) is completed. This is followed by the cooling down of the furnace to room temperature. Before the sample can be removed from the furnace, the turbo pump is turned off to bring the vacuum down while the fore pump was still on. Argon gas was let into the chamber to eliminate the vacuum and level the pressure to the atmospheric level.

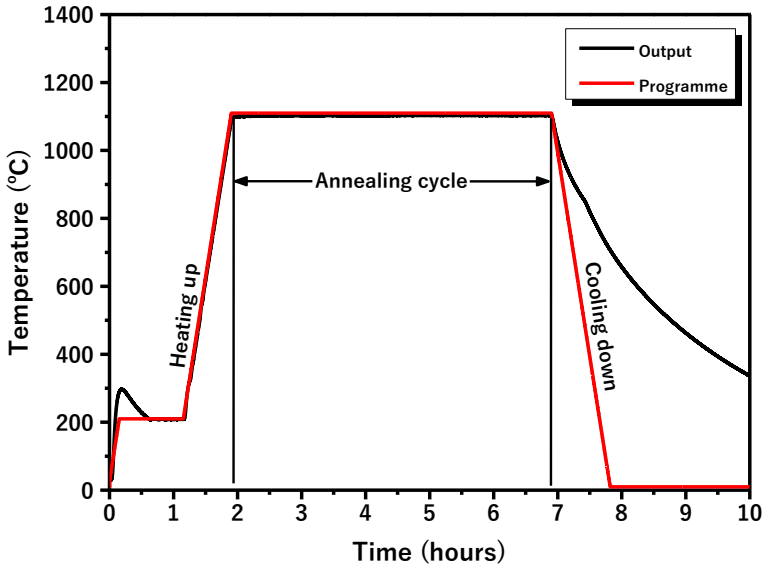

Figure 6.2. A graph showing the annealing process of a sample at 1100 °C for 5 hours.

6.4 Characterisation of the samples

The as-implanted and as-implanted then annealed samples were characterized using Transmission electron microscopy (TEM), Raman spectroscopy, Rutherford backscattering spectroscopy, and secondary ion mass spectrometry (SIMS).

6.4.1 Transmission electron microscopy

Transmission electron microscopy was used to analyse the as-implanted samples (TEM) to determine the level of radiation damage in the implanted samples. To achieve this, A FEI Helios Nanolab 650 FIB was used to prepare TEM lamellas using the Focused Ion Beam (FIB) technique. The samples were thinned by consecutive treatment of 30 and 5 keV Ga ions. Final polishing was carried out at 2 keV and 500 eV, yielding nearly damage-free TEM lamella. After that, TEM measurement was carried out using a JEOL JEM 2100 LaB6 transmission electron microscope, which runs at 200 kV acceleration voltage.

6.4.2 Raman investigations

The changes in the microstructure of the GC before and after implantation and after sequential isochronal annealing were monitored using a T64000 series II triple Raman spectrometer system by HORIBA scientific, Jobin Yvon technology. This instrument consisted of a coherent Innova 70C® series Ar/Kr excitation laser line and an Olympus microscope. For each Raman measurement, a 514.5 nm line Ar^+ laser was focused onto a spot size of ~ 2 μm^2 on the sample. The spectra were collected in the 200 – 1800 cm^{-1} range using an objective lens of 50× magnification. The integrated triple spectrometer was operated in a double subtractive mode to reject Rayleigh scattering and disperse the light onto the Symphony CCD detector. It was important to keep the laser power below 1 mW during the Raman measurement to prevent sample annealing.

6.4.3 RBS and SIMS measurements

The distribution of implanted Se in GC was monitored before and after isochronal annealing using Rutherford backscattering spectroscopy (RBS) and Secondary ion mass spectrometry (SIMS). The RBS was used to characterize the samples sequentially annealed (in vacuum) at 1000 – 1200 °C, in steps of 100 °C for 5 hours. The RBS was performed with 1.6 MeV He^+ particle from a Van de Graaff particle accelerator. The backscattered particles were counted at a silicon (Si) surface barrier detector positioned at a scattering angle of 165°. The sample tilt angle was preserved at 10° throughout the experiment. The ion beam current was measured on the sample (15 nA) and a ring-shaped electrode (in front of the sample) was kept at −200 V to suppress ejected secondary electrons. A total charge of 8 μC charge was collected per sample run. In order to prevent the pile-up effect and sample overheating, the analysing beam was collimated to a spot with a diameter of 1 mm, and the beam current was maintained at 15 nA.

Secondary ion mass spectrometry (SIMS) was carried out on the isochronally annealed samples to investigate the effect of radiation damage on the migration behaviour of Se in GC. Isochronal annealing is preferred to study the effect of radiation damage on the migration behaviour of an implant in a substrate. This is because sequential annealing is not starting at the same temperature with the same amount of defect. The SIMS instrumentation used was a Cameca IMS 7f microanalyser (operated in dynamic mode). The SIMS procedure involves rastering a primary O^{2+} beam of 10 keV energy and 100 nA current over a sample area of 150 x 150 μm^2. The detection of the secondary ions was restricted to the centre of the sputtered crater bottom by employing a secondary ion field aperture (with a circular gated region diameter of 33 μm). The as-implanted samples were used as a reference for the intensity-concentration calibration. The depth conversion (from sputtering time to depth) was accomplished by measuring the crater depth with a DEKTAK 8 stylus profilometer and assuming a constant erosion rate with time.

References

[www1] http://www.htw-germany.com/technology.php5?lang=en&nav0=2. Properties of glassy carbon. Hochtemperatur-werkstoffe GmbH, Germany, Accessed 19 February 2020.

[Njo14] E.G. Njoroge, “PhD thesis, University of Pretoria, Hatfield,” (2014).

Chapter 7

Results and Discussions

The overview results of all the analyses carried out with the instrumentations and software used in this research are presented and discussed in this chapter. Rutherford backscattering spectrometry (RBS) and secondary ion mass spectrometry (SIMS) was used to examine the migratory behaviour of implanted selenium in GC at various implantation temperatures. The structural modifications of the as-implanted and as-implanted then heat-treated samples were analyzed by Raman spectroscopy and the level of radiation damage in the as-implanted samples was checked using transmission electron microscopy (TEM).

7.1 Selenium implantation in GC: experiment, simulation, and radiation damage

The RBS spectra of 150 keV Se ions implanted in GC at room temperature (RT), 100, 150, and 200 °C to a fluence of 1×10^{16} ions/cm^2 are shown in Figure 7.1. The arrows are used to indicate the surface channel positions of carbon (C), oxygen (O) and selenium (Se) at channels 118, 176 and 416, respectively. The RBS spectrum of a typical SIGRADUR®G GC does not contain an oxygen peak [Shi19], so the oxygen peak may not be from the as-received sample. There is a possibility that the smaller oxygen concentration is due to contamination during the ion implantation process. Even though ion implantation is a fairly clean process, there is still a high possibility of many contaminant sources. Potential contaminants during implantation include ion implanter components, pump oils, cross-contamination from old source atoms and foreign particles during sample loading and unloading. Hence, the contamination of the GC substrate from residual gases source is also possible, which should be minimal due to the high vacuum pressure (10^{-5} range) used during implantation. However, the smaller oxygen impurity concentration is not expected to influence any of the measurements because of its dependence on temperature. The oxygen impurities introduced during Se implantation and found slightly below the surface of the GC samples, disappeared after annealing all the samples at temperatures higher than 300 °C.

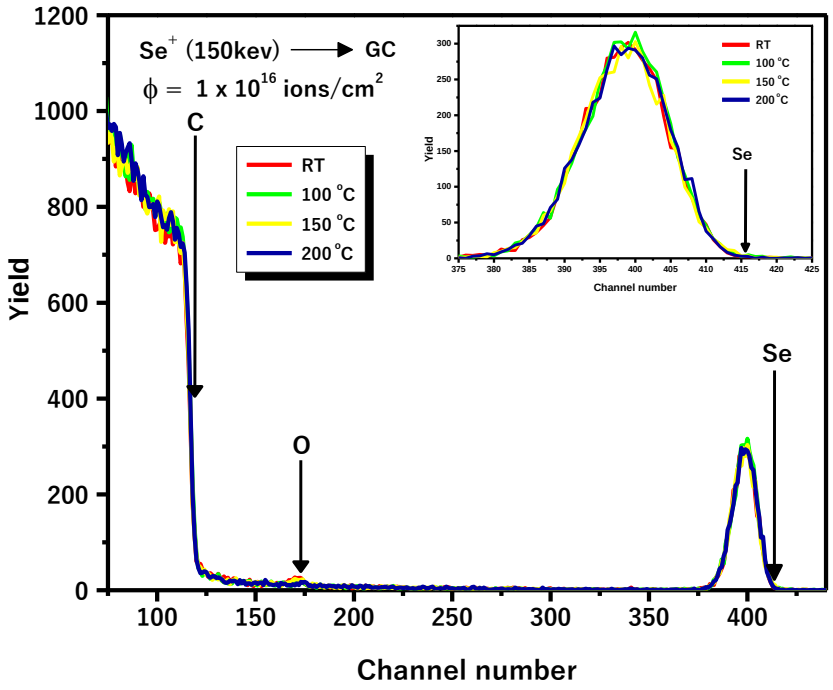

Figure 7.1. *Rutherford backscattering spectroscopy (RBS) spectra of 150 keV Se^+ implanted into GC at room temperature (RT), 100, 150, and 200 °C at a fluence of 1 × 10^{16} ions/cm^2.*

The energy calibration (keV/channel) is an important parameter needed for the depth profile analyses of Se in GC. This energy calibration was converted into depth calibration (nm/channel) using a depth conversion code, SPVERW, which does the conversion by using the energy loss data from Ziegler [Zie77]. The Se count obtained from the RBS was converted into relative atomic density (%) using Equation (7.1) below:

$$\text{Relative atomic density (\%)} = \frac{\left(\frac{\emptyset dn}{ND}\right)}{\rho_{GC}} \times 100 \qquad (7.1)$$

where $\left(\frac{\emptyset dn}{ND}\right)$ represents the density of selenium in the GC (Se-atoms/cm^3), $\emptyset$ is the Se ion fluence = 1 × 10^{16} ions/cm^2, *N* is the overall counts of Se, while *dn* is the count per channel, D is the RBS depth resolution (in cm/channel) and ρ_{GC} is the theoretical atomic density of GC, given as 7.12 × 10^{22} atoms/cm^3.

The secondary ion mass spectrometry concentration (atoms/cm^3) was converted to relative atomic density using Equation (7.2) below:

$$\text{Relative atomic density (\%)} = \frac{X_{se}}{\rho_{GC}} \times 100 \tag{7.2}$$

where X_{se} is the concentration of Se (atoms/cm^3).

Figure 7.2 shows the experimental (RBS and SIMS) depth profiles of 150 keV Se ions implanted in GC at all implantation temperatures. The simulated Se ion distribution and the radiation damage (in displacement per atom, dpa) are included in Figure 7.2. The stopping range of ion in matter (SRIM 2013) software was used to simulate the distribution of selenium in GC, with carbon's threshold displacement energy set to 20 eV [McK16] and the density of GC taken as 1.42 g/cm^3 (7.12×10^{22} atoms/cm^3).

The RBS profiles (Figure 7.2 (a)) are broader and have lower relative atomic density than the SIMS profiles, indicating slight differences between these two techniques. Although, it is expected that the RBS and SIMS Se profiles will be similar since an equal amount of Se was implanted in all the GC samples used in this study. The differences between the RBS and SIMS as-implanted profiles can be linked to differences between the two techniques as such with differences in their depth scale determination. The determination of the depth scale in RBS depends on the volume density parameter [Lor16]. The energy resolution in RBS reduces with depth. Often, poor energy resolution can result in an artificial broadening of any surface peak in the RBS spectra measured. Sometimes, the spectral shape becomes distorted relative to what it would be if the energy resolution is constant throughout measurement [Bar01]. Data analysis of RBS spectra can be challenging on rough surfaces [Bar02]. However, the SIMS depends on the sputtered crater depth for profile thickness determination [Lor16], which assures the constant bombardment of the primary beam during the measurement [Zin80]. However, the failure to ensure the consistency of the primary beam during the SIMS measurement can lead to inaccurate depth thickness [Zin80]. Despite ensuring optimum measuring conditions and precautions during the SIMS depth profiling, other factors may have contributed to the slight variations in the results. The implantation of the primary beam in the substrate is possible during the SIMS measurement [Tsa74], causing a change in the depth profiles at the surface. When the primary ions impinge on an area of the sample surface, sputtering begins in a different area. As the impinging progress, primary beam ions are implanted up to a particular concentration until sputter and implantation reach an equilibrium. The surface saturated with primary beam atoms has a different sputter rate than the original surface. Schulz et al. [Sch73] advised that such a change which occurs over a depth roughly equal to the implantation range of the

primary ion beam, must be considered for a precise SIMS depth profiling measurement. A variation in the SIMS depth profiling can also be caused by the knock-on of the implanted atoms by the primary ion beam, sputtering beam non-uniformity on the implanted area, and etch pit erosion [Ful75], [Zin80].

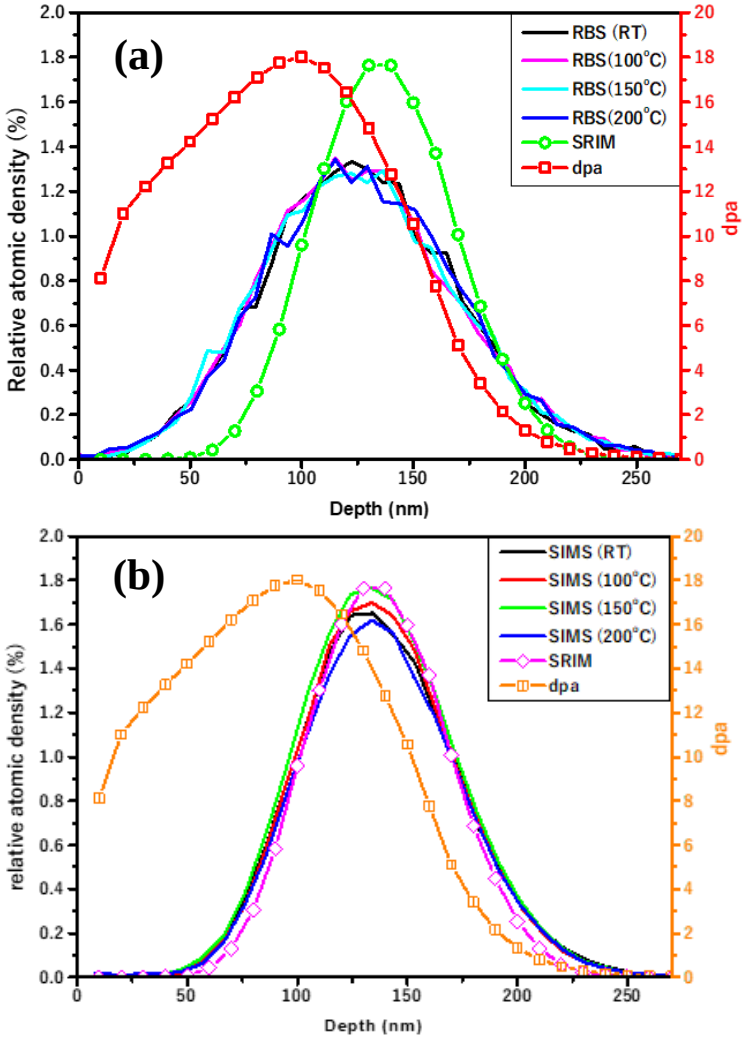

***Figure 7.2**. (a) RBS depth profiles and (b) SIMS depth profiles of 150 keV Se ions implanted in GC at RT, 100 °C, 150 °C, and 200 °C to a fluence of 1 × 10^{16} ions/cm^2. The displacement per atom (dpa) curve is included in both figures.*

The experimental depth profile data were fitted to an Edgeworth function to identify further the differences between the Se SIMS and RBS profiles. The first four moments of Se distribution in GC were obtained and compared with the SRIM calculated values, as shown in Table 7.1. The four moments are the projected range (R_p), projected range straggling (ΔR_p), skewness (γ), and kurtosis (β). The experimental R_p values (of all the implanted profiles) agree with the calculated value of 132.80 nm, within the 5% accuracy of the SRIM program. It was important to comment on the variation between the SIMS and RBS R_p

values, as seen in Table 7.1. The R_p values obtained after fitting the SIMS profiles are slightly higher by 1.7 – 2.4 % than the R_p values of the RBS profiles for all the as-implanted profiles. As mentioned above, this small variation may be due to etched pit erosion during the SIMS depth profiling of the Se-ions implanted GC samples, which causes the SIMS profile not starting from zero. The experimental ΔR_p values (calculated from Table 7.1) are larger than the SRIM calculation of 30.40 nm by 9 – 12% (for the SIMS results) and by 39 – 44% (for the RBS results). Studies on ion implantation in GC have shown that the experimental projected range straggling overestimates SRIM prediction by at least 23% [Njo17], 38% [Ism18], and 43% [Odu16].

Table 7.1. *The first four moments of Se ion distribution in GC. Rp – projected range, ΔRp – projected range straggling, γ – skewness and β – kurtosis obtained for SRIM, RBS and SIMS.*

		RT		**100 ºC**		**150 ºC**		**200 ºC**	
	Simulation	**Experiment**		**Experiment**		**Experiment**		**Experiment**	
Technique	**SRIM**	**SIMS**	**RBS**	**SIMS**	**RBS**	**SIMS**	**RBS**	**SIMS**	**RBS**
R_p	132.80	129.56	126.72	129.70	126.70	128.90	126.75	130.10	127.64
ΔR_p	30.40	35.40	42.38	34.50	43.79	34.93	43.49	35.07	42.74
γ	0.17	0.29	0.28	0.29	0.31	0.29	0.25	0.28	0.28
β	2.86	2.95	2.96	2.94	2.74	2.98	2.96	2.94	2.88

Larger experimental projected range straggling can also be linked to the nanopores in GC [Mal21]. The pore size in GC ranges between 0.3 – 0.5 nm, which is greater than the atomic radius of Se; hence the pores may serve as traps for the implanted Se atoms. The ion implantation process can also lead to larger experimental projected range straggling, which causes an increase in the atomic density of the GC [Mal21]. The variations between the observed and calculated Rp and ΔR_p values can be linked to several approximations of the SRIM program discussed in subsection 3.7 of chapter 3 of this work.

Also reported in Table 7.1 are the skewness (γ) and kurtosis (β) values. The as-implanted values of γ ranged between 0.28 and 0.29, while β ranged between 2.74 and 2.95. These values are close to $\gamma = 0$ and $\beta = 3$ for an ideal Gaussian distribution; hence both RBS and SIMS as-implanted profiles (in Figure 7.2) are nearly Gaussian.

One of the important reasons for carrying out SRIM simulation was to estimate the amount of radiation damage retained in the substrate due to ion implantation. Typically, the average number of displacements of atoms from a lattice during implantation is used to estimate the radiation damage induced in the material. Estimating radiation damage in SRIM is based on Kinchin-Pease (K-P) formalisms. This model is one of the models for

determining the damage produced in an irradiated material [Kin55]. The damage event in SRIM is processed as vacancy/ion (in Angstrom unit), which can be converted to displacement per atom (dpa) at a particular dose/fluence. The vacancies/ion (obtained from SRIM) was converted into displacement per atom (dpa) using Equation (7.3) below [Hla17]:

$$\mathrm{dpa} = \frac{\left({}^{\mathrm{V_{ac}}}/_{\mathrm{ion(Å)}} \times 10^{8}\right) \times \varphi \left(\frac{\mathrm{ion}}{\mathrm{cm^2}}\right)}{\rho_{GC}\left(\frac{\mathrm{atoms}}{\mathrm{cm^3}}\right)} \tag{7.3}$$

${}^{\mathrm{V_{ac}}}/_{\mathrm{ion(Å)}}$ is the vacancy per ion (in Angstrom unit), 10^8 is a conversion factor from Angstrom (Å) to a centimetre (cm), φ is the Se ion fluence (1×10^{16} ions/cm^2), and ρ_{GC} is the atomic density of the GC (7.12×10^{22} atoms/cm^3).

The dpa curve included in Figure 7.2 indicates that the maximum damage (in dpa) is at ~100 nm below the surface, which is less than the projected range of the implanted Se. This implies that more selenium atoms are displaced closer to the surface than the bulk. Consequently, this might lead to the preferred radiation-enhanced diffusion of Se atoms towards the surface at lower temperatures. With a critical dpa of 0.2 needed to distort the GC structure [McC94], the defective layer in the implanted GC can be estimated at about 240 nm (see Figure 7.2). This would imply that the implanted Se atoms are embedded in the defective region in the GC.

7.2 Transmission electron microscopy (TEM) of pristine GC samples implanted at room temperature (RT) and 200 °C

Figure 7.3 (a-c) shows the bright-field transmission electron microscopy (BFTEM) micrographs of the pristine GC and the GC samples implanted with 150 keV Se ions at RT and 200 ºC, to a fluence of 1×10^{16} ions/cm^2. The room temperature (RT) and 200 ºC represent the lowest and highest implantation temperatures used in this study. The TEM micrograph of the pristine GC has densely packed graphitic nanostructures surrounded by onion-like features. A similar structure of GC was observed by Odutemowo et al. [Odu18]. According to Harris, the onion-like features in the TEM micrograph of the pristine GC represent those of defective multi-layered fullerenes [Har04]. This implies GC contains fullerene constituents. Harris developed a model that explains that fullerenes are responsible for GC's low reactivity and impermeability properties [Har04].

The TEM micrographs of the as-implanted samples depict that Se ion implantation damaged the graphitic strands in the GC from the surface up to a depth of 159.60 nm and 156.91 nm in the RT and 200 ºC as-implanted GC samples, respectively. Comparing the dpa curve in Figure 7.2 with the TEM micrograph in Figure 7.3 (b), it can be deduced that the damaged thickness of about 159.60 nm (in the sample implanted at room temperature) corresponds to about 8.5 dpa, a value which is largely greater than the 0.2 critical dpa that will completely distort GC structure. Hence, the surface layer of the GC sample became highly defective due to Se ions implantation at room temperature. The selected area diffraction patterns (SAED) of the pristine GC and samples implanted at RT and 200 °C are shown in Figure 7.3 (d – f). Compared to the GC samples implanted at RT and 200 °C, the pristine GC shows more defined rings, indicating that the pristine sample is more graphitic than the as-implanted samples. The diffraction patterns of the GC samples implanted at RT and 200 °C exhibit diffuse rings, as shown in Figure 7.3 (e) and Figure 7.3 (f). This would imply that these samples contain fewer graphitic crystallites than the pristine GC.

Furthermore, the SAED patterns in Figure 7.3 (e) and Figure 7.3 (f) reveal that the surface of the two as-implanted samples appears damaged following Se ions implantation at RT and 200 °C. Although, no difference between these two figures indicating both samples are damaged to the same degree. The TEM micrographs of the RT and 200 °C as-implanted samples confirmed this observation.

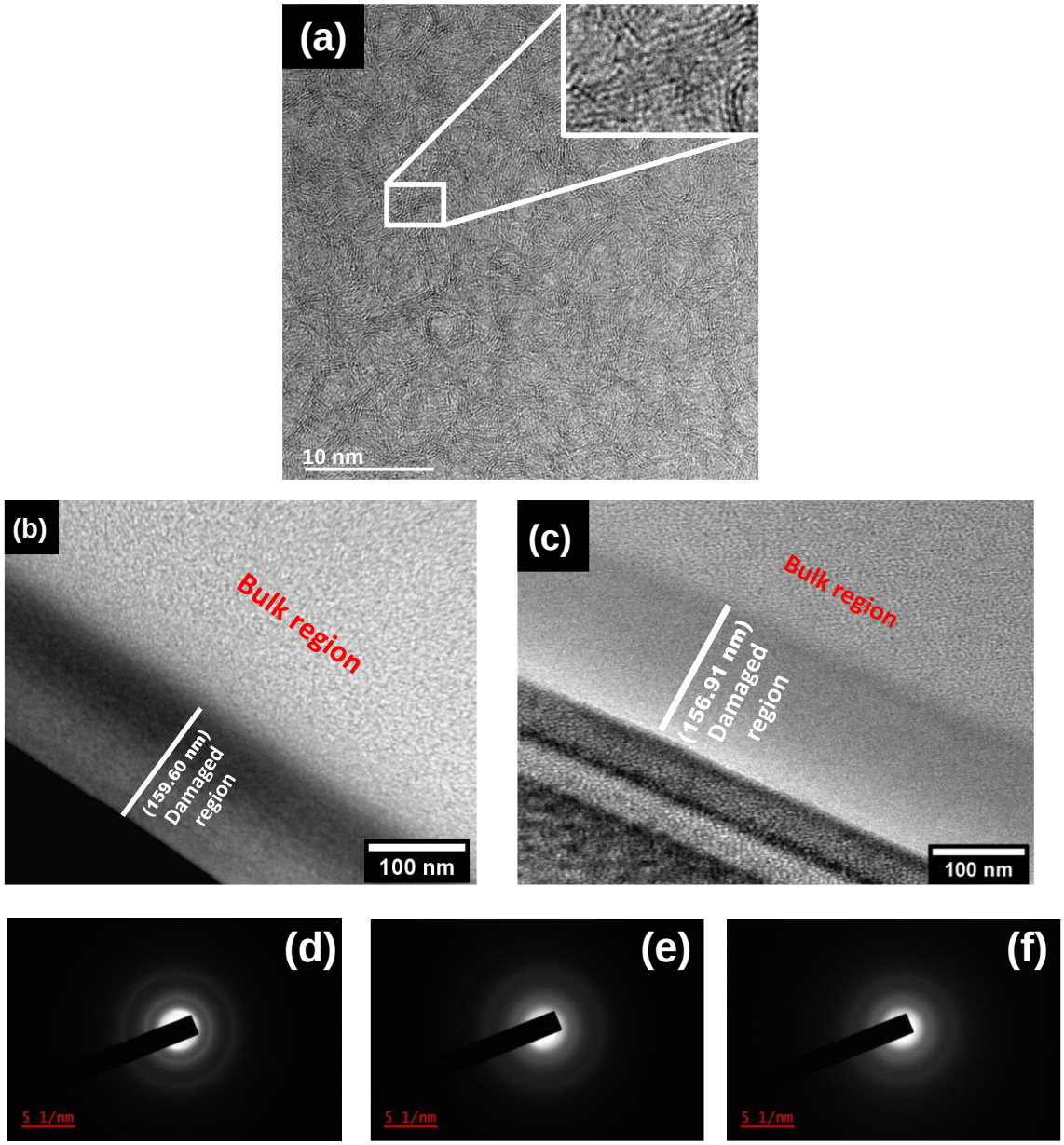

Figure 7.3. *Bright-field TEM micrographs (high magnification) of (a) The pristine GC (b) GC implanted at RT and (c) implanted at 200 °C with 150 keV Se ions to 1 × 10^{16} ions/cm^2. The selected area diffraction (SAD) patterns of (d) the pristine GC, (e) and (f) implanted region of the GC samples implanted at RT and 200 °C, with 150 keV Se ions to 1 × 10^{16} ions/cm^2, respectively.*

A TEM EDX (energy energy-dispersive X-ray spectroscopy) was used to characterize the elemental composition of the as-implanted samples. Even though TEM EDX analysis is not quantitative, it is used to detect low concentrations of contaminants in any material. Figure 7.4 (a&b) shows the TEM EDX result of the samples implanted at RT and 200°C. Five elements, carbon (C), oxygen (O), copper (Cu), platinum (Pt), and selenium (Se), were identified. The C and Se peaks are the expected main constituents in the as-implanted samples. The possible source of Cu is the TEM sample grid, while the Pt source is the protective layer on the GC sample (to protect the implanted region from being damaged during the thinning process). It is not strange to have seen an O peak in the EDX results because it was also observed in the RBS spectrum of the as-implanted samples.

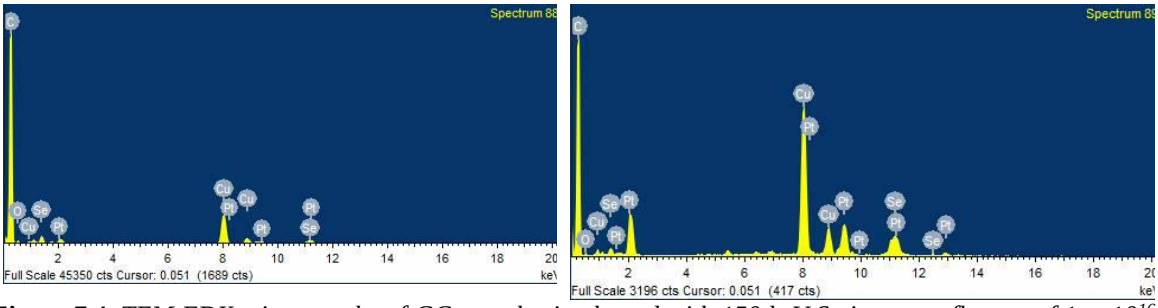

Figure 7.4. *TEM EDX micrographs of GC samples implanted with 150 keV Se ions to a fluence of 1 × 10^{16} ions/cm^2 at (a) RT and (b) 200 °C.*

7.3 Raman Spectroscopy Results of Pristine GC

Figure 7.5 shows the Raman spectrum of pristine GC, like those reported in other studies [McC94], [Lav08], [Odu16], [Hla17], [Njo17], [Ism18], [Shi19]. The Raman spectrum of the pristine was deconvoluted using the Breit-Wigner-Fano function (for the G peak) and a Lorentzian function to fit other peaks. The fitting produced information such as the D and G peak positions, corresponding intensities, the area under these peaks, and the full width at half maximum (FWHM) of the D and G bands. Two pronounced peaks were identified at about 1357 and 1588 cm^{-1} wavenumbers. These D and G peaks are characteristic of disordered carbon materials with sp^2 and sp^3 bonds, respectively [Fer00]. The sigma (σ) and pi (π) bonds are formed when two hybridised orbitals overlap, as in hybridisations (sp, sp^2, sp^3). In some forms of carbon (like GC), the sp^2 sites dominate because the π bond has lesser energy than the σ bond, causing the sp^3 sites to have a smaller Raman cross-section [Rob02]. The D peak represents a disordered graphite mode linked to the A_{1g} breathing mode with vibrations near the K zone boundary [Fer00]. The G peak can be identified as the sp^2 carbon networks in graphite [Fer00]. This peak is due to the Raman

optical mode and the E_{2g} symmetry. The peak at ~1090 cm^{-1} is mainly noticed when the acoustic and optic modes are mixed in the vibrational density state (VDOS) of carbon. The hump around the 1620 cm^{-1} peak is an identity of GC with small-sized crystallites, which is not present in highly crystalline graphite [Fer07].

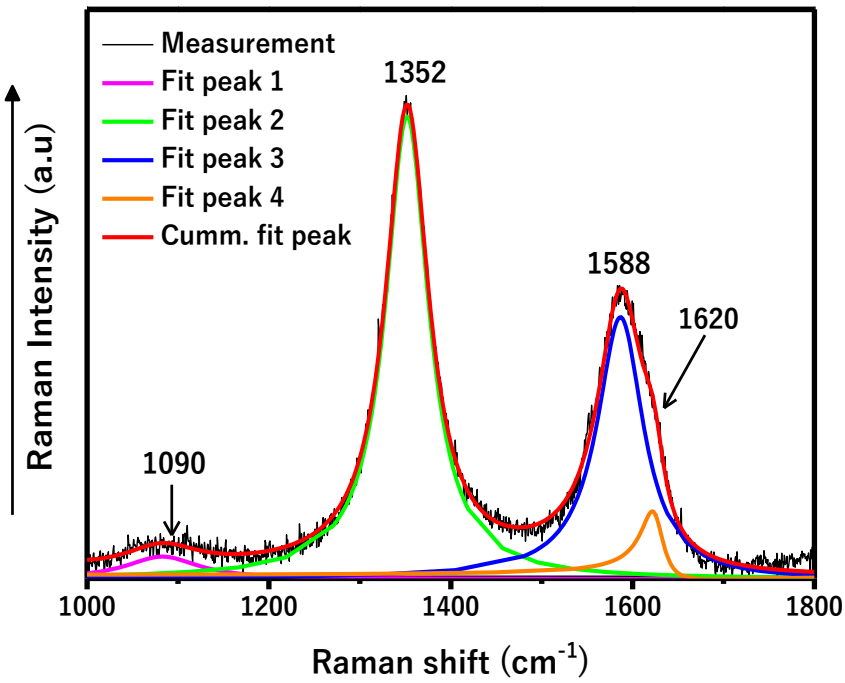

Figure 7.5. *Raman spectrum of pristine GC. Fit peaks 1, 2 and 4 (fitted with BWF function), Fit peak 3 (fitted with Lorentzian function).*

The ratio of the pristine GC's D and G peak intensities was calculated and found to be 1.43, which agrees with the values reported in other studies [Lav08], [Buk14], [Odu18]. The Tuinstra-Koenig relation [Tui70] given in Equation (7.3) was employed to evaluate the average crystallite size in the pristine GC.

$$\frac{\mathrm{ID}}{\mathrm{IG}} = \frac{C_\lambda}{L_a} \tag{7.3}$$

where L_a is the average crystal size, ID/IG is the intensity ratio of D and G peak of pristine GC. The C_λ is the laser excitation wavelength-dependent constant evaluated from the relation ($C_\lambda \approx C_0 + \lambda C_1$ for $400 < \lambda < 700$ nm) given by Matthew et al. [Mat99]. C_λ was calculated as 44.0 Å for $\lambda = 514.5$ nm, $C_1 = -12.6$ nm, and $C_0 = 0.033$ estimated from a plot of C_λ versus excitation wavelengths [Mat99]. The pristine GC had an average crystallite size of 2.97 nm, which agrees with previous studies [Lav08], [Tui70], [Odu16], [Njo17]. This value also falls in the 2.5 nm < La < 300 nm range, where the Tuinstra-Koening Equation

holds for different forms of graphitic carbon [Fer00]. Thus, GC can be classified as nanocrystalline graphite [Fer07].

The pristine GC was also characterized by a 532 nm laser excitation wavelength and the Raman spectrum was deconvoluted using a Voigt function (Figure 7.6). A Voigt function is a convolution product between a Lorentzian function and a Gaussian function as given by Equation (7.4):

$$y = y_0 + A\frac{2\ln 2}{\pi^{3/2}}\frac{\omega_L}{\omega_G^2}\int_{-\infty}^{\infty}\frac{e^{-t^2}}{(\sqrt{\ln 2}\frac{\omega_L}{\omega_G})^2+(\sqrt{4\ln 2}\frac{x-x_c}{\omega_G}-t)^2}dt \qquad (7.4)$$

For each Voigt profile, y_0 represents the offset value, x_c is the centre of the profile, A represents the area under the profile, ω_G = Gaussian full width at half maximum (FWHM), ω_L = Lorentzian FWHM. A constant (minimum) baseline mode was chosen for each Raman fittings.

With the Voigt function, it was possible to obtain an additional peak found at ~1495 cm^{-1} (D'' peak). This peak can be related to the amorphous carbon in the carbon lattice's interstitial sites. With this peak, it was possible to estimate the ID''/IG ratio, which represents the ratio of the amorphous carbon fraction relative to the graphitic carbon fraction in the GC [Mad20]. The ID''/IG ratio was calculated to be 0.10 for the pristine GC, which indicates the small amorphous fraction in the GC. As seen in Figure 7.6, the Voigt function reproduced other peaks with their corresponding positions as obtained by the BWF and Lorentzian functions in Figure 7.5. The D* peak is found at 1170 cm^{-1}, D peak at 1357 cm^{-1}, G peak at 1588 cm^{-1} and D'' peak at 1620 cm^{-1}.

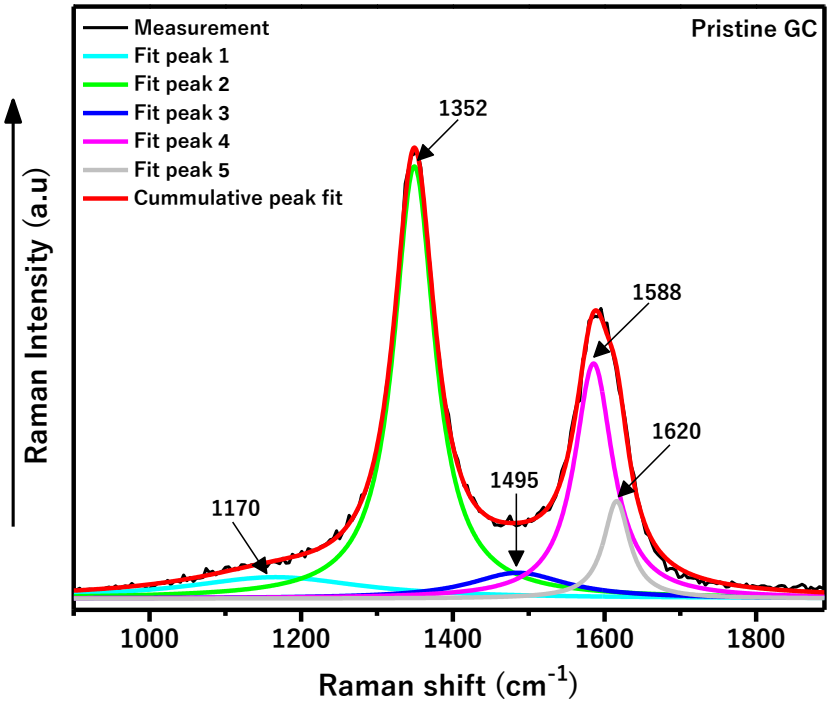

***Figure 7.6**. Raman spectrum of pristine GC. (All peaks fitted with Voigt function)*

7.4 Room Temperature Implantation

7.4.1 Raman results

Implantation of Se ions into GC at room temperature (RT) resulted in the merging of D and G peaks to a single broad peak, as shown in Figure 7.7. This indicates that the GC implanted layer is highly defective as it has been observed with other ions implanted in GC [Lav08], [Hla17], [Lan17], [Njo17], [Odu18], [Ken18]. After the implantation at RT, the broad peak is found between 1449 and 1555 cm^{-1}, wavenumbers, and deconvolution results in two separate peaks (D and G), as illustrated in Figure 7.7. It can be seen from this Figure that the deconvoluted G peak has shifted to a lower wavenumber (from 1588 to 1554 cm^{-1}), accompanied by a broadening of the G peak and a decrease in the D peak and G peak intensities ratio (ID/IG), from 1.43 to 1.01. These changes observed in the Raman features (in Figure 7.7 after deconvolution) reflect the transformation of GC into a highly defective material [Odu16], [Hla17], [Tak85]. Ferrari and Robertson's three-stage model can be used to determine the proportional quantity of sp^2 and sp^3 bonds in any carbon material [Fer00]. This model relies on the G peak positions and ID/IG ratio for estimating the relative amount of the sp^2 and sp^3 bonds. The detail of this model can be found in [Fer00]. The drop of ID/IG from 1.43 to 1.01 suggests that about 15% of sp^2 bonds (in the GC sample) were converted to sp^3 bonds due to Se ion implantation. This result is comparable with the results of cobalt

(Co^+) [Lav08] and xenon (Xe^+) [McC94] implantation in GC. To determine the contents of the sp^2 and sp^3 bond in any carbon material, Electron energy loss spectroscopy (EELS) would be required, and this will be one of the future studies.

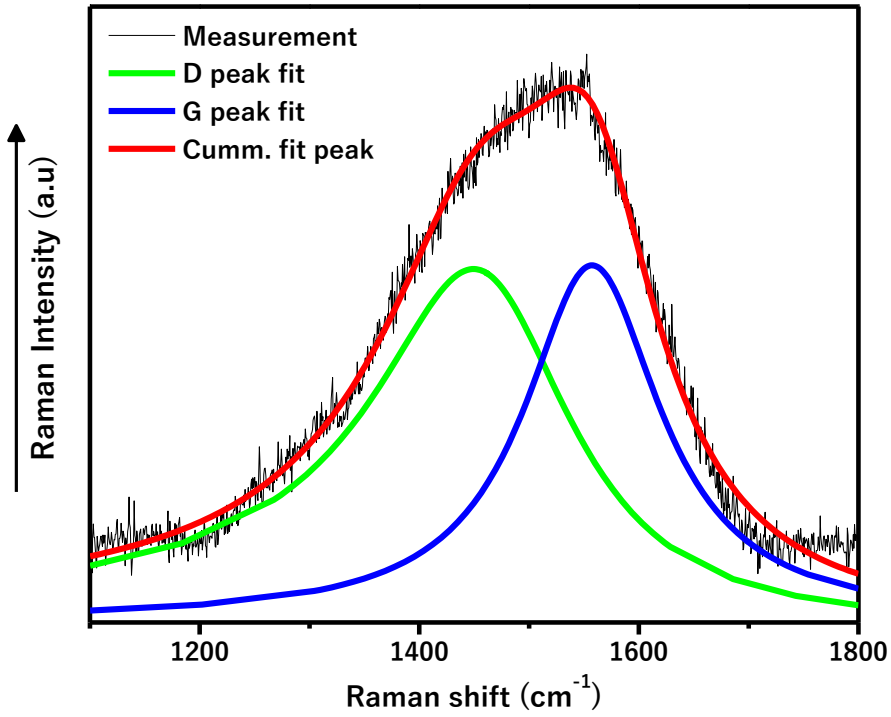

***Figure 7.7**. Raman spectra of Se implanted in GC at room temperature. (D peak fitted with BWF function and G peak fitted with Lorentzian function).*

The Tuinstra–Koening relation in Equation (7.3) breaks down after ion implantation [Fer00]. This Equation presumes that the ID/IG is proportional to the graphitic ordering in GC [Fer00]. Introducing defects in the GC by ion implantation caused some sp^2 bonds to be converted into sp^3 bonds, accompanied by a decrease in the D and G peak intensities. Hence, the average graphitic size of the resulting defective GC structure is disordered, and the Tuinstra–Koening relation will no longer hold to calculate the average crystal size. The average crystallite size of amorphised GC material was estimated using Equation (7.4) by Ferrari and Robertson [Fer00].

$$\frac{\mathrm{ID}}{\mathrm{IG}} = C'_{\lambda} L_a^2 \qquad (7.5)$$

where C'_{λ} is a constant taken as 0.0055 $Å^{-2}$ [Fer00], L_a is the average crystallite size and ID/IG carries the usual meaning already stated above. The calculated average crystallite size for the pristine GC, 3.1 nm, reduces to 1.36 nm after Se implantation at room temperature. The high fluence (1×10^{16} ions/cm^2) of Se ions implantation partially destroyed the graphite

crystallites in the GC's implanted region, leading to smaller crystallite sizes. This means that aside from the decrease of the ID/IG ratio, broadening of the G peak and its downshifting to a lower wavenumber, the reduced average crystallite size is another evidence that Se implantation into GC resulted in a highly disordered layer (with bond angle disorder), within the substrate.

It is interesting to note that cobalt (Co) and indium (In) ions implantation into GC at a fluence in the same order of magnitude (i.e., 10^{16} ions/cm^2) used in this study were characterized with different crystallite sizes, 1.1 and 3.1 nm for 150 keV Co^+ [Lav08] and 360 keV In^+ [Njo17], respectively. The variation in the crystallite sizes might be due to the different atomic masses of these elements.

7.4.2 Effects of annealing on the microstructure of the room temperature as-implanted GC sample

Figure 7.8 and Figure 7.9 shows the Raman spectra of Se implanted GC after annealing at low (300 – 700 °C) and high (1000 – 1200 °C) temperature regimes. The Raman spectra of the samples annealed at 300 and 400 °C are identical to the Raman spectrum of the as-implanted, indicating no appreciable recrystallization following annealing at these temperatures. The D and G peaks of the Raman spectra obtained after annealing at 500 ºC are somewhat discernible as compared to ones obtained in the RT as-implanted samples. Hence, the 500 °C annealing temperature can be considered a critical temperature where the defects within the implanted region become thermally activated and begin to anneal out. The peaks intensified when the annealing temperature was increased from 500 °C, and at the highest annealing temperature (1200 °C), the D and G peaks are clearly distinguishable. Information such as D and G peak heights, G peak position and FWHM, were extracted from the deconvoluted Raman spectra, which are plotted in Figure 7.10 and Figure 7.11. These parameters were used to obtain structural information about the effects of annealing on the as-implanted samples annealed at different temperatures.

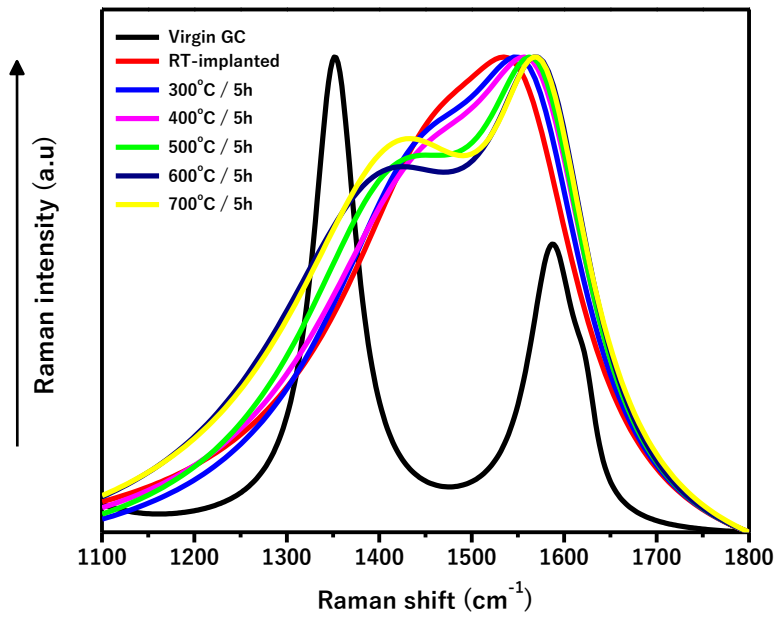

***Figure 7.8**. Raman spectra of pristine GC after Se ions implantation at RT and after sequential annealing at the low-temperature regime (300 – 700 ºC) in steps of 100 ºC and 5h annealing cycle.*

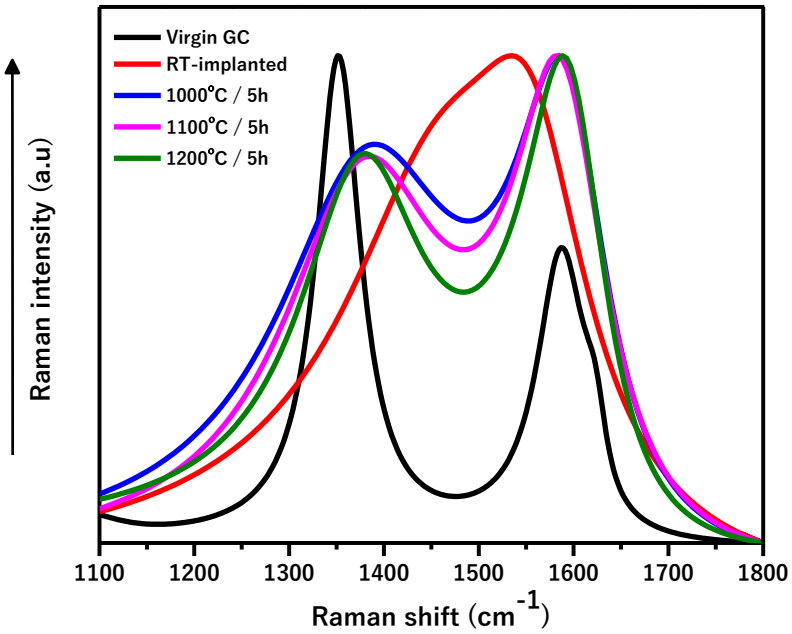

***Figure 7.9**. Raman spectra of pristine GC after Se ions implantation at RT and after sequential annealing at the high-temperature regime (1000 – 1200 ºC) in steps of 100 ºC and 5h annealing cycle.*

The gradual increase in the D and G peak intensities indicates progressive annealing of defects, which could mean an increase in graphitic ordering within the implanted region of the GC. The G peak position shifted progressively from about 1560 cm^{-1} at 300 °C to 1588 cm^{-1} at 1200 °C (see Figure 7.10). It can be seen in Figure 7.10 that the G peak position upshift was accompanied by a progressive decrease in the G peak FWHM as a function of

increasing annealing temperature (i.e., from 151.0 to 123.9 cm^{-1} and 118 to 112.1 cm^{-1} for the samples annealed at 300 – 700 °C and 1000 – 1200 °C, respectively). After annealing the RT as-implanted sample from 300 – 700 °C and 1000 – 1200 °C, the D to G peak intensity ratio (ID/IG) decreased steadily from 1.01 to 0.84 and 0.79 to 0.72, respectively (see Figure 7.11). It is reasonable to assume that annealing will recrystallize the implanted region of the glassy substrate. This assumption was verified by determining the average crystallite size, L_a, as a function of annealing temperature. Likewise, the Tuinstra-Koenig Equation was chosen based on the idea that annealing will increase crystallite size when the ID/IG ratio falls. The graphite crystallite sizes ranged from 4.75 to 5.21 nm and 5.57 to 6.07 nm for the samples annealed at 300 – 700 °C and 1000 – 1200 °C, respectively (as shown in Figure 7.11). The average crystallite sizes of the RT as-implanted then annealed sample have become larger (L_a = 3.1 nm) than those of the pristine (L_a = 1.36 nm). The average crystallite value is still within 2 – 300 nm, where the Tuinstra–Koening relation holds for any form of carbon material. The increase in the average crystallite size with increasing annealing temperature (for the two annealing regimes) aligns with the crystal growth theory [Bur51].

The gradual upward shift in the G peak positions with increasing annealing temperature indicated the growth of the crystallites into larger sizes in line with the above calculations. The narrowing of the G peak FWHM can also be attributed to the decrease in bond angle disorder [McC95]. It is important to note that the G peak FWHM did not return to its original value, 68.1 cm^{-1} at the highest annealing temperature, 1200 °C. This indicates that annealing only partially recovered the GC substrate and that some radiation damage remained in the GC structure after annealing at the highest temperature. It has been previously reported in some studies that heat treatment does not usually remove all radiation damage in highly defective carbon materials [Njo17], [Hla17], [Ism18], [Lav08]. The partial recovery of the GC substrate could be due to the retained Se in the substrate. All the changes observed in the G peak position, FWHM, ID/IG, and L_a (after annealing) show that annealing reduced the disorder within the implanted region, allowing the GC substrate to recrystallize. It should be noted that annealing GC samples at low temperatures (300 – 700 °C) resulted in minimal recovery, but the GC samples annealed at the high-temperature regime (1000 – 1200 °C) showed significant recovery after some Se atoms diffused out. Recrystallization in highly defective GC (due to annealing) has been reported in other studies [Odu16b], [Njo17], [Hla17], [Ism18], [Lav08].

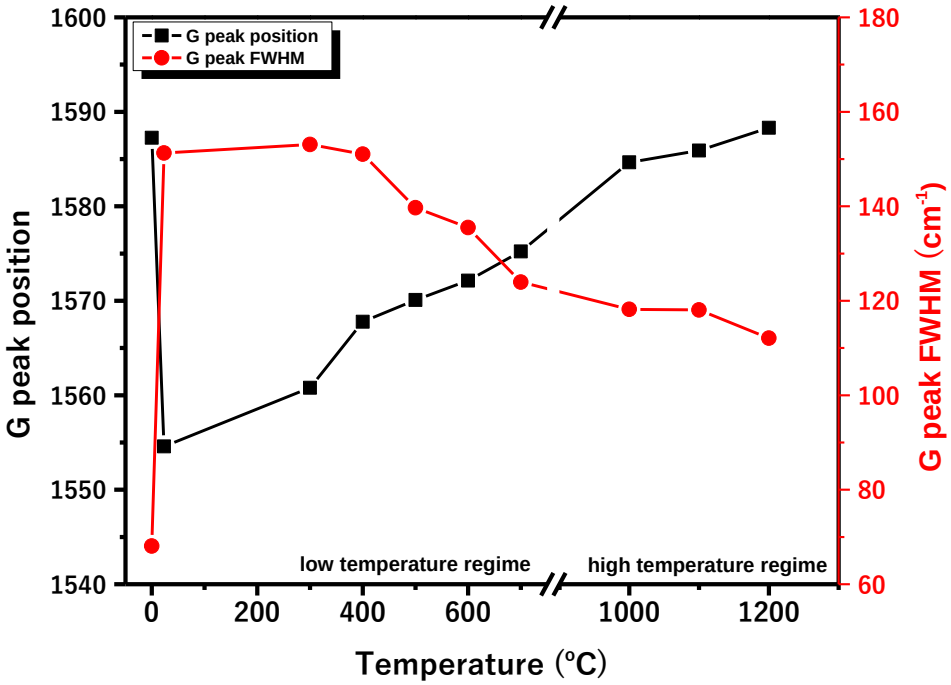

Figure 7.10. *G peak position and G peak bandwidth (FWHM) of Raman spectra of pristine GC after implantation with Se ions at RT and after sequential annealing at the low and high-temperature regimes.*

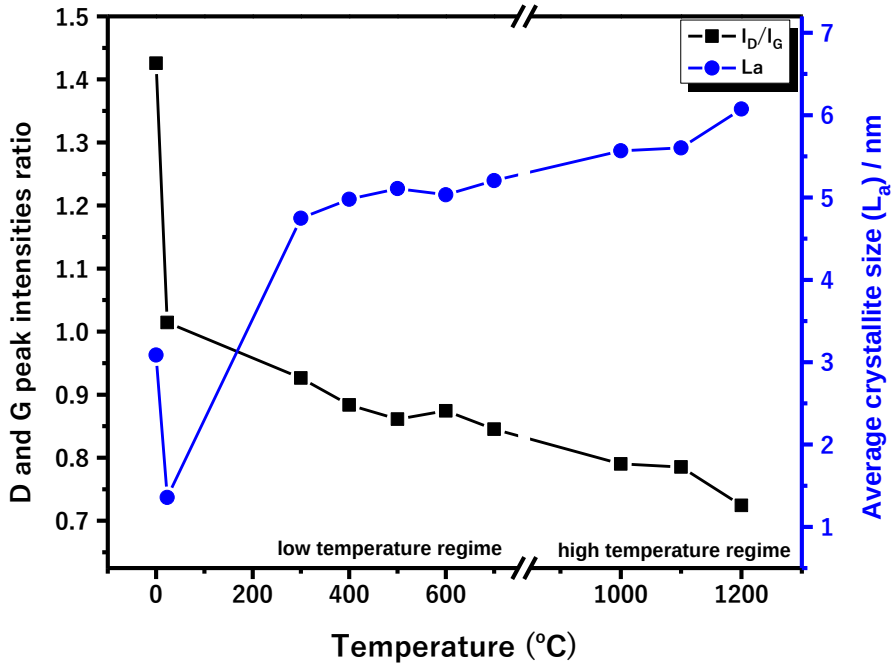

Figure 7.11. *ID/IG ratio and crystallite size (La) of Raman spectra of pristine GC after implantation with Se ions at RT and after sequential annealing at the low and high-temperature regimes.*

7.4.3 Migration behaviour of selenium in the room temperature implanted sample after sequential annealing

A room temperature (RT) implanted GC sample was subjected to sequential isochronal annealing from 300 to 700 °C in steps of 100 °C for 5 hours to explore the diffusion of Se atoms in the GC substrates. After each annealing phase, the depth profiles were measured with Rutherford backscattering spectrometry (RBS) and the results are shown in Figure 7.12 and Figure 7.13. Fitting the RBS depth profiles of the RT sample to a Gaussian function yielded the full width at half maximum (FWHM) and the peak positions. The diffusion of the implanted Se was investigated by comparing the square of the full width at half maximum ($FWHM^2$) of the depth profiles of the as-implanted and the as-implanted then annealed samples. This is because the diffusion of implanted ions is indicated by the broadening of a profile [Mal17]. The peak positions and $FWHM^2$ (as a function of annealing at the low-temperature regime) are plotted in Figure 7.14. The retained Se was calculated by comparing the areas under each Se profile (after each annealing temperature) to the as-implanted profile and plotted accordingly in Figure 7.15.

Figure 7.12 shows that the as-implanted Se profiles were nearly identical to those annealed between 300 and 700 °C. The slight variation in the $FWHM^2$ and the peak positions of the sample annealed from 300 to 700 °C are within the experimental uncertainty of the depth scale of the RBS measurements (see Figure 7.12), indicating no diffusion of Se atoms occurred at these low temperatures. The measurement error in the $FWHM^2$ was obtained from the standard deviation of the data up to 600 °C. Likewise, the measurement error in the peak positions was estimated from the standard deviations of the Se peak positions and the surface positions of the carbon RBS peak. These two standard deviations were added in the usual way. There is no reason why annealing would cause a change in the selenium peak position except when Se is lost due to out-diffusion. Due to the fitting of a Gauss function to the limited RBS data, there is also a possibility that the fitting might not give an exact peak position.

Following the non-diffusion of Se atoms in the GC at the low-temperature regime, another RT as-implanted GC sample was annealed between 800 and 900 °C for 5 h. Yet, no diffusion of Se atoms occurred, as the profiles look similar to the as-implanted RT profile, as seen in Figure 7.13. Based on the above, annealing at temperatures of up to 900 °C was insufficient to initiate the diffusion of the Se atoms in the GC. The non-diffusion of Se atoms

up to 900 °C is because Se atoms are still well trapped within the implanted region by the defects created during implantation in the GC.

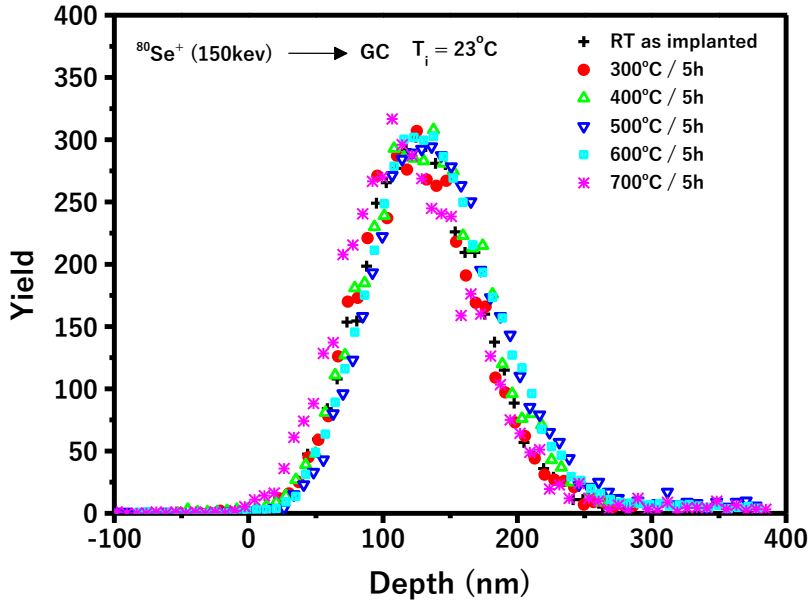

Figure 7.12. *RBS Depth profiles of 150 keV Se ions implanted in GC and after sequential annealing at the low-temperature regime (300 – 700 ºC) in steps of 100 ºC for 5h annealing cycle.*

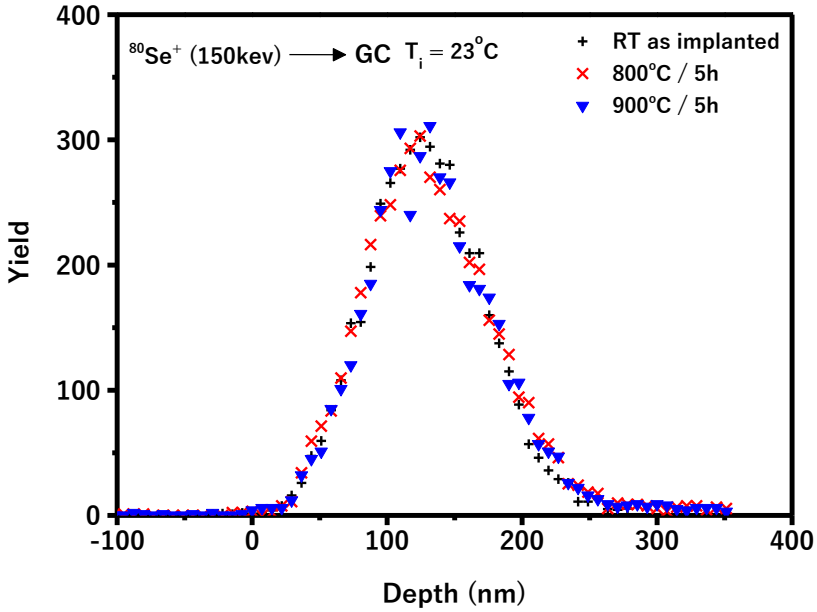

Figure 7.13*. RBS Depth profiles of 150 keV Se ions implanted in GC at RT and after sequential annealing at the low-temperature regime (800 – 900 ºC) in steps of 100 ºC for 5h annealing cycle.*

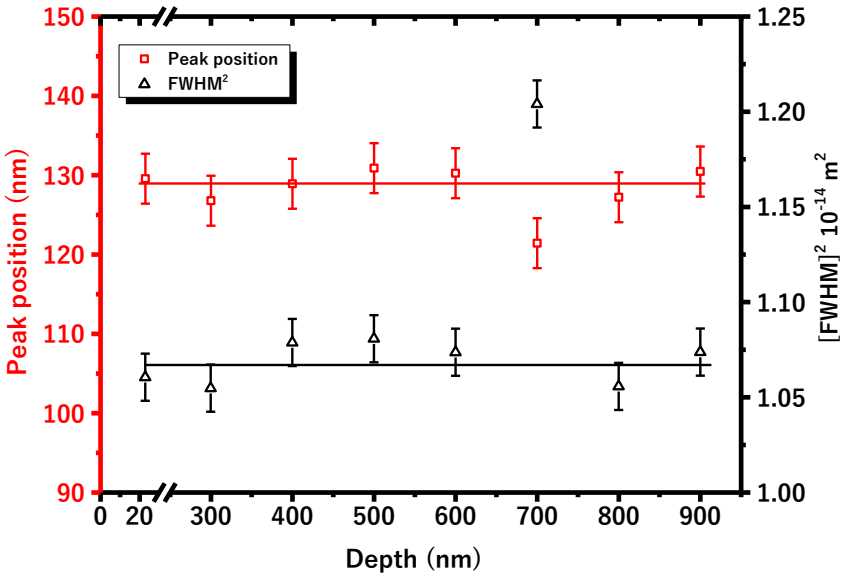

Figure 7.14. *Peak position (squares) and square of the full width at half maximum (triangles) of 150 keV Se ions implanted in GC at RT and after sequential annealing at the low-temperature regime (300–900 ºC) in steps of 100ºC for 5h annealing cycle.*

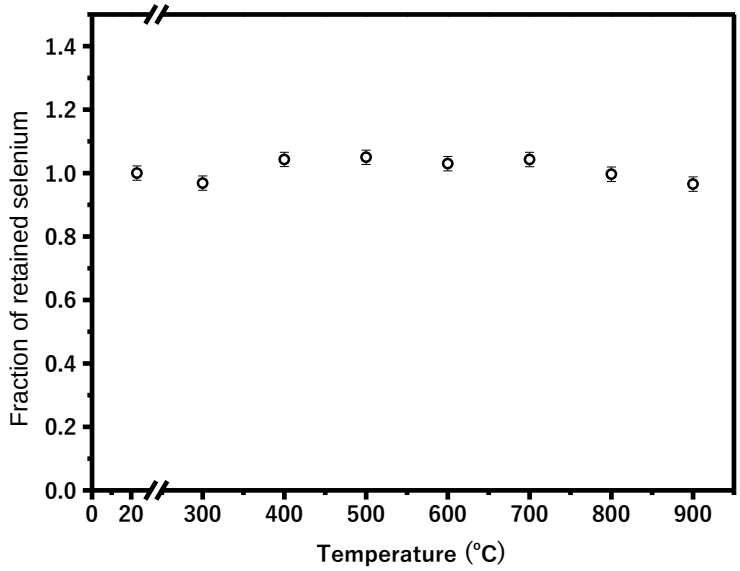

Figure 7.15*. The retained ratio of Se (calculated as the ratio of the total areas under each Se profile (after each annealing step) to that of the as-implanted profile) as a function of low-temperature annealing (300 – 900 ºC) in steps of 100 ºC for 5 h annealing cycle.*

A fresh RT implanted sample was sequentially annealed at high-temperature regime ranging from 1000 to 1200 °C in 100 °C increments for 5 h and the RBS depth profiles are shown in Figure 7.16. The sequential annealing of the RT implanted sample at 1000 °C resulted in the asymmetric broadening of the Se profile, as shown in Figure 7.16. The Se profile broadened more towards the bulk to about 380 nm depth. This profile's skewness indicates Se atoms' migration more into the bulk of the GC. Since no appreciable migration of Se towards the surface was seen at this temperature, no loss of Se was recorded, as seen

in Figure 7.17. The Se profile became more asymmetrical by increasing the annealing temperature to 1100 °C. It broadened more towards the surface and tailed into the bulk of the GC to about 400 nm (see Figure 7.16). The Se profile at this temperature indicates that more Se atoms have moved towards the surface and into the bulk of the GC, accompanied by a 5% loss of Se atoms (as illustrated in Figure 7.17). The loss of Se may be related to the evaporation of Se atoms into the vacuum during annealing since the melting point of Se, 220 °C, is much lower than the annealing temperatures. After annealing the RT as-implanted sample at 1200 °C, the profile was identical to that obtained at 1100 °C, showing a similar migration pattern exhibited by the Se atoms. At this temperature, 1200 °C, the tail of the Se profile was deeper into the bulk (approximately 450 nm), indicating a stronger migration of Se into the bulk accompanied by the loss of more Se atoms (of about 32%).

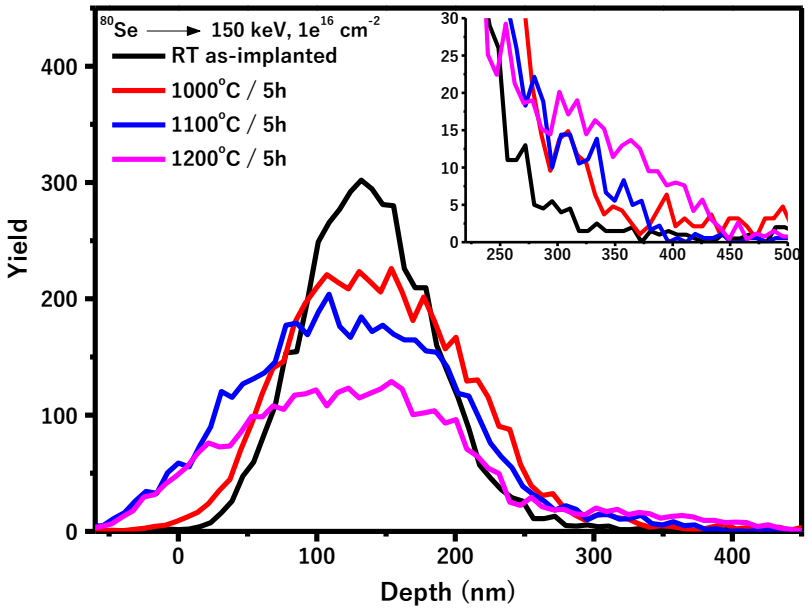

Figure 7.16. *RBS depth profiles of 150 keV Se ions implanted in GC and after sequential annealing at the high-temperature regime, 1000 – 1200 ºC, in steps of 100 ºC for 5h annealing cycle.*

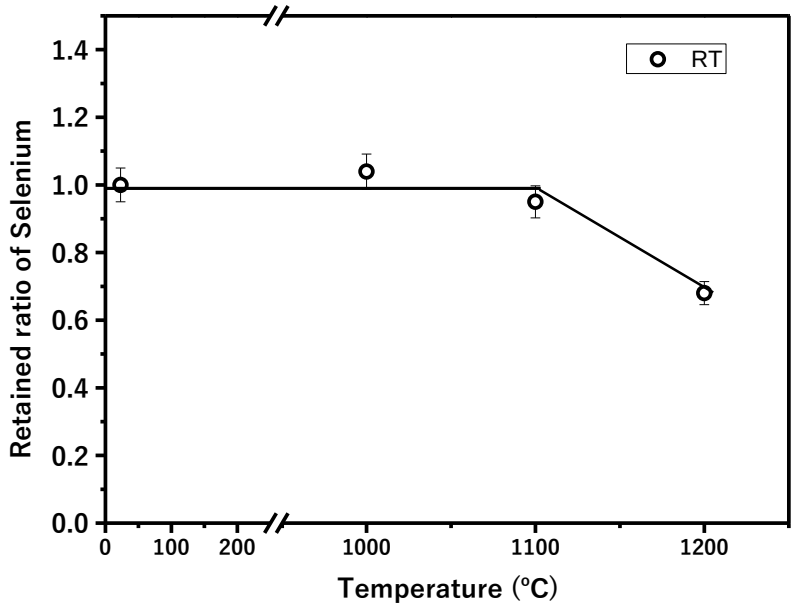

Figure 7.17. *The retained ratio of Se (calculated as the ratio of the total areas under each Se profile (after each annealing step) to that of the as-implanted profile) as a function of high-temperature annealing regimes (1000 – 1200 ºC).*

The negative side of the depth scale in the RBS profiles in Figure 7.16 indicates the presence of some Se atoms above the GC surface. This unusual event may be due to the poor energy resolution or the roughness of the GC surface. The energy resolution in RBS reduces with depth. Poor energy resolution can often result in an artificial broadening of any surface peak in the RBS spectra measured. Sometimes, the spectral shape becomes distorted relative to what it would be if the energy resolution is constant throughout measurement [Bar01]. Data analysis of RBS spectra can be challenging once surface roughness is present [Bar02]. The out-diffusion of Se at the high-temperature regime may have caused significant surface roughness, which thence affected the subsequent RBS depth profiling measurements.

A new set of GC samples implanted at RT were isochronally annealed in the high-temperature range of 1000 to 1200 °C in incremental steps of 100 °C for 5 hours to investigate the effect of radiation damage on the migration behaviour of Se in GC. These annealed samples were then characterized with secondary ion mass spectrometry (SIMS). Figure 7.18 shows an asymmetric broadening of the Se profile after the isochronal annealing of the RT as-implanted sample at 1000 °C. The Se profile was skewed to a depth of around 330 nm, as shown in Figure 7.18. The profile's skewness indicates the migration of Se atoms into the bulk of the GC. There was no detectable loss of Se at 1000 °C because there was no pronounced migration of Se atoms towards the surface. A similar observation was noted in the sequentially annealed sample characterized by RBS. Increasing the annealing

temperature to 1100 °C caused the Se profile to become more asymmetrical, broadened toward the surface and into the bulk of the GC, up to 350 nm (as seen in Figure 7.18). The Se profile at this temperature indicates that more Se atoms have moved to the surface and the bulk of the GC, accompanied by a 36% loss of Se atoms (as illustrated in Figure 7.19). The loss of Se can be related to the evaporation of Se atoms into the vacuum during annealing. The profile obtained after annealing the RT implanted sample at 1200 °C is identical to the one obtained at 1100 °C, indicating a similar migration pattern exhibited by the Se atoms at this temperature. At 1200 °C, the tail of the Se profile was deeper (to about 400 nm), indicating a further migration of Se into the bulk and the loss of more Se atoms by about 51% (as shown in Figure 7.19).

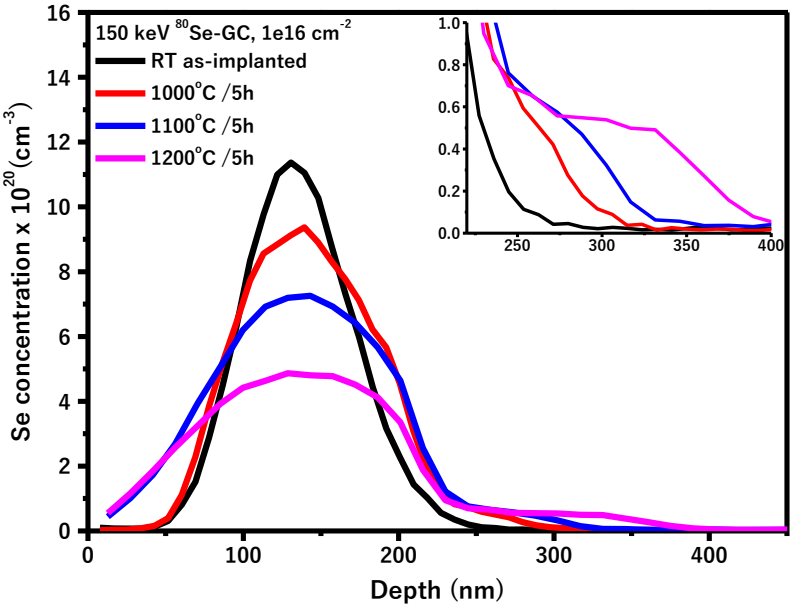

***Figure 7.18**. SIMS Depth profiles of 150 keV Se ions implanted in GC and after isochronal annealing at the high-temperature regime (1000 – 1200 ºC) in steps of 100 ºC for 5h annealing cycle.*

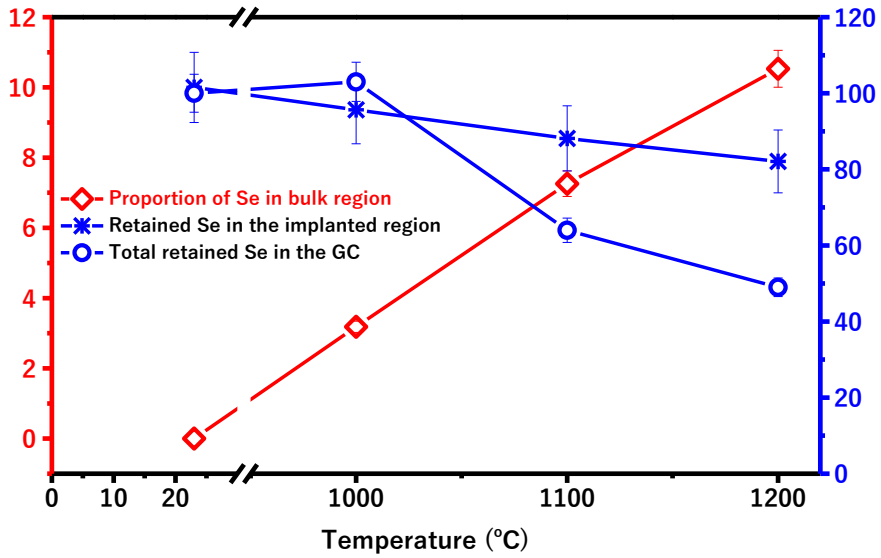

***Figure 7.19**. The proportion of migrated Se in the bulk of the GC samples (red diamonds); retained Se in the damaged region (blue asterisks) and retained Se in the GC substrate (blue circles).*

Overall, the SIMS depth profiles discussed above (in Figure 7.18) have some features that are similar to the RBS profiles (in Figure 7.16) but with a little discrepancy. The similarity between the RBS and SIMS features can be understood by referring to the dpa curve illustrated in Figure 7.2 (a) and Figure 7.2 (b). The radiation damage is lower at the end of range (i.e., at 240 nm) as compared to the rest of the implantation layer. Accordingly, the migration of the Se atoms is not expected in the bulk because most of the radiation damage is closer to the surface than the bulk of the GC substrates. However, as shown in Figure 7.16 and Figure 7.18, the migration of Se atoms began in the region with the least damage. It progressed to the area with moderate and high radiation damage as the annealing temperature increased. This type of migration behaviour exhibited by Se atoms in the bulk of the RT as-implanted the annealed sample can be explained in terms of trapping and de-trapping of the Se atoms by defects induced during implantation. Annealing at 1000 °C only caused the Se atoms to move in the less defective damaged region, while annealing at 1100 and 1200 °C caused the annealing of defects in the less radiation damage region, creating pathways for Se atoms to migrate deeper into the bulk of the RT GC samples. It is clear from Figure 7.16 and Figure 7.18 that most Se atoms were trapped in the high radiation damage region, limiting their migration to the surface in RT as-implanted and then annealed (sequential and isochronal) sample. A typical GC contains several nanopores responsible for its low density (1.42 gcm^{-3}). The average pore size in GC is about 0.3 nm [Pie93] but can vary depending on the preparation temperature. Harris has reported a pore size of about 5 nm in a pristine Sigradur®G GC (prepared at 3000 °C) [Har04]. A Se atom (with an atomic

radius of 0.19 nm) would successfully fit into either 0.3 nm or 5 nm pores in GC. An implanted GC sample would have fewer micropores because as the irradiation defects trapped the Se atoms [Odu18]. The experimental depth profiles are indications that Se atoms are trapped as these profiles are broader than the simulated one, as shown in Figure 7.2 (see also ΔR_p in Table 7.1).

The discrepancy between the SIMS and RBS profiles confirms the initial suspicion that the Se RBS depth profiling measurement in the high-temperature regime may have been hampered by sample surface roughness. Also, the different annealing methods (sequential for RBS measurement versus isochronal for SIMS measurement) may play a significant role in the disparity between the SIMS and the RBS results. As an illustration, the tailing of the Se profiles (which represents the movement of Se atoms in the bulk of the GC) is smaller in the isochronally annealed RT implanted sample than in the sequentially annealed ones (see Figure 7.16 and Figure 7.18). This explains why more Se atoms are lost in the isochronally annealed samples. Additionally, the samples' microstructures resulting from both annealing methods would differ, which is why the depth profiles also varied. The migration of Se atoms into the bulk of the GC was initially of great concern in this study, as this would limit the recommendation of GC as a nuclear waste storage container. The proportion of Se atoms that migrated into the bulk was estimated at each annealing temperature. The bulk region of the as-implanted GC was assumed to be the depth beyond the boundary of the critical dpa of 0.2 in the as-implanted GC (see profile in Figure 7.2). This depth would correspond to $R_p + 3\Delta R_p$ = about 240 nm. The proportion of Se atoms that have migrated into the bulk area of the GC was plotted alongside the retained Se atoms in the high radiation damage region at each isochronal annealing temperature (refer to Figure 7.19). The broad Se peak (within the high radiation region) has dropped progressively as the annealing temperature rises, resulting in outward diffusion and an increasing build-up of Se concentration in the bulk area of the GC substrate (beyond the low radiation damage region). It can be seen in Figure 7.19 that about 3, 7 and 10% of the retained Se have migrated into the bulk after annealing at 1000, 1100 and 1200 °C, respectively. The minute concentration of Se atoms in the bulk of the GC substrate is not expected to limit its applicability as a nuclear storage container. However, further studies will be carried out to investigate this observation (as outlined as one crucial objective in my future studies).

7.4.4 Diffusion coefficient of Se ions and other ions in defective GC: a short review

The diffusion coefficients of Se within the highly defective GC were estimated by fitting the RBS depth profiles data (of the RT as-implanted and as-implanted then annealed sample) to the solution of the Fick's diffusion equation for an initial Gaussian profile by Malherbe et al. [Mal17]. The fitted spectra are shown in Figure 7.20 for the RT as-implanted, 1000, and 1100 °C RBS data. The diffusion coefficients obtained in this study were governed by Equation (4.14 – 4.16) given in Chapter 4 of this thesis. This was achieved by incorporating the solution for a perfect reflecting surface because the Se signals at the surface for these profiles (as-implanted and as-sample then annealed at 1000 and 1100 °C sample) were zero. The diffusion coefficients for Se diffusion in defective GC after annealing at 1000 and 1100 °C were calculated to be 5.9×10^{-20} and 4.79×10^{-20} m^2s^{-1}, respectively. Although Figure 7.16 shows a slight broadening of the Se profile at 1200 °C, which is within the RBS statistical error, and as a result, no reliable diffusion coefficient could be estimated at this temperature.

Table 7.2 compares the diffusion coefficients of Se (this study) with the diffusion coefficients of other ions implanted in GC from previous studies. Contrary to expectations, the diffusion coefficient of Se falls as the annealing temperature rises. This could be due to the continuous annealing of defects during the sample's heat treatment. Because the sample was subjected to sequential annealing, one would expect that previous heat treatments would affect the sample's microstructure and consequently affect the diffusion coefficients. A similar trend in the reduction of the diffusion coefficients with increasing annealing temperature was reported for Ag diffusion in defective GC [Odu20]. The difference in the sample's microstructure was the same reason for this trend. The decreasing trend in the diffusion coefficients of beryllium (Be) reported by Koskelo et al. [Kos08] could be due to the different annealing durations and temperatures.

Previous studies have shown that radiation damage is induced when GC is bombarded by different ions at varying implantation energies and fluencies [Odu16], [Hla17], [Njo17], [Ism18]. While defects can trap the implanted ions at a particular implantation temperature, it is also possible for diffusion to occur above the defects' temperature via different diffusion mechanisms [Mal17]. The activation energy (E_a) would be a helpful parameter in characterizing the diffusion mechanism, but none has been reported in the literature. The activation energy of Se can only be determined with a minimum of three diffusion coefficient values and just only two were obtained in this study (by the RBS technique

employed). However, the diffusion of Se, alongside other atomic species in defective GC, has been classified by their diffusion coefficients in Table 7.2. Beryllium (Be) and Indium (In) with a diffusion coefficient in the order ($\times 10^{-17}$ m^2s^{-1}) exhibited fast diffusion, cadmium (Cd) and strontium (Sr) ($\times 10^{-19}$ m^2s^{-1}) manifested with intermediate diffusion rates, while europium (Eu), silver (Ag) and selenium (Se) ($\times 10^{-20}$ m^2s^{-1}) are characterized by slow diffusion, all given in Table 7.2. It is worth noting that all these ions were implanted into GC at room temperature (RT) before being annealed at higher temperatures and their different diffusion coefficients were determined.

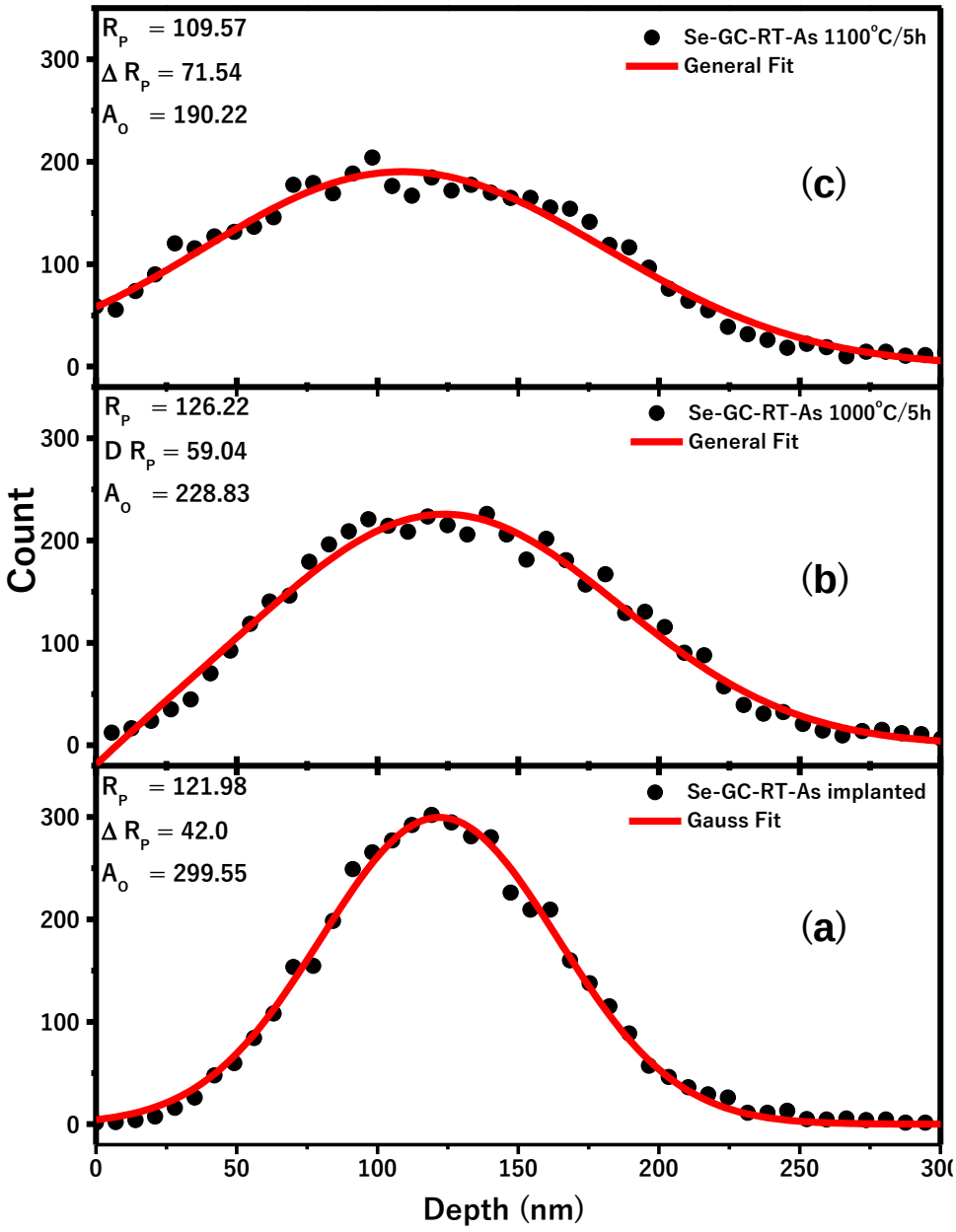

***Figure 7.20**. Examples of fitting of the diffusion equation solution to the experimental depth profile data of the GC sample (a) as-implanted (b) annealed at 1000 ºC for 5h and (c) annealed at 1100 ºC for 5h annealing cycle. The dotted lines represent the experimental data while the solid red lines are for the fittings.*

Table 7.2. *Diffusion coefficients (D) of different ions implanted in GC.*

Implanted ions	(D) (m^2s^{-1})	Annealing Temperature (ºC)	Annealing duration (hr)	Diffusion Type	References
Be	3.00×10^{-17}	1285	½	Fast	[Kos08]
Be	2.50×10^{-17}	1340	¾	Fast	[Kos08]
In	2.15×10^{-17}	300	1	Fast	[Njo17]
Cd	7.82×10^{-19}	350	1	Intermediate	[Hla17]
Eu	9.12×10^{-19}	300	1	Intermediate	[Ken18]
Sr	1.60×10^{-19}	300	1	Intermediate	[Odu20]
Sr	3.70×10^{-19}	400	1	Intermediate	[Odu20]
Ag	7.70×10^{-20}	500	1	Slow	[Odu20]
Ag	3.70×10^{-20}	550	1	Slow	[Odu20]
Ag	5.30×10^{-20}	575	1	Slow	[Odu20]
Se	5.90×10^{-20}	1000	5	Slow	this study
Se	4.79×10^{-20}	1100	5	Slow	this study

.

7.5 Higher temperatures implantation (100, 150, and 200 °C)

7.5.1 Raman results

Figure 7.21 (a-c) shows the Raman spectra of GC implanted with Se ions at high implantation temperatures (100, 150, and 200 °C). The Raman spectra obtained after sequential annealing (at the low-temperature regime) are also included and compared with the pristine GC in Figure 7.21. The D and G peaks merged in all the Raman spectra of the samples implanted at higher temperatures, as seen in Figure 7.21. The deconvolution of these Raman spectra resulted in a few changes and structural information was obtained from parameters such as the FWHM, G Peak positions, ID/IG ratio, and the average crystallite sizes plotted in Figure 7.22 (a-d). The G peak FWHM became broader for the GC sample implanted with Se ions at 100 °C, which became narrower with increasing implantation temperature, and a maximum FWHM of 156.2 cm (larger than 68.1 cm for the pristine GC) was recorded in the GC sample implanted at 200 °C (see Figure 7.22 (a)). The G peak position exhibited an inverse relationship with increasing implantation temperature. It can be seen in Figure 7.22 (b) that the G peak position shifted from 1588 cm^{-1} (the pristine) to 1563, 1565, and 1573 cm^{-1} at 100, 150 and 200 °C, respectively. Figure 7.22 (c) illustrates that the ID/IG ratio falls after implantation with Se ions at 200 °C and further reduces with decreasing implantation temperatures.

According to the three-stage model by Ferrari and Robertson [Fer00], the drop in the ID/IG ratio and the shifting of the G peak to a lower wavenumber can be related to the sp^2 and the sp^3 bonds content in the implanted GC substrate. Assuming this model implies

that all the as-implanted GC samples contained less than 15% sp^3 bonds, and the sample implanted at 200 °C has the least sp^3 bond content. Electron energy loss spectroscopy (EELS) is usually needed to quantitatively determine the sp^2 and sp^3 bond content of any carbon material. This will be one of the future studies.

The merging of D and G peaks, coupled with the changes in the FWHM and downshifting of the G peak positions, as in Figure 7.22 (a – c), indicate that a high level of disorder was introduced in the near-surface regions of the GC at elevated temperatures. Further, the distortion of the implanted layer in the GC resulted in smaller crystal sizes of 1.29, 1.30, and 1.31 nm after implantation at 100, 150, and 200 °C, respectively, as shown in Figure 7.22 (d). This result confirms that the implantation of Se ions in GC resulted in a disordered region characterized by smaller crystal sizes. Using the above result of the G peak FWHM, G peak position, and the ID/IG, the sample implanted at 100 °C is more damaged, followed by the ones implanted at 150 and 200 °C, respectively.

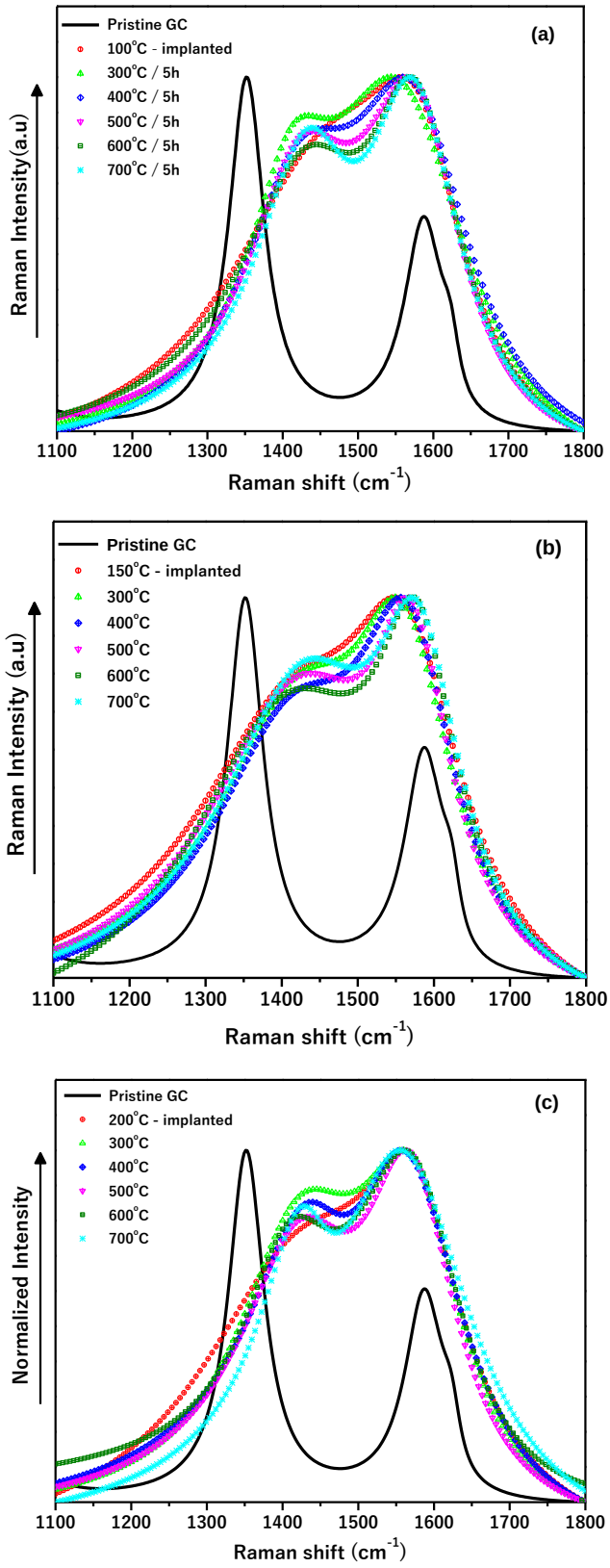

Figure 7.21. *Raman spectra of Se ions implanted in GC at higher temperatures (a) 100 ºC (b) 150 ºC and (c) 200 ºC after sequential annealing at the low-temperature regime (300 – 700 ºC) in steps of 100 ºC and 5h annealing cycle.*

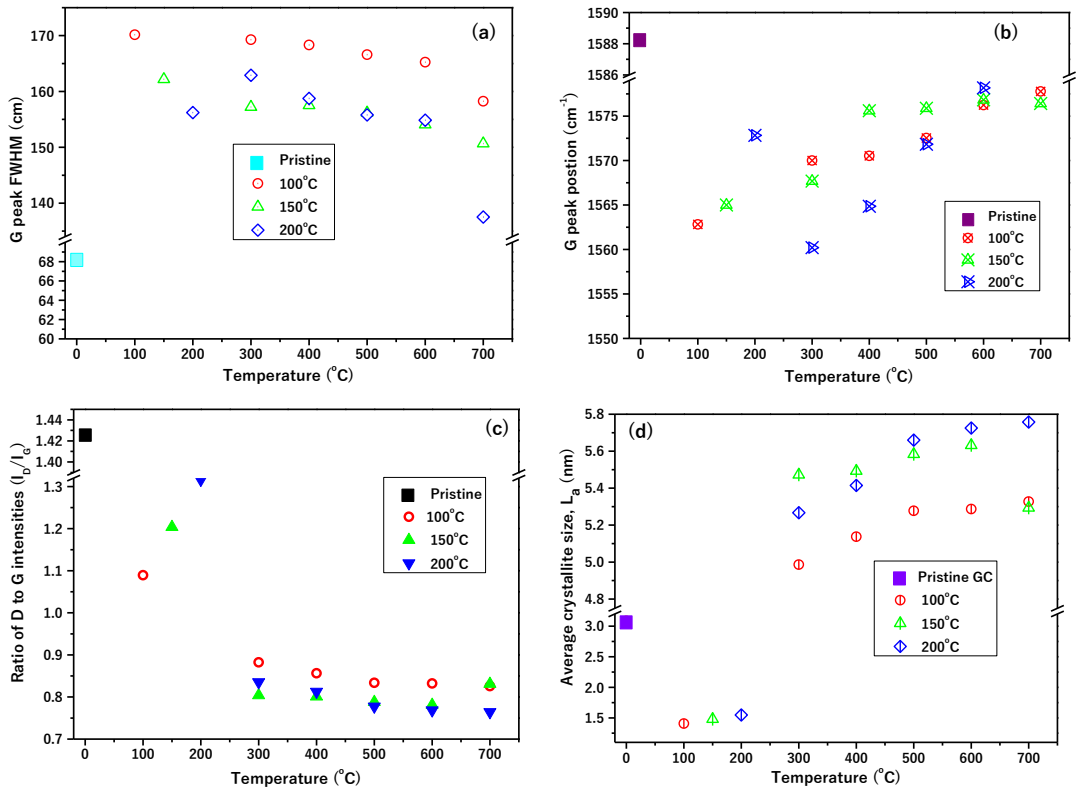

***Figure 7.22**. (a) G peak bandwidth (FWHM), (b) G peak position (c) ID/IG ratio and (d) average crystallite size (La) of the Raman spectra of GC samples implanted with Se ions at higher temperatures (i.e., 100, 150 and 200 ºC) and after sequential annealing at the low-temperature regime (300 – 700 ºC) in steps of 100 ºC for 5h annealing cycle.*

Comparing the structural evolution of the GC samples implanted (at a higher temperature) to the one implanted at room temperature (RT) (discussed in subsection 7.4.1), it is evident that the degree of disorder is high in the GC sample implanted at RT. This type of damage has been recorded in the studies of McCulloch et al. [McC95] and Hlatshwayo et al. [Hla17] when GC samples were implanted with different ion species at elevated temperatures. McCulloch et al. implanted Xe ions into GC at temperatures between 293 K and 873 K and characterized the samples by Raman spectroscopy. The resulting Raman spectra indicate structures with less damage were achieved at higher implantation temperatures. Hlatshwayo et al. presented another Raman study of Cd ions implanted in GC at room temperature (RT), 430, and 600 °C [Hla17]. The authors reported that the GC implanted at 600 °C became less damaged than those implanted at 430 °C and RT. This overall observation in the GC substrates implanted with Se, Xe, and Cd ions at temperatures higher than the RT is justified by the dependence of defect mobility on the implantation temperatures. Defects such as vacancies and interstitials become mobile at higher temperatures and recombine (as in Frenkel pairs), leaving the GC sample with a less defective structure.

7.5.2 Effect of annealing on the microstructure of the GC samples implanted at higher temperatures

The structural evolution of the GC samples implanted with 150 keV Se ions at 100, 150, and 200 °C to a fluence of 1×10^{16} ions/cm^2 after sequential annealing at the low and high-temperature regimes (300 – 700 °C and 1000 – 1200 °C) was studied by Raman spectroscopy. As shown in Figure 7.21, sequential heat treatment at the low-temperature regime (of the samples implanted at higher temperatures) caused the D and G peaks to become slightly observable and distinguishable. The G peak was more pronounced than the D peak in all the heat-treated GC samples implanted (at 100, 150, and 200 °C), and even after annealing at 700 °C, the peaks are still not comparable. This observation is due to the retained defects caused by implanted Se in the GC sample structures.

The Raman spectra of the samples implanted at higher temperatures and sequentially annealed at the high-temperature regime showed more distinguishable and identifiable D and G peaks, indicating lesser defective structures retained after annealing at this high-temperature regime (see Figure 7.23). It was noted that the G peaks are still more pronounced than the D peaks after annealing at the high-temperature regime. Comparing the Raman spectra in Figure 7.23, it is evident that the G peaks of the sequentially heat-treated (higher temperature implanted GC samples) have a higher intensity than the pristine GC. Since the G peak is a unique identity of graphitic carbon, it can be stated that the intense G peak regrowth symbolizes a more graphitizing structure with features of larger crystallite sizes. Polycrystalline graphite is a material with such peculiarities, where the G peak is more pronounced than the D peak [Fer00]. It can also be recalled that a more intense G peak was observed in the sequentially heat-treated room temperature as-implanted GC sample. The increased D and G peak intensities suggest defect annealing and increasing graphitic ordering within the GC implanted region [Ade20]. The Raman spectra of the GC samples implanted at higher temperatures are not the same as the pristine Raman spectrum after annealing at the highest temperature, 1200 °C. There is the possibility of having some radiation-induced damage retained in the GC substrates at this temperature. Studies have shown that heat treatment of implanted GC does not usually remove all radiation damage [Mc95], [Hla17], [Njo17], [Ism18], [Ade20].

More explicit information on the effects of sequential annealing on the GC samples (implanted at higher temperatures) was obtained by deconvoluting the original Raman spectra of these sequentially annealed GC samples (implanted at higher temperatures).

Figure 7.22 (a) and Figure 7.24 (a) show that annealing at the low and high regime temperatures caused the G Peak FWHM of the GC samples (implanted at higher temperatures) to get progressively smaller. The G peak bandwidth has values of 156.5, 150.7, and 137.5 cm after annealing the GC samples (as-implanted at 100, 150, and 200 °C) at the maximum annealing temperature, i.e., 700 °C (at the low-temperature regime), respectively (see Figure 7.22 (a)). The FWHM were 140.2, 129.3, and 116.3 cm for the samples implanted at 100, 150, and 200 °C, respectively and annealed at the highest temperature, 1200 C (at the high-temperature regime), as shown in Figure 7.24 (a)). Notably, none of the G peak FWHM values (for all samples implanted at higher temperatures) are comparable with the pristine value (68.1 cm), indicating their partial recovery after sequential heat treatment. However, comparing the ID/IG ratio, G peak positions and the FWHM of the samples implanted at higher temperatures and then annealed at the high-temperature regime, it can be mentioned that sequential annealing resulted in a stronger recovery of the GC sample implanted at 200 °C than the ones implanted at 100 and 150 °C. This result may imply that Se ion bombardment must have damaged the GC microstructures less at elevated implantation temperatures (other than the RT). This speculation is in accordance with the fact that defect annealing is enhanced in systems with less defect, as reported in heat-treated Cd ion-implanted GC substrate [Hla17] and Eu ion-implanted GC substrate [Ken18]. Heat treatment at the low and high-temperature regimes led to the shifting of the G peak to new positions, as shown in Figure 7.22 (b) and Figure 7.24 (b). After annealing the samples (implanted at higher temperatures) up to 1200 °C, the new G peak positions are close to the pristine G peak position, which is further evidence of the partial structural recovery of the GC substrates.

A progressive decrease in the ID/IG ratio was observed after annealing the GC samples (implanted at higher temperatures) at low and high-temperature regimes, as shown in Figure 7.22 (c) and Figure 7.24 (c). The decreasing order of the ID/IG ratio would imply some recovery within the implanted layer of the GC substrates. Also reported in Figure 7.22(d) and Figure 7.24 (d) is the corresponding average crystallite sizes of all the implants. Annealing led to crystal growth in all the GC samples (implanted at higher temperatures), which aligns with the crystal growth theory [Bur51]. The average crystallite sizes (L_a) ranged from 4.99 – 5.32 nm, 5.29 – 5.63 nm, and 5.26 – 5.76 nm after annealing as-implanted samples at higher temperatures (i.e., 100, 150, and 200 °C) at the low-temperature regime, respectively, as illustrated in Figure 7.22 (d). Annealing of the samples (implanted at higher temperatures) at the high-temperature regime caused the crystal sizes to grow

significantly. The crystal sizes ranged between 5.14 – 5.39 nm, 5.34 – 5.77 nm, and 5.35 – 5.94 nm after the samples implanted at high temperatures (100, 150 and 200 °C) were annealed at 1000, 1100, and 1200 °C, respectively (see Figure 7.24 (d)). As was initially suggested, the enhanced G peak intensities could imply larger crystal sizes. The enhanced G peak intensities justify the larger crystal sizes. The increased crystal sizes suggest that annealing led to the recrystallization (within the implanted region) of the GC substrates.

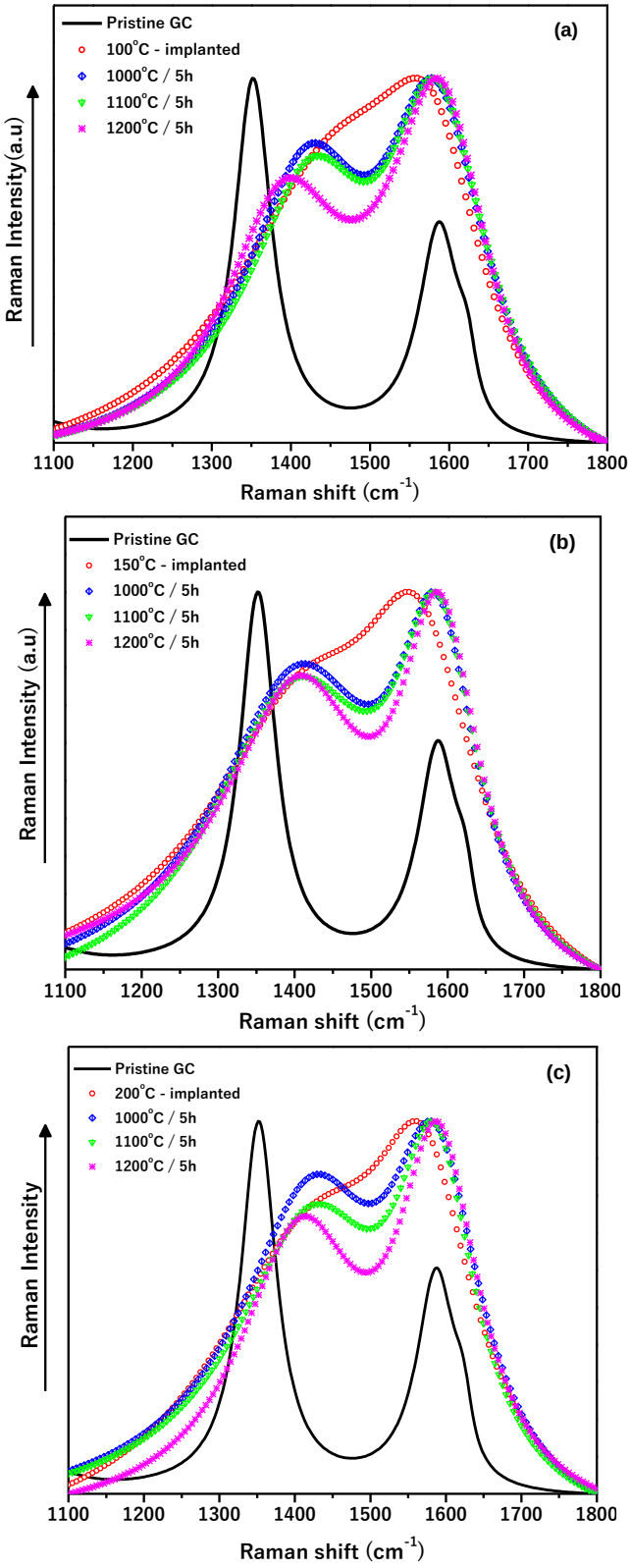

Figure 7.23. *Raman spectra of Se ions implanted in GC samples at (a) 100 ºC (b) 150 ºC and (c) 200 ºC after sequential annealing at the low-temperature regime (1000 – 1200 ºC) in steps of 100 ºC and 5 h annealing cycle.*

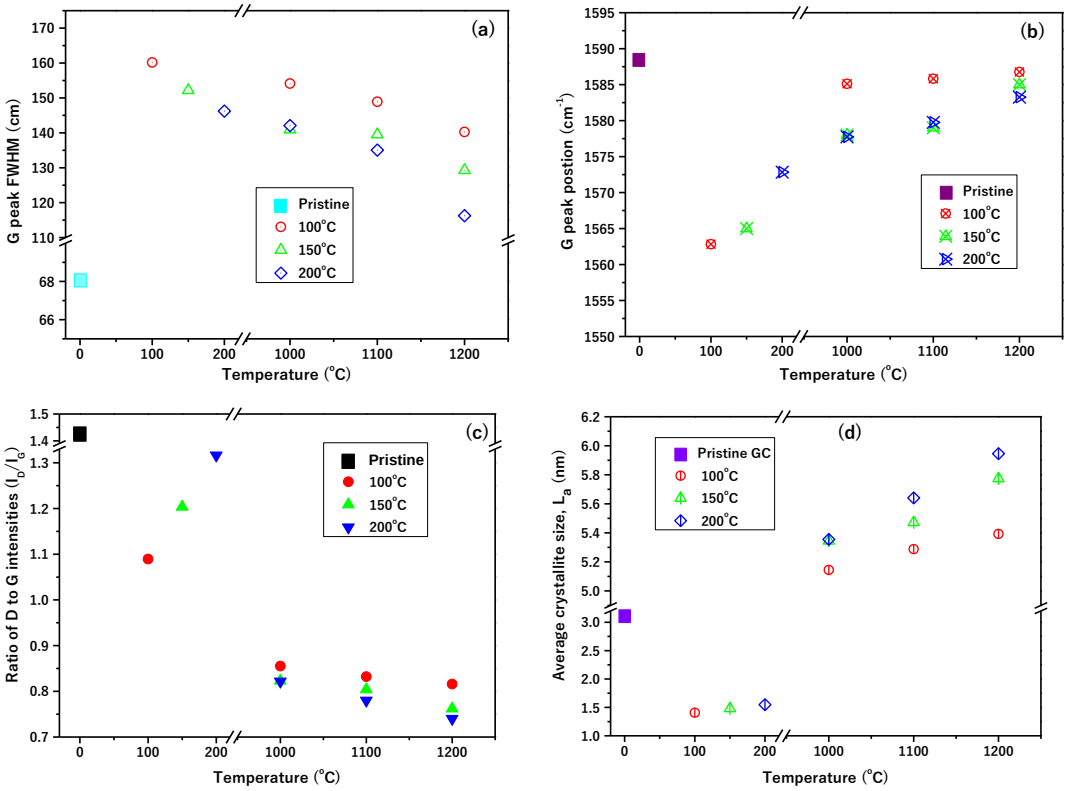

Figure 7.24*.(a) G peak bandwidth (FWHM), (b) G peak position (c) ID/IG ratio and (d) average crystallite size (La) of the Raman spectra of GC samples (implanted with Se ions at higher temperatures, i.e., 100, 150 and 200ºC), and after sequential annealing at the low-temperature regime (1000 – 1200 ºC) in steps of 100 ºC and 5h annealing cycle.*

7.5.3 Migration behaviour of selenium atoms in the GC samples (implanted at higher temperatures) after annealing – RBS and SIMS studies

The GC samples implanted at temperatures higher than RT (i.e., 100, 150 and 200 °C) were subjected to sequential annealing (at the low and high-temperature regimes). The migration behaviour of Se in the GC substrates was monitored by RBS and SIMS techniques. Figure 7.25 shows the RBS depth profiles of the GC samples (implanted at higher temperatures) and isochronally annealed at the low-temperature regime (300 – 700 °C). The selenium diffusion profiles after annealing the as-implanted samples (up to 600 °C) are comparable, indicating no diffusion of Se at these temperatures. However, the slight variations in the FWHM and peak positions (as seen in Figure **7.26**) are within the depth resolution of the RBS. The error (in the FWHM and peak position) has already been discussed in subsection 7.4.3. The Se profiles in all the GC samples (implanted at higher temperatures) were observed to have shifted after annealing at 700 °C. As mentioned under subsection 7.4.3, the out-diffusion of Se is the only reason

to justify the shift of the profile and no loss of Se was recorded up to 700 °C, as illustrated in

Figure **7.26**. The change in the Se profile at 700 °C is attributed to the systematic errors from the RBS. Systematic errors could be from the beam energy instability and inaccurate measurement geometry modification [Hna91].

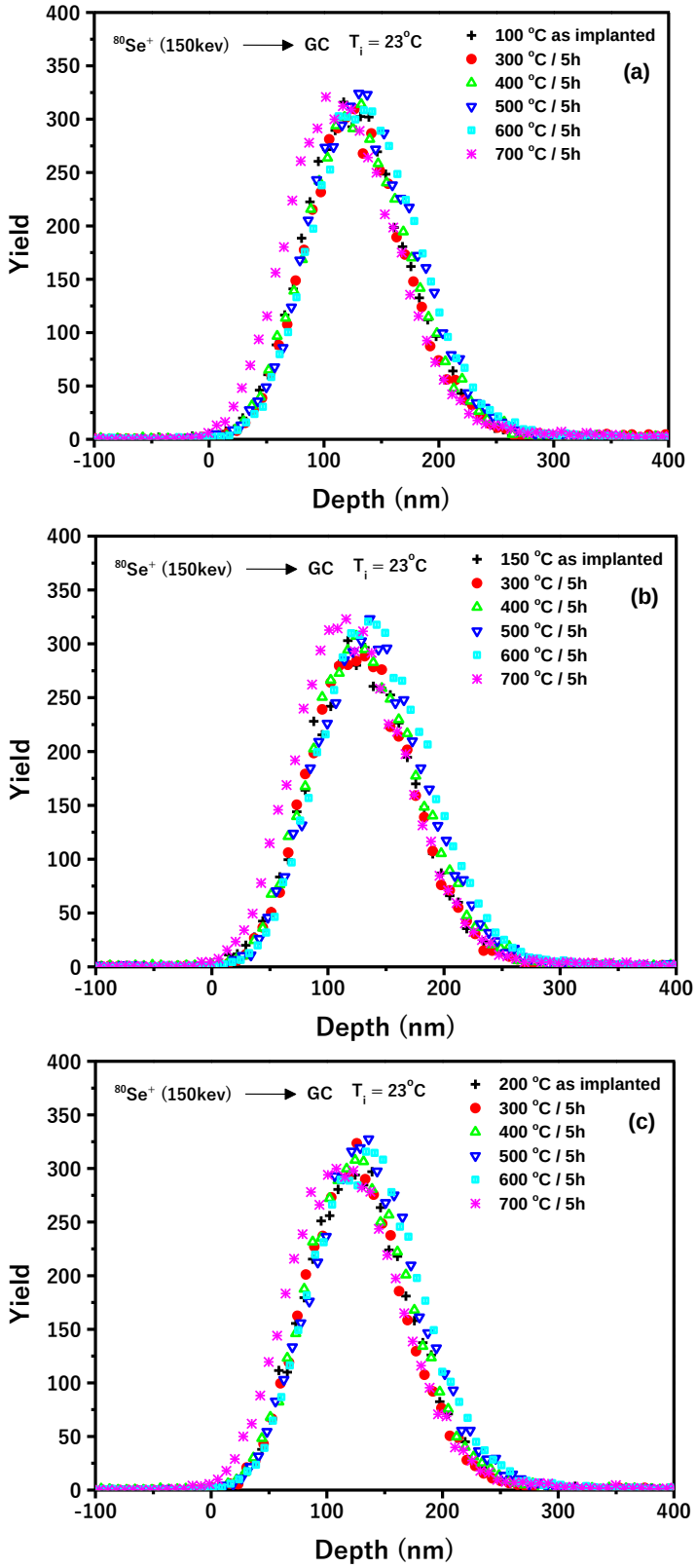

Figure 7.25. *Depth profiles of GC samples (implanted with Se ions at higher temperatures) and after sequential annealing in the low-temperature regime (300 – 700 °C) in steps of 100 °C for 5h annealing cycle.*

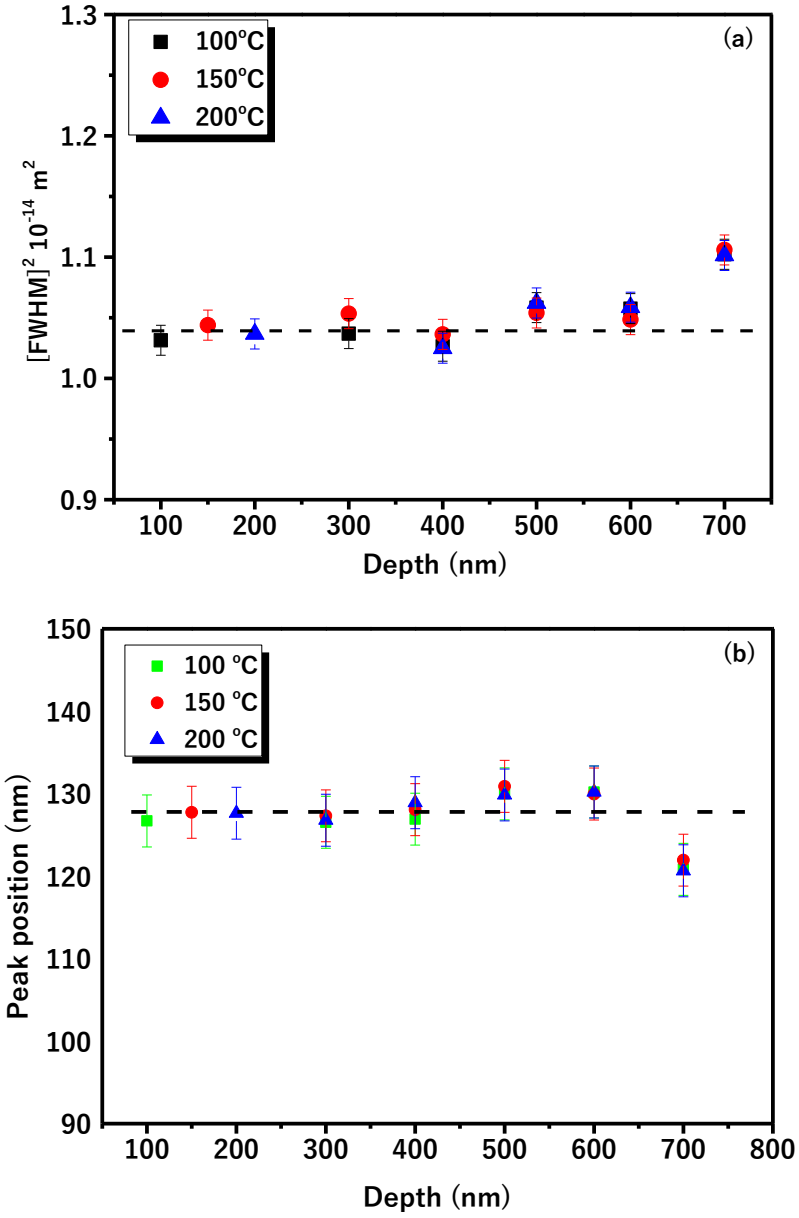

Figure 7.26.*(a) full width at half maximum and (b) peak position of GC samples (implanted with Se ions at higher temperatures) and after sequential annealing at the low-temperature regime (300–700 °C) in steps of 100 °C for 5h annealing cycle.*

The effect of sequential annealing at the high-temperature regime (1000 – 1200 °C in steps of 100 °C for 5 hours) on the migration behaviour of Se atoms in the GC samples (implanted at higher temperatures) was investigated by RBS, and the depth profiles are shown in Figure 7.27 (a-c). The ratio of retained Se is plotted in Figure 7.27 (d)

Figure 7.27 (a) shows the RBS depth profiles of the sample (implanted with Se ions at 100 °C then sequential annealed at 1000 to 1200 °C). Annealing this sample at 1000 °C resulted in the asymmetric broadening of the Se profile exhibiting a strong tailing (i.e.,

migration) towards the bulk of the GC substrate up to a depth of 400 nm. No loss of Se was recorded in this sample after annealing at 1000 °C. Also observed is the non-migration of Se towards the surface of the GC (implanted at 100 °C), which could be due to higher radiation damage in this region as compared with the bulk region of this sample (i.e., beyond the end of range). The Se profiles of the sample (implanted at 100 °C) and sequentially annealed at 1100 and 1200 °C are asymmetric and skewed more towards the surface, indicating enhanced migration of Se atoms towards the surface. However, the tail of these profiles extends to a depth of about 550 and 800 nm after sequential annealing at 1100 and 1200 °C, respectively, as shown in Figure 7.27 (a). No significant loss of Se was recorded in this sample up to 1200 °C, which is due to no out-diffusion of Se atoms.

Figure 7.27 (b) shows the depth profile of the 150 °C Se implanted GC after sequential annealing at 1000, 1100, and 1200 °C. The Se profile asymmetrically broadened more towards the surface, accompanied by the emergence of a surface peak at 1000 °C. The surface peak indicates the accumulation/segregation of Se atoms at the surface without any loss of the Se atoms. The tail of the Se profile deeper into the bulk to about 400 nm, indicating fewer Se atoms migrated into the bulk of the GC substrate, was also observed. Annealing the 150 °C implanted GC sample at 1100 and 1200 °C caused the Se profiles to broaden asymmetrically towards the surface and tailing towards the bulk of the GC substrate. This observation is accompanied by no loss of Se at 1100 °C, and a loss of about 15% of Se atoms was recorded at 1200 °C. The loss of the Se atoms is attributed to its out-diffusion (see Figure 7.27 (d)). The evaporation of Se atoms into the vacuum during annealing can be linked to the loss of Se from the surface. The melting point of Se is 220 °C, which is significantly lower than the annealing temperature range of 1000 – 1200 °C. Also observed is that the Se profiles tailed strongly towards the bulk at a depth of about 500 – 650 nm after annealing at 1000 – 1200 °C, indicating that Se atoms had migrated into the bulk of the GC.

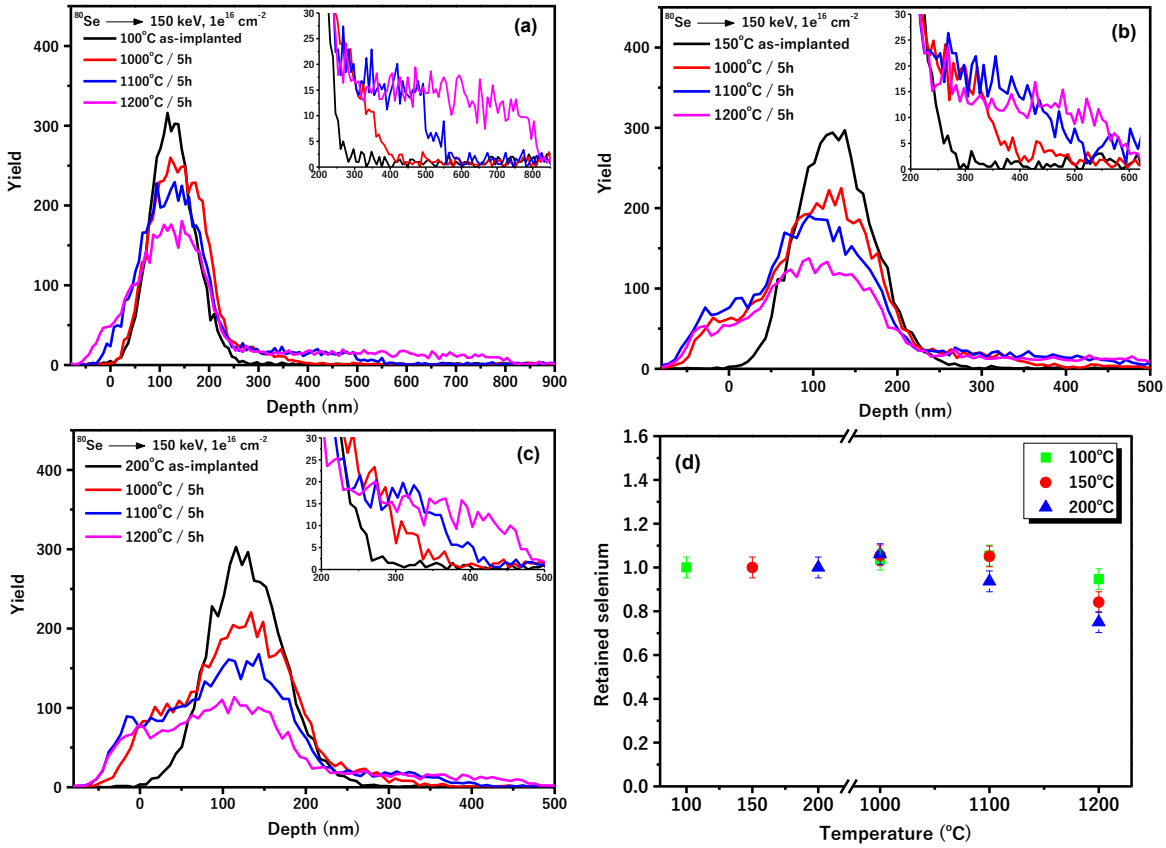

***Figure 7.27**. RBS depth profiles of GC samples implanted with Se ions at (a) 100 °C (b) 150 °C (d) 200 °C and their (d) corresponding retained ratio after sequential annealing at the high-temperature regime (1000 – 1200 ºC) in steps of 100 °C for 5h annealing cycle.*

The effect of sequential annealing at 1000 to 1200 °C on the migration behaviour of Se atoms in the GC sample implanted at 200 °C is shown in Figure 7.27 (c). Annealing the 200 °C implanted GC at 1000 – 1200 °C resulted in similar asymmetric Se profiles as those of the 150 °C implanted GC annealed in the same temperature range. However, the surface peaks in the annealed GC sample (implanted at 200 °C) after sequential annealing at 1000, 1100, and 1200 °C were more pronounced when compared with the GC samples implanted at 150 °C and annealed in the same temperature range (see Figure 7.27 (c)). The pronounced surface peak could suggest two things: more Se atoms are accumulating (segregating) at the surface, and fewer Se atoms are migrating into the bulk of the GC. This presumption may be valid because the tails of the Se profile extended to depths of about 390, 430, and 500 nm after sequential annealing at 1000, 1100 and 1200 °C, respectively. While no significant loss of Se was recorded in the sample implanted at 200 °C then sequentially annealed up to 1100 °C, a loss of about 25% Se was recorded after annealing at 1200 °C (as can be seen in Figure 7.27 (d)). The 25% loss of Se atoms can be linked with the enhanced surface segregation of Se atoms, which led to the eventual out-diffusion.

A new set of the GC implanted samples (implanted at higher temperatures) were isochronally annealed in the same high-temperature range (i.e., at 1000 – 1200 °C in steps of 100 °C for 5 hours of annealing duration time at each temperature). The migration behaviour of Se atoms was studied in these isochronally annealed GC samples by SIMS technique to study the effect of radiation damage on the migration behaviour of Se atoms in the GC substrate. The SIMS depth profiles are shown in Figure 7.28 (a – c), while the ratio of retained Se is in Figure 7.28 (d).

After subjecting the sample implanted (at 100 °C) to isochronal annealing at 1000 °C, the Se profile broadens asymmetrically and tails to about 320 nm, as shown in Figure 7.28 (a). No loss of Se accompanied this observation at this temperature. Increasing the annealing temperature to 1100 and 1200 °C caused the Se profiles to become increasingly asymmetric towards the surface, accompanied by tailings towards the bulk to depths of about 339 and 385 nm, respectively. These depth profiles at temperatures 1100 and 1200 °C indicate an enhanced migration of Se atoms to the surface and bulk. The migration towards the surface of the Se atoms was accompanied by a loss of about 10% and 20% after annealing the GC sample implanted at 100 °C at 1100 and 1200 °C, respectively (as shown in Figure 7.28 (d)). The Se profiles of the GC sample (implanted at 100 °C) and isochronally annealed at 1000 – 1200 °C (as in Figure 7.28 (a)) is somewhat similar to the Se profiles obtained from sequentially annealed GC sample (implanted at 100 °C) (in Figure 7.27 (a)) in the same temperature range. However, some differences were noted in these profiles. The tailing (towards the bulk) in the sequentially annealed Se profiles is more pronounced than the sequentially annealed ones. This could imply fewer Se atoms in the bulk of the isochronally annealed samples compared to the sequentially annealed ones. This answers why no loss of Se atoms was recorded in the GC sample implanted at 100 °C and sequentially annealed at 1000 – 1200 °C, while some losses were recorded in the sample implanted at 100 °C and isochronally annealed in the same temperature range.

After the GC samples implanted at 150 °C were isochronally annealed at 1000 °C, the Se profiles became asymmetric towards the surface. A peak at around 30 nm (below the surface) emerged, as shown in Figure 7.28 (b). As it was mentioned above, the surface peak denotes the concentration or segregation of Se atoms at the surface.

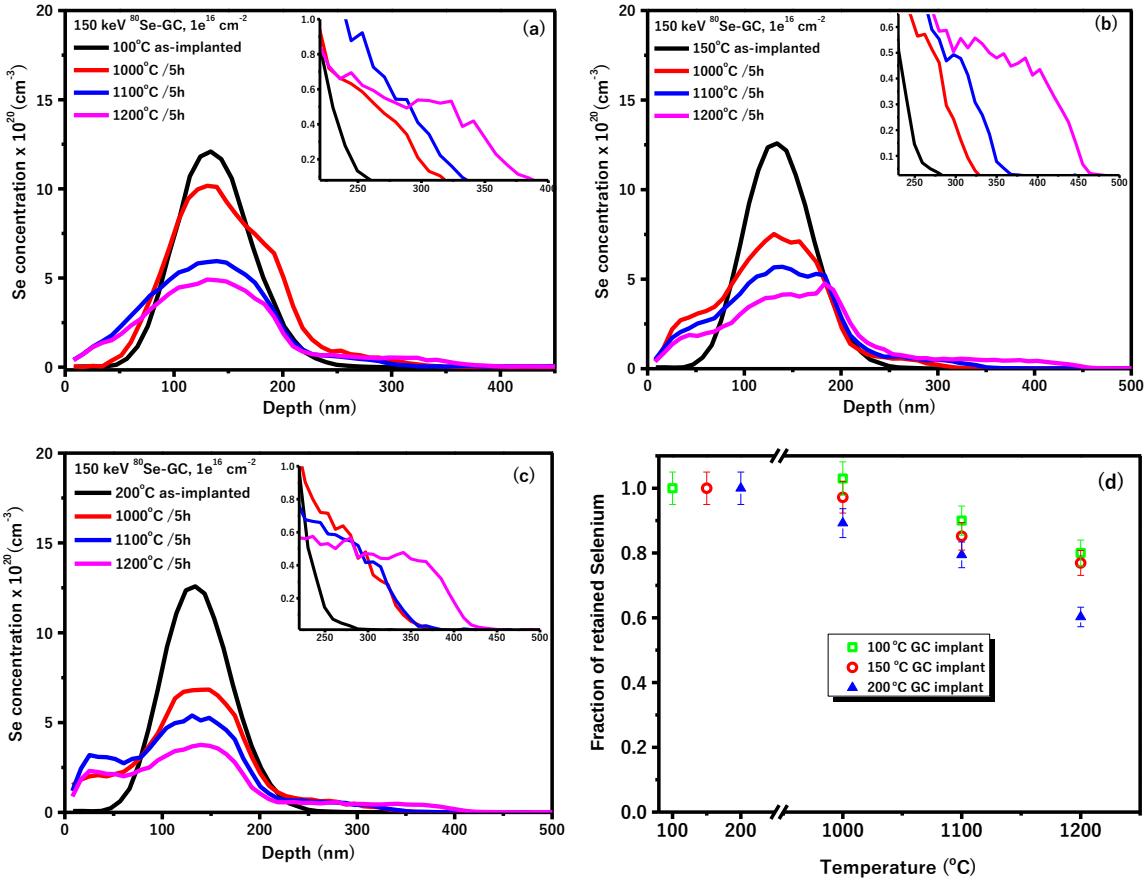

Figure 7.28 *(a-c) SIMS depth profiles of GC samples implanted with Se ions at (a) 100 °C (b) 150 °C and (d) 200 °C and their (d) corresponding retained ratio after isochronal annealing at the high-temperature regime (1000 – 1200 ºC) in steps of 100 °C for 5h annealing cycle.*

Accompanied by the surface segregation is the tailing of the Se profiles towards the bulk to about 328 nm. Further annealing of the 150 °C implanted GC sample at 1100 and 1200 °C caused the profiles to be more asymmetrical toward the surface and the profile tails are at 370 and 465 nm. This indicates that more Se atoms had moved into the bulk of the GC. This observation is accompanied by the out-diffusion-related loss of 15% and 23% of the Se atoms at 1100 and 1200 °C, respectively (see Figure 7.28 (d)). The Se depth profiles of the GC sample (implanted at 150 °C then isochronally annealed at 1000 – 1200 °C) are similar to those obtained for the GC sample implanted at 150 °C and then sequentially annealed in the same temperature range. A few differences were also noted in these two profiles (obtained from sequential and isochronal annealing). Longer tailings were observed in the Se profiles of the sequentially annealed GC sample (implanted at 150 °C) than in the profiles of the isochronally annealed GC sample (implanted at 150 °C). This means there are fewer Se atoms in the bulk of the isochronally annealed samples as compared to the sequentially annealed ones. Another implication of the longer tailing of the Se profile is that

more Se atoms are retained in the isochronally annealed GC sample (implanted at 150 °C), shown in Figure 7.28 (d) above.

Figure 7.28 (c) shows the depth profiles of the GC samples implanted at 200 °C and isochronally annealed between 1000 and 1200 °C in steps of 100 °C for 5 h. The Se profiles are similar to the ones of the GC sample (implanted at 150 °C) and isochronally annealed in the same temperature range, implying that the Se atoms exhibited a similar migration behaviour in the GC substrate implanted at 200 °C. However, the surface peak in the 200 °C profile is more enhanced than the 150 °C profile, indicating stronger segregation of Se atoms at the surface of this GC substrate. It was also observed that the surface peaks in the sample (implanted at 200 °C then isochronally annealed at the high-temperature regime) are more pronounced than in the sample implanted at 200 °C and sequentially annealed at the same temperature range). As seen in Figure 7.28 (c), the profiles of the sample implanted at 200 °C and isochronally annealed at 1000, 1100, and 1200 °C had longer tails towards the bulk at depths 368, 375, and 400 nm, respectively, indicating Se atoms migration into the bulk of the GC substrate. The increasingly enhanced surface segregation may have resulted in the fewer Se atoms migration into the bulk of this 200 °C sample and the accompanied continuous loss of Se atoms at the surface. The percentage of Se atoms lost in the sample implanted at 200 °C then isochronally annealed at 1000, 1100, and 1200 °C was calculated to be 11, 31, and 40%, respectively (see Figure 7.28 (d)).

A general explanation can be given for the above observations on the migration behaviour of Se atoms towards the bulk of the GC (due to the sequential and isochronal annealing). From this point onward, annealing would mean sequential or isochronal, except when otherwise stated. Annealing caused the Se atoms to exhibit a similar migration behaviour into the bulk of all the GC samples (implanted at higher temperatures). This can be attributed to the annealing of radiation damage at the end-of-range region (i.e., at 240 nm) in all the annealed GC samples (as in Figure 7.2). The resulting Se profiles after annealing the GC samples (implanted at higher temperatures) in Figure 7.27 (a-c) and Figure 7.28 (a-c) show that the migration of Se atoms started towards the region with the minimum damage and progressed to the moderate and high radiation damage region, respectively. This type of migration behaviour exhibited by the Se atoms in the bulk of all the (after annealing) can be explained in terms of trapping and de-trapping of the Se atoms by defects induced during implantation. It can be presumed that the migration of the Se atoms deeper into the bulk (of the annealed samples) occurred following the defect annealing in the less

radiation damage region. However, the trapping of most of the Se atoms in the high radiation damage region restricted its migration towards the surface, especially in the annealed GC implanted sample. A typical pristine GC contains several nanopores, which will become fewer after ion implantation. The implantation defects could have trapped the ions inside the pores. The average pore size in a typical pristine GC range between 0.3 and 0.5 nm [Pie93] is large enough to conveniently trap the Se atom (which has an atomic radius of 0.19 nm) [Odu18]. The large projected range straggling of the as-implanted depth profiles (in Table 7.1) proves that Se atoms are well-trapped by the implantation defects.

Similarly, the migration of Se atoms towards the surface in the annealed GC samples (implanted at higher temperatures) occurred after the radiation damage had been annealed out. Again, annealing would still mean sequential or isochronal, except when otherwise stated. The migration behaviour of the Se atoms towards the surface in all the annealed GC samples (implanted at higher temperatures) is different despite showing similar ion distribution at implantation and subjecting them to annealing in the same temperature range (i.e., 1000 – 1200 °C). For example, the migration of Se atoms toward the surface occurred after annealing the 100 °C implanted GC at 1100 °C (as seen in Figure 7.27 (a) and Figure 7.28 (a)). In contrast, the migration of the Se atoms towards the surface in the 150 and 200 °C as-implanted GC sample starts at 1000 °C (Figure 7.27 (b-c) and Figure 7.28 (b-c)). In addition, the segregation of Se atoms occurred at the surface of the annealed 150 and 200 °C as-implanted GC samples, and no such segregation occurred after annealing the 100 °C as-implanted GC samples in the same temperature range (see Figure 7.27 (a-c) and Figure 7.28 (a-c)).

The differences in the migration behaviour of Se atoms towards the surface of the GC samples implanted at higher temperatures (after annealing) suggest the initial effect of ions implantation on the GC substrates. Typically, radiation damage depends on the implantation temperatures, and due to dynamic annealing, more damage is expected in the sample implanted at lower temperatures than those performed at higher temperatures. The Raman spectra of the GC samples (implanted at higher temperatures) indicated less damage for the GC sample implanted at 100 °C than the ones implanted at 150 and 200 °C, respectively. The different migration behaviour of Se atoms toward the surface in both annealed as-implanted GC samples can be related to the trapping and de-trapping of the Se atoms in different amounts of implantation-induced defects in these samples. This was demonstrated by the different amounts of retained Se in these samples after each annealing step, as shown in Figure 7.27 (d) and Figure 7.28 (d). It is important to mention again that

the loss of Se in the 150 and 200 °C GC implanted samples can be related to the sublimation of Se atoms (i.e., the surface-segregated atoms) into the vacuum during annealing. The melting point of Se, which is 220 °C, is less than the high-temperature range, 1000 – 1200 °C.

Overall, comparing the effect of sequential annealing and isochronal annealing on the Se depth profile of the GC samples (implanted at higher temperatures), one would see that the two different annealing procedures/methods produced profiles with many similarities and minor differences. For instance, the tailing of the Se profiles (which indicates the migration of Se atoms in the bulk of the GC) in the isochronally annealed GC samples (implanted at higher temperatures) is smaller as compared to the sequentially annealed ones (illustrated shown Figure 7.27 and Figure 7.28). This justifies why more Se atoms were lost in the isochronally annealed samples. The differences in these depth profiles can be related to the different microstructures possessed by these two categories of samples (i.e., the isochronally and sequentially annealed GC samples implanted at higher temperatures). The prior heat treatments would significantly affect the substrate's microstructure of the sequentially annealed samples more than the isochronally annealed ones, affecting Se atoms' migration behaviour towards the bulk of the GC.

The migration behaviour of Se in GC compared with other previously studied fission product surrogates [Lan12], [Odu16], [Ism21] does not show a similar migration pattern (by the depth profiles) despite the segregation and bulk migration exhibited by these elements. For example, in Langa et al. work [Lan12], Cs ions were implanted into GC at RT, 350 and 600 °C at a fluence of 2×10^{16} cm^2, and these samples were isochronally annealed from 200 to 600 °C, in steps of 100 °C for 1 hour. The authors reported radiation-induced diffusion of the Cs atoms in the sample implanted at RT [Lan12]. The authors identified surface peaks in the 350 and 600 °C implanted samples, which indicates the segregation of Cs atoms at the surface. Annealing the RT sample caused the surface segregation of the Cs atoms accompanied by their significant loss at 500 °C, and 28% of Cs were retained after annealing at 600 °C.

Odutemowo et al. [Odu16] investigated the role of annealing on Sr ion-implanted in GC at RT. In their study, Fickian diffusion of Sr was observed after annealing in the temperature range of 450 – 560 °C in the 96th minute of the in-situ RBS analysis of the Sr depth profiles [Odu16]. After annealing another as-implanted sample at 650 °C for longer annealing times, the Sr atoms further diffused and segregated at the surface of the GC substrate without any loss of the Sr atoms. In another study carried out by Ismail et al.

[Ism21], the influence of annealing and swift heavy ion irradiation on the migration behaviour of Xe implanted in GC at room temperature was investigated. The Xe atoms migrated deeper into the bulk and towards the surface, accompanied by the segregation of a considerable amount of Xe atoms towards the surface of the as-implanted sample only and the as-implanted then irradiated sample after subjecting the samples to annealing at temperatures ranging from 1000 to 1300 °C. One of the key findings in their study is that the swift heavy ion irradiation assisted in trapping the Xe atoms within the GC substrates. This results in more Xe atoms retained in the as-implanted than irradiated GC sample (~23%) compared to the as-implanted GC sample only (~40 %) after annealing both sample types at 1400 °C. Also, the magnitude of the segregated atoms (close to the surface) decreased as a function of increasing annealing temperatures, accompanied by a stronger migration of the more Xe atoms into the undamaged bulk of the GC substrate.

The above shows that the migration behaviour of these other fission elements (Cs, Sr and Xe) shows a similar migration pattern (by the depth profiles) compared with Se results investigated in this study. However, the differences between this study and these other studies were observed in surface segregation and migration of the (implants) into the bulk of the GC substrates recorded at different annealing temperatures. This difference can be related to many factors, such as the type of implant (i.e., fission element), implantation temperature, and fluence. All these factors (during implantation) result in different levels of radiation damage and defect induced in different materials (with different microstructures). The variations in the microstructures of the initially implanted GC substrates following the annealing will otherwise influence the migration behaviour of the initially implanted fission components [Mal21]. Ions of heavier mass produce more lattice distortions (such as localized amorphous regions) at the end of the implantation range [Dre13]. A completely amorphised layer can be produced when the ion fluence exceeds a critical limit [Dre13]. Radiation damage to carbon materials increases with implantation fluence [McC94], [Buk14].

Another explanation to account for the variation in the migration pattern of Se and these other fission elements discussed above is the synergistic effect of an array of fission elements in the host material. The radioactivity of nuclear wastes produces many fission elements, which can coexist, resulting in a synergistic effect.

References

[Bar01] N.P. Barradas. Rutherford backscattering analysis of thin films and superlattices with roughness. *J. Phys. D. Appl. Phys.* **34,** (2001), 2109 – 2115.

[Bar02] N.P. Barradas, K. Arstila, G. Battistig, M. Bianconi, N. Dytlewski, C. Jeynes, E. Kótai, G. Lulli, M. Mayer, E. Rauhala, E. Szilágyi & M. Thompson. International Atomic Energy Agency intercomparison of ion beam analysis software. *Nucl. Inst. & Methods in Phys. Res. B.* **262,** (2007), 281 – 303.

[Buk14] S.S. Bukalov, L.A. Leites, A.I. Sorokin & A.S. Kotosonov. Structural changes in industrial glassy carbon as a function of heat treatment temperature according to Raman spectroscopy and X-ray diffraction data, *Nano Phys. Chem. Math.* **5**, (2014), 186 – 191.

[Bur51] W.K. Burton, N. Cabrera & F.C. Frank. The growth of crystals and the equilibrium structure of their surfaces. *Philos. Trans. R. Soc. A*. **243,** (1951), 299 – 358.

[Dre13] M.S. Dresselhaus, G. Dresselhaus & P.C. Eklund. Science of Fullerenes and Carbon Nanotubes. *J. Am. Chem. Soc.* **118,** (1996), 8987.

[Fer00] A.C. Ferrari & J. Robertson. Interpretation of Raman spectra of disordered and amorphous carbon. *Phys. Rev. B* **61,** (2000), 14095 – 14107.

[Fer07] A.C. Ferrari. Raman spectroscopy of graphene and graphite: disorder, electron- phonon coupling, doping and nonadiabatic effects, *Solid State Commun.* **143,** (2007), 47 – 57.

[Ful76] D. Fuller, J.S. Colligon & J.S.Williams: The application of correlated SIMS and RBS techniques to the measurement of ion implanted range profiles. *Surf. Sci*. **54**, (1976), 647 – 658.

[Har04] P.J.F. Harris. Fullerene-related structure of commercial glassy carbons, *Philos. Mag. A***. 84,** (2004), 3159 – 3167,.

[Hla17] T.T. Hlatshwayo, L.D. Sebitla, E.G. Njoroge, M. Mlambo & J.B. Malherbe. Annealing effects on the migration of ion-implanted cadmium in glassy carbon, *Nucl. Inst. & Methods in Phys. Res. B.* **395,** (2017), 34 – 38.

[Hna91] J.K. Hnatowicz & V. Havrhek. Statistical and systematical errors in RBS depth profiling of implanted atoms, *Nucl. Inst. & Methods in Phys. Res. B.* **35,** (1991), 337 – 341.

[Ism18] M.Y.A. Ismail, J.B. Malherbe, O.S. Odutemowo, E.G. Njoroge, T.T. Hlatshwayo, M. Mlambo & E. Wendler. Investigating the effect of heat treatment on the diffusion behaviour of xenon implanted in glassy carbon. *Vacuum*. **149**, (2018), 74 – 78.

[Ism21] M.Y.A. Ismail, Z.A.Y. Abdalla, E.G. Njoroge, O.S. Odutemowo & T.T. Hlatshwayo. Effect of high temperature annealing and SHI irradiation on the

migration behaviour of Xe implanted into glassy carbon. *Nucl. Inst. & Methods in Phys. Res. B.* **489,** (2021), 11 – 19.

[Ken18] M.F. Kenari, T.T. Hlatshwayo, O.S. Odutemowo, T.M. Mohlala, E. Wendler & J.B. Malherbe. Migration Behavior of 100 °C Europium Ion Implantation in Glassy Carbon. *22nd International Conference on Ion Implantation Technology (IIT)*, (2018), 377 – 380.

[Kin55] G.H. Kinchin & R.S. Pease. The Displacement of Atoms in Solids by Radiation. *Rep. Prog. Phys.* **18 (1),** (1955), 1 – 51.

[Kos08] O. Koskelo, U. Köster, I. Riihimäki & J. Räisänen. Migration kinetics of ion-implanted beryllium in glassy carbon. *Diam. Relat. Mater.* **17**, (2008), 1991–1993.

[Lan12] D.F. Langa, N.G. Van Der Berg, E. Friedland, J.B. Malherbe, A.J. Botha, P. Chakraborty, E. Wendler & W. Wesch. Heat treatment of glassy carbon implanted with cesium at room and high temperatures. *Nucl. Inst. & Methods in Phys. Res., B.* **273,** (2012), 68 – 71.

[Lav08] V. Lavrentiev, J. Vacik & H. Naramoto, Structural phenomena in glassy carbon induced by cobalt ion implantation. *Appl. Phys. Mater. Sci. Process.* **92,** (2008), 673 – 680.

[Lor16] J. Lorinčík, D. Veselá, S. Vytykáčová, B. Švecová, P. Nekvindová, A. Macková, R. Mikšová, P. Malinský & R. Böttger, Comparison of SIMS and RBS for depth profiling of silica glasses implanted with metal ions, *J. Vac. Sci. Technol. B – Nanotechnol. Microelectron. Mater. Process. Meas. & Phenom.* **34**, (2016), 1291 – 1294.

[Mad20] M.J. Madito, M.Y.A. Ismail, T.T. Hlatshwayo & C.B. Mtshali. The nature of surface defects in Xe ion-implanted glassy carbon annealed at high temperatures: Raman spectroscopy analysis. *Appl. Surf. Sci.* **506,** (2020), 145001.

[Mal17] J.B. Malherbe, P.A. Selyshchev, O.S. Odutemowo, C.C. Theron, E.G. Njoroge, D.F. Langa & T.T. Hlatshwayo. Diffusion of a mono-energetic implanted species with a Gaussian profile. *Nucl. Inst. & Methods in Phys. Res. B.* **406,** (2017), 708 – 713.

[Mal21] J.B. Malherbe, O.S. Odutemowo, C.C. Theron & E. Wendler. Diffusion of strontium implanted in glassy carbon. *Proc. R. Soc. A* **477**, (2021), 20200797.

[Matt99] M.J. Matthews, M.A. Pimenta, G. Dresselhaus, M.S. Dresselhaus & M. Endo. Origin of dispersive effects of the Raman d band in carbon materials, *Phys. Rev. B - Condens. Matter Mater. Phys.* **59**, (1999), 6585 – 6588.

[McK16] A.J. McKenna, T. Trevethan, C.D. Latham, P.J. Young & M.I. Heggie. Threshold displacement energy and damage function in graphite from molecular dynamics. *Carbon.* **99,** (2016), 71 – 78.

[McC94] D.G. McCulloch, S. Prawer & A. Hoffman. Structural investigation of xenon-ion-beam-irradiated glassy carbon. *Phys. Rev. B.* **50,** (1994), 5905 – 5917.

[McC95] D.G. McCulloch & S. Prawer. The effect of annealing and implantation temperature on the structure of C ion - beam - irradiated glassy carbon, *J. Appl. Phys.* **78,** (1995), 3040 – 3047.

[Njo17] E.G. Njoroge, L.D. Sebitla, C.C. Theron, M. Mlambo, T.T. Hlatshwayo, O.S. Odutemowo, V.A. Skuratov, E. Wendler & J.B. Malherbe. Structural modification of indium implanted glassy carbon by thermal annealing and SHI irradiation, *Vacuum*. **144**, (2017), 63 – 71.

[Odu16] O.S. Odutemowo, J.B. Malherbe, C.C. Theron, E.G. Njoroge & E. Wendler. In-situ RBS studies of strontium implanted glassy carbon, *Vacuum*. **126,** (2016), 101 – 105.

[Odu16b] O.S. Odutemowo, J.B. Malherbe, L. Prinsloo, D.F. Langa & E. Wendler. High temperature annealing studies of strontium ion implanted glassy carbon, *Nucl. Inst. & Methods in Phys. Res. B.* **371,** (2016), 332 – 335.

[Odu18] O.S. Odutemowo, J.B. Malherbe, L.C. Prinsloo, E.G. Njoroge, R. Erasmus, E. Wendler, A. Undisz & M. Rettenmayr. Structural and surface changes in glassy carbon due to strontium implantation and heat treatment. *J. Nucl. Mat.* **498,** (2018), 103 – 116.

[Odu20] O.S. Odutemowo, M.S. Dhlamini, E. Wendler, D.F. Langa, M.Y.A. Ismail & J. B. Malherbe. Effect of heat treatment on the migration behaviour of Sr and Ag CO-implanted in glassy carbon. *Vacuum*, **171,** (2020), 109027.

[Pie93] H.O. Pierson. Handbook of Carbon, Graphite, Diamond and Fullerenes: Properties, Processing and Applications. Noyes Publications, New Jersey, (1993), 244 – 371.

[Rob02] J. Robertson. Diamond-like amorphous carbon. *Mat Sci & Eng. R.* **37,** (2002), 129 – 281.

[Sch73] F. Schulz, K. Wittmaack & J. Maul. Implications in the use of secondary ion mass spectrometry to investigate impurity concentration profiles in solids. *Rad. Eff.* **18**, (1973), 211 – 215.

[Shi19] T.B. Shiell, S. Wong, W. Yang, C.A. Tanner, B. Haberl, R.G. Elliman, D.R. McKenzie, D.G. McCulloch & J.E. Bradby. The composition, structure and properties of four different glassy carbons. *J. Non-Crystalline Solids*, **522**, (2019), 119561.

[Tui70] F. Tuinstra & J.L. Koenig. Raman spectrum of graphite. *J. Chem. Phys*. **53,** (1970), 1126 – 1130.

[Tak85] K. Takahashi, K. Yoshida & M. Iwaki. Effect of ion implantation on electrochemical and surface properties of glassy carbon. *Nucl. Inst. & Methods in Phys. Res., B.* **7 – 8,** (1985), 526 – 529.

[Tsa74] J.C.C. Tsai & J.M. Morabito. The mechanism of simultaneous implantation and sputtering by high energy oxygen ions during secondary ion mass spectrometry (SIMS) analysis. *Surf. Sci.* **44**, (1974), 247 – 252.

[Zie77] J.F. Ziegler. The Stopping and Ranges of Ions in Matter, Pergamon Press, New York (1977).

[Zin80] E. Zinner. Depth Profiling by Secondary Ion Mass Spectrometry, *J. Scann Mic*. **3**(2), (1980), 57 – 78.

Chapter 8

Conclusions and future studies

The application of GC as a nuclear waste storage container material was drawn from some of its exceptional properties, which include high resistance against radiation damage, chemical attack resistance and its ability to restrict the diffusion of radiologically important fission elements such as selenium (Se). The effect of Se ions implantation and post-implantation annealing on the migration behaviour of Se and the microstructure of GC substrates (after Se ions implantation and annealing) was investigated in this study.

Se ions of 150 keV were implanted into GC at room temperature (RT), 100, 150 and 200 °C. Each implantation was done to a fluence of 1×10^{16} ions/cm^2. The as-received and as-implanted GC was characterized by Raman spectroscopy to compare the level of radiation damage with respect to the implantation temperatures. Some of the as-implanted samples (both RT and higher temperature implantations) were sequentially annealed under vacuum conditions at a low-temperature (300 – 900 °C) and high-temperature (1000 – 1200 °C) regimes for 5 h in steps of 100 °C. These sequentially annealed samples were studied by Raman spectroscopy and Rutherford backscattering spectrometry (RBS) for the microstructural changes in the GC substrates and migration behaviour of implanted Se atoms, respectively. To get more insight into the effect of radiation damage on the migration behaviour of Se ions implanted into GC, a new set of GC samples implanted at room temperature and higher temperature were isochronally annealed at 1000 – 1200 °C in steps of 100 °C for 5 h and were characterized by secondary ion mass spectroscopy (SIMS).

8.1 Pristine GC and implantation at room temperature (RT)

Se ion distribution in GC was simulated using Stopping and Range of Ions in Matter (SRIM) software and the resulting Se depth profile was compared with experiments (i.e., RBS and SIMS Se profiles). The experimental projected range(s) compares well with the calculation, within the 5% accuracy of the SRIM program. The BF-TEM micrograph of the pristine GC shows densely packed graphitic nanostructures surrounded by onion-like features. The onion-like features are identities of multilayered fullerenes. The TEM micrographs of the as-implanted sample showed that the Se implantation induces highly defective layers of relatively the same depth in GC samples implanted at room temperature and at 200 °C. The damaged layer in the room temperature implanted GC sample

corresponds to about 8.5 dpa, greater than the 0.2 critical dpa required to distort the GC structure.

The Raman spectrum of the pristine GC had two main peaks, the D and G peaks at around 1357 and 1588 cm^{-1}, respectively. These peaks are characteristics of a disordered carbon with sp^2 and sp^3 bonds. The D peak represents a disordered graphite mode linked to the A_{1g} breathing mode with vibrations near the K zone boundary. The G peak can be identified as the sp^2 carbon networks in graphite, which is linked to the Raman optical mode and the E_{2g} symmetry. By deconvoluting the Raman spectra of the pristine GC, it was possible to obtain information such as FWHM, ID/IG ratio and average crystallite size, L_a. The ID/IG ratio was calculated as 1.43 for the pristine and the average crystallite size (L_a) was estimated as 3.1 nm, indicating that GC is a nano-crystalline graphite.

The implantation of 150 keV Se ions (at a fluence of 1×10^{16} ions/cm^2) into the GC at room temperature caused the Raman D and G peaks to merge. This is an indication that the microstructure of the GC samples (implanted at room temperature) was damaged by Se ions implantation. After deconvoluting the Raman spectra of the sample implanted at room temperature, the G peak has shifted to a lower wavenumber, accompanied by the broadness of the G peak FWHM and a decrease in ID/IG intensity ratio. All these changes point to a highly defective GC microstructure. The calculated average crystallite size of room temperature implanted GC sample is 1.36 nm. This smaller value indicates that the Se ions implantation at high fluence partially destroyed the graphite crystallites within the implanted region of the GC.

The reappearance of Raman peaks in the GC sample implanted at room temperature was only observed after annealing at 500 °C. Hence, this temperature was considered a critical temperature where the defects within the implanted GC region became thermally activated and began to anneal out. Increasing the annealing temperature (in steps of 100 °C) resulted in continuous gradual defects removal in the sample implanted at room temperature. When compared with the pristine GC, the Raman spectra of the sample implanted at room temperature and annealed at 1200 °C showed an appreciable recovery of its microstructure but with some retained defects. This limited recovery after annealing the room temperature implanted sample at 1200 °C was due to the retained Se, as confirmed by RBS.

The RBS Se depth profiles of the sample (implanted at room temperature) and annealed sequentially at the low-temperature regime showed no notable diffusion of Se atoms in the GC substrate. Sequential annealing at the high-temperature regime caused the migration of Se atoms towards the surface of the GC substrate, accompanied by 5% and

32% loss of Se after annealing at 1100 and 1200 °C, respectively. Limited migration of Se towards the bulk was also observed at the high-temperature regime. Fresh GC samples (implanted at room temperature) were isochronally annealed at the same high-temperature regime and characterized by SIMS to get more insight into the role of radiation damage in the migration of Se in the GC substrates. The Se depth profiles (obtained by SIMS) were similar to the ones obtained by RBS, with minor differences. The differences in the RBS and SIMS profiles were attributed to the different microstructures possessed by these two samples (i.e., the sequentially and isochronally annealed samples). Generally, the migration behaviour exhibited by Se atoms in the bulk of the samples implanted at room temperature (after annealing) can be explained in terms of trapping and de-trapping of the Se atoms by defects induced during implantation. The high-temperature annealing caused the annealing of defects in the less radiation damage region, creating pathways for Se atoms to migrate deeper into the bulk of the RT as-implanted GC sample.

The diffusion coefficients of Se obtained in this study were compared with other previously studied atomic species in defective GC. Beryllium (Be) and indium (In) with a diffusion coefficient in the order ($\times 10^{-17}$ m^2s^{-1}) exhibited fast diffusion, cadmium (Cd) and strontium (Sr) ($\times 10^{-19}$ m^2s^{-1}) manifested with intermediate diffusion, while europium (Eu), silver (Ag) and selenium (Se) ($\times 10^{-20}$ m^2s^{-1}) are characterized by slow diffusion.

8.2 Higher implantation temperatures

Implantation of Se ions into GC at higher temperatures (100, 150 and 200 °C) resulted in the partial merging of D and G Raman characteristics of GC with broad peaks at around 1563 and 1573 cm^{-1}. The deconvolution of these Raman spectra revealed information about the differences in these spectra. For example, The G peak FWHM became broader after implantation at 100 °C and became narrower with increasing implantation temperatures in steps of 50 °C. A maximum G peak FWHM of 156.2 cm ((larger than 68.1 cm for the pristine GC) was recorded in the GC sample implanted at 200 °C. The G peak positions was also observed to have shifted to lower wavenumbers, from 1588 to 1563 cm^{-1} after implantation at 100 °C, to 1565 cm^{-1} at 150 °C and 1573 cm^{-1} at 200 °C. The ID/IG ratio calculated for these samples implanted at higher temperatures reduces with increasing implantation temperatures.

The merging of D and G peaks, coupled with the changes in the FWHM and downshifting of the G peak positions, indicate the damage of the near-surface region of the

GC due to Se ion implantations. By using the results of the G peak FWHM, G peak position, and the ID/IG, the level of disorder in these GC samples implanted with Se ions at higher temperatures can be ranked – the one implanted at 100 °C having the most disorder, followed by the ones implanted at 150 and 200 °C, respectively. The overall comparison of the samples implanted at higher temperatures with those implanted at room temperature shows that the sample has more disorder and is more structurally damaged.

The sequential heat treatment of the samples (implanted at the higher implantation temperatures) at the low-temperature regime resulted in the emergence of the D and G peaks, which were only slightly distinguishable. This observation was due to the retained defects initially retained by the microstructures of these as-implanted samples. The D and G peaks became more identifiable and distinguishable after annealing at the high-temperature regime, indicating lesser defective structures and graphitic ordering within the implanted region of the GC. A notable feature in the Raman spectra of these GC samples (implanted at higher temperatures) and then annealed in the high-temperature regime is that the G peak is more pronounced than the D peaks (for all the samples implanted at higher temperatures). Also, the G peak of these samples was more enhanced than the pristine GC. This intense G peak could symbolize a more graphitizing structure with features of larger crystals (crystallite sizes). Another reason for the pronounced G peak is the possibility of having some radiation-induced damage retained in the GC substrates.

The depth profiles of the samples implanted with Se ions at higher temperatures showed no broadening after annealing at the lower annealing temperature regime (300 – 700 °C), indicating no detectable migration of Se atoms in the GC substrates. Sequential annealing at the high-temperature regime (1000 – 1200 °C in steps of 100 °C for 5 hours) caused the Se depth profiles (of all the samples implanted at higher implantation temperatures) to broaden asymmetrically. This observation comes with some clear differences in the Se migration patterns exhibited by these samples implanted at higher implantation temperatures (i.e., 100, 150 and 200 °C). For example, the Se profile of the sample implanted at 100 °C broadens asymmetrically towards the bulk region after annealing at 1000 °C and the profile further broadens asymmetrically towards the surface (without any loss of Se atoms) after annealing at 1100 and 1200 °C. The broadening of the Se profile is an indication of the migration of Se atoms. Asymmetric Se profiles broadening towards the surface and tailing in the bulk region was also observed in the samples implanted at 150 and 200 °C after annealing them between 1000 and 1200 °C. This observation was accompanied by a peak at the surface, which became more pronounced

with increasing annealing temperature in the samples implanted at 150 and 200 °C. The surface peak indicates the segregation of Se atoms which led to its eventual out-diffusion at the surface. Notably, more Se atoms were lost at the surface of the sample implanted at 200 °C and then annealed at the high-temperature regime than the one implanted at 150 °C annealed at the same temperature range. This was due to the pronounced surface peak when this sample (implanted at 200 °C) was annealed.

For further clarification on the migration behaviour of Se atoms in the GC, a fresh set of samples (implanted at higher implantation temperature) was isochronally annealed and characterized by secondary ion mass spectroscopy (SIMS). Because of isochronal annealing, it was also easy to use these SIMS results to study and compare the effect of radiation damage on the migration behaviour of Se in the as-implanted GC substrates. The obtained Se depth profiles indicated a similar migration pattern as in the sequentially annealed GC samples (implanted at higher implantation temperature). Although, a few differences were noted in these two sample types (i.e., the sequentially and isochronally annealed samples). For example, the tailing of these Se profiles (which indicates Se atoms migration in the bulk region of the GC substrates) in the isochronally annealed GC samples (implanted at higher temperatures) is smaller as compared with the sequentially annealed ones. This is why more Se atoms were recorded lost in the isochronally annealed samples. Moreso, the samples' microstructures resulting from both annealing types would be different, which is why their depth profiles also varied.

8.3 Future studies

- One of the initial concerns in this research was the concentration of migrated Se atoms in the bulk of the GC, as this will not be good for using GC as a potential nuclear waste storage container. With a minute concentration of Se atoms estimated in the bulk region of the GC, the integrity of GC (as a nuclear storage container) cannot be limited. However, HRTEM investigation on the GC samples annealed at temperatures where the migration of Se initially occurred would give more information about the migration behaviour of Se atoms at an atomic scale.
- The diffusion behaviour of selenium in GC is just one of the few existing studies of fission products in GC. More diffusion studies of fission products in GC are needed to get more insight into the diffusion capability of GC material. Since the radioactivity of nuclear wastes produces many fission elements, these fission

elements can coexist, resulting in a synergistic effect. Furthermore, the effects of many other fission products on the migration of selenium in GC will be investigated.

- Electron energy loss spectroscopy (EELS) will be applied to determine the sp^2 and sp^3 bond contents in GC implanted with Se, Co and Xe, which will be compared with the three-stage model results.

Appendix

The PhD research project presented in this thesis has contributed to publications and conference presentations, as highlighted below:

Publications in peer-reviewed/refereed journals

1. **S.A. Adeojo**, J.B. Malherbe, E.G. Njoroge, M. Mlambo, O.S. Odutemowo, T.T. Thabethe, Z.A.Y. Abdalla, T.T. Hlatshwayo, Effect of sequential isochronal annealing on the structure and migration behaviour of selenium-ion implanted in glassy carbon, *Vacuum*. **182** (2020), 1 – 12.

2. **S.A. Adeojo**, A. Azarov, O.S. Odutemowo, E. Njoroge, H.A.A. Abdelbagi, J.B. Malherbe, T.T. Hlatshwayo, The influence of implantation temperature and annealing on ion-implanted selenium in glassy carbon: structural changes and migration behaviour investigation, *Solid State Sciences*, **129** (2022), 1 – 10.

Conference Presentations

1. Faculty of Science 2021 International Conference, held at the Obafemi Awolowo University, Ile-Ife, Nigeria from June 8 – 9, 2021. (Oral presentation).

2. The 66th Annual Conference of the South African Institute of Physics (SAIP 2021). Department of Physics, held at North-West University, South Africa from 22-30 July 2021, (Poster presentation).